EFFECT OF APERTURE VARIABILITY, SPECIFIC DISCHARGE, AND IONIC STRENGTH ON COLLOID TRANSPORT IN SINGLE FRACTURES

By

QINGHUAI ZHENG, M. Sc.

Faculty of Engineering
Department of Civil Engineering

A Thesis
Submitted to the School of Graduate Studies
in Partial Fulfillment of the Requirements
for the Degree

Doctor of Philosophy

McMaster University
Hamilton, Ontario, Canada
September 2008

Doctor of Philosophy (2008) McMaster University
(Civil Engineering) Hamilton, Ontario

TITLE: Effect of Aperture Field Variability, Specific Discharge, and Ionic Strength on Colloid Transport in Single Fractures

AUTHOR: Qinghuai Zheng, M. Sc.

SUPERVISOR: Dr. Sarah E. Dickson, Dr. Yiping Guo

NUMBER OF PAGES: xvii, 258

Abstract

An improved understanding of colloid transport in fractured media is required to assess the potential for microorganisms to contaminate groundwater, to develop groundwater management/protection plans, to design remedial action strategies based on the application of microorganisms, and to quantify colloid-facilitated transport of many organic and inorganic contaminants. Although colloid transport has been investigated to an extent in porous media environments, this field is still in its infancy in fractured media environments.

Colloid transport in fractured media involves a host of complex and interacting processes, including (among others): advection, hydrodynamic dispersion, attachment and detachment, straining, size/charge exclusion, and gravitational settling. These processes are, in turn, influenced by the physicochemical properties of fractured media, the geochemical properties of groundwater, hydrodynamics, and the colloid properties. This research program focused on investigating the effects of aperture field variability, specific discharge, and ionic strength on colloid transport in saturated, variable-aperture, single fractures. An extensive literature review was first conducted, and a combination of physical model experiments and numerical simulations were then employed to achieve this goal.

Three transparent fracture replicas were fabricated, and the light transmission method was employed to obtain a direct measurement of each of the three aperture fields. A systematic series of hydraulic and tracer tests was conducted on each of the three experimental fractures, and the cubic law, mass balance and frictional loss apertures were calculated. Additionally, the experimental breakthrough curves were fit to the one-dimensional advection-dispersion equation. The results clearly demonstrate that the mass balance aperture is the only appropriate 'equivalent aperture' for describing transport in a single variable-aperture fracture, and that the mass balance aperture is an excellent approximation of the arithmetic mean aperture.

A 3^3 factorial experimental design was then implemented to numerically investigate the interactive effect of the arithmetic mean (μ_b), standard deviation (σ_b), and anisotropic ratio (AR=λ^b_x/λ^b_y, where λ^b_x and λ^b_y is the correlation length of the aperture field along *x*- and *y*- direction respectively) of single fracture apertures on dispersion regimes (specifically Taylor dispersion and geometric dispersion) and dispersivity. The simulation results show that: (1) for a fixed hydraulic gradient: (a) the dominant dispersion regime is controlled by μ_b, and to a lesser degree, σ_b, and (b) geometric dispersion becomes more dominant as the coefficient of variation (CoV = σ_b/μ_b) increases; (2) for a fixed mean aperture, the dispersivity and the spread in dispersivity for varying ARs increase with the CoV; and (3) the AR has a significant effect on dispersivity only when the CoV is large (>0.2).

Numerical simulations investigating colloid and solute transport in single parallel-plate fractures, conducted using the Random Walk Particle Tracking (RWPT) method, demonstrated that: 1) There exists a threshold value, δ_o, of the aspect ratio, δ ($\delta = 2r_c/b$, where r_c and b represent the colloid radius and fracture aperture respectively), where the average transport velocities of colloids and solutes are similar. When $\delta > \delta_o$, the Taylor-Aris assumption is satisfied, and τ_p ($\tau_p = t_c/t_s$, where t_c and t_s represent colloid and solute retention times respectively) decreases as δ increases, as is well documented in the hydrodynamic chromatography literature. However, when $\delta < \delta_o$, the Taylor-Aris assumption is violated, and τ_p increases as δ increases. This has never been documented before, and it helps to explain some seemingly contradictory work in the literature. 2) The Taylor dispersion coefficient and its extension by James and Chrysikopoulos (2003) will overestimate the colloid dispersion coefficient significantly when the Taylor-Aris assumption is violated. Additionally, these simulations demonstrated that τ_p and $D_{L,coll}/D_{L,solute}$ (where $D_{L,coll}$ and $D_{L,solute}$ represent the dispersion coefficients of colloids and solutes respectively) decrease with increasing CoV, and that the anisotropy ratio, AR, only plays a minor role on these two ratios compared to the CoV. These observations have never been documented before to the knowledge of these authors, and have important implications towards the interpretation of colloid transport in both porous and fractured media.

A combination of physical experiments, numerical simulations and visualization techniques was employed to investigate the impact of aperture variability, specific discharge, and ionic strength on colloid transport processes. The mean colloid transport velocity and colloid dispersion coefficient were obtained by fitting the analytical solution of the one-dimensional advection-dispersion equation (ADE) to the measured breakthrough curves. Two significant observations were made from the colloid transport experiment images: (1) colloids migrate along preferential pathways, and bypass some aperture regions; and (2) the colloid plume is irregular in shape, and becomes more irregular with increasing specific discharge, indicating non-Fickian transport. It is therefore postulated that the dispersivity cannot be completely determined by the aperture field characteristics alone; it is also a function of specific discharge. The colloid recovery in all fractures was found to increase with increasing specific discharge. For each specific discharge, it was found that the colloid recoveries in F2 and F3 were similar, and were always larger than the recovery in F1. This is consistent with the fact that the arithmetic mean apertures of F2 and F3 were similar ($\mu_{b,F2}$ = 1.57 mm, $\mu_{b,F3}$ = 1.75 mm), and larger than that of F1 ($\mu_{b,F1}$ = 0.88 mm). This suggests that it is the transport step (the step in which the colloids are transported from the bulk fluid to the vicinity of the fracture wall), and not the attachment step, that plays the dominant role in the colloid sorption process. It was also found that the mean transport velocity and dispersion coefficient of colloids are larger than those of solutes in F3 (CoV = 0.29), but similar to those of solutes in F1 (CoV = 0.78) and F2 (CoV = 0.71). This confirms the numerical simulation results from this work indicating that τ_p and $D_{L,coll}/D_{L,solute}$ decrease with increasing CoV. These findings have significant implications on the interpretation of colloid transport data.

Acknowledgement

I would like to thank my supervisors, Dr. Sarah E. Dickson and Dr. Yiping Guo, for their guidance and support throughout my research at McMaster University. I greatly appreciate the opportunities they gave me to develop my skills as a researcher. I especially appreciate the regular meetings with Dr. Sarah E. Dickson, even during the period she had a family emergency. I greatly appreciate the interest and guidance I received from my supervisory committee, Dr. Brian W. Baetz and Dr. James E. Smith.

Gratefully acknowledged are the research grants received from the Natural Science and Engineering Research Council of Canada (Sarah E. Dickson and Yiping Guo).

I greatly appreciate the assistance from Mr. Peter Koudys at the Geotechnical Laboratory during my experimental setup. I would also like to thank my colleagues, Kevin G. Mumford and Erika Ryter, for their enlightening discussions and for their suggestions.

Last, but definitely not least, I am indebted to my family, my wife Liying Wu, my son Edwin, my daughter Jessica, my parents, my parents-in-law, and my sister-in-law for their enduring support. I promise to spend more time with you from now on.

This thesis is dedicated to my wife and children.

Preface

This thesis has been prepared in accordance with the regulations for the "sandwich" thesis format, or as a compilation of papers, stipulated by the Faculty of Graduate Studies at McMaster University. The preface describes the five published/prepared papers included in this thesis, and specifically my contribution to these co-authored publications.

Chapter 2

Title: A review of saturated subsurface microbial transport processes: fractured vs. porous media.

Authors: Qinghuai Zheng, Sarah E. Dickson, and Yiping Guo

Planned submission to: *Transport in Porous Media*

This is a review paper, which examines the relatively extensive literature regarding colloid (abiotic and biotic) transport in porous media and attempts to derive lessons from this literature that is instructive towards the understanding of colloid transport in fractured media. The extensive literature review was conducted by Q. Zheng in consultation with S. E. Dickson. The text was written by Q. Zheng and edited by S. E. Dickson.

Chapter 3

Title: On the appropriate ''equivalent aperture'' for the description of solute transport in single fractures: laboratory-scale experiments.

Authors: Qinghuai Zheng, Sarah E. Dickson, and Yiping Guo

Published in: *Water Resources Research*, 2008

The experiments were designed by Q. Zheng in consultation with S. E. Dickson, and conducted by Q. Zheng. The data analysis was conducted by Q. Zheng in consultation with S.E. Dickson. The text was written by Q. Zheng and edited by S. E. Dickson.

Chapter 4

Title: The influence of aperture field heterogeneity and anisotropy on dispersion regimes and dispersivity in single fractures

Authors: Qinghuai Zheng, Sarah E. Dickson, and Yiping Guo

Accepted by: *Journal of Geophysical Research (Solid Earth)*, 2008

The numerical simulations were conceived, designed, and conducted by Q. Zheng. Interpretation of the results was conducted by Q. Zheng. The text was written by Q. Zheng and edited by S.E. Dickson.

Chapter 5

Title: Observation of a new phenomenon for the differential transport of colloids and solutes in single, variable-aperture fractures

Authors: Qinghuai Zheng, Sarah E. Dickson, and Yiping Guo

Submitted to: *Journal of Colloid and Interface Science* (October 2008)

The numerical simulations were conceived, designed, and conducted by Q. Zheng. Interpretation of the results was conducted by Q. Zheng. The text was written by Q. Zheng and edited by S.E. Dickson.

Chapter 6

Title: Colloid transport in laboratory-scale variable-aperture single fractures: visualization experiments and modeling results

Authors: Qinghuai Zheng, Sarah E. Dickson, and Yiping Guo

Planned Submission to: *Water Research* (Fall 2008)

The experiments were designed by Q. Zheng in consultation with S.E. Dickson, and conducted by Q. Zheng. The colloid transport visualization system and aperture measurement system were developed by Q. Zheng. Numerical simulations were designed and conducted by Q. Zheng. Analyses and interpretation of the data from the experiments and numerical simulations were conducted by Q. Zheng in consultation with S. Dickson. The text was written by Q. Zheng and edited by S.E. Dickson.

Permission has been granted to McMaster University and to the National Library of Canada by the American Geophysical Union to reproduce the material in chapters 3 and 4, respectively, as part of this thesis. The material in chapters 2, 5 and 6 have either been submitted very recently, or not yet been submitted, to the following journals respectively: *Transport in Porous Media*, *Journal of Colloid and Interface Science,* and *Water Research*; therefore copyright has not yet been assigned.

Table of Contents

List of Tables

List of Figures

Chapter 1 Introduction

Fractures are defined as discontinuous planar features within any rock mass that may have developed as a result of pressure and temperature differences during and/or after the formation of the rock (Sen, 1995). Fractures are generally more numerous at the rock surface and become sparser with depth. They dissect the host rock mass into intact fragments, which are referred to as blocks or the matrix. From a geological point of view, joints, faults, and fissures are special types of fractures, depending on the relative movement of adjacent rock blocks. Fractured geological formations are ubiquitous throughout the world.

An increasing interest in the transport of colloids (both biotic and abiotic) in fractured media is motivated by several factors. Colloids can be appropriate tracers to study the complex flow field in fractured media (Harvey 1997). A major feature of groundwater flow in fractured media is the appearance of preferential flow paths (Neretnieks 1993; Brown et al. 1998). Colloids typically migrate with the aqueous flow in saturated fractures and have limited ability to diffuse into the porous matrix due to their physical size or the interaction forces between the colloid and solid surfaces, thus making them a good indicator of flow channeling (e.g., Champ and Schroeter 1989; McKay et al. 1993; Beeder et al. 1996; Hinsby et al. 1996; Strong- Gunderson and Palumbo 1997). In safety assessments of nuclear waste repositories, the migration of radionuclides through rock fractures has been considered as one of the most serious potential hazards among various transport mechanisms (Degueldre et al. 1989). Researches have found that sorption of contaminants (e.g., radionuclides) on groundwater colloids may significantly influence their transport behaviour through fractured media (Smith and Degueldre 1993; Grindrod 1993; van der Lee et al. 1992). Due to an increasing dependence on limited and fragile groundwater resources, the potential microbial contamination to drinking-water aquifers through quick migration in fractures has become a significant concern (Allen and

Morrison 1973). Additionally, Field- and lab-scale bioremediation and bioaugmentation experiments have been conducted in fractured media to study the possibility of using microbes to recover the contaminated fracture aquifers (Yager et al. 1997; McLinn and Rehm 1997; Ross et al. 2001; Ross and Bickerton 2002; Hill and Sleep 2002). All of these challenges require a good understanding of the processes governing the transport of colloids under the specific physical, chemical, and biological conditions involved in fractured media. However, few theoretical and experimental efforts have been conducted to investigate the fate and transport of colloids in fractures to date (e.g. Bales et al., 1989; Champ and Schroeter, 1989; McKay et al, 1993, 1999, 2000; Hinsby et al., 1996; Harton et al., 1996; Geller et al., 2000; Ross et al., 2001; Hill et al., 2002; Ross and Bickerton, 2002), and therefore a complete understanding is currently in its early stages of development. Microbial transport in a discrete rough-walled fracture, the basic constructive unit of fractured media, is an appropriate starting point for studies of more complex issues of microbial transport in fracture networks, and hence is the focus of this research.

1.1 Research Goal and Objectives

Colloid transport in fractured media involves a host of complex and interacting processes, including (among others): advection, hydrodynamic dispersion, attachment and detachment, straining, size/charge exclusion, and gravitational settling. These processes are, in turn, influenced by the fractured media properties (e.g., fracture wall roughness, aperture variability, physicochemical characteristics of the solid surface, etc.), the geochemical properties of groundwater (e.g., ionic strength, pH, etc.), hydrodynamics, and the colloid properties (e.g., surface properties, size, density, etc.). The objective of this research is to investigate the effect of aperture field variability, specific discharge, and ionic strength on colloid transport (i.e., advection, dispersion, and retention mechanisms) in discrete saturated variable-aperture fractures. This goal was achieved through both physical model experiments and numerical simulations as described below:

- Three transparent fracture replicas were fabricated and the aperture fields were measured using light transmission techniques.
- A series laboratory hydraulic and solute tracer tests were conducted to determine the appropriate “equivalent aperture” for describing solute transport in single variable-aperture fractures.
- Numerical simulations were conducted to explore the relationship between aperture field geometry (heterogeneity and anisotropy), dispersion regimes, and dispersivity in single fractures.
- A series of numerical simulations was conducted to investigate differential transport between colloids and solutes through parallel-plate and variable-aperture fractures.
- A 3^3 factorial series of laboratory colloid tracer tests, with the assistance of visualization system and numerical simulations, was conducted to investigate the effects of aperture field variability, specific discharge, and ionic strength on colloid transport (i.e., advection, dispersion, attachment/detachment, straining, gravitational settling, and size exclusion).

1.2 Thesis Scope

This thesis is comprised of six additional chapters. Chapter 2 reviews the literature that exists concerning the physicochemical and biological processes governing biotic (specifically microbial) and abiotic colloid transport in saturated subsurface fractured media. Chapter 3 presents a series of laboratory-scale hydraulic and conservative solute tracer experiments conducted to demonstrate the appropriate “equivalent aperture” for the description of solute transport in single fractures. Chapter 4 describes numerical simulations conducted to investigate the effects of aperture field heterogeneity and anisotropy on dispersion regimes and dispersivity in single fractures. Chapter 5 demonstrates a differential transport phenomenon in saturated, single, parallel-plate fractures that has not been reported before, and describes the impact of aperture field heterogeneity and anisotropy on differential transport. Chapter 6 describes an investigation on the effects of aperture field variability, specific discharge, and ionic strength on colloid transport (i.e., advection, dispersion, attachment/detachment, straining, gravitational settling, and size exclusion) through a combination of physical colloid tracer tests and numerical simulations. Chapter 7 offers the conclusions and important contributions stemming from this work, and provides recommendations for future work.

References

Allen, M. J., and S. M. Morrison (1973), Bacterial movement through fractured bedrock, *Ground Water*, 11(2), 6-10.

Bales, R. C., C. P. Gerba, G. H. Grondin, and S. L. Jensen (1989), Bacteriophage transport in sandy soil and fractured tuff, *Appl. Environ. Microbiol.*, 55, 2061-2067.

Beeder, J., R. K. Nilsen, T. Thorstenson, T Torsvik (1996), Penetration of sulphate reducers through a porous North Sea oil reservoir, *Appl. Environ. Microbial.*, 62, 3551-3553.

Brown, S., A. Caprihan, R. Hardy (1998), Experimental observation of fluid flow channels in a single fracture, *J. Geophys. Res.*, 103(B3), 5125-5132.

Champ, D. R., and J. Schroeter (1989), Bacterial transport in fractured rock-- a field-scale tracer test at the Chalk River Nuclear Laboratories, *Wat. Sci. Tech.*, 20(11/12), 81-87.

Degueldre, C., B. Baeyens, W. Goerlich (1989), Colloids in water from a subsurface fracture in granitic rock, Grimsel Test Site, Switzerland, *Geochimica et Cosmochimica Acta*, 53, 603-610.

Geller, J. T., H. Y. Holman, G. Su, M. E. Conrad, K. Pruess, J. C. Hunter-Cevera (2000), Flow dynamics and potential for biodegradation of organic contaminants in fractured rock vadose zones, *J. Contam. Hydrol.*, 43, 63-90.

Grindrod, P. (1993), The impact of colloids on the migration and dispersal of radionuclides within fractured rock, *J. Contam. Hydrol.*, 13, 167-181.

Harton, A. D. (1996), Influence of flow rate on transport of bacteriophage in a column of highly weathered and fractured shale, Master's thesis, Department of Geol. Sci., University of Tennessee, Knoxville.

Harvey, R. W. (1997), Microorganisms as tracers in groundwater injection and recovery experiments: a review, *FEMS Microbiol. Rev.*, 20, 461-472.

Hill, D. D., B. E. Sleep (2002), Effects of biofilm growth on flow and transport through a glass parallel plate fracture, *J. Contam. Hydrol.*, 56, 227-246.

Hinsby, K., L. D. McKay, P. Jorgensen, M. Lenczewski, C. P. Gerba (1996), Fracture aperture measurements and migration of solutes, viruses, and immiscible creosote in a column of clay-rich till, *Ground Water*, 34(6), 1065-11075.

Mckay, L. D., J. A. Cherry, R. C. Bales, M. T. Yahya, and C. P. Gerba (1993), A field example of bacteriophage as tracers of fracture flow, *Environ. Sci. Technol.*, 27, 1075-1079.

Mckay, L. D., J. Fredericia, M. Lenczewski, J. Morthorst, and K. E. Klint (1999), spatial variability on contaminant transport in a fractured till, Avider Denmark, *Nord. Hydrol.*, 30, 333-360.

Mckay, L. D., W. E. Sanford, and J. M. Strong (2000), Field scale migration of colloidal tracers in a fractured shale saprolite, *Ground Water*, 38, 139-147.

McLinn, E. L., B. W. Rehm (1997), Biodegradation of petroleum hydrocarbons in fractured, unsaturated dolomite at a field site, *Ground Water Monit. Rem.*, 17(4), 73–80.

Neretnieks, I. (1993), Solute transport in fracture rock—applications to radionuclide waste repositories. In: Bear J, Tsang CF, de Marsily G, editors. Flow and contaminant transport in fractured rock. San Diego: Academic Press, Inc., P. 39-127.

Ross, N., R. Villemur, L. Deschenes, R. Samson (2001), Clogging of a limestone fracture by stimulating groundwater microbes, *Wat. Res.*, 35(8), 2029-2037.

Ross, N., G. Bickerton (2002), Application of biobarriers for groundwater containment at fractured bedrock sites, *Remediation Journal*, 3(3), 5-21.

Sen, Z. (1995), Applied hydrology for Scientists and Engineers, CRC Press, Inc.

Smith, P. A., C. Degueldre (1993), Colloid-facilitated transport of radionuclides through fractured media, *J. Contam. Hydrol.*, 13, 143-166.

Strong-Gunderson, J. M., A. V. Palumbo (1997), Laboratory studies identify a colloidal groundwater tracer: implications for bioremediation, *FEMS Microbiol. Lett.*, 148, 131-135.

Van der Lee J, Ledoux E, de Marsily G. 1992. Modeling of colloidal uranium transport in a fractured medium, *J. Hydrol.*, 139, 135-158.

Yager, R. M., S. E. Bilotta, C. L. Mann, E. L. Madsen (1997), Metabolic adaptation and in situ attenuation of chlorinated ethenes by naturally occurring microorganisms in a fractured dolomite aquifer near Niagara Falls, New York, *Environ. Sci. Technol.*, 31(11), 3138–3147.

Chapter 2 A Review of Saturated Subsurface Colloid Transport Processes: Fractured vs. Porous Media

Abstract

There is a growing concern over the fate and transport of colloids in groundwater, however most of the research that has been conducted in this field to date has been directed at porous media environments. Fractured subsurface environments are ubiquitous throughout North America and are a common source of drinking water, and therefore it is important to gain a better understanding of colloid transport in these environments. This paper reviews the existing literature concerning the physicochemical processes governing colloid transport in saturated subsurface fractured environments. Additionally, because porous media concepts are often instructive to our understanding of fractured media, this paper reviews the extensive literature concerning the physicochemical processes governing colloid transport in saturated porous media environments, and examines the applicability of these concepts to fractured environments.

Key Words: colloid transport, fractured media, porous media, groundwater contamination

2.1. Introduction

Fractured geological formations are ubiquitous throughout the world, and are a common source of drinking water. An increasing interest in the transport of colloids (including biotic and abiotic colloids) in fractured media is motivated by several factors. Microorganisms can be appropriate tracers to study complex flow field in fractured media (Harvey 1997). A major feature of groundwater flow in fractured media is the appearance of preferential flow paths (Neretnieks 1993; Brown et al. 1998). Microorganisms typically migrate with the aqueous flow preferential pathways within the fracture, and have limited ability to diffuse into porous matrix (due to physical size and/or interaction forces between microbes and solid surface). This makes microorganisms a good indicator of flow channelling (e.g., Champ and Schroeter 1989; McKay et al. 1993a; Beeder et al. 1996; Hinsby et al. 1996; Strong- Gunderson and Palumbo 1997). In safety assessments of nuclear waste repositories, the migration of radionuclides through fractures in the rock has been considered as one of the most serious potential hazards among various transport mechanisms (Degueldre et al. 1989). Researches have found that sorption of contaminants (e.g., radionuclides) on groundwater colloids (including microbes) may significantly influence their transport behaviour through fractured media (Smith and Degueldre 1993; Grindrod 1993; van der Lee et al. 1992). Due to an increasing dependence on limited and fragile groundwater resources, the potential microbial contamination to drinking-water aquifers through quick migration in fractures has become a big concern (Allen and Morrison 1973). Additionally, field- and lab-scale bioremediation and bioaugmentation experiments have been conducted in fractured media to study the possibility of using microbes to recover contaminated fracture aquifers (Yager et al. 1997; McLinn and Rehm 1997; Ross et al. 2001; Ross and Bickerton 2002; Hill and Sleep 2002). All of these challenges require a good understanding of the processes governing the fate and transport of colloids under the specific physical, chemical, and biological conditions involved in fractured media. However, few theoretical and experimental efforts have been conducted to investigate the fate and transport of colloids in fractures to date. Conversely, the literature pertaining to colloid transport in porous media is substantial; much of this work has been reviewed by Yates and Yates (1988), Lawrence and Hendry (1996), Clement et al. (1999), Murphy and Ginn (2000), Schijven and Hassanizadeh (2000), Harvey and Harms (2001), and Ginn et al. (2002) among others.

Groundwater flow in fractured media is distinct from that in unconsolidated porous media. However, it is expected that factors influencing colloid transport, such as adsorption and desorption, should be similar in both media, and results of investigations of colloid transport involving unconsolidated porous media may be instructive to our understanding of fractured media. In light of the postulated similarities between fractured and unconsolidated porous media, this paper will draw upon the literature relating to both of these fields of study, and specifically review important concepts and recent findings relating to colloid transport in fractured media. In addition, references will be cited from the extensive research conducted in the field of microbiology. These results, particularly those related to microbial transport in parallel plate flow chamber (e.g., Sjollema 1988, 1989; Bos et al. 1995), will be instrumental in developing a better understanding of microbial transport in fractures.

2.2. Processes Controlling Colloid Transport in the Subsurface

Colloid transport in the subsurface involves a host of complex and interacting processes. Although many of the details of these processes are still under investigation, it is generally agreed that the transport of microbes in the subsurface is broadly governed by physicochemical, and for biotic colloids, biological processes (Fletcher 1980; Murphy and Ginn 2000; Ginn et al. 2002). Physicochemical processes include advection-dispersion transport, gravitational sedimentation and size dependent transport, sorption, straining, and size and charge exclusion. These processes provide the framework for modeling microbial transport in fractured media, within which the impact of biological processes can be incorporated to study the complex physico-chemical-biological processes in a flowing groundwater system. However, relatively little attention has been paid to biological processes in the development of hydrogeological transport models due to their intractable characteristics. Therefore this paper will focus on physicochemical processes in fractured media. Readers are referred to reviews by Ginn et al. (2002) and Murphy and Ginn (2000) among others for extensive discussions of biological processes in the subsurface. Since Colloid transport in subsurface environments is an interdisciplinary topic, which is still in its early stages of research, the terminology used in the literature is not consistent.

2.2.1 Advection-Dispersion Transport

Fractured media is comprised of fractures (e.g., cracks, fissures, joints, and faults in a geological formation) and matrix blocks which surround the fractures. Fractures can be characterized at two different scales: a single fracture, and fracture networks (Sahimi 1995; Berkowitz 2002). A single fracture is usually described by its size, surface roughness, aperture field, and orientation, while fracture networks can be characterized by the fracture density and connectivity, as well as by spatial correlation among fractures. These features, which are often described by statistical and fractal techniques, control fluid flow and transport behaviour in fractured media. Field and laboratory experiments in natural fractures and fracture replicas have provided strong evidence of flow channelling and preferential flow paths, in both single fractures and fracture networks (Neretnieks 1993; Brown et al. 1998), due to the degree of fracture connectivity and distribution of hydraulic conductivity (Smith and Schwartz 1984; Tsang and Tsang 1987; Tsang et al. 1988; Margolin et al. 1998). Flow and transport are intimately coupled processes. These preferential flow pathways are key features governing microbial transport in fractures (see Section 2.2.5 for further discussion).

Mechanical dispersion in fractured media can occur at three different scales, including, a single fracture, fracture junctions, and fracture networks. At the elementary level of a single fracture, dispersion can be caused by a combination of Brownian diffusion and the more or less parabolic velocity profile across the aperture (Taylor dispersion, e.g., Kessler and Hunt 1994). Dispersion within single fractures can also occur due to the different advective velocity of different channels (Detwiler et al. 2000; Lee et al. 2003), leading to more dispersion along the overall flow direction than in homogenous media. It may also be caused by the advective exchange between immobile and mobile fluid fractions (Becker and Shapiro 2000). Fluid mechanics predict the formation of laminar eddies in channels with widely varying aperture (Pozrikidis 1987), which can act as a transfer mechanism between mobile and immobile fluid (Raven et al. 1988).

Fracture aperture heterogeneity and anisotropy significantly influence groundwater flow and colloid transport behaviour. For example, microbes tend to migrate along the flow channels due to size and/or charge exclusion, causing them to disperse less than a molecular-scale solute tracer would (Bales et al. 1989). Vilks and Bachinski (1996) found in their experiments that colloid transport was very sensitive to flow pathways and flow direction. Chrysikopoulos and Abdel-Salam (1997) employed numerical simulations to demonstrate that fracture variability could increase colloid spreading. Chrysikopoulos and James (2003) studied colloid transport in a fracture with a spatially variable and anisotropic aperture within a Lagrangian framework, and found that aperture field anisotropy oriented parallel to the primary flow direction substantially enhances colloid spreading, whereas aperture field anisotropy oriented transverse to the flow direction delays colloid migration.

At the scale of fracture junctions, research has demonstrated that mixture of solute and solvent could range from complete mixing to streamline routing depending on the Peclet number (Berkowitz et al. 1994; Stockman et al. 1997; Park et al. 1999). Sahimi (1995) stated that the degree of mixing at the junctions has a strong influence on the solute distribution in fracture networks. Park et al. (2003) has also shown through transport simulations in fracture intersections that local flow circulation can arise from the interplay between the hydraulic head distribution along fracture intersections and no flow conditions along fracture boundaries. They concluded that the local flow circulation could enhance the observed long breakthrough tailing in discrete fracture networks. However, Park et al. (2001a, b), by simulating solute transport in random fracture networks, concluded that the choice of mixing rules (i.e., complete mixing or streamline routing) is of little importance compared with the uncertainty of parameters defining the geometry of the fracture networks.

At the scale of fracture networks, transport may occur primarily by rapid advection in a high-conductivity, interconnected network of preferential flow channels, and by very slow advection in low-conductivity regions (Becker and Shapiro 2000), thus producing longitudinal and transverse plume spreading depending on the relative direction between individual flow paths and the macroscopic mean flow. It has been found that the controlling factors at this scale are the orientation of the fracture sets with respect to the macroscopic mean flow, the fracture connectivity, and the distribution of the fracture apertures (Kim et al. 2004). Due to the limited knowledge regarding colloid transport in fractured media, these findings regarding dispersion in fractured media are typically based on solutes, and therefore the applicability of these results to colloid transport in fractures is not clear.

Matrix blocks can range from being very porous to containing negligible void space. Generally, fractured media is complex with vast differences in porosity and permeability between the fractures and the porous matrix (Oswald 2001). Fracture-matrix interaction plays an important role in solute transport in fractured media (e.g., Bales et al. 1989; McKay et al. 1993a, b; McKay et al. 2000). However, its impact on colloid transport remains unclear. Field and lab experiments have shown that microbes mainly migrate in fractures with very limited diffusion into porous matrix. In a laboratory experiment conducted in fractured rock, Bales et al. (1989) found that phage f2 was largely excluded from the porous matrix of the two fractured rock cores studied, although they still attributed the retardation of the phage to the either diffusion into large but shallow pores, or adsorption. McKay et al. (1993a) conducted a field experiment through a weathered and fractured clay-rich till, and observed that the bacteriophages MS-2 and PRD-1 behaved markedly differently from bromide tracers, with the bacteriophages travel time on the order of 0.5-1% of those for the bromide. They reasoned that the bacteriophages mainly travelled through the fractures, with minimal diffusion into the porous clay matrix. They also suggested that either colloid adsorption or limited diffusion into large pores was responsible for the colloidal attenuation that was observed. Cumbie and McKay (1999) conducted column experiments using a fractured shale saprolite, and dismantled the soil column after a tracer tests to examine the distribution of the retained fluorescent microspheres under UV light. They found that both colloid particles and solutes diffused to varying depths into the porous matrix (up to 3-4 mm for the smallest colloids of 0.05-0.1 μm in diameter in their experiments). For colloids, the distance travelled in the porous matrix was a function of diameter, with smaller colloids migrating further into the matrix than larger ones. However they still suggested that the losses due to colloid diffusion into matrix were small. Kosakowski (2004) conducted field experiments with colloids and radionuclides in a shear zone. By analyzing the observed breakthrough curve using different transport model, they concluded that matrix diffusion was of minor importance in their colloid transport experiments.

The effect of colloid diffusion into the matrix is not usually considered in mathematical modeling (e.g., Ibaraki and Sudicky 1995; Abdel-Salam and Chrysikopoulos 1995; Chrysikopoulos and Abdel-Salam 1997; Kosakowski 2004; James and Chrysikopoulos 2000). However, Oswald and Ibaraki (2001) performed numerical experiments simulating colloid transport in discretely fractured porous media to investigate the importance of matrix diffusion at different scales. They also performed simulations in attempt to replicate the results of a laboratory column study conducted by Cumbie and McKay (1999), and demonstrated that the filtration of colloid particles in the porous matrix can greatly affect the tailing of breakthrough curves once the colloid source has been removed. Additionally, they performed field-scale simulations involving colloid transport in shale fracture networks, and the results indicated that the matrix diffusion process can significantly retard the migration of colloids in fracture networks. Thus, they concluded that in environments where porosity is relatively high, and colloid particles are small enough to diffuse into the matrix, the process of matrix diffusion becomes dominant in controlling the migration of colloids in discretely fractured porous media. James and Chrysikopoulos (1999) studied the influence of matrix diffusion on variably sized colloids in a fracture with a uniform aperture using a particle tracking method, and found that increasing the matrix porosity leads to higher matrix diffusion, which in turn delays the particle breakthrough. However, given the limited research that has been conducted to date with varying results, the influence of matrix diffusion on colloid transport in fractured media cannot be known with certainty.

2.2.2 Sedimentation and Size-Dependent Transport

Colloid transport differs from solute transport in many aspects, such as colloid-colloid interactions (e.g. aggregation), and colloid-solid surface interactions (e.g., adsorption), mechanical clogging effects, gravity settling, and size-dependent transport. Gravitational sedimentation and size-dependent dispersion will be addressed in this Section, and the other processes will be dealt with later in this paper.

Gravitational sedimentation can potentially contribute to either adsorption or downward movement of suspended particles. Viruses and some bacteria are neutrally buoyant (Corapcioglu and Haridas 1985; Yates and Yates 1988) (i.e., their densities are similar to that of groundwater), and therefore gravity sedimentation can be neglected, particularly when flow rates are high and residence timescales are short (Hornberger et al. 1992). However, bacteria sedimentation has been shown to contribute errors in laboratory assays of motility and chemotaxis (Shonnard et al. 1992). Median bacteria sedimentation velocities of 7-17 mm/d in saturated sand columns under hydrostatic conditions were reported (Wan et al. 1995), which may be a significant mechanism for bacterial transport when time scales are sufficiently large. Becker et al. (1999) conducted lab- and field-scale experiments in fractured media using different sizes of microspheres as the tracer, and found that some attenuation of microspheres was evident at all scales, and larger microspheres were immobilized to a greater extent than smaller microspheres. By comparing the rates of Brownian motion and Stokes settling of the microspheres, they suggested that aggregation and/or sedimentation were responsible for the attenuation. Cumbie and Mckay (1999) also showed through lab experiments in fractured media that gravitational settling is likely an important process for larger micropsheres. The gravitational sedimentation velocity can be approximated using Stokes' velocity for spherical particles:

$$v_s = \frac{g}{18\mu}\left(\rho_c - \rho_f\right)d_c^2 \tag{2.1}$$

where μ [$M \cdot L^{-1} \cdot t^{-1}$] is the fluid dynamic viscosity, g [$L \cdot t^{-2}$] is the gravitational acceleration, ρ_c [$M \cdot L^{-3}$] is colloid density, ρ_f [$M \cdot L^{-3}$] is the fluid density, and d_c [L] is the colloid diameter. Yao et al. (1971) incorporated the sedimentation velocity into the advection-dispersion equation by superimposing a downward component, expressed by equation (2.1), on the advective velocity to study particle filtration in porous media. Adamczyk and van der Ven (1981) also considered the effect of gravity when they analytically derived the particle deposition rate in a parallel-plate flow channel. Chrysikopoulos and James (2003) investigated the effect of gravitational sedimentation velocity on the transport of colloids in a single saturated fracture with a spatially variable aperture using a particle-tracking model. They found that the transport of dense colloid suspensions was retarded compared to neutrally buoyant colloid suspensions. Jen and Li (2001) studied colloid-facilitated migration of radionuclides in fractured rock, and found that gravitational forces strongly affect the average velocity of colloids.

Another distinct feature of colloid transport relative to solute transport is that the colloid velocity, dispersion, and recovery all exhibit size dependence (see Sections 2.2.4 and 2.2.5 for further discussion). Colloids disperse within a fracture due to Brownian diffusion and the parabolic velocity profile. Colloid diffusion is usually assumed isotropic, and Brownian diffusivity can be approximated by the Stokes-Einstein equation (Weber and DiGiano 1996):

$$D_B = \frac{k_B T}{3\pi\mu d_c} \tag{2.2}$$

where k_B [$M \cdot L^2 \cdot t^{-2} \cdot T^{-1}$] is the Boltzmann constant, T [T] is the absolute temperature, μ [$M \cdot L^{-1} \cdot t^{-1}$] is the fluid dynamic viscosity, and d_c [L] is the colloid diameter. If Taylor dispersion conditions have been established, the longitudinal Taylor dispersion coefficient, D_L [$L^2 \cdot t^{-1}$], within a fracture is given (e.g., Kessler and Hunt 1994):

$$D_L = D_B + {v_m}^2 b^2 / 210 D_B \tag{2.3}$$

where v_m [$L \cdot t^{-1}$] is the mean velocity in the fracture, and b [L] is the fracture aperture. Equations (2.2) and (2.3) have often been employed to model colloid transport in fractures (e.g., Grindrod and Lee 1997; James and Chrysikopoulos 1999, 2000). One can see that colloid diffusivity is inversely dependent on its size. This has some implication on colloid transport. At the laboratory scale, the reduced rate of Brownian diffusivity related to a larger particle will prevent it from migrating out of the high-velocity centre streamline in the fracture (Taylor 1953). At larger scales, the slower diffusivity of larger colloids may mean that stagnant fluid volumes contained in dead-end fractures, wall asperities, fracture detritus, etc. will be relatively inaccessible to larger colloids (Becker et al. 1999). Also, because Taylor dispersion is proportional to the colloid size, larger colloids will spread more than smaller colloids. All of these factors may contribute to the findings that colloids migrate faster than solute, and larger colloids travel faster than smaller colloids.

Size-dependent transport has been observed in both lab and field experiments. In a laboratory experiment performed in a fractured tuff block, it was found that the larger microspheres arrived on average earlier than the smaller ones (Becker et al. 1999). This finding is consistent with the well-documented hydrodynamic chromatography literature in porous media (e.g., Yau et al. 1979). Numerical models showed a similar trend to the physical experiments (e.g., James and Chrysikopoulos 1999, 2000). James and Chrysikopoulos (1999, 2000) also demonstrated, in their study on colloid transport in fractures with uniform and spatially variable apertures using a particle tracking model, that 1) lognormal-distributed polydisperse colloids exhibit greater spreading than monodisperse suspension, 2) spreading of the polydisperse colloids increases with increasing variance in the particle diameter, and 3) size separation based on colloid size occurs along the primary flow direction in the fracture. However, Kosakowski (2004) conducted field experiments in a shear zone, and observed that the normalized colloid breakthrough curves are independent of the colloid size. Vilks and Bachinski (1996) also found in their experiments that, within the size range of colloids used in their studies (0.022-0.090 μm), colloid size did not influence colloid migration. Another important feature of size-dependent colloid transport is that the recovery rate of colloids can be very low (e.g., Vilks et al. 1997; Cumbie and McKay 1999; Kosakowski 2004), with larger colloids having even lower recovery rates. The effect of the colloid size on transport cannot be stated with the current state of knowledge.

2.2.3 Sorption

For the purposes of this paper, the term attachment refers to all processes by which suspended colloid is transferred to the solid phase. Detachment refers to the loss of colloids from the solid phase, and its re-entrainment into the aqueous phase. The sorption process is conveniently divided into two sequential steps: transport and attachment (Elimelech and O'Melia 1990).

(1) In the first step, colloids are transported from the bulk fluid to the vicinity of a stationary surface as a result of convection, diffusion, gravity, fluid drag, or some combination of these processes.

(2) Colloid attachment to the solid surface can occur due to various interaction forces, including the Lifshitz-van der Waals forces, electrostatic forces, Lewis acid-base interactions, Brownian movement forces, gravity, and hydrodynamic forces (Wan et al. 1995; Bos et al. 1999). It is important to point out that the fundamental non-covalent forces involved in adsorption between biological and non-biological macromolecules, solid surfaces and particulates include the Lifshitz-van der Waals forces, electrostatic forces, Lewis acid-base interactions, and Brownian movement forces (van Oss 1994). Other forces, such as hydrophobic interactions, hydration forces, steric interactions etc., all originate from these fundamental forces.

2.2.3.1 Dynamic Aspects of Colloid Sorption

Sorption is a time-dependent dynamic process. As colloids attach onto solid surface, the attachment rate will either increase or decrease, depending on the nature of colloid-colloid interactions. If the colloid-colloid interactions are favourable (i.e., in the absence of an electrostatic energy barrier), the attached colloids enhance the attachment rate by acting as additional collectors (Yao et al. 1971; Tien 1989; Darby and Lawler 1990). This dynamic phenomenon is known as ripening, and may occur in groundwater with elevated levels of dissolved solids or hardness. As opposed to ripening, "blocking" phenomena (also referred to as surface exclusion) will occur when the colloid-colloid interactions are repulsive, so that attached colloids prevent attachment of other colloids in a certain area, and a declining attachment rate results (Schaaf and Talbot 1989; Sjollema and Busscher 1990). This phenomenon may prevail in groundwater having low ionic strength and reduced levels of hardness.

Accumulation of colloids (particularly microbes) in the subsurface has the ability to clog pores or fracture void spaces, thereby reducing both the porosity and permeability of the porous media (Cunningham et al. 1997; Hiebert et al. 2001; Baveye et al. 1998; Vandevivere and Baveye 1992 a, b, c; Dennis and Turner 1998), as well as the fractured media (Yager et al. 1997; McLinn and Rehm 1997; Ross et al. 2001; Ross and Bickerton 2002; Hill and Sleep 2002). Reduced porosity and permeability will in turn affect groundwater flow rates, as well as contaminant transport, thus leading to a coupled non-linear transport problem. Attempts have been made to develop a mathematical model that can predict the effects of colloid clogging on the properties of porous media (e.g., Okubo and Matsumoto 1979; Taylor et al. 1990 a, b; Cunningham et al. 1991, Vandevivere and Baveye 1995, Clement et al. 1996). However, to the knowledge of these authors, no such efforts have been made in fractured media.

2.2.3.2 DLVO Theory and Interaction Forces between Colloids and Solid Surface

Two physicochemical approaches are available to describe the interaction forces between colloids and solid surface, i.e., the thermodynamic approach (based on surface free energy) (Absolom et al. 1983; Busscher et al. 1984) and the Derjaguin-Landau-Verwey-Overbeek (DLVO) theory (Rutter and Vincent 1980; Tadros 1980). The DLVO theory is commonly used in the hydrogeological community, so the thermodynamic approach will not be discussed here. The classical DLVO theory describes the interaction forces between the colloids and the solid surface in profiles of the intersurface potential energy. Such profiles are constructed through summing the Lifshitz-van der Waals (ϕ^{LW}), and electrostatic interaction energies (ϕ^{EL})

$$\phi^{tot} = \phi^{LW} + \phi^{EL} \qquad (2.4)$$

where ϕ^{tot} [$M \cdot t^{-2}$] denote the total interaction energy. Van Oss et al. (1986) introduced a so-called extended DLVO theory by including short-range Lewis acid-base interactions (ϕ^{AB}) in (2.4) as follows:

$$\phi^{tot} = \phi^{LW} + \phi^{EL} + \phi^{AB} \qquad (2.5)$$

Although the DLVO theory provides a useful conceptual framework for characterizing the interaction between colloids and solid surfaces under varying conditions (e.g., pH, ionic strength, and colloid size), its unsuitability has been noticed in many cases. It has generally been shown that under favourable conditions (i.e., the absence of repulsive energy barriers or the presence of attractive double-layer interactions), colloid attachment models within the framework of the DLVO theory are satisfactory for predicting the effect of solution ionic strength, fluid velocity, and particle size. However, under unfavourable conditions, DLVO theory underestimates attachment by many orders of magnitude (Ryan and Elimelech 1996). The discrepancy between experiments and theory may be caused by among others (Elimelech et al. 1995): solid surface roughness at the molecular, colloidal, and granular scales; solid surface charge heterogeneity; interfacial electrodynamics; and sorption in secondary minima (according to DLVO theory).

2.2.3.3 Modeling Attachment/Detachment

Theoretically, the rate of colloid deposition can be calculated by solving the convection-dispersion equation, which incorporates the effects of convection, dispersion, and interaction forces between colloids and fracture walls. However, the exact analytical solution is too difficult to obtain, and only approximate solutions are available. In the Smoluchowski-Levich approximation, the analytical deposition rate, j_0^*, for the parallel plate flow configuration is (Bowen et al. 1976; Adamczyk and van de Ven 1981):

$$j_0^* = \frac{D_\infty \cdot C}{0.89 \cdot a_h} \left(\frac{2}{9} \frac{\left(\frac{1}{2}b\right) \cdot P_e}{x} \right)^{\frac{1}{3}} \tag{2.6}$$

where C [L^{-3}] is the colloid concentration in suspension, a_h [L] is the hydrodynamic radius of colloids, b [L] is the aperture of the parallel plate flow chamber, x [L] is the longitudinal distance from the entrance of the flow chamber, D_∞ [L^2·t^{-1}] is the colloid diffusion coefficient, and P_e [-] is the Peclet number given for the parallel plate configuration as

$$P_e = \frac{3}{4} \frac{Q \cdot a_h^{\,3}}{\left(\frac{1}{2}b\right)^3 \cdot w \cdot D_\infty} \tag{2.7}$$

where Q [L^3·t^{-1}] is the volumetric flow rate, w [L] is width of the parallel plate flow chamber. The analytical Smoluchowski-Levich approximation was obtained using the perfect sink boundary conditions, which means that all colloids arriving at the collector surface are irreversibly sorbed to the collectors. James and Chrysikopoulos (1999) incorporated Equation (2.6) into a Random Walk Particle Tracking model to describe the colloid adsorption rate in fractured media.

However, the assumptions underlying the Smolochowski-Levich approximation are seldom completely met. If j_0 denotes the actual sorption rate of colloids, the ratio

$$\alpha = \frac{j_0}{j_0^*} \tag{2.8}$$

is sometimes referred to as the deposition efficiency and describes the fraction of colloids arriving at the surface which result in attachment (Adamczyk and Van de Ven 1981; Dabros and Van de Ven 1982; Xia et al. 1989). A parallel plate flow chamber system incorporating a real image analysis system has been often used to measure the actual attachment/detachment rate of microorganisms, J_0 (Bos et al. 1999).

In practice, phenomenological models are typically used to investigate colloid attachment/detachment due to the incomplete knowledge of the interaction forces between colloids and solid surfaces. Kinetic sorption models, both reversible (e.g., James and Chrysikopoulos 1999, Chrysikopoulos and Abdel-Salam 1997, Oswald and Ibaraki 2001, van der Lee et al. 1992) and irreversible (e.g., James and Chrysikopoulos 2003a, Abdel-Salam and Chrysikopoulos 1995), and equilibrium isotherms (e.g. Chrysikopoulos and Abdel-Salam 1997, James and Chrysikopoulos 2003a, Ibaraki and Sudicky 1995), have been used to model the attachment /detachment rate of colloids in fractures. The time dependence of colloid attachment/detachment has been investigated theoretically. The residence time-dependent detachment rate has been investigated by assuming that it is an exponential function of residence time (Dabros and Van de Ven 1982). Johnson et al. (1995) provided a heuristic account of the effect of residence time on the reversibility of attachment/detachment through zeroing the detachment rate for microbes whose residence time exceeded a particular threshold. Ginn (1999) developed a theoretical approach enabling the tracking of residence time effects on arbitrary reaction terms. This approach supports both variable methods of accounting for residence time (e.g., cumulative vs. contiguous) as well as arbitrary specification of the effect of residence time on the overall partitioning kinetics. Moreover, the "blocking" (James and

Chrysikopoulos 1999, Chrysikopoulos and Abdel-Salam 1997) and “ripening” (e.g., Tien 1989) effects have been also incorporated into colloid attachment/detachment models.

2.2.4 Straining

Straining refers to the trapping of particles in down-gradient pore throats that are too small to allow particle passage (McDowell-Boyer et al. 1986). In principle, colloid straining depends on both the colloid size and the pore size distribution characteristics. However, few efforts have been made to study the influence of pore size distribution characteristics on colloid straining. Experiments have shown that increased colloid retention in porous media can be caused by increasing colloid size (Harvey et al. 1993) and/or decreasing the media grain size (Bradford et al. 2002); these observations were attributed to the straining mechanism. Sakthivadivel (1966, 1969) and Herzig et al. (1970) developed geometric relations between colloids and media grains with ideal spherical shapes to predict the influence of straining on colloid removal. Matthess and Pekdeger (1985) expanded this rule by considering the grain size distribution in porous media. Bradford et al. (2002) suggested that capillary pressure-saturation curves can be used to estimate the volume fraction of the pore space that has pores less than some critical diameter for straining. Bradford et al. (2002) demonstrated through soil column experiments and numerical simulations that traditional colloid attachment theory is not well suited to describe colloid transport in systems when straining is important—the fitted attachment coefficient would be unreasonably high if straining was not considered. Mathematical models have been put forward to account for colloid straining in porous media (Bradford et al. 2003; 2004).

Natural fractures have variable apertures; aperture field distributions are bounded by zero as a minimum, and tend to be skewed, suggesting either a lognormal (Keller 1998) or a gamma (Tsang an Tsang 1987) distribution. Colloids moving through fractures can be removed due to straining in small aperture regions or dead-end fractures. Kosakowski (2004) found in their field experiments in a shear zone that the recoveries for the different colloid size classes (from 50 nm to 500nm) decreased systematically with increasing size. They proposed straining (referred as mechanical filtration) and/or gravitational settling as possible mechanisms for this phenomenon. Cumbie and McKay (1999) conducted experiments in an undisturbed, saturated column of weathered and fractured shale saprolite using fluorescent carboxylate-coated microspheres as tracers. Their experiments showed that an optimum particle diameter existed (approximately 0.5-1.0 μm), which experienced the smallest losses. Haun (1998) also found in his experiments that there was an optimum colloid size, of approximately 1.0 μm, which experienced minimum retention. The existence of an optimum colloid size is consistent with the findings in granular media (Yao et al. 1971), which predict greater retention of larger than optimum particles, due to physical straining and/or gravitational settling, and greater retention of smaller than optimum particles, related to their higher rates of diffusion resulting in more frequent collisions with, and attachment to the media. Research on the effects of straining in saturated fractured media is in its infancy. To the knowledge of these authors, no researchers have attempted to address the straining process in a quantitative way in fractured media.

2.2.5 Exclusion: Effects due to Size and Charge

The terminology used to describe exclusion in the literature is not consistent, and the concepts used here are adapted from Ginn et al. (2002). Size exclusion is a phenomenon where transported colloids tend to be excluded from the lower-velocity regions near the solid wall in a pore throat or fracture due to their physical size, which is a fundamental effect in hydrodynamic chromatography. The separation of different particle sizes in uniform porous media due to hydrodynamic chromatography is well documented (e.g. Yau et al. 1979). When the colloid size is on the same scale as a significant fraction of pores or fracture aperture regions, the colloids will be excluded from these pores or regions due to their inability to fit, thereby being rerouted to larger pores or aperture regions. This phenomenon is referred to as pore exclusion. If the electrostatic forces between the colloids and the media surfaces are repulsive, the colloids may also be excluded from the location adjacent to solid surface due to charge exclusion. Figure 2.1 illustrates size/charge and pore exclusion in unconsolidated porous media and in single parallel-plate fractures. In all of these cases, the colloid particles will experience the higher end of the velocity distribution. By contrast, conventional Taylor-Aris transport theory assumes that molecular-scale solutes eventually thoroughly sample the full distribution of pore velocities, including those low velocities very close to solid surfaces. Therefore the average (Darcy scale) advective velocity of colloid particles will be higher than that of a conservative solute, with larger colloids being faster than smaller colloids.

Field and laboratory experiments conducted in porous media have demonstrated that microbial tracers and other colloid-sized particles can appear at downstream observation points in advance of inert solute tracers (e.g., Camper et al. 1993; Harvey et al. 1993; Powelson et al. 1993; Shonnard et al. 1994; DeBorde et al. 1999; Sinton et al. 2000; Zhang et al. 2001). This phenomenon is most commonly attributed to the processes of size or anion exclusion. However, exclusion effects are not consistently manifested in some field-scale experiments (e.g., Bales et al. 1995; Harvey et al. 1995). Alternative explanations also appear in the literature, including preferential flow through high-conductivity regions (Rehmann et al. 1999, 2000), or apparent retardation of the conservative tracer due to mass diffusion into secondary porosity zones that are unavailable to colloidal particles (Wood et al. 1990; Zhang et al. 2001).

Field and lab scale experiments in fractured media (Champ and Schroeter 1989; Bales et al. 1989; McKay et al. 1993a, b, 2000; Hinsby et al. 1996; Vilks and Bachinski 1996; Harvey 1997; Becker et al. 1999; Knapp et al. 2000) have also shown that colloids can travel faster, and disperse less than conservative molecular-scale tracers (Table 2.1), and larger colloids move faster than smaller colloids (Becker et al. 1999). These phenomena were also demonstrated in mathematical computation for simple geometries (Grindrod 1993). These phenomena are usually attributed to one or a combination of the following mechanisms: (1) size/pore exclusion and/or charge exclusion; (2) colloid transport along preferential flow pathways caused by macroscopic heterogeneity; and (3) diffusion of molecular-scale solutes into porous matrix (matrix diffusion). Knapp et al. (2000) stated that lift forces were partly responsible for the accelerated travel of colloids in their experiments, since lift forces can cause colloids to migrate from the channel walls toward the higher-velocity regions in the centre of the channel. Hydrodynamic chromatography phenomenon (i.e., the separation of particles due to size exclusion) has been observed in experiments in fractured media. Cumbie and McKay (1999) conducted experiments in an undisturbed saturated column of weathered and fractured shale saprolite, and found that there was substantial size-segregation of the microspheres between different fractures, and different regions within a single fracture.

Scale-dependent dispersion, characterized by unusually early breakthrough times or unusually long late-time tails in measured breakthrough curves, is often described as "non-Fickian" or "non-Gaussian" transport. Kosakowski (2004) observed both the early breakthrough and long late tailing in colloid transport experiments conducted in a shear zone, and attributed these phenomena to the structure of the flow field. Experimental studies showed that hydrodynamic dispersion (the so-called nondiffusive effect or advective processes in the original literatures) can cause non-Fickian spreading of colloids and anomalous tailing of breakthrough curves for both solutes and colloids (e.g., Hatano and Hatano 1998; Sidle et al. 1998; Becker and Shapiro 2000). James and Chrysikopoulos (2000) demonstrated, through modeling colloid transport in a fracture with spatially variable aperture, that increasing the variance of the aperture distribution results in increased tailing for both monodisperse and polydisperse colloid suspension. Park et al. (2003) suggested that local flow circulation in fracture junctions could also cause long breakthrough tailing.

Different methods have been developed to model the exclusion effects within the Eulerian framework using the advection-dispersion equation. Brenner and Edwards (1993) described the movement of neutrally-buoyant finite-sized Brownian spheres in

Poiseuille flow in a circular cylindrical tube employing the continuity equation of probability density. By constraining the spheres' center from accessing positions closer to the tube wall than their radius, they showed that the spheres move, on average, faster than the mean velocity of the carrier fluid. Shonnard et al. (1994) analyzed early breakthrough of cells relative to phenol red in a capillary tube mathematically based on Taylor-Aris theory, by assigning the microbes a lower radial diffusivity than the phenol red, and stated that the earlier breakthrough of the cells is accounted for by the difference in Taylor dispersion between the cell and the phenol red tracers. Gvirtzman and Gorelick (1991) simulated the exclusion effects on the migration of anions in an unsaturated field-scale porous media by reducing the porosity by an "excluded" fraction, which is inaccessible to the anions. Bradford et al. (2003) used a similar approach to investigate the exclusion effect on colloid transport in a saturated lab-scale porous media. Within the Lagrangian context, Ginn (2002) developed a mathematical approach to account for the exclusion phenomenon by associating the trajectories of the excluded particles with those of locally averaged ideal solute tracers on a one-to-one basis. The excluded particle trajectories are formed by detouring parts of the ideal particle trajectories that are unavailable to the excluded tracer. Scheibe and Wood (2003) developed a particle tracking model to simulate exclusion effects. In this approach, exclusion was modeled by truncating the lower end of the distribution of the longitudinal dispersive displacement. This approach leads to increased mean velocity of colloid-sized particles relative to conservative solute tracers and decreased apparent dispersion.

Researchers have also attempted to model the exclusion process in fractured media. Chrysikopoulos and Abdel-Salam (1997) developed a model to study colloid transport in a saturated fracture with a spatially variable aperture, accounting for colloid exclusion by eliminating both the advective and dispersive fluxes onto fracture elements with apertures smaller than 12 times the colloidal particle diameter. Their simulation illustrated that the exclusion effect increases colloid dispersion and leads to earlier breakthrough, especially for large-sized colloids. The dispersion enhancement, however, seems counterintuitive.

James and Chriysikopoulos (2003b) derived analytical expressions, considering the size exclusion effect, for the effective velocity and dispersion coefficient of particles migrating in a uniform fracture. Their study showed that, because of size exclusion, the effective particle velocity is increased while overall particle dispersion is reduced. James and Chriysikopoulos (2003a) derived analytical solutions describing the transport of a suspension of monodisperse and polydisperse neutrally buoyant colloids within a fracture with a uniform aperture, and found that both the finite colloid size and the characteristics of the colloid diameter distribution significantly influenced the shape of colloid breakthrough curve. Considering the important influence of exclusion on particle transport, the limited experimental and theoretical efforts, and the inconsistent research results, this mechanism merits further investigation.

2.3. Modeling Colloid Transport in Fractured Media

Progress in modeling colloid transport processes in the subsurface is essential towards improving the current understanding of the coupling of different physicochemical processes in saturated fractured subsurface systems, the evolution of geochemistry, bioremediation, and reactive transport.

2.3.1 Conceptual Models of Fractured Media

An important consideration in the study of flow and transport in fractured media is that conceptual pictures and modeling approaches of problems of interest are a function of scale. Often, a number of conceptual models have been developed for a problem, depending on its scale. These modeling approaches, all of which can be formulated in deterministic and stochastic frameworks, include (Altman et al. 1996): (1) equivalent porous medium model and its extension composite porosity model; (2) dual porosity model and its extension dual permeability model; (3) multi-region model; and (4) discrete fracture model with or without matrix effects (the individual fracture is a special case of this conceptual model). The equivalent porous medium model is applicable to the largest of scales, and the discrete fracture model is applicable to the smallest of scales where flow and transport in individual fractures may be important. The applicability range of the dual porosity model falls in between these cases (i.e., at scales where heterogeneity effects between fractures and their matrix are significant, but both can be represented by a continuum). The range of applicability of these alternative models depends on the scale of the heterogeneity in relation to the scale of the region of interest.

2.3.2 Eulerian and Lagrangian Approaches

Two theoretical approaches have been employed to model colloid transport in fractured media, namely: (1) the Eulerian method in which colloid concentrations in space and time are considered, and (2) the Lagrangian method in which individual colloid pathways are followed along their trajectories. Both approaches will be discussed here.

2.3.2.1 Eulerian Approaches

Eulerian methods are concerned with obtaining the concentration distribution of particles in space, as well as the orientation distribution for non-spherical particles. In the much more general form, such distributions are described by a set of coupled ordinary differential equations termed the Fokker-Planker equations (Adamczyk et al. 1983; Jia and Williams 1990; Peters and Ying 1991). For colloid particles dispersed in fluids, the Fokker-Plank equations reduce to the continuity equation, also called the convective diffusion equation (Levich 1962; van de Ven 1989).

For colloid transport in porous or fractured media, where the length scales associated with the colloid size may be comparable with that of the pores or fracture aperture, the surface interactions between the colloid and the solid play an important role in determining colloid transport behaviour. The mathematical model that incorporates the surface colloid-solid interactions at the microscopic (pore) scale in its general form is given by (Ryan and Elimelech, 1996):

$$\frac{\partial C}{\partial t} + \nabla \cdot J = S \tag{2.9}$$

$$J = -\boldsymbol{D} \cdot \nabla C + \boldsymbol{v} C + \frac{\boldsymbol{D} \cdot \boldsymbol{F}}{k_B T} C \tag{2.10}$$

where C [L^{-3}] is the colloid number concentration, t [t] is the time, J [$L^{-2} \cdot t^{-1}$] is the colloid flux vector, S [$L^{-3} \cdot t^{-1}$] is a source term, $\boldsymbol{D}$ [$L^2 \cdot t^{-1}$] is the colloid diffusion tensor, $\boldsymbol{v}$ [$L \cdot t^{-1}$] is the colloid velocity induced by the fluid flow, k_B [$M \cdot L^2 \cdot t^{-2} \cdot T^{-1}$] is the Boltzmann constant, T [T] is the absolute temperature, and $\boldsymbol{F}$ [$M \cdot L \cdot t^{-2}$] is the external force vector. The terms on the right-hand side of equation (2.10) describe the transport of colloids by diffusion, convection, and external forces respectively.

For particle transport in aquatic systems, the relevant external forces are colloid and gravitational forces, that is

$$\boldsymbol{F} = \boldsymbol{F}_{col} + \boldsymbol{F}_G \tag{2.11}$$

$$\boldsymbol{F}_{col} = -\nabla \phi^{tot} \tag{2.12}$$

where $\boldsymbol{F}_{col}$ [$M \cdot L \cdot t^{-2}$] represents the colloidal forces acting between suspended colloids and collector surfaces, and $\boldsymbol{F}_G$ [$M \cdot L \cdot t^{-2}$] is the gravitational force. The colloid force can be obtained from the total interaction potential, ϕ^{tot}, as calculated by equation (2.4) or (2.5) within the framework of the DLVO theory.

At the micro-scale, equation (2.9) provides the complete description of the evolution of a colloid suspension. Literature in the field of chemistry has employed this equation to simulate particle transport and deposition in parallel plate channels (e.g., Adamczyk and Van De Ven 1981). Jen and Li (2001) also considered the colloid forces (double-layer and van der Waals interactions) in studying colloid-facilitated migration of radionuclides in single rock fractures. However, due to the complexity of fractured media (e.g., surface roughness, surface charge heterogeneity) and incomplete knowledge of surface interactions, researchers in the hydrogeological community typically use the advection-dispersion equation to model colloid transport in single fractures, and incorporate empirical terms to account for attachment/detachment, straining, gravity sedimentation, and decay (e.g., Oswald and Ibaraki 2001; Abdel-Salam and Chrysikopoulos 1995; van der Lee et al. 1992; Chrysikopoulos and Abdel-Salam 1997; Ibaraki and Sudicky 1995; James and Chrysikopoulos 2003a). Assuming that colloids are stable and of equal size, and the colloid concentration variation across the fracture aperture is negligible, the governing partial differential equation for colloid transport in a two-dimensional fracture is given by:

$$\begin{aligned} b(x,y)\frac{\partial C(t,x,y)}{\partial t} + \nabla\cdot\left[b(x,y)vC - b(x,y)D\cdot\nabla C(t,x,y)\right] \\ + 2q + b(x,y)\lambda C + 2\frac{\partial s}{\partial t} + 2\lambda s = 0 \end{aligned} \tag{2.13}$$

where b [L] is the variable fracture aperture, C [L^{-3}] is the mobile colloid concentration, s [L^{-2}] is the immobile colloid concentration, on fracture surfaces, expressed as the number of colloids per unit area of the fracture surface, x [L] is the coordinate along the fracture length, y [L] is the coordinate along the fracture width, v [$\mathrm{L}\cdot\mathrm{t}^{-1}$] is the suspended colloid velocity, D [$\mathrm{L}^2\cdot\mathrm{t}^{-1}$] the hydrodynamic dispersion coefficient, and q [$\mathrm{L}^{-2}\cdot\mathrm{t}^{-1}$] the colloid flux through the fracture wall. The underlying assumption here is that the surface interaction force layer is much smaller than the average fracture aperture, and can thus be incorporated into the boundary conditions which take the form of a first order reaction at the fracture surface.

If it is assumed that colloids can penetrate the rock matrix surrounding the fracture, the colloid transport equation (assuming both advection and dispersion occur) in the porous matrix is given by:

$$\begin{aligned} \frac{\partial C'(t,x,y,z)}{\partial t} + \nabla\cdot\left[vC'(t,x,y,z) - D'\cdot\nabla C'(t,x,y,z)\right] \\ + \lambda C'(t,x,y,z) + \frac{\rho_b}{\theta}\frac{\partial s'(t,x,y,z)}{\partial t} + \frac{\rho_b}{\theta}\lambda s'(t,x,y,z) = 0 \end{aligned} \tag{2.14}$$

where C' [L^{-3}] is the mobile colloid concentration, s' [M^{-1}] is the number of the immobile colloids per unit mass of solid in the porous matrix, v [$L \cdot t^{-1}$] is the velocity of mobile colloids, x [L] is the coordinate along the fracture length, y [L] is the coordinate along the fracture width, z [L] is the coordinate perpendicular to the fracture, D' [$L^2 \cdot t^{-1}$] is the hydrodynamic dispersion coefficient, ρ [$M \cdot L^{-3}$] is the bulk density of the matrix, and θ [-] is the porosity of the matrix.

For larger scale problems in fractured media, where equivalent porous media or double porosity models are assumed valid, the application of equation (2.9) in practice will encounter additional difficulties (similar to those discussed by Ginn et al. 2002) : (1) equation (2.9) is a micro-scale equation, whereas the larger scale problems are at the Darcy scale; (2) the length scale associated with surface interactions, advection and dispersion are generally disparate, making the problem difficult to solve numerically. To the knowledge of these authors, however, no efforts have been made to upscale equation (2.9) from a single fracture to an equivalent porous model or double porosity model. In porous media, similar upscaling has been made via volume averaging (Gray et al. 1993; Whitaker 1999) and other scaling techniques (Panfilov 2000), but it is not clear if these techniques are applicable to fractured media.

2.3.2.2 Lagrangian Approaches

Among Lagrangian approaches, the random walk particle tracking (RWPT) method has been commonly used in the hydrogeological community to solve subsurface flow and transport problems for a long time (e.g., Scheidegger 1954; De Josselin de Jong 1958; Ahlstrom et al. 1977; Smith and Schwartz 1980; Prickett et al. 1981; Tompson and Gelhar 1990; Kinzelbach and Uffink 1991; James and Chrysikopoulos 1999). What makes the RWPT method particularly appealing in transport problems is that, unlike most classical numerical methods of transport, it performs well at large Peclet numbers. However, when the Peclet number is large, the advection-dispersion transport equation behaves as a hyperbolic partial differential equation for which solutions from the direct application of finite difference or finite element formulations usually exhibit numerical dispersion or oscillation (Huyakorn and Pinder 1983). Another advantage of RWPT method is that it is the only method which can facilitate the use of variably sized colloids (James and Chrysikopoulos 1999).

The RWPT method has many potential applications in different fields, such as in heat flow, estuary flow, unsaturated flow, plasma physics, astrophysics, and so on. It is based on representing the spatial distribution of some extensive quantity, such as the mass of a particular chemical constituent, by a large collection of particles (Tompson and Gelhar 1990). For colloid transport in fractured media, the particles will naturally represent the colloids which are transported under the influence of fluid velocity field and diffusion processes. The only attribute we are concerned with is the location of the colloids with respect to time. In vector notation, a particle is displaced according to the simple relationship:

$$\boldsymbol{X}^{n} = \boldsymbol{X}^{n-1} + \boldsymbol{A}\left(\boldsymbol{X}^{n-1}\right)\Delta t + \boldsymbol{B}\left(X^{n-1}\right)\cdot \boldsymbol{Z}\sqrt{\Delta t} \tag{2.15}$$

where $\boldsymbol{X}^n$ is the colloid position at time $n\Delta t$, $\boldsymbol{A}(\boldsymbol{X}^{m-1})$ is a deterministic forcing vector (i.e., the velocity profile) evaluated at $\boldsymbol{X}^{m-1}$, $\boldsymbol{B}(\boldsymbol{X}^{m-1})$, which has a nonzero terms, $\sqrt{2D}$, along the diagonal (Ahlstrom et al., 1977), is a deterministic scaling matrix evaluated at $\boldsymbol{X}^{m-1}$, and $\boldsymbol{Z}$ is a vector of three independent random numbers with a mean of zero and a variance of one. The motion of one particle will thus be statistically independent from that of another. If an infinite number of particles move simultaneously, their number density $f(x,t)$, determined using the equation (2.15) will converge towards the solution of the Ito Fokker-Plank equation:

$$\frac{\partial f}{\partial t} + \nabla\cdot(\boldsymbol{A}f) - \nabla\nabla : \left(\frac{1}{2}\boldsymbol{B}\cdot\boldsymbol{B}^{T} f\right) = 0 \tag{2.16}$$

If $\boldsymbol{A}$ and $\boldsymbol{B}$ are defined by:

$$\mathbf{A} \equiv \mathbf{v} + \nabla\cdot\mathbf{D} + \frac{1}{\theta}\mathbf{D}\cdot\nabla\theta \tag{2.17a}$$

$$\boldsymbol{B}\cdot\boldsymbol{B}^T \equiv 2\boldsymbol{D} \tag{2.17b}$$

then the Ito Fokker-Plank equation (2.16) will have the same form as the general transport equation for a conservative constituent

$$\frac{\partial(\theta C)}{\partial t}+\nabla\cdot(\theta C\mathbf{v})-\nabla\cdot(\theta\mathbf{D}\cdot\nabla C)=0 \tag{2.18}$$

where $\boldsymbol{v}$ [$L\cdot t^{-1}$] is the particle velocity vector, $\boldsymbol{D}$ [$L^2\cdot t^{-1}$] is the hydrodynamic dispersion tensor, and θ [-] is porosity. Therefore, in principle, the RWPT method yields the same result as that obtained from the advection-dispersion equation.

The RWPT technique has been frequently used to investigate colloid transport in discretely fractured media. Grindrod and Lee (1997) studied colloid migration in symmetrical, non-uniform fractures using a three-dimensional flow model (assuming the velocity profile across the aperture is parabolic) and a three-dimensional particle-tracking model. James and Chrysikopoulos (1999) investigated the transport of polydisperse colloids in a fracture with a uniform aperture using a one-dimensional flow model and a two-dimensional particle-tracking model, incorporating the effect of matrix diffusion and colloid deposition (perfect sink approximation and kinetic relationship). James and Chrysikopoulos (2000) and Chrysikopoulos and James (2003) demonstrated the effect of aperture variability and anisotropy on colloid transport based on a two-dimensional flow model and three-dimensional particle tracking model. Grindrod and Lee (1997) presented a quasi-three-dimensional flow model — the fluid velocity field was constructed by asserting that the velocity profile across the fracture aperture is parabolic — to study colloid transport in non-uniform fractures. Their model also considered the colloid-fracture wall interactions. James and Chrysikopoulos (2003) also derived expressions for the effective velocity and effective dispersion coefficient for finite-sized, spherical, with neutrally-buoyant particles migrating in a water-saturated fracture formed by two semi-infinite parallel plates, and suggested that the effective velocity and dispersion coefficient is ideally suited for use in particle tracking models.

2.4. Summary and Directions for Future Research

This paper has reviewed the current understanding of (biotic and abiotic) colloid transport in fractured media at various scales, and identified many gaps in the research. Some of the findings and needs for future research are summarized here.

Aperture variability and fracture connectivity are critical factors controlling groundwater flow and colloid transport in fractured media. Experimental and theoretical studies regarding single fractures have shown that fracture aperture heterogeneity and anisotropy can significantly influence colloid transport. However, the effect of fracture intersections and fracture aperture distribution in fracture networks on colloid transport remains unclear. Due to the well-known difficulty in characterizing real fractures, it is a great challenge to incorporate fracture geometry into models to simulate colloid transport in fracture networks. The accelerated transport of colloids relative to conservative tracers could be caused by preferential flow paths and exclusion effects. However, the relative importance of these mechanisms is not clear. Model approaches for these phenomena in fracture networks deserves further study.

The low recovery of colloids from lab and field experiments could be caused by sorption, gravitational sedimentation, straining, or a combination of these mechanisms. Researchers have typically depended on fitting simulation results to experimental breakthrough curves in order to identify the relative contribution of these mechanisms. Unfortunately, this practice results in a non-unique solution to the problem involved. Well-designed experiments with isolated factors (such as colloid size, density, flow velocity etc.) coupled with flow and transport visualization techniques may be used to directly observe where colloids are retained within fractures. Combining these observations with three-dimensional simulations of flow and colloid transport could improve our understanding of the retention mechanisms.

Quasi-three-dimensional flow model (assuming the velocity profile across the fracture aperture is parabolic) has been used to obtain the velocity field in single fractures. This velocity field has then been incorporated into particle tracking algorithms to simulate colloid transport in single fractures with uniform or variable apertures. However, in actual fact, the velocity profile is not perfectly parabolic (Brush and Thomson 2003). A real three-dimensional velocity structure obtained through a full Navier-Stokes analysis of the flow within fractures, with well-defined geometries, would be an improvement, helping to clarify the relative contributions of the advection, dispersion, and retention mechanisms.

DLVO theory provides a useful paradigm to characterize the interaction forces between microbes and solid surfaces. However, the degree of success decreases as the complexities of the colloid and solid surfaces increase. However, a model that considers the physical and chemical heterogeneity distribution of the solid surface, and the shape, size, and surface characteristics of the colloids is beyond the reach of current technology. A method of upscaling the advection-dispersion equation, incorporating the colloid-solid surface interactions, from single fractures to equivalent porous media poses another challenge.

The effect of colloid clogging on groundwater flow and contaminant transport in fractured media is critical to the success of bioremediation. Mathematical modeling of these effects is a formidable task, and merits further investigations.

Acknowledgement

The authors would like to thank the Natural Science and Engineering Research Council of Canada (NSERC) for funding this work.

References

Abdel-Salam, A., Chrysikopoulos C.V.: Analysis of a model for contaminant transport in fractured media in the presence of colloids. J. Hydrol. **165**, 261-281 (1995)

Absolom, D.R., Lamberti, F.V., Policova, Z., Zingg, W., Van Oss, C.J., Neumann, A.W.: Surface thermodynamics of bacterial adhesion. Appl. Environ. Microbiol. **46**, 90–97 (1983)

Adamczyk, Z., van de Ven, T.G.M.: Deposition of particles under external forces in laminar flow through parallel-plate and cylindrical channels. J. Colloid Interf. Sci. **80**(2), 340-356 (1981)

Adamczyk, Z., Dabros, T., Czarnecki, J., van de Ven, T.G.M.: Particle transfer to solid surfaces. Adv. Colloid Interfac. **19**, 183-252 (1983)

Ahlstrom, S.W., Foote, H.P., Arnett, R.C., Cloe, C.R., Serne, R.J.: Multicomponent mass transport model: theory and numerical implementation (discrete parcel random-walk version). Rep. BNWL-2127, Battelle Pacific Northwest Lab., Richland, Washington (1977)

Allen, M.J., Morrison, S.M.: Bacterial movement through fractured bedrock. Ground Water, **11**(2), 6-10 (1973)

Altman, S.J., Arnold, B.W., Barnard, R.W., Bar, G.E., Ho, C.K., McKenna, S.A., Eaton, R.R.: Flow calculations for Yucca Mountain groundwater travel time (GWTT-95). Report SAND96-0819. Albuquerque, N. Mex.: Sandia National Laboratories (1996)

Bales, R.C., Gerba, C.P., Grondin, G.H., Jensen, S.L.: Bacteriophage transport in sandy soil and fractured tuff. Appl. Environ. Microb. **55**, 2061-2067 (1989)

Bales, R.C., Li, S., Maquire, K.M., Yahya, M.T., Gerba, C.P., Harvey, R.W.: Virus and bacteria transport in a sandy aquifer at Cape Cod, MA. Ground Water **33**, 653-661 (1995)

Baveye, P., Vandevivere, P., Hoyle, B.L., DeLeo, P.C., Sanchez de Lozada, D.: Environmental impact and mechanisms of the biological clogging of saturated soils and aquifer materials. Crit. Rev. Env. Sci. Tec. **28**, 123-191 (1998)

Becker, M.W., Reimus, P.W., Vilks, P.: Transport and attenuation of Carboxylate-modified latex microspheres in fractured rock laboratory and field tracer tests. Ground Water **37**(3), 387-395 (1999)

Becker, M.W., Shapiro, A.M.: Tracer transport in fractured crystalline rock: evidence of nondiffusive breakthrough tailing. Water Resour. Res. **36**(7), 1677-1686 (2000)

Beeder, J., Nilsen, R.K., Thorstenson, T., Torsvik, T.: Penetration of sulphate reducers through a porous North Sea oil reservoir. Appl. Environ. Microbial. **62**, 3551-3553 (1996)

Berkowitz, B.: Characterization flow and transport in fractured geological media: a review. Adv. Water Resour. **25**, 861-884 (2002)

Berkowitz, B., Neumann, C., Smith. L.: Mass transfer at fracture intersections: an evaluation of mixing models. Water Resour. Res. **30**(6), 1765–1773 (1994)

Bos, R., van der Mei, H.C., Busscher, H.J.: Physico-chemistry of initial microbial adhesive interactions-its mechanisms and methods for study. FEMS Microbiol. Rev. **23**, 179-230 (1999)

Bos, R., Van der Mei, H.C., Busscher, H.J.: A quantitative method to study co-adhesion of microorganisms in a parallel plate flow chamber. II: Analysis of the kinetics of co-adhesion. J. Microbiol. Methods **23**, 69–182 (1995)

Bowen, B.D., Levine, S., Epstein, N.: Fine particles deposition in laminar flow through parallel plate and cylindrical channels. J. Colloid Interface Sci. **54**, 375–390 (1976)

Bradford, S.A., Yates, S.R., Bettahar, M., Simunek, J.: Physical factors affecting the transport and fate of colloids in saturated porous media. Water Resour. Res. **38**(12), 1327, (2002) doi:10.1029/2002WR001340.

Bradford, S.A., Simunek, J., Bettahar, M., Van Genuchten, M.T., Yates, S.R.: Modeling colloid attachment and exclusion in saturated porous media. Environ. Sci. Technol. **37**, 2242-2250 (2003)

Bradford, S.A., Bettahar, M., Simunek, J., Van Genuchten, M.T.: Straining and attachment of colloids in physically heterogeneous porous media, Vadose Zone J. **3**, 384-394 (2004)

Brown, S., Caprihan, A., Hardy, R.: Experimental observation of fluid flow channels in a single fracture. J. Geophys. Res. **103**(B3), 5125-5132 (1998)

Brenner, H., Edwards, D.A.: Macrotransport Processes. Butterworth-Heinemann, Woburn, Mass. (1993)

Brush, D.J., Thomson, N.R.: Fluid flow in synthetic rough-walled fractures: Navier-Stokes, Stokes, and Local Cubic Law simulations. Water Resour. Res. **39**(4), 1085 (2003) doi:10.1029/2002WR001346.

Busscher, H.J., Weerkamp, A.H., Van der Mei, H.C., Van Pelt, A.W.J., De Jong, H.P., Arends, J.: Measurement of the surface free energy of bacterial cell surfaces and its relevance for adhesion. Appl. Environ. Microbiol. **48**, 980–983 (1984)

Camper, A.K., Hayes, J.T., Sturman, P.J., Jones, W.L., Cunningham, A.B.: Effects of Motility and Adsorption Rate Coefficient on Transport of Bacteria through Saturated Porous Media. Appl. Environ. Microbiol. **59**, 3455-3462 (1993)

Champ, D.R., Schroeter, J.: Bacterial transport in fractured rock-- a field-scale tracer test at the Chalk River Nuclear Laboratories. Wat. Sci. Tech. **20**(11/12), 81-87 (1989)

Chrysikopoulos, C.V., Abdel-Salam, A.: Modeling colloid transport and deposition in saturated fractures. Colloid Surface A **121**, 189-202 (1997)

Chrysikopoulos, C.V., James, S.C.: Transport of neutrally buoyant and dense variably sized colloids in a two-dimensional fracture with anisotropic aperture. Transport Porous Med. **51**, 191-210 (2003)

Clement, T.P., Hooker, B.S., Skeen, R.S.: Macroscopic models for predicting changes in saturated porous media properties caused by microbial growth. Ground Water **34**, 934-942 (1996)

Clement, T.P., Peyton, B.M., Ginn, T.R., Skeen, R.S.: Modeling bacterial transport and accumulation processes in porous media: a review. Advances in Nuclear Science and Technology **26**, 59-78 (1999)

Corapcioglu, M.Y., Haridas, A.: Microbial transport in soils and groundwater: a numerical model. Adv. Water Resour. **8**(4), 188-200 (1985)

Cumbie, D.H., McKay, L.D.: Influence of diameter on particle transport in a fractured shale saprolite. J. Contam. Hydrol. **37**, 139-157 (1999)

Cunningham, A.B., Characklis, W.G., Abdeeden, F., Crawford, D.: Influence of biofilm on porous media hydrodynamics. Environ. Sci. Technol. **25**, 1304-1311 (1991)

Cunningham, A., Warwood, B., Sturman, P., Horrigan, K., James, G., Costerton, J.W., Hiebert, R.: Biofilm processes in porous media-Practical applications. In: Amy, P.S., Haldeman, D.L. (Eds.), The microbiology of the deep subsurface, pp. 325-344. Boca Raton: Lewis Publishers (1997)

Dabros, T., Van de Ven, T.G.M.: Kinetics of coating by colloidal particles. J. Colloid Interface Sci. **89**, 232–244 (1982)

Darby, J. L., Lawler, D.F.: Ripening in depth filtration: effect of particle size on removal and head loss. Environ. Sci. Technol. **24**, 1069 – 1079 (1990)

DeBorde, D.C., Woessner, W.W., Kiley, Q.T., Ball, P.: Rapid transport of viruses in a floodplain aquifer. Water Res. **33**(10), 2229–2238 (1999)

Degueldre, C., Baeyens, B., Goerlich, W.: Colloids in water from a subsurface fracture in granitic rock, Grimsel Test Site, Switzerland. Geochimica et Cosmochimica Acta, **53**, 603-610 (1989)

De Josselin de Jong, G.: Longitudinal and transverse diffusion in granular deposits. Trans. Am. Geophys. Union **39**, 67-74 (1958)

Dennis, M.L., Turner, J.P.: Hydraulic conductivity of compacted soil treated with biofilm. J. Geotech. Geoenviron. **124**(2), 120-127 (1998)

Detwiler, R.L., Rajaram, H., Glass, R.J.: Solute transport in variable-aperture fractures: an investigation of the relative importance of Taylor dispersion and macrodispersion. Water Resour. Res. 36(7), 1611-1625 (2000)

Elimelech, M., Gregory, J., Jia, X., Williams, R.A.: Particle depositions and Aggregation: Measurement, Modeling, and Simulation. Butterworth-Heinemann, Oxford. (1995)

Fletcher, M.: The question of passive versus active attachment mechanisms in non-specific bacterial adhesion. In: Berkeley, R.C.W., Lynch, J.M., Melling, J., Rutter, P.R., Vincent, B. (eds.), Microbial adhesion to surfaces. Ellis Horwood Limited, England (1980)

Ginn, T.R.: On the distribution of multicomponent mixtures over generalized exposure time in subsurface flow and reactive transport: Foundations, and formulations for groundwater age, chemical heterogeneity, and biodegradation. Water Resour. Res. **35**(5), 1395–1407 (1999)

Ginn, T.R., Wood, B.D., Nelson, K.E., Scheibe, T.D., Murphy, E.M., Clement, T.P.: Processes in microbial transport in the natural subsurface. Adv. Water Resour. **25**, 1017-1042 (2002)

Ginn, T.R.: A travel time approach to exclusion on transport in porous media. Water Resour. Res. **38**(4), 1041 (2002) doi:10.1029/2001WR000865.

Gray, W.G., Leijnse, A., Kolar, R.L., Blain, C.A.: Mathematical tools for changing spatial scales in the analysis of physical systems. CRC Press, Boca Raton (FL) (1993)

Grindrod, P.: The impact of colloids on the migration and dispersal of radionuclides within fractured rock. J. Contam. Hydrol. **13**, 167-181 (1993)

Grindrod, P., Lee, A.J.: Colloid migration in symmetrical non-uniform fractures: particle tracking in three dimensions. J. Contam. Hydrol. **27**, 157-175. (1997)

Gvirtzman, H., Gorelick, S.M.: Dispersion and advection in unsaturated porous media enhanced by anion exclusion. Nature **352**, 793-795 (1991)

Harvey, R.W., Kinner, N.E., MacDonald, D., Metge, D.W., Bunn, A.: Role of physical heterogeneity in the interpretation of small-scale laboratory and field observations of bacteria, microbial-sized microspheres, and bromide transport through aquifer sediments. Water Resour. Res. **29**, 2713-2721 (1993)

Harvey, R.W., Kinner, N.E., Bunn, A., MacDonald, D., Metge, D.W.: Transport behaviour of groundwater protozoa and protozoan-sized microspheres in sandy aquifer sediments. Appl. Environ. Microbiol. **61**(1), 209-217 (1995)

Harvey, R.W.: Microorganisms as tracers in groundwater injection and recovery experiments: a review. FEMS Microbiol. Rev. **20**, 461-472 (1997)

Harvey, R.W., Harms, H.: Transport of microorganisms in the terrestrial subsurface: in situ and laboratory methods. In: Hurst, C.J., Crawford, R.L., Knudsen, G.R., McInerney, M.J., Stetzenbach, L.D. (eds.), Manual of Environmental Microbiology, 2nd ed., pp. 753-776. ASM Press, Washington, D. C. (2001)

Hatano, Y., Hatano, N.: Dispersive transport of ions in column experiments: an explanation of long-tailed profiles. Water Resour. Res. **34**(5), 1027-1033 (1998)

Haun, D.B.: Influence of ionic strength and cation valence on transport of colloid-sized microspheres in fractured shale saprolite. M. S. thesis, Department of Geological Sciences, University of Tennessee, Knoxville (1998)

Herzig, J.P., Leclerc, D.M., Le Goff, P.: Flow of suspensions through porous media. In: Flow through porous media, pp. 129-157. American Chemical Society. Washington, D. C. (1970)

Hiebert, R., Sharp, R., Cunningham, A., & James, G.: Development and demonstration of subsurface biofilm barriers using starved bacterial cultures. Contaminated Soil, Sediment, and Water, 45-47 (2001)

Hill, D.D., Sleep, B.E.: Effects of biofilm growth on flow and transport through a glass parallel plate fracture. J. Contam. Hydrol. **56**, 227-246 (2002)

Hinsby, K., McKay, L.D., Jorgensen, P., Lenczewski, M., Gerba, C.P.: Fracture aperture measurements and migration of solutes, viruses, and immiscible creosote in a column of clay-rich till. Ground Water **34**(6), 1065-11075 (1996)

Hornberger, G.M., Mills, A.L., Herman, J.S.: Bacterial transport in porous media: evaluation of a model using laboratory observations. Water Resour. Res. **28**, 915-938 (1992)

Huyakorn, P.S., Pinder, G.F.: Computational Methods in Subsurface Flow. Academic, San Diego, Calif. (1983)

Ibaraki, M., Sudicky, E. A.: Colloid-facilitated contaminant transport in discretely fractured porous media 1. numerical formulation and sensitivity analysis. Water Resour. Res. **31**(12), 2945-2960 (1995)

James, S.C., Chrysikopoulos, C.V.: Transport of polydisperse colloid suspensions in a single fracture. Water Resour. Res. **35**(3), 707-718 (1999)

James, S.C., Chrysikopoulos, C.V.: Transport of polydisperse colloids in a saturated fracture with spatially variable aperture. Water Resour. Res. **36**(6), 1457-1465 (2000)

James, S.C., Chrysikopoulos, C.V.: Analytical solutions for monodisperse and polydisperse colloid transport in uniform fractures. Colloid Surface A **226**, 101-118 (2003a)

James, S.C., Chrysikopoulos, C.V.: Effective velocity and effective dispersion coefficient for finite-sized particles flowing in a uniform fracture. J. Colloid Interf. Sci. **263**, 288-295 (2003b)

Jen, C.P., Li, S.H.: Effects of hydrodynamic chromatography on colloid-facilitated migration of radionuclides in the fractured rock. Waste Manage., **21**, 499-509. 2001.

Jia, X., Williams, R.A.: Particle deposition at a charged solid/liquid interface, Chem. Eng. Commun. **91**(1), 127- 198 (1990)

Johnson, W.P., Blue, K.A., Logan, B.E., Arnold, R.G.: Modeling bacterial detachment during transport through porous media as a residence-time-dependent process. Water Resour. Res. **31**(11), 2649–2658 (1995)

Keller, A.: High resolution, non-destructive measurement and characterization of fracture apertures. Int. J. Rock Mech. Min. Sci. **35**(8), 1037-1050 (1998)

Kessler, J.H., Hunt, J.R.: Dissolved and colloidal contaminant transport in a partially clogged fracture. Water Resour. Res. **30**(4), 1195-1206 (1994)

Kinzelbach, W., Uffink, G.: The random walk method and extensions in groundwater modeling. In: Bear, J., Corapcioglu, M.Y. (eds.), Transport Processes in Porous Media, pp. 763-787, Kluwer Academic Publishers, Boston (1991)

Knapp, R.B., Chiarappa, M.L., Durham, W.B.: An experimental exploration of the transport and capture of abiotic colloids in a single fracture. Water Resour. Res. **36**(11), 3139-3149 (2000)

Kosakowski, G.: Anomalous transport of colloids and solutes in a shear zone. J. Contam. Hydrol. **72**, 23-46 (2004)

Lawrence, J.R., Hendry, M.J.: Transport of bacteria through geologic media. Can. J. Microbiol. **42**, 410-422 (1996)

Lee, J., Kang, J.M., Choe, J.: Experimental analysis of the effect of variable apertures on tracer transport. Water Resour. Res. **39**(1), 1015 (2003) doi: 10.1029/2001WR001246.

Levich, V.G.: Physicochemical Hydrodynamics. Prentice-Hall, Englewood Cliffs, NJ (1962)

Margolin, G., Berkowitz, B., Scher, H.: Structure, flow, and generalized conductivity scaling in fracture networks. Water Resour. Res. **34**(9), 2103–21 (1998)

Matthess, G., Pekdeger, A.: Survival and transport of pathogenic bacteria and viruses in groundwater. In: Ground Water Quality, Ward, C.H., Giger, W., McCarty, P. (eds.) pp. 472-482, John Wiley, New York (1985)

McDowell-Boyer, L.M., Hunt, J.R., Sitar, N.: Particle transport through porous media. Water Resour. Res. **22**(13), 1901-1921 (1986)

McKay, L.D., Cherry, J.A., Bales, R.C., Yahya M.T., Gerba, C.P.: A field example of bacteriophage as tracers of fracture flow. Environ. Sci. Technol. **27**, 1075-1079 (1993a)

McKay, L.D., Gillham, R.W., Cherry, J.A.: Field experiments in a fractured clay till 2. solute and colloid transport. Water Resour. Res. **29**(12), 3879-3890 (1993b)

McKay, L.D., Sanford, W.E., Strong, J.M.: Field-scale migration of colloid tracers in a fractured shale saprolite. Ground Water **38**(1), 139-147 (2000)

McLinn, E.L., Rehm, B.W.: Biodegradation of petroleum hydrocarbons in fractured, unsaturated dolomite at a field site. Ground Water Monit. Rem. **17**(4), 73–80 (1997)

Murphy, E.M., Ginn, T.R.: Modeling microbial processes in porous media. Hydrogeol. J. **8**(1), 142-158 (2000)

Neretnieks, I.: Solute transport in fracture rock—applications to radionuclide waste repositories. In: Bear, J., Tsang, C.F., de Marsily, G. (eds.) Flow and contaminant transport in fractured rock, pp. 39-127. San Diego: Academic Press, Inc. (1993)

Okubo, T., Matsumoto, J.: Effect of infiltration rate on biological clogging and water quality changes during artificial recharge. Water Resour. Res. **15**, 1536-1542 (1979)

Oswald, J.G., Ibaraki, M.: Migration of colloids in discretely fractured porous media: effect of colloidal matrix diffusion. J. Contam. Hydrol. **52**, 213-244 (2001)

Panfilov, M.: Macroscale models of flow through highly heterogeneous media. Kluwer Academic, Dordrecht (2000)

Park, Y.J., Lee, K.K.: Analytical solutions for solute transfer characteristics at continuous fracture junctions. Water Resour. Res. **35**(5), 1531–1537 (1999)

Park, Y.J., Lee, K.K., Berkowitz, B.: Effects of junction transfer characteristics on transport in fracture networks. Water Resour. Res. **37**(4), 909–23 (2001a)

Park, Y.J., de Dreuzy, J.R., Lee, K.K., Berkowitz, B.: Transport and intersection mixing in random fracture networks with power law length distributions. Water Resour. Res. **37**(10), 2493–501 (2001b)

Park, Y.J., Lee, K.K., Kosakowski, G., Berkowitz, B.: Transport behaviour in three-dimensional fracture intersections, Water Resour. Res. **39**(8), 1215, (2003) doi:10.1029/2002WR001801.

Peters, M.H., Ying, R.: Phase-space diffusion equations for single Brownian particle motion near surface, Chem. Eng. Commun. **108**(1), 165-184 (1991)

Powelson, D.K., Gerba, C.P., Yahya, M.T.: Virus transport and removal in waste water during aquifer recharge. Water Res. **27**, 583-590 (1993)

Pozrikidis, C.: Creeping flow in two-dimensional channels. J. Fluid Mech. **180**, 495-514 (1987)

Prickett, T.A., Naymik, T.G., Lonnquist, C.G.: A "random walk" solute transport model for selected groundwater quality evaluations. Illinois State Water Survey, Bulletin 65 (1981)

Raven, K.G., Novakowski, K.S., Lapcevic, P.A.: Interpretation of field tracer tests of a single fracture using a transit solute storage model. Water Resour. Res. **24**(12), 2019-2032 (1988)

Rehmann, L.L.C., Welty, C., Harvey, R.W.: Stochastic analysis of virus transport in aquifers. Water Resour. Res. **35**(7), 1987-2006 (1999)

Rehmann, L.L.C., Welty, C., Harvey, R.W.: Reply to comment by T. R. Ginn on "Stochastic analysis of virus transport in aquifers" by Linda L. Campbell Rehmann, Claire Welty, and Ronald W. Harvey. Water Resour. Res. **36**(7), 1983-1984 (2000)

Ross, N., Villemur, R., Deschenes, L., Samson, R.: Clogging of a limestone fracture by stimulating groundwater microbes. Wat. Res. **35**(8), 2029-2037 (2001)

Ross, N., Bickerton, G.: Application of biobarriers for groundwater containment at fractured bedrock sites. Remediation Journal, **3**(3), 5-21 (2002)

Rutter, P.R., Vincent, B.: The adhesion of micro-organisms to surfaces, physico-chemical aspects. In: Berkeley, R.C.W., Lynch, J.M., Melling, J., Rutter, P.R., Vincent, B. (eds.) Microbial Adhesion to Surfaces, pp. 79–91. Ellis Horwood, London (1980)

Ryan, J.N., Elimelech, M.: Review: Colloid mobilization and transport in groundwater. Colloid Surface A **107**, 1-56 (1996)

Sahimi, M.: Flow and Transport in Porous Media and Fractured Rock: from classical methods to modern approaches. VCH Verlagsgesellschaft mbH, Weinheim (Federal Republic of Germany) (1995)

Sakthivadivel, R.: Theory and mechanism of filtration of non-colloid fines through a porous medium. Report HEL 15-5. Hydraulic Engineering Laboratory, University of California, Berkeley (1966)

Sakthivadivel, R.: Clogging of a granular porous medium by sediment. Report HEL 15-7. Hydraulic Engineering Laboratory, University of California, Berkeley (1969)

Schaaf, P., Talbot, J.: Surface exclusion effects in adsorption processes. J. Chem. Phys. **91**, 4401–4409 (1989)

Scheibe, T.D., Wood, B.D.: A particle-based model of size or anion exclusion with application to microbial transport in porous media. Water Resour. Res. **39**(4), 1080, (2003) doi: 10.1029/2001WR001223.

Scheidegger, A E.: Statistics hydrodynamics in porous media. J. Geophys Res., **66**(10), 3273-3278 (1954)

Schijven, J.F., Hassanizadeh, S.M.: Removal of viruses by soil passage: overview of modeling, processes, and parameters. Crit. Rev. Environ. Sci. Technol. **30**(1), 49-127 (2000)

Shonnard, D.R., Taylor, R.T., Hanna, M.L., Boro, C.O., Duba, A.G.: Injection-attachment of *Methylosinus trichosporium* OB3b in a two-dimensional miniature sand-filled aquifer simulator. Water Resour. Res. **30**, 25-36 (1994)

Shonnard, D.R., Taylor, R.T., Tompson, A., Knapp, R.B.: Hydrodynamic effects on microcapillary motility and chemotaxis assays of Methylosinus trichosporium OB3b. Appl. Environ. Microbiol. **58**, 2737-2743 (1992)

Sidle, C.R., Nilsson, B., Hansen, M., Fredericia, J.: Spatially varying hydraulic and solute transport characteristics of a fractured till determined by field tracer tests, Funen, Denmark. Water Resour. Res. **34**(10), 2515-2527 (1998)

Sinton, L.W., Noonan, M.J., Finlay, R.K., Pang, L., Close, M.E.: Transport and attenuation of bacteria and bacteriophages in an alluvial gravel aquifer, N. Z. J. Mar. Freshwater Res. **34**(1), 175–186 (2000)

Sjollema, J., Busscher H.J., Weerkamp, A.H.: Deposition of oral streptococci and polystyrene lattices onto glass in a parallel plate flow cell. Biofouling **1**, 101–112 (1988)

Sjollema, J., Busscher, H.J., Weerkamp, A.H.: Real-time enumeration of adhering microorganisms in a parallel plate flow cell using automated image analysis. J. Microbiol. Methods **9**, 73–78 (1989)

Sjollema, J., Busscher, H.J.: Deposition of polystyrene particles in a parallel plate flow cell 2. pair distribution functions between deposited particles. Colloid Surface **47**, 337-352 (1990)

Smith, L., Schwartz, F.W.: Mass transport 1. A stochastic analysis of macrodispersion. Water Resour. Res. **16**(2), 303-313 (1980)

Smith, L., Schwartz, F.W.: An analysis of the influence of fracture geometry on mass transport in fractured media. Water Resour. Res. **20**(9), 1241–1252 (1984)

Smith, P.A., Degueldre, C.: Colloid-facilitated transport of radionuclides through fractured media. J. Contam. Hydrol. **13**, 143-166 (1993)

Stockman, H.W., Li, C., Wilson, J.L.: A lattice-gas and lattice Boltzmann study of mixing at continuous fracture junctions: importance of boundary conditions. Geophys. Res. Lett. **24**(12), 1515–1518 (1997)

Strong-Gunderson, J.M., Palumbo, A.V.: Laboratory studies identify a colloidal groundwater tracer: implications for bioremediation. FEMS Microbiol. Lett. **148**, 131-135 (1997)

Tadros, Th.F.: Particle-surface adhesion. In: Berkeley, R.C.W., Lynch, J.M., Melling, J., Rutter, P.R., Vincent, B. (eds.) Microbial Adhesion to Surfaces, pp. 93–113. Ellis Horwood, London (1980)

Taylor, S.W., Jaffe, P.R.: Biofilm growth and the related changes in the physical properties of a porous medium, 1. Experimental investigations. Water Resour. Res. **30**, 3243-3252 (1990a)

Taylor, S.W., Jaffe, P.R.: Biofilm growth and the related changes in the physical properties of a porous medium, 1. Dispersivity and Model Verifications. Water Resour. Res. **26**, 2171-2180 (1990b)

Tompson, A.F.B., Gelhar, L.W.: Numerical simulation of solute transport in three-dimensional, randomly heterogeneous porous media. Water Resour. Res. **26**(10), 2541-2562 (1990)

Tien, C.: Granular filtration of Aerosols and Hydrosols Butterworth, Stoneham, M.A. (1989)

Tsang, Y.W., Tsang, C.F.: Channel model of flow through fractured media. Water Resour. Res. **23**(2), 467-478 (1987)

Tsang, Y.W., Tsang, C.F., Neretnieks, I., Moreno, L.: Flow and tracer transport in fractured media: a variable aperture channel model and its properties. Water Resour. Res. **24**(12), 2049–2060 (1988)

Van de Ven, T.G.M.: Colloidal Hydrodynamics. Academic Press, London (1989)

Van der Lee, J., Ledoux, E., de Marsily, G.: Modeling of colloidal uranium transport in a fractured medium. J. Hydrol. **139**(1-4), 135-158 (1992)

Van Oss, C.J., Good, R.J., Chaudhury, M.K.: The role of van der Waals forces and hydrogen bonds in 'hydrophobic interactions' between biopolymers and low energy surfaces. J. Colloid Interf. Sci. **111**, 378–390 (1986)

van Oss, C.J.: Interfacial Forces in Aqueous Media. Marcel Dekker, Inc. New York (1994)

Vandevivere, P., Baveye, P.: Effect of bacterial extracellular polymers on the saturated hydraulic conductivity of sand columns. Appl. Environ. Microbiol. 58 (5), 1690-1698 (1992a)

Vandevivere, P., Baveye, P.: Relationship between transport of bacteria and their clogging efficiency in sand columns. Appl. Environ. Microbiol. 58(8), 2523-2530 (1992b)

Vandevivere, P., Baveye, P.: Saturated hydraulic conductivity reduction caused by aerobic bacteria in sand columns. Soil Sci. Soc. Am. J. 56, 1-13 (1992c)

Vandevivere, P., Baveye, P., Sanchez de Lozada, D.: Microbial clogging of saturated soils and aquifer materials: Evaluation of mathematical models. Water Resour. Res. **31**, 2173-2180 (1995)

Vilks, P., Bachinski, D.B.: Colloid and suspended particle migration experiments in a granite fracture. J. Contam. Hydrol. **21**, 269-279 (1996)

Vilks, P., Frost, L.H., Bachinski, D.B.: Field-scale colloid migration experiments in a granite fracture. J. Contam. Hydrol. **26**, 203-214 (1997)

Wan, J., Tokunaga, T.K., Tsang, C.F.: Bacterial sedimentation through a porous medium. Water Resour. Res. **31**(7), 1627-1636 (1995)

Weber, W.J., Digiano, F.A.: Process Dynamics in Environmental Systems. John Wiley & Sons, Inc. New York (1996)

Whitaker, S.: The method of volume averaging. Kluwer, Dordrecht (1999)

Wood, W., Kraemer, T., Hearn, P.P.: Intragranular diffusion-an important mechanism influencing solute transport in clastic aquifers? Science **247**, 1569-1572 (1990)

Xia, Z., Woo, L., Van de Ven, T.G.M.: Microrheological aspects of adhesion of *Escherichia coli* on glass. Biorheology **23**, 359–375 (1989)

Yager, R.M., Bilotta, S.E., Mann, C.L., Madsen, E.L.: Metabolic adaptation and in situ attenuation of chlorinated ethenes by naturally occurring microorganisms in a fractured dolomite aquifer near Niagara Falls, New York. Environ. Sci. Technol. 31(11), 3138–3147 (1997)

Yao, K.M., Habibian, M.T., O'Melia, C.R.: Water and wastewater filtration: concepts and applications. Environ. Sci. Technol. **5**, 1105-1112 (1971)

Yates, M.V., Yates, S.R.: Modeling microbial fate in the subsurface environment. Crit. Rev. Environ. Control **17**, 307-344 (1988)

Yau, W.W., Kirkland, J.J., Bly, D.D.: Modern Size Exclusion Liquid Chromatography: Practice of Gel Permeation and Gel Filtration Chromatography. John Wiley, New York (1979)

Zhang, P., Johnson, W.P., Piana, M.J., Fuller, C.C., Naftz, D.L.: Potential artifacts in interpretation of differential breakthrough of colloids and dissolved tracers in the context of transport in a zero-valent iron permeable reactive barrier, Ground Water **39**(6), 831–840 (2001)

Tables

Table 2.1. Comparison of colloid and conservative tracer transport in fractured media

Aquifer Type and Scale	Colloid Type	$\frac{D_{\text{conservative tracer}}}{D_{\text{colloid}}}$	$\frac{v_{\text{conservative tracer}}}{v_{\text{colloid}}}$	References
Weathered and highly fractured clay-rich till (4 m)	Bacteriophages (MS-2 and PRD1)	na	0.01	McKay et al. (1993 a, b)
Fractured and highly weathered shale saprolite (35m)	Bacteriophages and microspheres	na	0.002-0.02	McKay et al. (2000)
Fractured crystalline rock (13m)	*Escherichia coli*	>1	0.1	Champ and Schroeter (1988)
Cylindrical fractured, highly weathered clay-rich till (0.5m diameter by 0.5m in length)	Virus	na	Approximately 0.2	Hinsby et al. (1996)
Fractured tuff (830 cm^3)	Phage f2	5	0.31	Bales et al. (1989)
Fractured, layered basalt (27 m)	Bacteria	na	0.62	Harvey (1997)
Fractured rock (lab- and field-scale)	Latex micropsheres	na	>1	Becker et al. (1999)
Fractured granite block (83cm×90cm×60cm)	Latex spheres, glass spheres, colloidal silica	na	>1	Vilks and Bachinski (1996)
Cylindrical Topopah Springs tuff with a single fracture (47.8 mm diameter by 75.4/76.1mm in length)	Latex spheres	na	>1	Knapp et al. (2000)

Notes:

1. na: not available

2. $D_{\text{conservative tracer}}$ and D_{colloid}: dispersion coefficient for conservative tracer and colloids respectively.

3. $v_{\text{conservative tracer}}$ and v_{colloid}: the observed average velocities of the peak concentrations of the conservative tracers and colloids respectively.

Figures

(a)

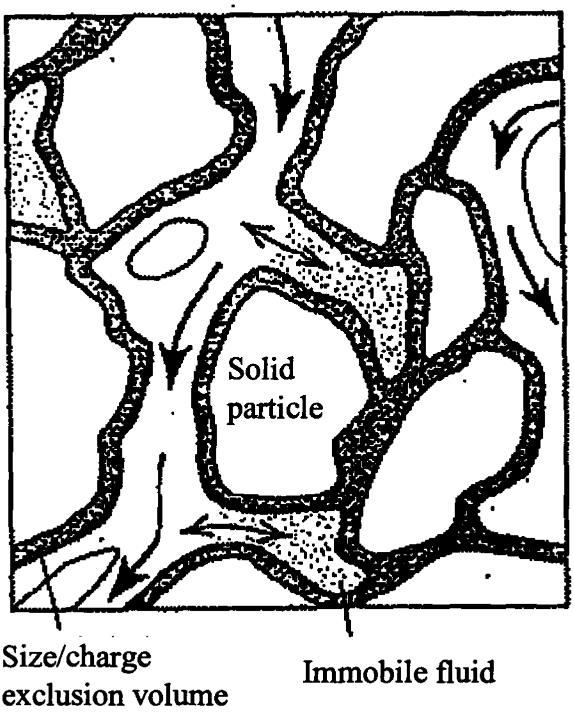
Solid particle
Size/charge exclusion volume
Immobile fluid

(b)

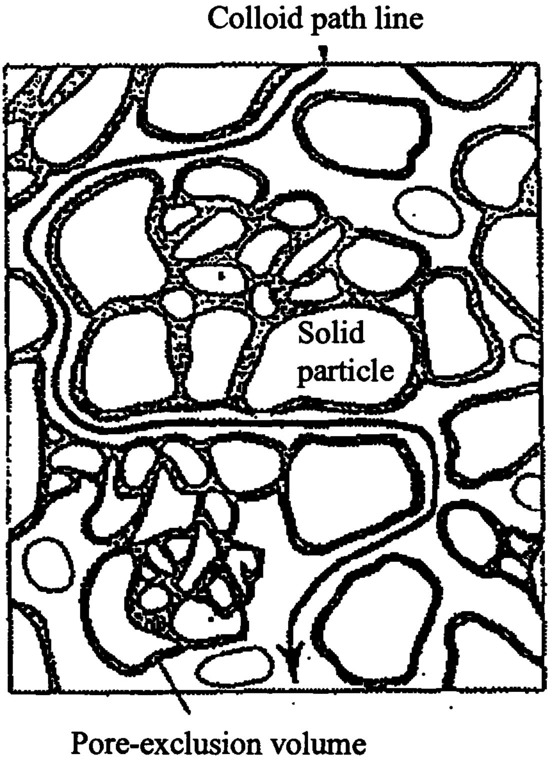
Colloid path line
Solid particle
Pore-exclusion volume

(c)

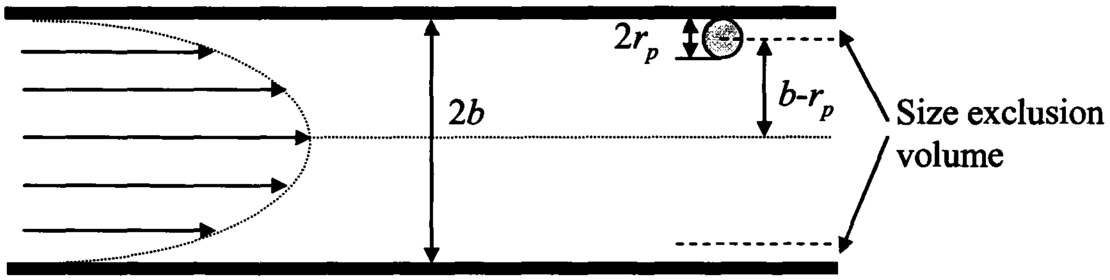

Figure 2.1. Illustration of (a) size and charge exclusion in porous media, (b) pore exclusion in porous media, and (c) size exclusion in parallel-plate fractures.
((a) and (b) modified from Gvirtzman and Gorelick, 1991)

Chapter 3 On the Appropriate 'Equivalent Aperture' for the Description of Solute Transport in Single Fractures: Laboratory-scale Experiments

The material in this chapter has been published in *Water Resource Research*, and is reproduced by permission of American Geophysical Union.
Zheng, Q, S. Dickson, and Y. Guo (2008), On the appropriate "equivalent aperture" for the description of solute transport in single fractures: Laboratory-scale experiments, *Water Resource Research*, vol. 44, W04502, 2008. Copyright [2008] American Geophysical Union.

Abstract

Three distinct definitions of 'equivalent aperture' have been used in the literature to describe variable-aperture fractures; however, significant inconsistencies exist in the literature as to which 'equivalent aperture' is appropriate for simulating solute transport. In this work, a systematic series of hydraulic and tracer tests was conducted on three laboratory-scale fracture replicas, and the cubic law, mass balance and frictional loss apertures were calculated. The analytical solution of the one dimensional advection-dispersion equation was fit to the experimental breakthrough curves. Additionally, one of the experimental aperture fields was measured directly using a light transmission technique. The results clearly demonstrate that the mass balance aperture is the only appropriate 'equivalent aperture' for describing solute transport in a single variable aperture fracture, and that the mass balance aperture is an excellent approximation of the arithmetic mean aperture. Previously, these conclusions have been reached based only on theoretical and numerical analyses.

Key words: equivalent fracture aperture, solute transport, tracer test, mass balance aperture, cubic law aperture, hydraulic aperture

3.1. Introduction

Prior to the 1980s, researchers in the field of fracture flow and transport conceptualized a single fracture, the basic unit of fractured media, as a pair of parallel plates with a constant aperture. It is now well recognized in the literature that single fractures are rough-walled conduits with variable apertures and points of contact (e.g., Durham and Bonner, 1994; Novakowski and Lapcevic, 1994; Brown et al., 1998). Fracture apertures can be described by normal (e.g., Lee et al., 2003), lognormal (e.g., Keller, 1998; Keller et al., 1999), or gamma distributions (e.g., Tsang and Tsang, 1987), or a self-affine scale invariance (e.g., Plouraboue et al., 1995). The natural fracture wall surface roughness can also be well described by a self-affine scale invariance (Brown and Scholz, 1985; Schmittbuhl et al., 1995; Bouchaud, 1997). Although the combination of surface roughness and aperture field variability render the parallel plate description of fractures inadequate for the majority of flow and transport problems (e.g., Durham and Bonner, 1994; Brown, 1995; Keller et al., 1999), researchers often find it convenient to represent aperture fields in terms of an 'equivalent aperture' in both theoretical studies and experimental investigations. Various definitions of 'equivalent apertures' appearing in the literature caused some confusion until Tsang (1992) reviewed the literature and categorized three distinct 'equivalent apertures'. Specifically, Tsang (1992) described the mass balance aperture (μ_m), the cubic law aperture (μ_c), and the frictional loss aperture (μ_l), which typically have the following relationship: $\mu_m \geq \mu_c \geq \mu_l$ (Tsang, 1992) with some exceptions (Silliman, 1989). The mass balance and cubic law aperture correspond to the arithmetic and geometric mean of the aperture field respectively (Tsang, 1992).

Smith and Freeze (1979) employed numerical simulations to verify that the geometric mean permeability gives the correct volumetric flow rate for linear flow in a two dimensional random field of permeabilities. Gelhar (1993) and Tsang (1992) concluded from their theoretical analyses that the geometric mean aperture is the appropriate 'equivalent aperture' for use in hydraulic calculations, while the mass balance aperture is more appropriate for evaluating the mean displacement of a solute. Moreno et al. (1988) confirmed by numerical simulations that the mean tracer residence time based on the mass balance aperture agreed very well with that derived from the time moment of the tracer breakthrough curve obtained from particle-tracking simulations.

However, these conclusions lack support from experimental observations in well-characterized fractures. Moreover, in practice, researchers do not always distinguish between the above-mentioned three equivalent apertures, and therefore do not always use the mass balance aperture in their interpretation of solute tracer tests (e.g., Hinsby et al., 1996; Kosakowski, 2004). Therefore, the conventional procedure of fitting one-dimensional analytical solutions to experimental breakthrough curve data will lead to erroneous estimates of transport parameters. Furthermore, transport in fractured media is often affected by diffusion into the porous matrix and infill material among other factors. The discrepancy in breakthrough curve fit caused by using the hydraulic or frictional loss aperture instead of the mass balance aperture can be compensated for by adjusting parameters related to these factors, which may lead to additional errors when estimating solute transport parameters. The goal of this research is to demonstrate and confirm that the mass balance aperture is the only equivalent aperture appropriate for simulating solute tracer transport in single fractures in which the effects of both matrix diffusion and infill material are negligible. This goal was accomplished through conducting a series of systematic solute transport experiments at the laboratory-scale, in well-characterized fractures with isolated parameters, and fitting the measured breakthrough curves to mathematical models.

3.2. Experimental Design

3.2.1 Materials and Methods

A series of hydraulic and solute tracer transport tests were conducted in three transparent fracture replicas, F1, F2, and F3 (Table 3.1). These tests were designed as a 3^2 factorial experiment, with three specific discharges (based on μ_c) applied in each of the three synthetic fractures, and all other variables held constant. The fabrication of the fracture replicas was based on the method presented by Dickson (2001), and employed an impervious epoxy thereby negating any matrix effects on flow and transport in the fracture.

The experimental setup, illustrated in Figure 3.1, involved sealing the two opposite long edges of each fracture replica to serve as no-flow boundaries and operating the remaining two edges as constant-pressure boundaries. The fractures were oriented horizontally in all of the hydraulic and tracer tests. For the no-flow boundaries along each side of the fracture, a 0.2 cm thick gasket and a 1.1 cm thick piece of plexiglass were cut to the same dimensions as the side surface of the fracture block. The gasket was placed over the fracture trace along the edge of the fracture block, and the plexiglass was placed over the gasket. A steel frame was built (Figure 3.1 (b) and (c)) in which each fracture replica was mounted. Bolt holes were drilled every 6.0 cm along each side of the frame so that the plexiglass could be tightened to compress the gasket thus sealing the fracture (Figure 3.1 (b) and (c)). The bolts, as shown in Figure 3.1 (b) and (c), were tightened, and silicone sealant was then used to coat the seam between the plexiglass, the gasket, and the edge of the fracture to prevent any leaks.

The upstream and downstream ends of each fracture were sealed in a manner similar to the sides, except that a channel was cut out of the center of a 0.5 cm thick gasket, which served as a constant-pressure flow manifold. Additionally, four to six holes were drilled into the plexiglass and tapped to serve as flow ports, as shown in Figure 3.1 (a). The plexiglass pieces U1, U2, D1, and D2 (Figure 3.1 (b) and (c)) were installed for two purposes. First, the plexiglass served as a support when the apparatus was suspended over a light box to facilitate photography. Second, it was found that when the aperture is too large, the pressure difference between the upstream and downstream manifolds is too small to be measured reliably. Therefore, pressure was applied to the fracture by tightening the bolts through U2 and D2, and U1 and D1 served to distribute the applied pressure evenly over the fracture. This procedure effectively reduced the fracture aperture.

The recirculation system for the upstream and downstream flow manifolds is illustrated in Figure 3.1 (a), and consists of Teflon tubing strung through two bolt holes; one located at each the highest and lowest points of the manifold. The Teflon tube was perforated approximately every 5 mm, and each end of the tube was attached to pump tubing (MasterFlex, L/S 16) to form a closed-loop system. Throughout the duration of each experiment, the solution in the flow manifold was continuously re-circulated using a peristaltic pump (MasterFlex, L/S 7543-20).

3.2.2 Hydraulic Tests

Hydraulic tests were performed on each fracture plane to determine the equivalent hydraulic aperture as defined by Tsang (1992). A peristaltic pump (MasterFlex, L/S 7523-70) was employed to inject water through the fracture plane, and an inclined piezometer was attached to the upstream and downstream manifolds to measure the head loss across the fracture. For F1, a pulsation dampener was used to eliminate pressure pulses in the inlet manifold caused by the pump. For F2 and F3, a multi-channel peristaltic pump was used to minimize pulsations. Water exited the system through a constant-head port on the downstream end of the fracture. A tipping bucket rain gauge (Davis, Rain Collector II) was installed directly below the constant-head outlet to measure the volumetric flow rate. The rain gauge was connected to a data logger (Lakewood Systems Ltd., UL16 GC), which recorded the number of tips at set time intervals. The rain gauge was calibrated regularly throughout the course of these experiments.

The water employed in these experiments was prepared by degassing distilled water and equilibrating it to room temperature. This procedure prevented any gaseous phase from developing in the fracture plane during the experiments. Each fracture plane was saturated prior to commencing any experiments by first conducting a carbon dioxide flush to remove any air present in the system, and then injecting the prepared water.

Once the fracture plane was completely saturated, hydraulic tests were conducted by injecting water through the fracture at a constant flow rate, and measuring the resulting head difference across the fracture plane. Hydraulic tests were repeated at various flow rates on each fracture. Each time a fracture plane was re-saturated, hydraulic tests were performed to ensure that the equivalent hydraulic aperture remained unchanged.

3.2.3 Solute Tracer Tests

The solute tracer tests were designed to determine the mass balance and frictional loss apertures under a range of flow rates. Tracer tests were performed using a pulse input of solute. Bromide was selected as the conservative tracer, and was prepared as a 0.1 M solution using distilled water. The solution was then degassed and equilibrated to room temperature.

The procedure for conducting the solute tracer experiments involved first saturating the fracture plane with deionized water as described above. Next, the tubing was clamped at C2 and C3 (Figure 3.1 (a)) to prevent the loss of solute mass to the fluid in the manometer, and at C1 (Figure 3.1(a)) to ensure that the solute mass entered the recirculation system rather than migrating upstream. A 5 mL disposable plastic syringe (BD 5 mL syringe) was used to inject 5 mL of 0.1 M bromide solution into the tubing immediately upstream of the recirculation system, and re-circulation pump 2 was turned on for 20 s to mix the bromide solution evenly throughout the upstream manifold. A dye test was conducted prior to these experiments to determine the 20 s mixing requirement for this phase. Finally, the clamp was removed at C1 (Figure 3.1 (a)), and feed pump 1 and recirculation pumps 2 and 3 were turned on simultaneously to begin the tracer test. Samples were collected at E2 (Figure 3.1(a)) every one minute until the effluent bromide concentration was below the detection limit of the high performance liquid chromatograph (HPLC) (Varian, ProStar)

The samples collected from the tracer tests were analyzed using an HPLC (Varian ProStar) equipped with an autosampler (Varian, 410), a solvent delivery module (Varian, 230), and a conductivity detector (Dionex, CD25) at flow rate of 1.5 mL/min. A 4 x 200 mm column (Dionex, AS12A) was employed with a chemical suppressor (Dionex, AMMS III 4mm). The eluent solution was comprised of 0.3 mM $NaHCO_3$ and 2.7 mM Na_2CO_3. The regenerant for the chemical suppressor was a 12.5 mM H_2SO_4 solution.

3.2.4 Direct Aperture Field Measurement

One of the fracture replicas, F2, was measured directly using the light transmission technique described by Renshaw et al. (2000). The technique is based on measuring the transmitted light intensity of an aperture field, filled with Milli-Q water and subsequently dyed water, at each pixel on a digital image. A scientific grade charge-coupled device (CCD) camera (Photometrics, CoolSNAP$_{ES}$) was employed to shoot 100 images (50 Milli-Q-filled and 50 dye-filled), which were then averaged. The intensity at each pixel was then related to the aperture at that pixel through the Beer-Lambert Law. The reader is referred to Renshaw et al. (2000) for a discussion of the light transmission technique and Detwiler et al. (1999) for a discussion of the associated error.

3.3. Results and Discussion

Hydraulic tests were conducted to determine the range of flow rates under which laminar flow dominates in F1, F2 and F3. Three 'equivalent apertures', specifically, the cubic law (μ_c), mass balance (μ_m), and frictional loss (μ_l) apertures, were calculated based on the hydraulic and conservative solute tracer tests as follows (Tsang, 1992):

$$\mu_c = \left(\frac{12\eta Q L}{\gamma W |\Delta H|} \right)^{1/3} \tag{3.1}$$

$$\mu_m = \frac{Q t_m}{L W} \tag{3.2}$$

$$\mu_l = L \left(\frac{12\eta}{\gamma |\Delta H| t_m} \right)^{1/2} \tag{3.3}$$

with (Fahim and Wakao, 1982)

$$t_m = \frac{\int_0^\infty C_{out}(t) t\,dt}{\int_0^\infty C_{out}(t)\,dt} - \frac{\int_0^\infty C_{in}(t) t\,dt}{\int_0^\infty C_{in}(t)\,dt} \tag{3.4}$$

where Q ($L^3 \cdot T^{-1}$) is the volumetric flow rate, L (L) represents the length of the fracture in the direction of flow, W (L) is the fracture width (perpendicular to the direction of flow), ΔH (L) is the hydraulic head loss across the length of the fracture, η ($M \cdot L^{-1} \cdot T^{-1}$) is the dynamic viscosity of the fluid, γ ($M \cdot L^{-2} \cdot T^{-2}$) is the specific weight of the fluid, t_m (T) is the mean residence time of tracer transport, and $C_{in}(t)$ and $C_{out}(t)$ represent the tracer concentration at time t in the upstream and downstream manifolds respectively.

The corresponding specific discharges, v_c ($L \cdot T^{-1}$), v_m ($L \cdot T^{-1}$), and v_l ($L \cdot T^{-1}$), which are based on the cubic law, mass balance, and frictional loss apertures respectively, are given by

$$v_c = \frac{Q}{W \mu_c} \tag{3.5}$$

$$v_m = \frac{Q}{W \mu_m} \tag{3.6}$$

$$v_l = \frac{Q}{W\mu_l} \tag{3.7}$$

Table 3.1 lists the equivalent apertures specific discharges, estimated fracture volumes, and Peclet and Reynolds numbers calculated from these hydraulic and conservative tracer experiments.

Figure 3.2 demonstrates a linear relationship between the specific discharge and hydraulic gradient across the fracture within the range of specific discharges employed in these experiments. The Reynolds number, calculated based on the hydraulic aperture and the corresponding specific discharge, is near to or less than one at each specific discharge employed in these experiments (Table 3.1). These data indicate that the flow is laminar within the range of specific discharges applied in F1, F2, and F3, and therefore the assumption of laminar flow made in the derivation of the cubic law is satisfied.

Assuming that the experimental fractures can be represented by parallel plates with an 'equivalent aperture', the following one-dimensional transport equation was used to model the conservative tracer transport (van Genuchten, 1981):

$$\frac{\partial C(x,t)}{\partial t} = D\frac{\partial^2 C(x,t)}{\partial x^2} - v\frac{\partial C(x,t)}{\partial x} \tag{3.8a}$$

$$C(x,0) = 0,\ x > 0 \tag{3.8b}$$

$$\left.\frac{\partial C(x,t)}{\partial x}\right|_{(\infty,t)} = \text{(finite)},\ t \geq 0 \tag{3.8c}$$

$$C(0,t) = C_0 \exp(-\lambda t) \tag{3.8d}$$

where x (L) is the distance along the x-axis in the direction of flow, t (T) is the time from the beginning of the solute pulse release, $C(x,t)$ ($M \cdot L^{-3}$) is the solute concentration at distance x and time t, v ($L \cdot T^{-1}$) is the specific discharge, C_0 ($M \cdot L^{-3}$) is the concentration at $x = 0$ and $t = 0$, D ($L^2 \cdot T^{-1}$) is the hydrodynamic dispersion coefficient and λ (T^{-1}) is a decay constant. The solution to (8) is (van Genuchten, 1981):

$$C(x,t) = C_0 \exp(-\lambda t)\left\{\frac{1}{2}\exp\left[\frac{(v-\xi)x}{2D}\right]erfc\left[\frac{x-\xi t}{\sqrt{4Dt}}\right] + \frac{1}{2}\exp\left[\frac{(v+\xi)x}{2D}\right]erfc\left[\frac{x+\xi t}{\sqrt{4Dt}}\right]\right\} \quad (3.9)$$

with

$$\xi = v\left[1 - 4\lambda D / v^2\right]^{1/2} \quad (3.10)$$

and (Bear, 1972):

$$D = \alpha_L v + D_m \quad (3.11)$$

where α_L (L) is the dispersivity, and D_m ($L^2 \cdot T^{-1}$) is the molecular diffusion coefficient in water.

Due to the significant volume of the flow manifolds at the upstream and downstream ends of each experimental fracture, the measured concentration was adjusted to represent the actual concentration of the solute entering and exiting the fracture. The upstream manifold was modeled using a mass balance on a completely mixed continuous flow reactor:

$$QC_{in}(t) - QC_{out}(t) = V_{ol}\frac{dC_{out}(t)}{dt} \quad (3.12a)$$

$$C_{out}(t)\Big|_{t=0} = \frac{M}{V_{ol}} \tag{3.12b}$$

where Q ($L^3 \cdot T^{-1}$) represents the flow rate through the system, $C_{in}(t)$ ($M \cdot L^{-3}$) represents the concentration of the solute entering the manifold at time t, $C_{out}(t)$ ($M \cdot L^{-3}$) represents the concentration of the solute exiting the flow manifold at time t (i.e., entering the fracture), V_{ol} (L^3) represents the combined volume of the manifold and re-circulation system, and M (M) is the mass of the tracer injected. Equation (3.12b) assumes that the Br^- concentration at t=0 is uniform in the upstream manifold. The solution to equations (3.12a) and (3.12b) is:

$$C_{out}(t) = \frac{M}{V_{ol}} \exp\left(-\frac{Q}{V_{ol}} t\right) \tag{3.13}$$

Equation (3.13) indicates that the solute concentration in the upstream manifold decreased exponentially over the course of each tracer experiment, as shown in Figure 3.3. Therefore, the constants C_0 and λ in equations (3.8), (3.9) and (3.10) are given by:

$$\lambda = \frac{Q}{V_{ol}} \tag{3.14a}$$

$$C_0 = \frac{M}{V_{ol}} \tag{3.14b}$$

Also shown in Figure 3.3 is the measured concentration profile in the upstream manifold of F2 when the flow rate is 7.38 mL/min (v_c = 1.09 mm/s). The measured concentration profile is well approximated by the theoretical equation (3.13). The slight difference between the measured and theoretical concentration profiles can be explained by the existence of a dead volume or bypassing in the upstream manifold.

The concentration entering the downstream flow manifold from the fracture can also be described by equation (3.12a). Rearranging (3.12a) into difference form gives:

$$C_{eff-frac}(t) = \frac{V_{ol}}{Q}\left(\frac{C_{eff}^{t+\Delta t} - C_{eff}^{t-\Delta t}}{2\Delta t}\right) + C_{eff}^{t} \tag{3.15}$$

where $C_{eff\text{-}frac}$ ($M{\cdot}L^{-3}$) represents the solute concentration exiting the fracture at time t, C_{eff} ($M{\cdot}L^{-3}$) represents the concentration measured in the effluent manifold at time t, and Δt (T) is the time between sampling events. The measured concentration of each sample taken from the downstream manifold was adjusted using equation (3.15) to reflect the concentration exiting the fracture. Additionally, all effluent samples were corrected for time due to the tubing volume, $V_{E1\text{-}E2}$, (see Figure 3.1a) between the downstream flow manifold and the sampling point as follows:

$$t_{corr} = t_{mea} - \frac{V_{E1-E2}}{Q} \tag{3.16}$$

where t_{corr} (T) represents the corrected time of each sampling event and t_{mea} (T) represents the time from the start of the experiment at which the sample was actually taken.

The adjusted experimental breakthrough curves were fit to equation (3.9) using PEST (Watermark Numerical Computing, Version 9.0). The dispersivity (α_L), both alone and in combination with the specific discharge (v), was employed as the fitting parameter(s). It is noteworthy that an "effective volume", rather than the actual volume, of the downstream re-circulation system was employed in equation (3.15) as there was likely a dead volume present in the downstream flow manifolds of F2 and F3. The actual volumes of each fracture's downstream re-circulation system are listed in Table 3.1. When the effluent concentration profiles from F1 were adjusted using the actual manifold volume of 17 mL in equation (3.15), the analytical and experimental breakthrough curves matched well. However, for F2 and F3, the simulated breakthrough curves fit the experimental observations best when the values of V_{0l} in equation (3.15) were reduced to 17 mL. Since the pump capacity and tubing lengths of the downstream recirculation systems are identical for F1, F2, and F3, it is reasonable that the "effective volume" of the downstream manifolds, which represent the volumes completely mixed by the recirculation system, are also identical.

Two approaches were employed to fit equation (3.9) to the measured experimental breakthrough curves using PEST. The first approach, hereafter referred to as the single-parameter approach, employed the specific discharges calculated from the measured experimental breakthrough curves using equations (3.5), (3.6), and (3.7), and dispersivity was the only fitting parameter. This approach generated three distinct breakthrough curves for fitting purposes, one based on each of the three equivalent apertures calculated from the experimental breakthrough curves. The second approach, hereafter referred to as the two-parameter approach, employed both dispersivity and specific discharge as fitting parameters. Figure 3.4 shows the experimental breakthrough curve for the solute tracer test through F2 with v_c = 1.09 mm/s, together with the three analytical breakthrough curve fits based on the single-parameter approach and the analytical breakthrough curve fit based on the two-parameter approach. The fracture dispersivities obtained from the first fitting approach, together with the specific discharges and dispersivities obtained from the second fitting approach, are listed in Table 3.2. The magnitude of the fit dispersivities relative to that of the fracture length is within the range of that reported by others (e.g., Thompson and Brown, 1991; Keller et al., 1995). Additionally, the fit specific discharge, v_f, was very similar to the specific discharge based on the mass balance aperture, v_m, obtained from the experimental breakthrough curves. Therefore, the breakthrough curve fits appear reasonable upon examination of the fitting parameter(s).

The analytical curve fits were very sensitive to the specific discharge. Figure 3.4 clearly shows that when the specific discharge based on the mass balance aperture was employed in equation (3.9), very good agreement was obtained between the simulated and experimental breakthrough curves. The slight difference between the experimental curve and the simulated single-parameter mass balance and two-parameter fit curves can be attributed to the existence of dead volumes in both the upstream and downstream manifolds. These dead volumes resulted in slight discrepancies between the measured and theoretical input functions (Figure 3.3) and the adjusted and actual breakthrough curves. Figure 3.4 also shows that when the specific discharges based on the cubic law and frictional loss apertures were employed in equation (3.9), the resulting simulated fits to the experimental data were very poor. The fits between the analytical and experimental breakthrough curves shown on Figure 3.4 are typical of those obtained in all eight solute transport experiments. The observed breakthrough curves together with the analytical curve fits from the remaining seven experiments are provided as accompanying material on-line. It should be reiterated here that these experiments were conducted under flow conditions in which inertial forces were negligible.

Table 3.3 shows the aperture field statistics of F2 obtained from the direct aperture field measurement. The mean experimental mass balance aperture (1.61mm) is within 2% of the arithmetic mean aperture $<b_a>$, which confirms Tsang's (1992) theoretical conclusion that the mass balance aperture is a good approximation of the arithmetic mean aperture. Additionally, the actual fracture volume obtained from the direct aperture field measurement (Table 3.3) lies within the 99.9% confidence interval of the mean volume of F2 calculated based on the mass balance aperture (Table 3.1) (120 mL ± 38 mL). The root mean square errors (RMSE) presented in Table 3.3 appear very low; however, each measurement presented in Table 3.3 is based on 50 million data points. The large number of data points significantly reduces the error associated with the standard deviation of $<b_a>$. It is also noteworthy that the RMSEs presented in Table 3.3 are within the range of those presented by Detwiler et al. (1999).

Figure 3.5 shows that the specific discharge based on the mass balance aperture, v_m, agrees very well with that obtained through the two-parameter fitting approach, v_f. The fitting results shown in Figures 3.4 and 3.5 clearly demonstrate the theoretical conclusion proposed by Gelhar (1993), and the simulation results presented by Moreno et al. (1988), that the mass balance aperture is the only 'equivalent aperture' appropriate for describing solute transport in single variable aperture fractures under laminar flow conditions.

The data presented in Table 3.1 reveal two additional noteworthy observations. First, the relative magnitude of the three equivalent apertures follows the relationship $\mu_m \geq \mu_c \geq \mu_l$, which is consistent with the argument presented by Tsang (1992). Second, although the hydraulic aperture remains relatively stable under the range of specific discharges tested in these experiments, the mass balance aperture increases and the frictional loss aperture decreases (to a lesser extent) with increasing specific discharge. This is due to the fact that smaller specific discharges provide the tracer with access to fewer flow paths than larger specific discharges. Therefore, in equation (3.2), when Q increases by a factor of n, t_m decreases by a factor of $1/m$ where $m<n$. Therefore, μ_m increases with increasing specific discharge. Since μ_l is inversely proportional to $t_m^{1/2}$, it is less sensitive to specific discharge than μ_m, although it does decrease with increasing specific discharge. These observations are supported by those of Moreno et al. (1990), who also found that the mass balance aperture was sensitive to flow rate in their numerical experiments.

Table 3.2 shows that the dispersivity was not constant in any of the experimental fractures; it increased with the specific discharge. This is consistent with the experimental data presented by Dronfield and Silliman (1993) and Detwiler et al. (2000), which also demonstrate an increase in dispersivity with the specific discharge if a linear relationship between the hydrodynamic dispersion coefficient and the specific discharge is assumed (equation (3.11)). However, rather than assuming a linear relationship, Dronfield and Silliman (1993) derived a unique dispersivity for each aperture field in their research by assuming that the hydrodynamic dispersion coefficient is a function of the velocity raised to a power *n* ($D = \alpha v^n$), and demonstrated that *n* took on values ranging from 1.3 to 2.0 depending on the fracture roughness. Detwiler et al. (2000) agreed that the hydrodynamic dispersion coefficient is nonlinearly dependent on velocity; however, they presented a different expression to describe this nonlinear dependence:

$$D_L = \tau D_m + \alpha_{macro} Pe D_m + \alpha_{Taylor} Pe^2 D_m$$

$$\text{where } Pe = \frac{v\langle b_a \rangle}{D_m} \tag{3.17}$$

where τ (-) represents the tortuosity factor for molecular diffusion along the fracture, α_{Taylor} and α_{macro} are nondimensional coefficients representing the contributions of Taylor dispersion and macrodispersion respectively, *Pe* (-) is the Peclet number, v ($L \cdot T^{-1}$) is the mean solute velocity (equivalent v_m in this research), and $<b_a>$ (L) is the arithmetic mean aperture. Currently, there is no agreement in the literature regarding the relationship between dispersivity and velocity in fractures, and therefore this subject merits further investigation.

3.4. Summary

Laboratory-scale conservative solute tracer experiments were conducted at three different specific discharges through three distinct single fracture replicas. An analytical solution to the one-dimensional advection-dispersion equation was fit to each experimental breakthrough curve three times, each time applying v based on one of the three 'equivalent apertures' derived from the tracer experiments, and employing α as the only fitting parameter, and a fourth time employing both v_f and α_f as fitting parameters. Additionally, one of the experimental fractures (F2) was measured directly. The excellent agreement between the experimental breakthrough curves and the simulated curves based on the single-parameter curve fit applying the mass balance aperture clearly demonstrates that the mass balance aperture is the only equivalent aperture appropriate for describing solute transport in single variable-aperture fractures. Additionally, the concurrence between the experimental mass balance aperture and the arithmetic mean aperture from the direct aperture measurement in F2 supports Tsang's (1992) arguments, which lend additional weight to this conclusion. This is the first set of laboratory data to explicitly demonstrate this fact, which is an important verification of the theoretical conclusions presented by Tsang (1992) and Gelhar (1993), and those based on numerical simulations presented by Moreno et al. (1988).

Acknowledgement

Funding for this work was provided by the NSERC Discovery Grant Program.

References

Bear, J. (1972), *Dynamics of Fluids in Porous Media*, American Elsevier, New York.

Bouchaud, E. (1997), Scaling properties of crack surfaces, *J. Phys. Condens. Matter, 9*, 4319-4344.

Brown, S. R. (1995), Simple mathematical model of a rough fracture, *J. Geophys. Res.*, *100*(B4), 5941-5952.

Brown, S. R., and C. H. Scholz (1985), Broad bandwidth study of the topography of natural rock surfaces, *J. Geophys. Res.*, *90*, 12575-12582.

Brown, S., A. Caprihan, and R. Hardy (1998), Experimental observations of fluid flow channels in a single fracture, *J. Geophys. Res.*, *103*(B3), 5125-51321.

Detwiler, R. L., H. Rajaram, and R. J. Glass (2000), Solute transport in variable-aperture fractures: an investigation of the relative importance of Taylor dispersion and macrodispersion, *Water Resour. Res.*, *36*(7), 1611-1625.

Dickson, S.E. (2001), Dissolution of entrapped DVAPLS in variable aperture fractures, Ph.D. thesis, University of Waterloo, Waterloo, Ontario, Canada.

Dronfield, D. G., and S. E. Silliman (1993), Velocity dependence of dispersion for transport through a single fracture of variable roughness, *Water Resour. Res.*, *29*(10), 3477-3483.

Durham, W. B., and B. P. Bonner (1994), Self-propping and fluid flow in slightly offset joints at high effective pressures, *J. Geophys. Res.*, *99*(B5), 9391-9399.

Gelhar, L. W. (1993), *Stochastic Subsurface Hydrology*, Prentice-Hall, Old Tappan, N. J.

Fahim, M. A., and N. Wakao (1982), Parameter estimation from tracer response measurements, *Chem. Eng. J.*, *25*, 1-8.

Hinsby, K., L. D. McKay, P. Jorgensen, M. Lenczewski, and C. P. Gerba (1996), Fracture aperture measurements and migration of solutes, viruses, and immiscible creosote in a column of clay-rich till, *Ground Water*, *34*(6), 1065-1075.

Keller, A. (1998), High resolution, non-destructive measurement and characterization of fracture apertures, *Int. J. Rock Mech. Min. Sci.* , *35*(8),1037-1050.

Keller, A. A., P. V. Roberts, and M. J. Blunt (1999), Effect of fracture aperture variations on the dispersion of contaminants, *Water Resour. Res.*, *35*(1), 55-63.

Keller, A. A., P. V. Roberts, and P. K. Kitanidis (1995), Prediction of single phase transport parameters in a variable aperture fracture, *Geophys. Res. Lett.*, *22*(11), 1425-1428.

Kosakowski, G. (2004), Anomalous transport of colloids and solutes in a shear zone, *J. Contam. Hydrol.*, *72*, 23-46.

Lee, J., J. M. Kang, J. Choe (2003), Experimental analysis on the effects of variable apertures on tracer transport, *Water Resour. Res.*, 39(1), 1015, doi:10.1029/2001WR001246.

Moreno, L., Y. W. Tsang, C. F. Tsang, F. Hale, and I. Neretnieks, (1988), Flow and tracer transport in a single fracture: A stochastic model and its relation to some field observations, *Water Resour. Res.*, 24(12), 2033-2048.

Moreno, L., C. F. Tsang, Y. W. Tsang, and I. Neretnieks, (1990), Some anomalous features of flow and solute transport arising from fracture aperture variability, *Water Resour. Res.*, *26*(10), 2377-2391.

Novakowski, K. S., and P. A. Lapcevic (1994), Field measurement of radial solute transport in a fractured rock, *Water Resour. Res.*, *30*(1), 37-44.

Plouraboue, F., P. Kurowski, J. P. Hulin, S. Roux, and J. Schmittbuhl (1995), Aperture of rough crack, *Phys. Rev. E*, *51*, 1675-1685.

Renshaw, C. E., J. S. Dadakis, and S. R. Brown (2000), Measuring fracture apertures: a comparison of methods, *Geophys. Res. Lett.*, 27(2), 289-292.

Silliman, S. E. (1989), An interpretation of the difference between aperture estimates derived from hydraulic and tracer tests in a single fracture, *Water Resour. Res.*, *25*(10), 2275-2283.

Smith, L., and R. A. Freeze (1979), Stochastic analysis of steady state groundwater flow in a bounded domain, 2, Two-dimensional simulation, *Water Resour. Res.*, *15*(6), 1543-1559.

Schmittbuhl, J., F. Schmitt, and C. H. Scholz (1995), Scaling invariance of crack surfaces, *J. Geophys. Res.*, *100*, 5953-5973.

Thompson, M. E., and S. R. Brown (1991), The effect of anisotropic surface roughness on flow and transport in fractures, *J. Geophys. Res.*, *96*(B13), 21923-21932.

Tsang, Y. W., and Tsang, C. F. (1987), Channel model of flow through fractured media, *Water Resour. Res.*, *23*(2), 467-478.

Tsang, Y. W. (1992), Usage of 'equivalent apertures' for rock fractures as derived from hydraulic and tracer tests, *Water Resour. Res.*, *28*(5), 1451-1455.

Van Genuchten, M. Th. (1981), Analytical solutions for chemical transport with simultaneous adsorption, zero-order production, first-order decay, *J. Hydrol.*, *49*, 213-233.

Table 3.1[a] Summary of hydraulic and solute tracer test results

Fracture ID	Dimension (mm)	Manifold volume[e]		μ_c[f] (mm)	v_c (mm/s)	μ_m[f] (mm)	v_m (mm/s)	μ_l[f] (mm)	v_l (mm/s)	Estimated fracture aperture volume (mL)[b]			Peclet Number[c]	Reynolds Number[d]
		Upstream (mL)	Downstream (mL)							Based on μ_c	Based on μ_m	Based on μ_l		
F1	241.5×149.0	19	17	0.40 ±0.07	0.55	0.79 ±0.07	0.28	0.29 ±0.05	0.77	14	28	10	248	0.25
				0.40	1.09	0.93		0.27		14				0.49
				0.40 ±0.03	1.67	1.08 ±0.03	0.63	0.24 ±0.09	2.72	14	39	9	750	0.74
F2	350.0×214.5	45	43	0.54 ±0.03	0.55	1.53 ±0.02	0.21	0.33 ±0.10	0.97	41	115	25	352	0.36
				0.54 ±0.02	1.09	1.58 ±0.01	0.38	0.33 ±0.12	1.83	41	119	25	666	0.71
				0.54 ±0.01	1.67	1.71 ±0.01	0.53	0.32 ±0.16	2.84	41	128	24	1001	1.10
F3	349.0×230.0	49	52	0.60 ±0.03	0.55	1.49 ±0.02	0.22	0.41 ±0.10	0.80	48	120	33	369	0.41
				0.60 ±0.01	1.09	1.54 ±0.01	0.39	0.39 ±0.12	1.55	48	124	31	670	0.81
				0.40 ±0.07	1.67	1.93 ±0.01	0.46	0.34 ±0.18	2.60	48	155	27	989	1.24

[a] All experiments were conducted at 25±2°C, and the value of the parameters used in these calculations corresponds those at 25°C (i.e., ρ=997 kg/m^3, η = 0.00089 N.s/m^2).

[b] Estimated fracture aperture volume=$L \times W \times \mu$, where μ represents μ_c, μ_m, or μ_l.

[c] Peclet Number = $v_m \times \mu_m / D_m$

[d] Reynolds Number=$\rho \times v_c \times \mu_c / \eta$

[e] Manifold volume includes the volume of the manifold, sampling and recirculation systems.

[f] Plus or minus one standard deviation.

Table 3.2[a] Dispersivity and specific discharge values obtained from fitting the experimental breakthrough curves to the 1D advection dispersion equation.

acture ID	v_c (mm)	α_c (mm)[a] (95% confidence limit)	α_m (mm)[a] (95% confidence limit)	α_l (mm)[a] (95% confidence limit)	With 95% confidence limit[b]	
					α_f (mm)[b]	v_f (mm/s)[b]
F1	**0.55**	36 (24, 48)	114 (99, 128)	46 (18, 73)	85 (72, 99)	0.33 (0.31, 0.35)
	1.67	49 (31, 68)	186 (160, 212)	63 (6,121)	149 (117, 182)	0.72 (0.64, 0.80)
F2	**0.55**	82 (45, 118)	135 (128, 142)	173 (47, 300)	149 (137, 160)	0.20 (0.19, 0.20)
	1.09	79 (44, 115)	171 (162, 180)	152 (45, 259)	156 (144, 167)	0.40 (0.39, 0.42)
	1.67	81 (41, 121)	214 (199, 229)	141 (168, 265)	173 (157, 190)	0.60 (0.57, 0.63)
F3	**0.55**	65 (41, 90)	123 (114, 133)	122 (53, 191)	124 (112, 137)	0.22 (0.21, 0.23)
	1.09	67 (40, 93)	185 (164, 207)	120 (43, 197)	223 (181, 265)	0.35 (0.31, 0.38)
	1.67	74 (40, 108)	241 (211, 271)	145 (28, 263)	275 (211, 340)	0.42 (0.36, 0.48)

[a] α_c, α_m, and α_l represent the dispersivities calculated through fitting equation (3.8) to the experimental data using the single-parameter fitting approach with specific discharges v_c, v_m, and v_l respectively (calculated from the experimental breakthrough curves).

[b] α_f and v_f represent the dispersivity and specific discharge from the two-parameter fitting approach.

Table 3.3. F2 Aperture statistics derived from the direct aperture field measurement.

Fracture ID	F2
Arithmetic mean aperture ($<b_a>$, mm)	1.57 (RMSE = 0.3%)[1]
Standard deviation (σ, mm)	1.12
Coefficient of variation ($=\sigma/<b_a>$)	0.71
Geometric mean aperture ($<b_g>$, mm)	0.90
Harmonic mean aperture ($<b_h>$, mm)	0.13
Fracture volume (mL)	102 (RMSE = 0.3%)[1]

[1] RMSE $=\frac{\sigma(x)}{x}$, where x represents $<b_a>$ or fracture volume.

Figures

(a)

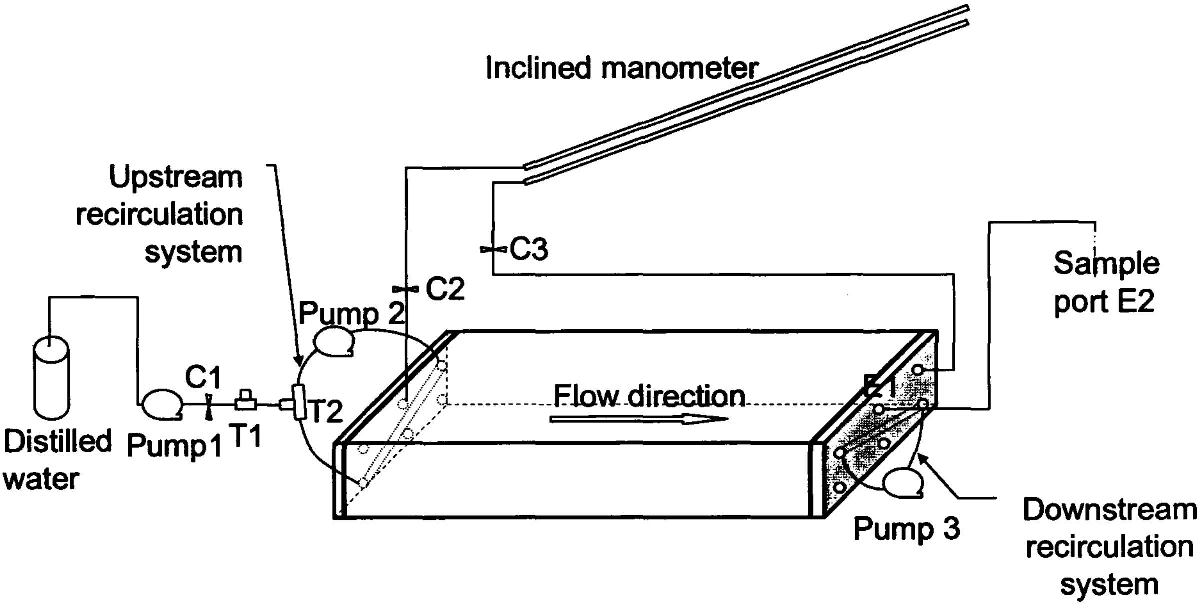
Inclined manometer
Upstream recirculation system
C3
C2
Sample port E2
Pump 2
C1
Flow direction
E1
T2
Distilled water
Pump1
T1
Pump 3
Downstream recirculation system

(b)

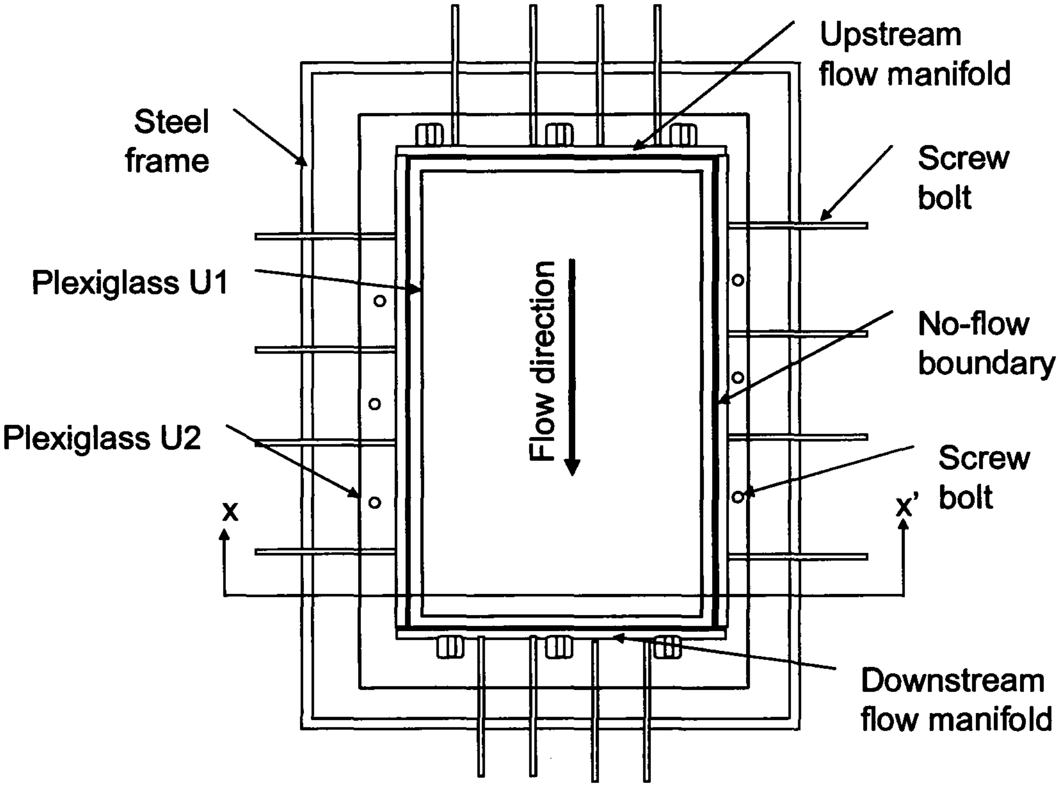
Upstream flow manifold
Steel frame
Screw bolt
Plexiglass U1
Flow direction
No-flow boundary
Plexiglass U2
Screw bolt
X
X'
Downstream flow manifold

(c)

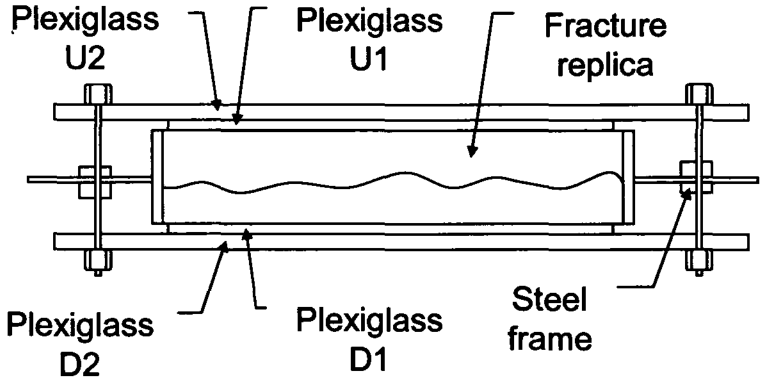

Figure 3.1. Schematic diagram of the experimental apparatus for the hydraulic and tracer tests showing a) the experimental setup, b) a plan view of the fracture mounted in the steel frame, and c) cross-section x-x′ of the experimental fracture mounted in the steel frame.

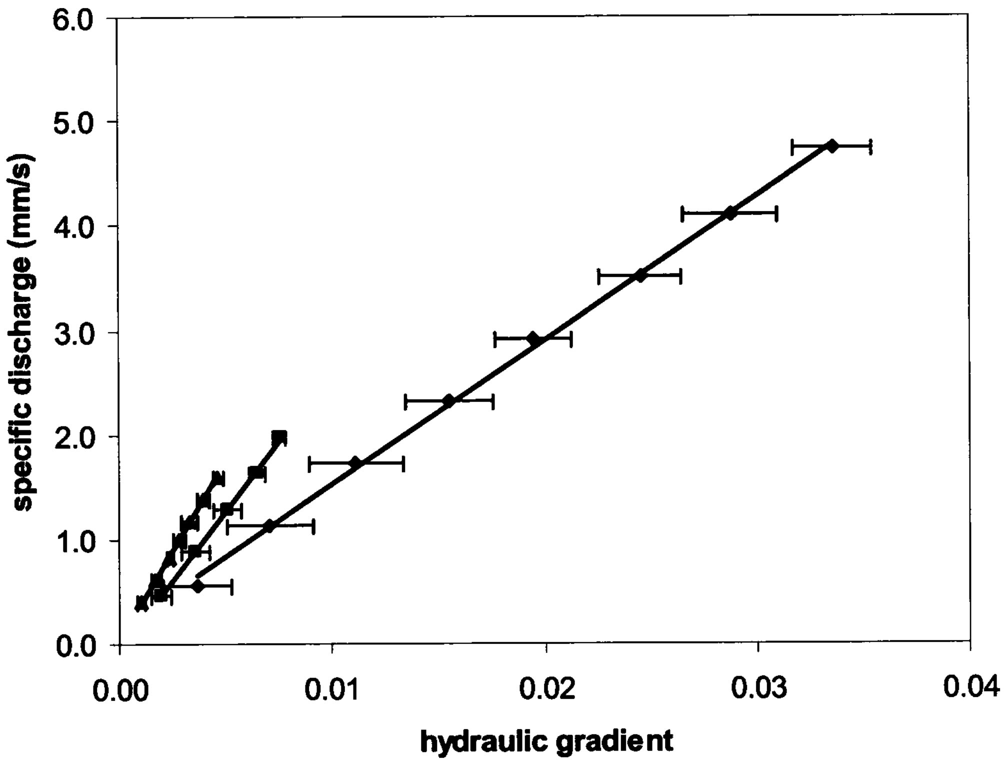

Figure 3.2. Hydraulic test results for F1 (♦: data; —— : regression line ($R^2 \approx 1$)); F2 (■: data; —— : regression line ($R^2 \approx 1$)); and F3 (▲: data; —— : regression line ($R^2 \approx 1$)).

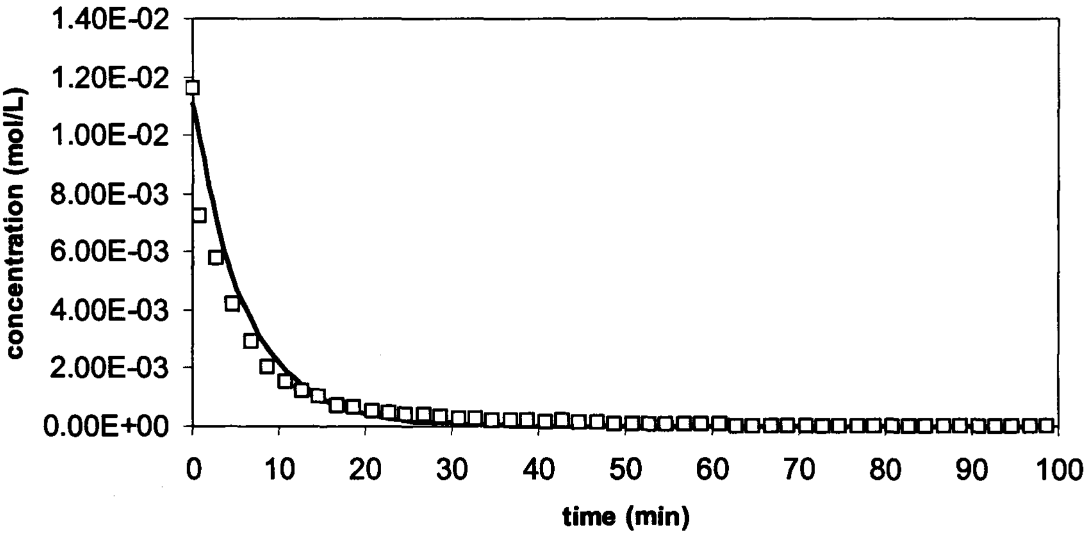

Figure 3.3. The concentration profile in the upstream manifold of F2 when v_c = 1.09 mm/s. —— shows the theoretical exponentially decreasing concentration profile and □ shows the measured concentration profile.

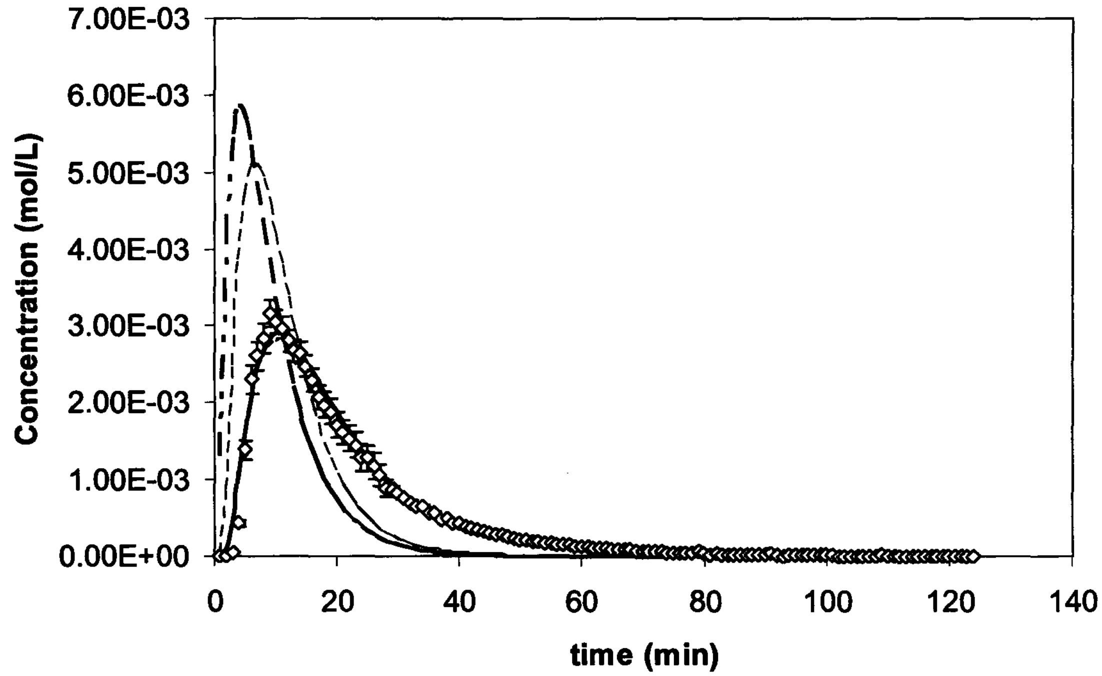

Figure 3.4. Breakthrough curves for the solute tracer test in F2 with v_c = 1.09 mm/s. ◊: experimental measurement (error bars represent one standard deviation); - - - - : simulation based on μ_c from physical experiment and α_c as the fitting parameter; ············ : simulation based on μ_m from physical experiment and α_m as the fitting parameter; — · · : simulation based on μ_l from the physical experiment and α_l as the fitting parameter, and ——— : simulation employing both v_f and α_f as fitting parameters.

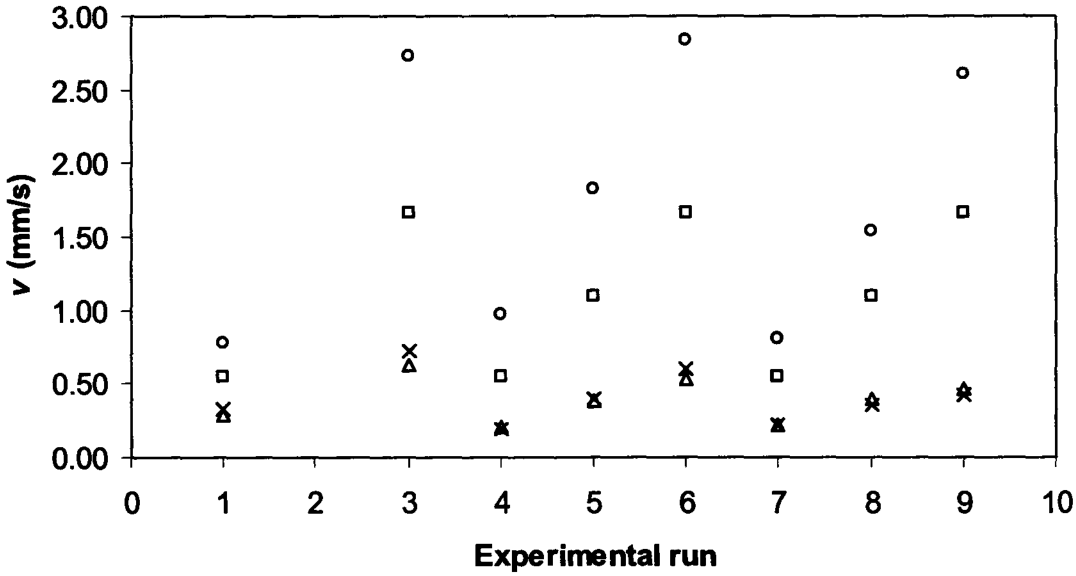

Figure 3.5. Comparison of discharge rates based on the different equivalent apertures.

Δ: v_m, ×: v_f, □: v_c, ○: v_l.

Chapter 4 The Influence of Aperture Field Heterogeneity and Anisotropy on Dispersion Regimes and Dispersivity in Single Fractures

Abstract

A 3^3 factorial experimental design was implemented to numerically investigate the interactive effect of the mean (μ_b), standard deviation (σ_b), and anisotropic ratio (AR: (λ^b_x/ λ^b_y) of single fracture apertures on dispersion regimes (specifically Taylor dispersion and geometric dispersion) and dispersivity. The Reynolds equation was solved to obtain the flow fields in each computer-generated fracture, and the random walk particle tracking method was used to simulate solute transport. The simulation results show that: (1) for a fixed hydraulic gradient: (a) the dominant dispersion regime is controlled by μ_b, and to a lesser degree, σ_b, and (b) geometric dispersion becomes more dominant as the coefficient of variation (σ_b/μ_b) increases; (2) for a fixed mean aperture, the dispersivity and the spread in dispersivity for varying ARs increases with the CoV; and (3) the AR has a significant effect on dispersivity only when the CoV is large (>0.2).

Key words: single fracture, aperture statistics, dispersivity, dispersion, dispersion regime, geometric dispersion, Taylor dispersion

4.1. Introduction

The geometry of aperture fields and the morphology of fracture walls are among the primary factors influencing flow and transport in single fractures; however, the relative importance of these properties remains to be evaluated (Gentier et al., 1997; Meheust and Schmittbuhl, 2001). Aperture field measurement using destructive (e.g., surface topography, casting, and injection methods) and nondestructive (e.g., magnetic resonance, x-ray, and light transmission techniques) methods suggest that fracture apertures follow normal (e.g., Lee et al., 2003), lognormal (e.g., Keller, 1998; Keller et al., 1999), and gamma distributions (e.g., Tsang and Tsang, 1987), and can also be self-affine when facing surfaces are uncorrelated (Plouraboue et al., 1995). The characterization of natural fracture wall surface morphology has shown that fracture wall roughness is well described by a self-affine scale invariance (Schmittbuhl et al., 1995; Bouchaud, 1997; Brown and Scholz, 1985). It is noteworthy that the statistical characteristics of the aperture field are not necessarily the same as those of the wall surface (Roberds et al., 1990).

Numerical studies (e.g., Tsang and Tsang, 1990), theoretical analyses (e.g., Gelhar, 1993), and experimental investigations (e.g., Keller et al., 1999) have shown that the mean (μ_b), standard deviation (σ_b) and correlation length (λ) of a fracture aperture field can be used to predict both the transmissivity and the dispersion coefficient. In addition to these factors, the anisotropy of both the aperture field and the fracture wall influence flow and transport in variable-aperture fractures. Natural fracture walls often show anisotropic roughness, particularly in plumose structures (e.g., Brown and Scholz, 1985) and fault zones (e.g., Power et al., 1987), which may also be manifested in the aperture field (Thompson and Brown, 1991). Thompson and Brown (1991) investigated the effect of anisotropic wall roughness on flow and transport in single fractures using numerical techniques, and concluded that the directional characteristics of the fracture wall play a more important role in determining fracture transport properties than the degree of wall roughness. This observation does not hold for the aperture field itself, however, as Lee et al. (2003) demonstrated that the effect of aperture field anisotropy is insignificant compared with the variability and correlation length of the aperture field in their laboratory-scale experiments. It should be noted, however, that the conclusion presented by Lee et al. (2003) was based on experimental results from five fracture replicas with a limited range of coefficients of variation (CoV: σ_b/μ_b) and anisotropic ratios (AR: λ^b_x/λ^b_y).

Recent scaling analyses (Roux et al., 1998), and experimental and numerical investigations (Plouraboue et al., 1998; Detwiler et al., 2000) have revealed that there exist three distinct dispersion regimes for solute transport in variable-aperture fractures, specifically the molecular diffusion regime, the geometric dispersion regime and the Taylor dispersion regime, which dominate within different ranges of the Peclet number, *Pe*:

$$Pe = v\mu_b / D^* \tag{4.1}$$

where v [$L \cdot t^{-1}$] is the mean solute velocity, μ_b [L] is the arithmetic mean aperture, and D^* [$L^2 \cdot t^{-1}$] is the molecular diffusion coefficient. The range of *Pe*, in turn, is controlled by the mean, variance, and correlation structure of the aperture field. Detwiler et al. (2000) numerically delineated the range of *Pe* in which different dispersion mechanisms dominate for four isotropic aperture fields with the same arithmetic mean aperture by changing the hydraulic gradient. The effects of mean aperture (μ_b) and anisotropy on the dominance of each dispersion regime were, however, beyond the scope of their investigation. Relatively few studies have been devoted to investigating the effects of aperture field heterogeneity and anisotropy on solute transport properties in single fractures, and therefore the understanding of the effects of these properties on transport remains limited. The effects of these parameters play a key role in furthering our understanding of solute transport in saturated fractured environments, which is required in order to build reliable predictive models. Fractured rock environments are important due to their prevalence throughout North America, and the speed at which contaminants can migrate through these environments relative to unconsolidated porous media. Additionally, transport in saturated fractured rock environments has not been investigated to the same extent that it has been in unconsolidated porous media environments, and therefore the understanding of these environments is still lacking significantly. Accurate and reliable predictive models are required in order to: develop sound management strategies for fractured rock aquifers; assess the risk to human and environmental health posed by the migration of contaminants in fractured environments; and develop remedial strategies for contaminated fractured rock environments.

Therefore, the goal of this research is to: (1) investigate the influence of an aperture field's arithmetic mean, variance, and AR on the predominance of each dispersion regime; and (2) systematically investigate the interactive influence of the mean, variance, and AR of fracture aperture fields on dispersivity in variable-aperture fractures.

4.2. Methods

To reach this goal, a 3^3 factorial experiment (Table 4.1) was designed to investigate the influence of the arithmetic mean (μ_b), standard deviation (σ_b), and anisotropy ratio (AR) of the aperture field on dispersivity and the predominance of each dispersion regime. Computer-generated aperture fields were employed, and aperture-averaged velocity fields were obtained by solving the Reynolds equation numerically. Solute transport in a single fracture was simulated using the random walk particle tracking (RWPT) technique.

4.2.1 Fracture aperture field generation

It was assumed that aperture fields follow a log-normal distribution, and the anisotropic covariance function, $C_{\ln(b)}$, of the log-aperture has the form (Chrysikopoulos and James, 2003):

$$C_{\ln(b)}(\boldsymbol{r}) = \sigma^2_{\ln b} \exp\left[-\left(\frac{r_x^2}{\lambda_x^2} + \frac{r_y^2}{\lambda_y^2}\right)^{\frac{1}{2}}\right] \tag{4.2}$$

where b [L] is the fracture aperture, $\sigma^2_{\ln b}$ is the variance of the ln-aperture, ln$b$, $\boldsymbol{r} = (r_x, r_y)^T$ is a two-dimensional vector whose magnitude is the separation distance between two aperture measurements, and λ_x [L] and λ_y [L] are the correlation length scales of ln$b$ in the x- and y- directions respectively. The μ_b and σ_b are related to their log-transformations by

$$\sigma_{\ln b} = \left[\ln\left(\frac{\sigma_b^2}{\mu_b^2} + 1 \right) \right]^{\frac{1}{2}} \tag{4.3}$$

$$\mu_{\ln b} = \ln \mu_b - 0.5\sigma_{\ln b}^2 \tag{4.4}$$

The quasi-three-dimensional fracture aperture fields employed in this research are 16.0 meters (x-direction) by 2.0 meters (y-direction). Each aperture field was discretized into a grid of 400 elements (x-direction) by 50 elements (y-direction) such that each 4 cm by 4 cm element had a distinct aperture. The aperture fields were generated using SPRT2D (Gutjahr, 1989), which is based on the Fast Fourier Transform technique. Figure 4.1(a) shows a typical aperture field generated in this manner. Fifty realizations for each set of aperture field statistics (μ_b, σ_b, and AR) were generated by changing the seed number supplied to the random field generator. The random noise present in the stochastic simulations was smoothed out using ensemble averages of the breakthrough curves generated by each of the 50 aperture field realizations (James et al., 2005).

4.2.2 Flow Field Calculation

The steady state flow field in each fracture plane was obtained by solving the Reynolds equation using a fully implicit finite difference technique (Chrysikopoulos and James, 2003):

$$\frac{\partial}{\partial x}\left[b^3(x,y)\frac{\partial h(x,y)}{\partial x} \right] + \frac{\partial}{\partial y}\left[b^3(x,y)\frac{\partial h(x,y)}{\partial y} \right] = 0 \tag{4.5a}$$

$$\left.\frac{\partial h(x,y)}{\partial y}\right|_{y=0.0} = 0 \tag{4.5b}$$

$$\left.\frac{\partial h(x,y)}{\partial y}\right|_{y=2.0} = 0 \tag{4.5c}$$

$$h(x,y)\big|_{x=0.0} = h_0 \tag{4.5d}$$

$$h(x,y)\big|_{x=16.0} = 0 \tag{4.5e}$$

where x [L] is the coordinate along the fracture length, y [L] is the coordinate along the fracture width, $h(x,y)$ [L] is the local hydraulic head, and $b(x,y)$ [L] is the local fracture aperture. The boundary conditions described in equation (4.5) represent no-flow boundaries on the sides of a horizontal fracture, and constant head upstream and downstream boundaries. The equivalent aperture between adjacent elements is approximated by the harmonic mean aperture of the two elements (Reimus, 1995). The mean fluid velocity components in both the x- and y- directions are calculated by (Chrysikopoulos and James, 2003):

$$v_x = -\frac{\gamma b^2(x,y)}{12\eta}\frac{\partial h(x,y)}{\partial x} \tag{4.6a}$$

$$v_y = -\frac{\gamma b^2(x,y)}{12\eta}\frac{\partial h(x,y)}{\partial y} \tag{4.6b}$$

where γ [$M \cdot L^{-2} \cdot t^{-2}$] is the fluid specific weight, and η [$M \cdot L^{-1} \cdot t^{-1}$] is the fluid dynamic viscosity. Figure 4.1(b) gives a schematic illustration of the coordinate system and the boundary conditions employed in these simulations. The model parameters are listed in Table 4.2. Further details regarding the finite difference modeling scheme for the flow field are included in Chrysikopoulos and James (2003).

It is well-recognized that the Reynolds equation employs numerous simplifying assumptions, the most limiting of which is that inertial forces are negligible. Several studies have demonstrated that the Reynolds equation over predicts the flow rate by up to twice the actual value (e.g., Hakami and Larsson, 1996; Yeo et al., 1998). However, Brush and Thomson (2003) conducted simulations to compare the Reynolds equation to both the Stokes and Navier Stokes equations under various geometric and kinematic conditions, and concluded that the Reynolds equation may be considered valid when the following criteria are satisfied:

$$Re < 1; \quad Re\langle b\rangle/\lambda_b < 1; \quad Re\sigma_b/\langle b\rangle < 1$$

The further beyond these ranges the parameters get, the more the Reynolds equation will over predict the flow. These conditions are met in a majority of the simulations conducted here (except when COV=1.2), and are never exceeded significantly. Therefore, it is sound to assume that the Reynolds equation is a reasonable approach for modeling the flow field.

4.2.3 Conservative solute transport

There are two theoretical approaches for modeling solute transport in single fractures: the Eulerian approach and the Lagrangian approach. In an Eulerian framework, partial differential equations governing solute transport are solved, generally using numerical techniques, to obtain the solute concentration distribution in space and time. However, these numerical methods are often plagued by numerical dispersion and artificial oscillation when applied to advectively dominated transport problems (Zheng and Bennett, 2002). The RWPT method, which falls within the Lagrangian framework, offers an alternative to the Eulerian approach particularly when the *Pe* and dispersive anisotropy are large (Kinzelbach, 1991). Since the purpose of this research is to investigate the effects of aperture field variability and AR on dispersion, and any numerical dispersion could seriously influence the conclusions drawn from this work, the RWPT technique was chosen to simulate solute transport.

The RWPT technique has been applied in numerous studies to investigate contaminant transport in fractured media (e.g., Moreno et al., 1988; Detwiler et al., 2000; Chrysikopoulos and James, 2003; James et al., 2005). In vector form, the RWPT equation is given by (Thompson and Gelhar, 1990):

$$\boldsymbol{X}^n = \boldsymbol{X}^{n-1} + \boldsymbol{A}(\boldsymbol{X}^{n-1})\Delta t + \boldsymbol{B}\left(\boldsymbol{X}^{n-1}\right)\cdot \boldsymbol{Z}\sqrt{\Delta t} \tag{4.7}$$

where n [-] refers to the time step, $\boldsymbol{X}^n$ [L] is the three-dimensional particle position vector at time $n\Delta t$, $\mathbf{A}(\boldsymbol{X}^{n-1})$ is the absolute forcing vector evaluated at $\boldsymbol{X}^{n-1}$, $\boldsymbol{B}(\boldsymbol{X}^{n-1})$ is a deterministic scaling second-order tensor evaluated at $\boldsymbol{X}^{n-1}$, and $\boldsymbol{Z}$ is a vector of three independent normally distributed random numbers with a mean of zero and a unit variance.

The same discretization scheme was employed for the solute transport simulations as for the flow field simulations, and the aperture within each discretized element remained constant. It was assumed that the aperture field is symmetric about the centre plane of the fracture. Upon calculation of the two-dimensional flow field, a parabolic velocity profile was imposed across the fracture and the quasi-three-dimensional RWPT equations were employed to simulate transport process (James et al., 2005):

$$x^n = x^{n-1} + \bar{v}_x\left(x^{n-1}, y^{n-1}, z^{n-1}\right)\frac{3}{2}\left\{1 - 4\left[\frac{z}{b(x,y)}\right]^2\right\}\Delta t + Z(0,1)\sqrt{2D^*\Delta t} \qquad (4.8a)$$

$$y^n = y^{n-1} + \bar{v}_y\left(x^{n-1}, y^{n-1}, z^{n-1}\right)\frac{3}{2}\left\{1 - 4\left[\frac{z}{b(x,y)}\right]^2\right\}\Delta t + Z(0,1)\sqrt{2D^*\Delta t} \qquad (4.8b)$$

$$z^n = z^{n-1} + Z(0,1)\sqrt{2D^*\Delta t} \qquad (4.8c)$$

where v_x [L·t^{-1}] and v_y [L·t^{-1}] are the local mean fluid velocities in the x- and y- directions respectively, and D^* [L^2·t^{-1}] is the molecular diffusion coefficient.

The initial condition involves the instantaneous release of 10,000 conservative particles across the inlet of the fracture. The particles are then distributed based on the local volumetric flow rate and velocity vectors as detailed by James et al. (2005). The RWPT model parameters are listed in Table 4.2.

4.2.4 Dispersion in Variable Aperture Fractures

The hydrodynamic dispersion of a conservative tracer migrating through single fractures is governed by a combination of molecular diffusion (D^*), Taylor dispersion (D_{Taylor}) (Taylor 1953), and geometric dispersion (D_G) (Roux et al., 1998; Plouraboue et al., 1998; Detwiler et al., 2000). Each of these dispersion regimes becomes dominant in different ranges of the *Pe*. Molecular diffusion dominates for Pe << 1. Taylor dispersion, which results from the combined effects of molecular diffusion and the velocity distribution across the fracture aperture, is as follows for parallel plate fractures;

$$D_{Taylor} = D^* + \frac{v^2 b^2}{210 D^*} \tag{4.9}$$

where *b* [L] is the local aperture, *v* [$\mathrm{L \cdot t^{-1}}$] is the local mean velocity in the fracture and D^* [$\mathrm{L^2 \cdot t^{-1}}$] is the molecular diffusion coefficient. In this work D_{Taylor} was approximated for variable aperture fractures by replacing the local aperture *b* [L] in equation (4.9) with the arithmetic mean aperture μ_b [L] (e.g., Detwiler et al., 2000):

$$D_{Taylor} = D^* + \frac{v^2 {\mu_b}^2}{210 D^*} = D^* + \frac{1}{210} D^* Pe^2 \tag{4.10}$$

Geometric dispersion results from the velocity variations induced by aperture field variability. The geometric dispersion coefficient, D_G [$\mathrm{L^2 \cdot t^{-1}}$], is based on a stochastic analysis of solute transport in variable-aperture fractures, and is given by Gelhar (1993):

$$D_G = [3 + g(\sigma^2_{\ln b})]\sigma^2_{\ln b} \lambda v \tag{4.11a}$$

$$g\left(\sigma^2_{\ln b}\right) = 1 + 0.205\sigma^2_{\ln b} + 0.16\sigma^4_{\ln b} + 0.045\sigma^6_{\ln b} + 0.0115\sigma^8_{\ln b} \qquad for 0 < \sigma^2_{\ln b} < 5 \tag{4.11b}$$

Gelhar's (1993) analysis was based on the assumptions that the logarithm of the fracture aperture (ln*b*) is a statistically stationary, isotropic, two-dimensional Gaussian random field, and that flow within a variable-aperture fracture can be modeled by the Reynolds equation. For the anisotropic aperture fields employed in this research, the correlation length, λ, was replaced by the omni-directional correlation length, λ_s, obtained by fitting a combination of the nugget effect and the spherical model to the semivariogram of the aperture field:

$$\gamma(H)=\begin{cases} nugget + A & h > \lambda_s \\ nugget + A\left[\dfrac{1.5H}{\lambda_s}-\dfrac{0.5H^3}{\lambda_s{}^3}\right] & h \le \lambda_s \end{cases} \tag{4.12}$$

where H [L] is the lag distance, A [L^2] is the scale of the spherical variogram model, and λ_s [L] is the range of the spherical model and represents the omni-directional correlation length.

A fourth dispersion coefficient, the fitted dispersion coefficient (D_f [$L^2 \cdot t^{-1}$]), is employed in this work and represents the effective dispersion coefficient with contributions from D^*, D_{Taylor} and D_G. D_f was calculated by fitting the one-dimensional analytical solution for solute transport in parallel plate fractures to the numerically generated breakthrough curves. The one-dimensional mathematical model employed to simulate solute transport in parallel plate fractures is given by:

$$\frac{\partial C}{\partial t}=D_f\frac{\partial^2 C}{\partial x^2}-v\frac{\partial C}{\partial x} \tag{4.13a}$$

$$C(0,t)=\frac{M}{Q}\delta(t) \tag{4.13b}$$

$$C(x,0)=0 \qquad x>0 \tag{4.13c}$$

$$\lim_{x\to\infty} C(x,t)=0 \tag{4.13d}$$

where C [$M \cdot L^{-3}$] is the solute concentration, v [$L \cdot t^{-1}$] is the mean solute transport velocity, M [M] is the mass of solute injected, Q [$L^3 \cdot t^{-1}$] is the volumetric flow rate, x [L] is the spatial coordinate, t [t] is the time, and $\delta(t)$ is the Dirac delta function for the time variable.

The analytical solution for equations (4.13a-d) is given by (Kreft and Zuber, 1978):

$$C(x,t)=\frac{M}{Q}\frac{x}{\sqrt{4\pi D_f t^3}}\exp\left(-\frac{(x-vt)^2}{4D_f t}\right) \tag{4.14}$$

$$D_f=\alpha_L v+D^* \tag{4.15}$$

where α_L [L] is the longitudinal dispersivity. PEST (Watermark Numerical Computing, version 9.0) was employed for the fitting process, in which both v and α_L were used as fitting parameters.

4.3. Results and Analysis

Tsang and Tsang (1990) calculated the dispersion for several realizations of aperture fields with a specific set of CoV and λ. They repeated this exercise for several sets of CoV and λ values in isotropic aperture fields, and found that the range for their measure of dispersion increased with increasing CoV. The numerically generated breakthrough curves reported here, however, represent an average of 50 statistical realizations for each set of aperture field statistics (i.e., CoV, λ). Therefore these breakthrough curves describe the central tendency of dispersion, and are not skewed based on the CoV. Figure 4.2 shows the numerically generated breakthrough curve from run 11. The error bars represent one standard deviation of the effluent concentration from the 50 aperture field realizations.

4.3.1 The Influence of Aperture Field Statistics on the Dispersion Regime

Several researchers (Roux et al., 1998; Detwiler et al., 2000) have suggested that the overall hydrodynamic dispersion coefficient (D_{TL}, $[L^2 \cdot t^{-1}]$) in variable-aperture fractures can be described by a sum of the Taylor and geometric dispersion coefficients as follows:

$$D_{TL} = D_{Taylor} + D_G \tag{4.16}$$

Therefore, the dominance of either the Taylor or geometric regime in the overall dispersion coefficient can be determined by a ratio of D_{Taylor} to D_G, based on equations (4.10) and (4.11) as follows:

$$\frac{D_{Taylor}}{D_G} = \frac{\frac{1}{210}}{\alpha_G} Pe \tag{4.17a}$$

$$\alpha_G = \frac{\sigma_{\ln b}^2 \lambda \left[3 + g\left(\sigma_{\ln b}^2\right)\right]}{\mu_b} \tag{4.17b}$$

where α_G is introduced to simplify Equation (4.17a). Equation (4.17a) shows that D_{Taylor}/D_G is linearly dependent on Pe, with a slope of $(1/210)/\alpha_G$. If $D_{Taylor}/D_G > 1$, the Taylor dispersion regime dominates, and if $D_{Taylor}/D_G < 1$, the geometric dispersion regime dominates. Together, equations (4.1) and (4.17) clearly show that it is a combination of the hydraulic gradient and the aperture field characteristics that control the dispersion regime.

Figure 4.3 illustrates the dependence of D_{Taylor}/D_G on Pe, μ_b, and σ_b. It shows that, for a constant value of $(1/210)/\alpha_G$, D_G becomes more dominant as Pe decreases, and when Pe is fixed, D_G becomes more dominant as $(1/210)/\alpha_G$ decreases. For a fixed mean aperture, D_G becomes increasingly dominant as σ_b increases with the exception of the case where μ_b = 100 μm and σ_b = 120 μm. This particular case has the largest CoV (1.2) of all those presented in this research. This inconsistency can likely be explained by the inadequacy of the Reynolds equation to simulate flow in fractures with CoVs in this range.

Figure 4.3 also shows that, for aperture fields following a log-normal distribution, the dominant dispersion regime is controlled by μ_b and, to a lesser degree, σ_b. An explanation to this phenomenon is provided by equation (4.18a), which was obtained by substituting the Cubic Law (equation 4.18b) into equation (4.17a).

$$\frac{D_{Taylor}}{D_G}=\frac{\frac{1}{210}}{\alpha_G}Pe=\frac{\gamma}{12\eta D^*}\frac{\frac{1}{210}\mu_b^4}{\ln(\frac{\sigma_b^2}{\mu_b^2}+1)\lambda\left[3+g\left(\ln\left(\frac{\sigma_b^2}{\mu_b^2}+1\right)\right)\right]}\frac{\Delta h}{\Delta L} \qquad (4.18a)$$

$$v=-\frac{\gamma}{12\eta}\mu_b^2\frac{\Delta h}{\Delta L} \qquad (4.18b)$$

Since it is well recognized that the Cubic Law does not describe fluid flow in variable-aperture fractures accurately, the information derived from equation (4.18a) must be considered qualitative. An examination of equation (4.18a) indicates, however, that μ_b has a larger influence on the value of D_{Taylor}/D_G than σ_b.

Figure 4.3 also illustrates the relationship between the dispersion regime, μ_b, and AR. It can be seen that if all else is held constant, D_G has a slightly larger influence for anisotropic aperture fields than it does for isotropic aperture fields. However, Figure 4.3 clearly shows that the AR has a much smaller influence on the dispersion regime than σ_b.

Figure 4.4(a) shows the numerically generated breakthrough curve from run 11 fit to the 1D analytical solution for solute transport (equation 4.14). Figure 4.4(b) shows the magnitude of D_f, determined from fitting equation (4.14) to the numerically generated breakthrough curves, compared with D_{TL}, calculated by equation (4.16). For comparison purposes, eight additional simulations were conducted in isotropic aperture fields. It was found that D_f is typically between 2% and 60% smaller than D_{TL}, with the exception of a few simulations with $\mu_b = 100$ μm, where D_f is between 2 and 37% larger than D_{TL}. Two possible explanations for this discrepancy are (1) errors associated with the first order approximations made by the stochastic analysis in deriving equation (4.16) (Keller et al., 1999), and (2) errors introduced by solving the Reynolds equation to obtain the three dimensional velocity field, which required the imposition of a local parabolic velocity profile across the aperture. Flow simulations in variable-aperture fractures based on the Stokes and Navier-Stokes equations have shown that velocity profiles, in fact, deviate from the ideal parabolic distribution (Brush and Thomson, 2003). Equation (4.10) has, in fact, been employed to represent the Taylor dispersion coefficient in variable-aperture fractures by others (e.g. Detwiler et al., 2000), however further theoretical and numerical analyses are required in order to confirm the validity of this application. Figure 4.4 confirms the validity of using the omni-directional correlation length in equation (4.16) to estimate the dispersion coefficient, as no significant difference between the isotropic and anisotropic aperture fields were notable in the comparison between D_f and D_{TL}.

4.3.2 The Influence of μ_b, σ_b, and AR on α_L

In this section, dispersivity refers to that obtained through the fitting technique. Equation (4.15) assumes that D_f is linearly dependent on v, and therefore α_L is solely a function of aperture field statistics. Figure 4.5 shows dispersivity plotted against the CoV for a range of ARs. Table 4.3 presents the ratio of the average of the anisotropic dispersivities to the isotropic dispersivities calculated for each CoV. Several trends emerge upon the examination of Figure 4.5 and Table 4.3. First, in general, dispersivity increases with increasing CoV, which is consistent with equation (4.11). However, the dispersivities for cases of $\mu_b = 900$ μm are significantly larger than those with the same CoV but different mean aperture. This phenomenon can be explained through a change in the dominant dispersion regime. As shown in Figure 4.3, D_G dominates in fractures with μ_b of 100, 300, and 600 μm, and therefore the relationship between the dispersion coefficient and the velocity is linear (equation 4.11a). Conversely, in fractures with a mean aperture of 900 μm, D_{Taylor} dominates, and the dispersion coefficient is proportional to the square of the velocity (Equation 4.10). However, the fitting procedure employed to calculate the dispersivity values in Figure 4.5 assumes a linear relationship between the dispersion coefficient and the velocity (Equation 4.15). The authors postulate, therefore, that it is not appropriate to assume a linear dependence of dispersion coefficient on velocity when D_{Taylor} dominates, as the result will be erroneously large.

Second, the difference between dispersivities due to the AR is statistically insignificant for aperture fields with small CoVs and the three ARs considered in this work; however the spread in dispersivity for these ARs increases as the CoV increases. This implies that the effect of AR on dispersivity is significant only when the CoV is large (Figure 4.5). Table 4.3 indicates that the effect of the AR on dispersivity also depends on the μ_b. For the same CoV, the ratio of the anisotropic dispersivity ($\alpha_{L,\mathrm{AR}=5.0}$, $\alpha_{L,\mathrm{AR}=0.2}$) to isotropic dispersivity ($\alpha_{L,\mathrm{AR}=1.0}$) is larger for fractures with smaller μ_b (Table 4.3). Lee et al. (2003) investigated the influence of CoV, λ, and AR on dispersivity through laboratory-scale experiments, and concluded that the effect of AR is insignificant compared with those of the CoV and λ. However, their conclusion was reached by comparing the dispersivities obtained from the moment method of breakthrough curve analysis (Yu et al., 1999) with those calculated from equation (4.11), in which λ for isotropic aperture fields was replaced by an omni-directional correlation length for anisotropic aperture fields. It is not entirely appropriate to evaluate the effect of AR on dispersivity through this comparison, however, as the fact that there were only small differences (at most 32%) between the dispersivities obtained from the moment method and equation (4.11) only indicates that an 'effective' correlation length for λ in equation (4.11) can be employed to approximate the dispersivity. Figure 4.6 shows the dispersivities obtained by Lee et al. (2003) through the fitting technique plotted against CoV, and illustrates that the data from their experiments were insufficient to reach a definite conclusion with respect to the effect of AR on dispersivity.

The finding that anisotropy is significant only when the CoV is large has important implications for numerical modeling. For real problems, it is difficult to obtain a dispersion tensor for single anisotropic fractures, and therefore isotropic dispersion tensors are typically employed in modeling practice. This finding suggests that such a simplification provides a reasonable estimation of dispersivity as long as the aperture field variability is not large. The data presented in Figures 4.5a and 4.5b suggest that a CoV of approximately 0.2 may be an appropriate cut-off for simplifying anisotropic apertures with isotropic dispersion tensors; however, more work is required to confirm this suggestion.

It was further noted from this work that for aperture fields with different ARs, the relative magnitude of dispersivity changes with the CoV as follows:

$$\alpha_{L,AR=0.2} > \alpha_{L,AR=5.0} > \alpha_{L,AR=1.0} \qquad \mathit{for}\, 0.4 < CoV \leq 1.2 \qquad (4.19a)$$

$$\alpha_{L,AR=5.0} > \alpha_{L,AR=0.2} > \alpha_{L,AR=1.0} \qquad \mathit{for}\, 0.08 \leq CoV \leq 0.4 \qquad (4.19b)$$

Equation (4.19) shows that for a single fracture with the same μ_b and σ_b, those with anisotropic aperture fields (either AR >1 or AR<1) have higher dispersivities than those with isotropic aperture fields. This is due to the fact that, for aperture fields with the same CoV, anisotropic aperture fields lead to a larger spatial variation in fluid velocity, which therefore results in larger dispersivities. However, it is not clear why the relative magnitude of $\alpha_{L,\mathrm{AR}=5.0}$ and $\alpha_{L,\mathrm{AR}=0.2}$ depends on the CoV.

Thompson (1991) investigated the effect of CoV on dispersivity for fractures with isotropic walls, and Thompson and Brown (1991) calculated the longitudinal dispersivity as a function of fracture wall anisotropy and aperture field CoV. Their observations support those from this work that the dispersivity increases with the CoV. The spread of dispersivity, however, due to the AR of the aperture field observed in this work is not consistent with the spread in dispersivity observed by Thompson and Brown (1991) due to the AR of fracture walls. This discrepancy is likely due to the fact that the AR of the fracture walls has a different effect on dispersivity than the AR of the aperture field itself.

Figure 4.7 shows D_f plotted against CoV for a range of ARs, and reveals a different trend than that of Figure 4.5. For a fixed μ_b, the dispersion coefficient, as well as the spread in the dispersion coefficient with different ARs, increases with increasing values of the CoV, with an exception for case of μ_b = 100 μm and σ_b = 120 μm. This is likely due to the inadequacy of the Reynolds equation for larger CoVs, as discussed in Section 3.1. However, for fractures with different μ_b, a larger CoV does not necessarily correspond to a larger dispersion coefficient. This is due to the fact dispersion coefficient depends on both dispersivity and fluid velocity; and μ_b plays a more important role than σ_b in determining the fluid velocity. Although the dispersivities increase as the CoV increases (equation 4.11a), the decrease in μ_b causes a decrease in velocity to a larger extent. The resulting dispersion coefficients (equation 4.15) therefore decrease with decreasing μ_b.

4.4. Summary

A 3^3 factorial experiment was designed to investigate the effect of aperture field statistics (i.e., μ_b, σ_b, and AR) on dispersivity and dispersion regimes numerically. Flow fields were calculated using the Reynolds equation, and a two-dimensional random walk particle tracking technique was used to simulate solute transport. It was demonstrated that the arithmetic mean aperture μ_b and, to a lesser degree, the standard deviation σ_b, influence the value of D_{Taylor}/D_{G}., and hence the dominant dispersion regime. When the hydraulic gradient is fixed, D_G accounts for a larger fraction of D_{TL} for aperture fields with a larger CoV. The influence of AR on dispersion regimes, however, seems insignificant for the correlation structure of the aperture fields employed in this research. Additional simulation studies using aperture fields with a larger range of correlation lengths and ARs would help to clarify the effect of anisotropy on dispersion regime.

The results also revealed the interactive effects of the CoV and the AR on dispersivity in fractures. It was found that the dispersivity, as well as the spread of dispersivity, increases as the CoV increases. The effect of the AR is significant only when the CoV is large. Therefore, if the CoV is not large (<0.2), the isotropic dispersivity tensor can be used to replace the anisotropic dispersivity tensor in numerical models simulating solute transport in variable-aperture fractures without introducing unacceptable errors.

Acknowledgement

This research was funded by the NSERC Discovery Grant Program (S. Dickson and Y. Guo). The authors would like to thank Dr. James for generously providing the code employed in this research. This work was made possible by the facilities of the Shared Hierarchical Academic Research Computing Network (SHARCNET:www.sharcnet.ca).

References

Aris, R. (1956), On the dispersion of a solute in a fluid flowing through a tube, *Proc. R. Soc. London, Ser. A*, *235*, 67-77.

Bouchaud, E. (1997), Scaling properties of crack surfaces, *J. Phys. Condens. Matter*, *9*, 4319-4344.

Brown, S. R., and C. H. Scholz (1985), Broad bandwidth study of the topography of natural rock surfaces, *J. Geophys. Res.*, *90*, 12575-12582.

Chrysikopoulos, C. V., and S. C. James (2003), Transport of neutrally buoyant and dense variably sized colloids in a two-dimensional fracture with anisotropic aperture, *Transport Porous Med.*, *51*, 191-210.

Brush, D. J., and N. R. Thomson (2003), Fluid flow in synthetic rough-walled fractures: Navier-Stokes, Stokes, and local cubic law simulations, *Water Resour. Res.*, *39*(4), 1085, doi: 10.1029/2002WR001346.

Detwiler, R. L., H. Rajaram, and R. J. Glass (2000), Solute transport in variable-aperture fractures: an investigation of the relative importance of Taylor dispersion and macrodispersion, *Water Resour. Res.*, *36*(7), 1611-1625.

Gelhar, L. W. (1993), *Stochastic Subsurface Hydrology*, pp. 272-279, Prentice-Hall, Old Tappan, N. J.

Gentier S., E. Lamontagne, G. Archambault, and J. Riss (1997), Anisotropy of flow in a fracture undergoing shear and its relationship to the direction of shearing and injection pressure, *Int. J. Rock Mech. & Min. Sci.*, *34*(3-4), paper No. 094.

Gutjahr, A. L. (1989), *Fast Fourier transform for random field generation*, Report 4-R58-2690R, New Mexico Institute of Mining and Technology, Socorro, NM.

Hakami, E. and Larsson E., (1996), Aperture measurement and flow experiments on a single natural fracture, *Int. J. Rock Mech. Min. Sci. Geomech Abstr.*, 33(4), 395-404.

James, S. C., T. K. Bilezikjian, and C. V. Chrysikopoulos (2005), Contaminant transport in a fracture with spatially variable aperture in the presence of monodisperse and polydisperse colloids, *Stoch. Env. Res. Risk A.*, *19*(4), 266-279.

Keller, A. (1998), High resolution, non-destructive measurement and characterization of fracture apertures, *Int. J. Rock Mech. Min. Sci.*, *35*(8), 1037-1050.

Keller, A. A., P. V. Roberts, and M. J. Blunt (1999), Effect of fracture aperture variations on the dispersion of contaminants, *Water Resour. Res.*, *35*(1), 55-63.

Kinzelbach, W., and G. Uffink (1991), The random walk method and extensions in groundwater modeling, in *Transport Processes in Porous Media*, edited by J. Bear and M. Y. Corapcioglu, pp. 763-787, Kluwer Academic Publishers, Boston.

Kreft, A., and A. Zuber (1978), On the physical meaning of dispersion equation and its solutions for different initial and boundary conditions, *Chem. Eng. Sci.*, *33*, 1471-1480.

Lee, J., J. M. Kang, and J. Choe (2003), Experimental analysis on the effects of variable apertures on tracer transport, *Water Resour. Res.*, *39*(1), 1015.

Meheust, Y., and J. Schmittbuhl (2001), Geometrical heterogeneities and permeability anisotropy of rough fractures, *J. Geophys. Res.*, *106*(B2), 2089-2102.

Moreno, L., Y. W. Tsang, C. F. Tsang, F. Hale, and I. Neretnieks (1988), Flow and tracer transport in a single fracture: A stochastic model and its relation to some field observations, *Water Resour. Res.*, *24*(12), 2033-2048.

Plouraboue, F., P. Kurowski, J. P. Hulin, S. Roux, and J. Schmittbuhl (1995), Aperture of rough crack, *Phys. Rev. E*, *51*, 1675-1685.

Plouraboue, F., J. P. Hulin, S. Roux, and J. Koplik (1998), Numerical study of geometric dispersion in self-affine rough fractures, *Phys. Rev. E*, *58*(3), 3334-3346.

Power, W. L., T. E. Tullis, S. R. Brown, G. N. Boitnott, and C. H. Scholz (1987), Roughness of natural fault surfaces, *Geophys. Res. Lett.*, *14*, 29-32.

Reimus, P. W. (1995), The use of synthetic colloids in tracer transport experiments in saturated rock fractures, Report LA-13004-T, Los Alamos National Laboratory, Los Alamos, NM.

Roberds, W. J., M. Iwano, and H. H. Einstein (1990), Probabilistic mapping of rock joints surface, in *Rock Joints*, edited by N. Barton and O. Stephansson, pp. 681-691, A. A. Balkema Publishers, Brookfield, V. T., USA.

Roux, S., F. Plouraboue, and J. Hulin (1998), Tracer dispersion in rough open cracks. *Transport Porous Med.*, *32*, 97-116.

Schmittbuhl, J., F. Schmitt, and C. H. Scholz (1995), Scaling invariance of crack surfaces, *J. Geophys. Res.*, *100*, 5953-5973.

Thompson, M. E. (1991), Numerical simulation of solute transport in rough fractures, *J. Geophys. Res.*, *96*(B3), 4157-4166.

Thompson M. E., S. R. Brown (1991), The effect of anisotropic surface roughness on flow and transport in fractures, *J. Geophys. Res.*, *96*(B13), 21923-21932.

Tompson, A. F. B., and L. W. Gelhar (1990), Numerical simulation of solute transport in three-dimensional randomly heterogeneous porous media, *Water Resour. Res.*, *26*(10), 2541-2562.

Tsang, Y. W., and Tsang, C. F. (1987), Channel model of flow through fractured media, *Water Resour. Res.*, *23*(2), 467-478.

Tsang, Y. W., and C. F. Tsang (1990), Hydrological characterization of variable-aperture fractures, in *Rock Joints*, edited by N. Barton and O. Stephansson, pp. 423-430, A. A. Balkema Publishers, Brookfield, V. T., USA.

Yeo, I.W., DeFreitas M.H. and Zimmerman R.W. (1998), Effect of shear displacement on the aperture and permeability of a rock fracture, Int. J. Rock. Mech. Min. Sci., 35(8), 1051-1070.

Yu, C., A. W. Warrick, and M. H. Conklin (1999), A moment method for analyzing breakthrough curves of step inputs, *Water Resour. Res. 35*(11), 3567-3572.

Zheng, C., and G. D. Bennett (2002), *Applied Contaminant Transport Modeling*, John Wiley and Sons, Inc., New York.

Tables

Table 4.1. (a) Factorial Experimental Design.

Run number	Mean μ_b (m)	Standard deviation σ_b (m)	Coefficient of variation (CoV= σ_b / μ_b)	Longitudinal correlation length λ^b_x (m)	Transverse correlation length λ^b_y (m)	Anisotropic ratio (AR= $\lambda^b_x / \lambda^b_y$)
1	0.0001	0.00004	0.40	0.40	0.08	5.0
2	0.0001	0.00008	0.80	0.40	0.08	5.0
3	0.0001	0.00012	1.20	0.40	0.08	5.0
4	0.0001	0.00004	0.40	0.08	0.08	1.0
5	0.0001	0.00008	0.80	0.08	0.08	1.0
6	0.0001	0.00012	1.20	0.08	0.08	1.0
7	0.0001	0.00004	0.40	0.08	0.40	0.2
8	0.0001	0.00008	0.80	0.08	0.40	0.2
9	0.0001	0.00012	1.20	0.08	0.40	0.2
10	0.0003	0.00004	0.13	0.40	0.08	5.0
11	0.0003	0.00008	0.27	0.40	0.08	5.0
12	0.0003	0.00012	0.40	0.40	0.08	5.0
13	0.0003	0.00004	0.13	0.08	0.08	1.0
14	0.0003	0.00008	0.27	0.08	0.08	1.0
15	0.0003	0.00012	0.40	0.08	0.08	1.0
16	0.0003	0.00004	0.13	0.08	0.40	0.2
17	0.0003	0.00008	0.27	0.08	0.40	0.2
18	0.0003	0.00012	0.40	0.08	0.40	0.2
19	0.0006	0.00004	0.07	0.40	0.08	5.0
20	0.0006	0.00008	0.13	0.40	0.08	5.0
21	0.0006	0.00012	0.20	0.40	0.08	5.0
22	0.0006	0.00004	0.07	0.08	0.08	1.0
23	0.0006	0.00008	0.13	0.08	0.08	1.0
24	0.0006	0.00012	0.20	0.08	0.08	1.0
25	0.0006	0.00004	0.07	0.08	0.40	0.2
26	0.0006	0.00008	0.13	0.08	0.40	0.2
27	0.0006	0.00012	0.20	0.08	0.40	0.2
28	0.0009	0.00004	0.04	0.40	0.08	5.0
29	0.0009	0.00008	0.09	0.40	0.08	5.0
30	0.0009	0.00012	0.13	0.40	0.08	5.0
31	0.0009	0.00004	0.04	0.08	0.08	1.0
32	0.0009	0.00008	0.09	0.08	0.08	1.0
33	0.0009	0.00012	0.13	0.08	0.08	1.0
34	0.0009	0.00004	0.04	0.08	0.40	0.2
35	0.0009	0.00008	0.09	0.08	0.40	0.2
36	0.0009	0.00012	0.13	0.08	0.40	0.2

Table 4.1(b). Experimental Design for Isotropic Aperture Fields.

Run number	Mean μ_b (m)	Standard deviation σ_b (m)	Coefficient of variation (CoV= σ_b / μ_b)	Longitudinal correlation length λ^b_x (m)	Transverse correlation length λ^b_y (m)	Anisotropic ratio (AR= $\lambda^b_x / \lambda^b_y$)
37	0.0009	0.00002	0.02	0.08	0.08	1.0
38	0.0009	0.00006	0.07	0.08	0.08	1.0
39	0.0009	0.00014	0.16	0.08	0.08	1.0
40	0.0009	0.00016	0.18	0.08	0.08	1.0
41	0.0009	0.00018	0.20	0.08	0.08	1.0
42	0.0009	0.00020	0.22	0.08	0.08	1.0
43	0.0009	0.00024	0.27	0.08	0.08	1.0
44	0.0009	0.00036	0.40	0.08	0.08	1.0

Table 4.2. Flow and transport simulation parameters.

	Parameter	Value
Flow simulation	Fracture dimensions (length×width)	16.0 m×2.0 m
	Fracture discretization (elements×elements)	400×50
	Element size (dx×dy)	0.04 m×0.04 m
	Temperature	20 °C
	Dynamic viscosity η	1.002×10^{-3} N·m·s^{-2}
	Specific weight γ	9789 N·m^{-3}
	Hydraulic gradient	0.25/16 for μ_b = 100 μm 0.025/16 for μ_b = 300 μm, μ_b = 600μm, and μ_b = 900 μm
Transport simulation	Molecular dispersion coefficient D^*	9.0×10^{-10} m^2·s^{-1}
	Time step Δt	1 s

Table 4.3. The Effect of AR and CoV on Dispersivity.

CoV	$\frac{(\alpha_{L,AR=5.0}+\alpha_{L,AR=0.2})/2}{\alpha_{L,AR=1}}$
0.04	1.05 (for μ_b=900 μm)
0.07	1.30 (for μ_b=600 μm)
0.09	1.15 (for μ_b=900 μm)
0.13	1.32 (for μ_b=900 μm), 1.64 (for μ_b=600 μm), 1.83 (for μ_b=300 μm),
0.20	1.84 (for μ_b=600 μm)
0.27	1.98 (for μ_b=300 μm)
0.4	2.27 (for μ_b=100 μm), 2.25 (for μ_b=300 μm)
0.8	1.98 (for μ_b=100 μm)
1.2	2.13 (for μ_b=100 μm)

* $\alpha_{L,\mathrm{AR}=0.2}$, $\alpha_{L,\mathrm{AR}=5.0}$, and $\alpha_{L,\mathrm{AR}=1.0}$ represent the dispersivity corresponding to the ARs of 0.2, 5.0, and 1.0 respectively.

Figures

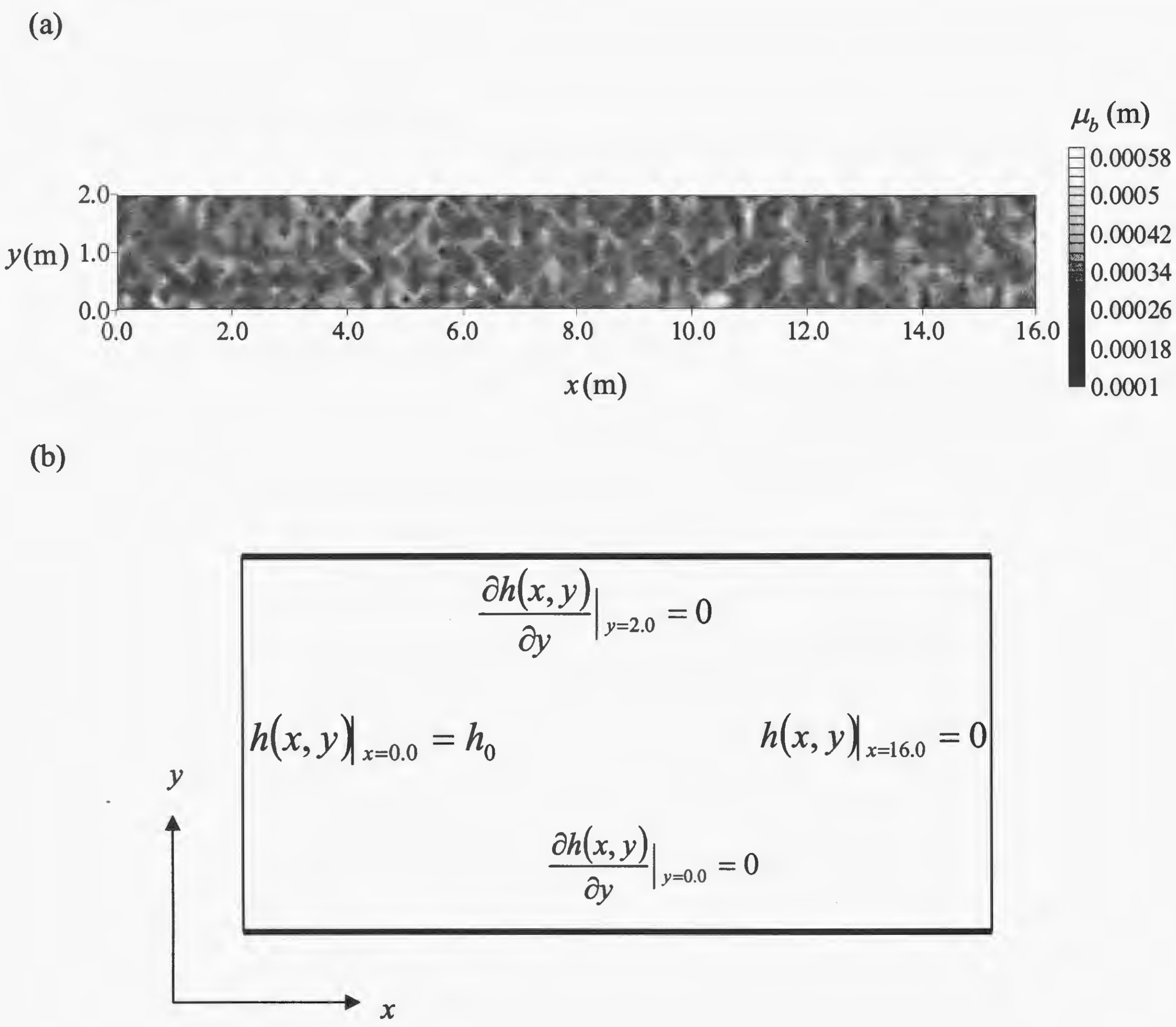

Figure 4.1. Illustration of (a) a contour plot of a fracture aperture field and (b) a schematic diagram of the coordinate system and boundary conditions for the flow and solute transport simulations.

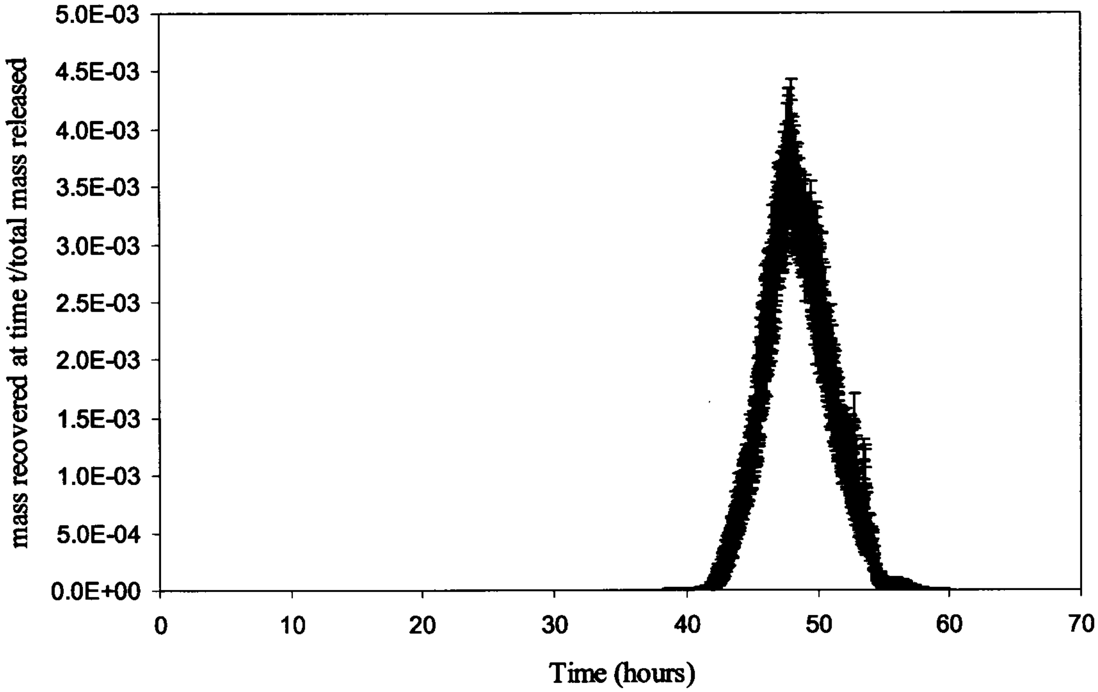

Figure 4.2. The numerically generated breakthrough curve from run 11 (μ_b = 0.0003 m, σ_b = 0.00008 m, AR = 5). The error bars represent one standard deviation of the 50 effluent breakthrough curves generated using these same aperture field statistics.

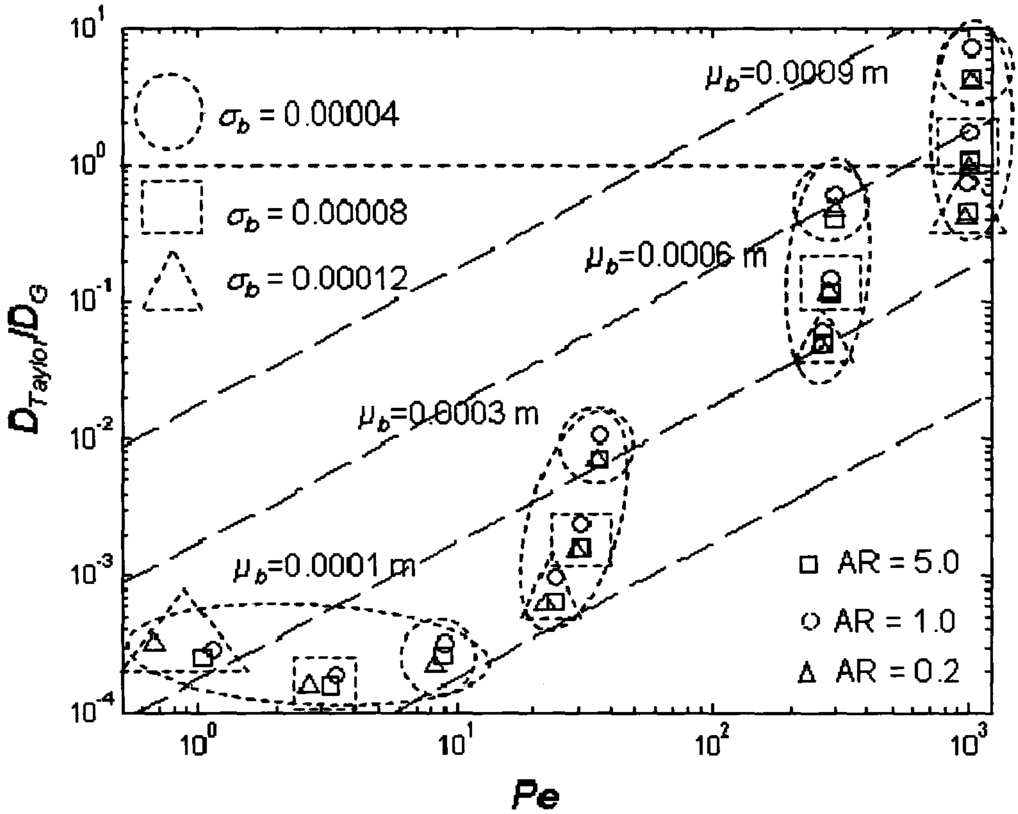

Figure 4.3. Dispersion regime dependence on *Pe* with respect to μ_b, σ_b, and AR.

Notes: (1) The hydraulic head loss across different fractures is 0.25m for μ_b = 100 μm, and 0.025m for μ_b = 300 μm, μ_b = 600 μm, and μ_b = 900 μm. (2) The dotted lines corresponds to various values of the slope, i.e., $\frac{1}{210}\bigg/\frac{\sigma_{\ln b}^2\lambda\left[3+g\left(\sigma_{\ln b}^2\right)\right]}{\mu_b}$. It should be noted here that both D_{Talyor}/D_G and *Pe* are plotted on a log scale, and therefore although these dotted lines appear parallel, they are not.

(a)

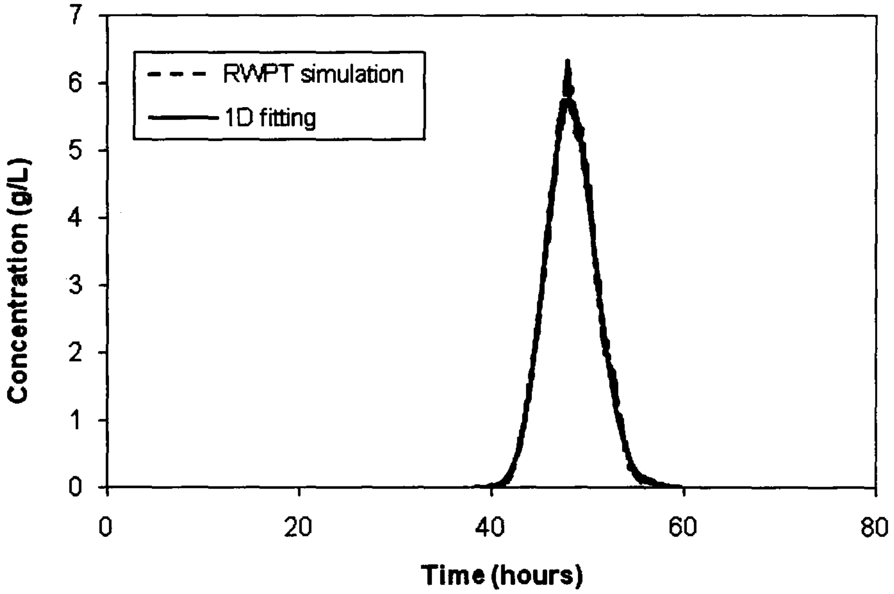
RWPT simulation
1D fitting
Concentration (g/L)
Time (hours)
0
1
2
3
4
5
6
7
0
20
40
60
80

(b)

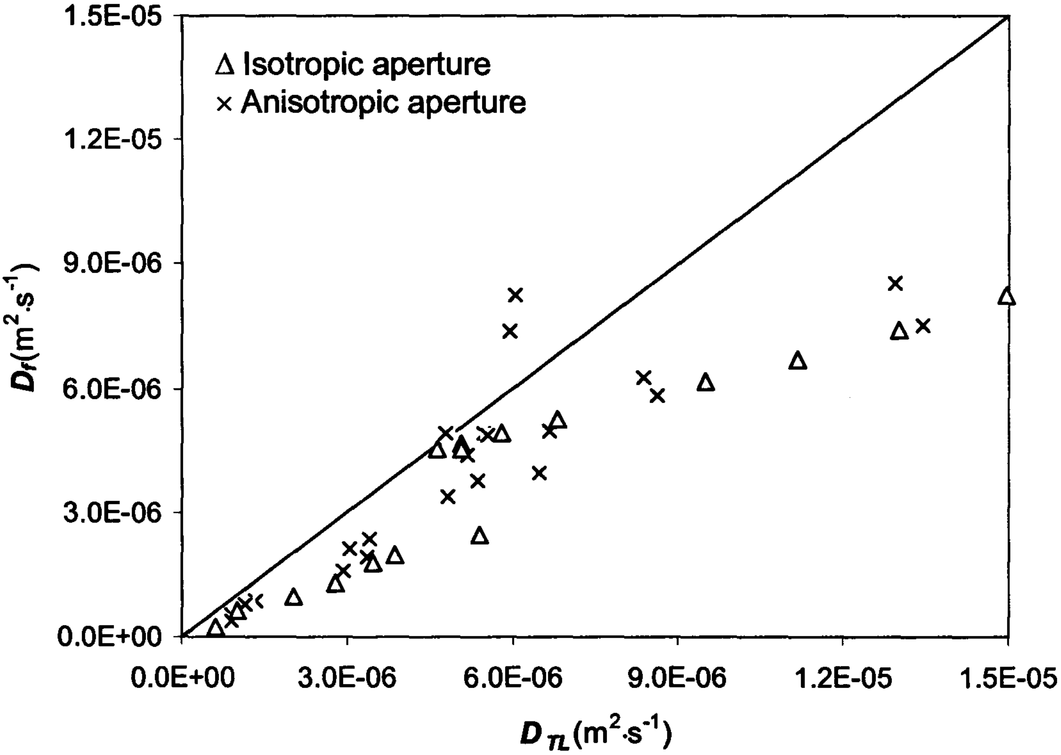
Δ Isotropic aperture
× Anisotropic aperture
D_f(m^2·s^{-1})
D_{TL}(m^2·s^{-1})
0.0E+00
3.0E-06
6.0E-06
9.0E-06
1.2E-05
1.5E-05
0.0E+00
3.0E-06
6.0E-06
9.0E-06
1.2E-05
1.5E-05

Figure 4.4. (a) the fit between the numerically generated breakthrough curve from run 11 (μ_b = 0.0003 m, σ_b = 0.00008 m, *AR* = 5) with the 1D analytical solution for solute transport; and (b) a comparison of D_f with D_{TL}.

(a)

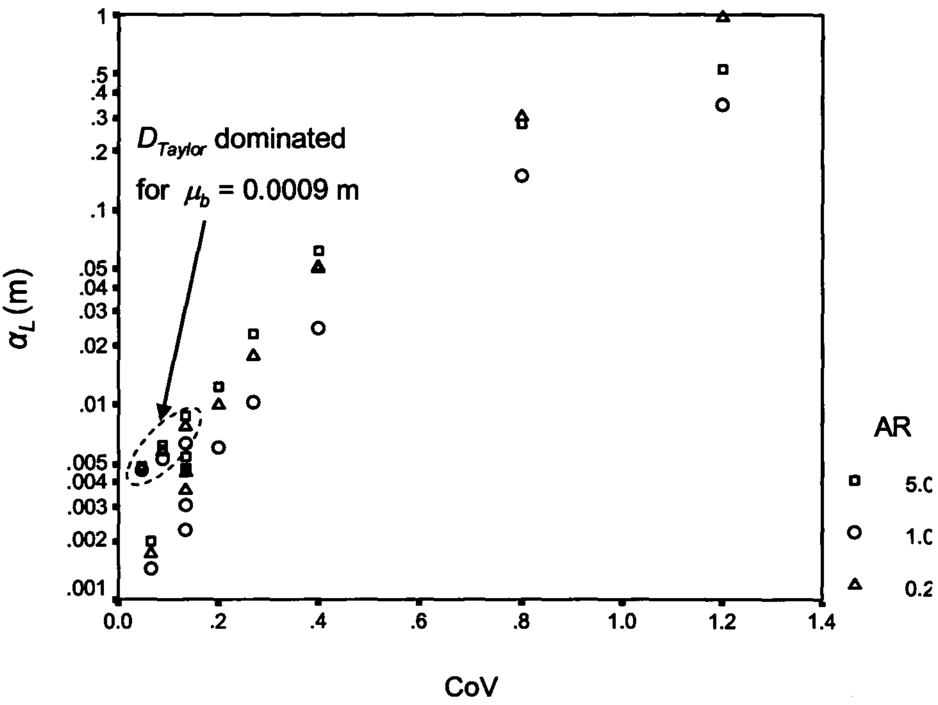

(b)

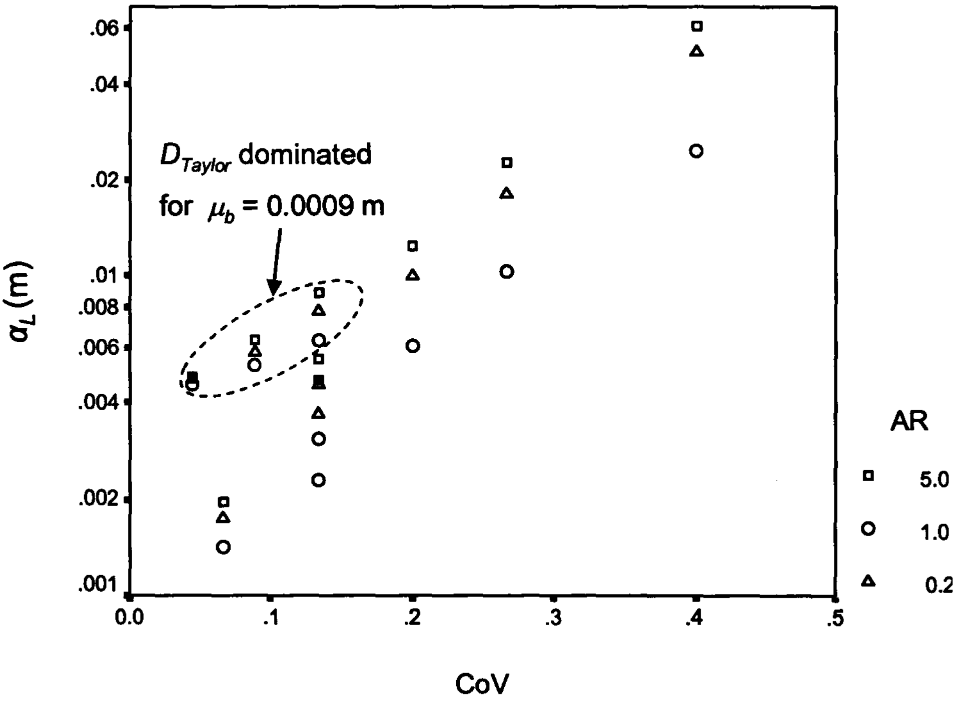

Figure 4.5. Dispersivity vs. CoV for (a) all 36 fracture aperture fields investigated in this research, and (b) an enlarged view showing aperture fields with small CoVs.

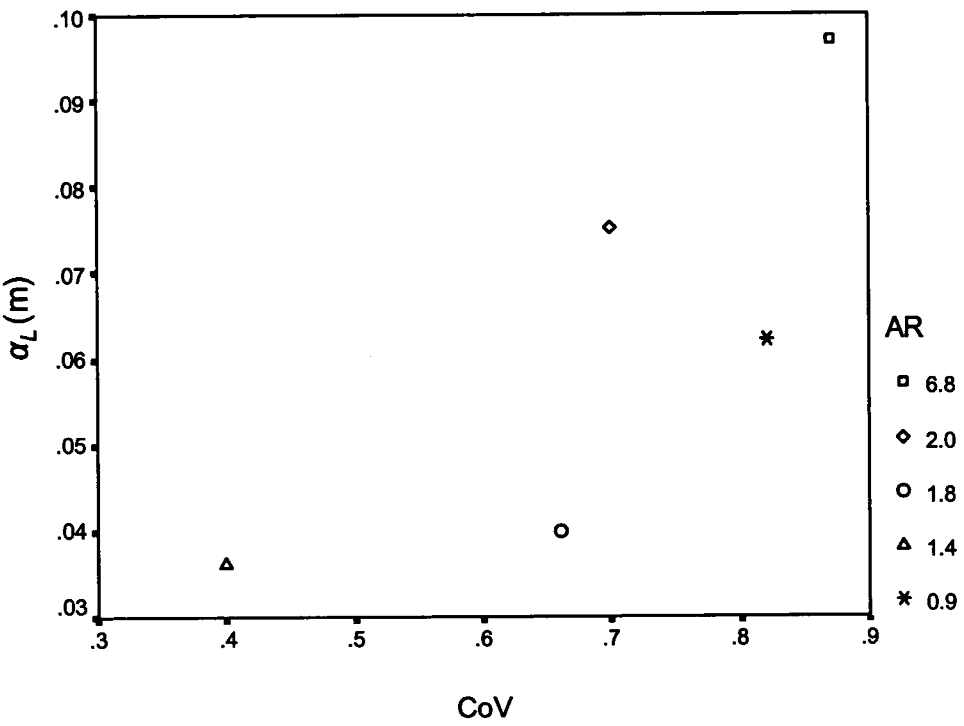

Figure 4.6. Dispersivities vs. CoV for different ARs (data from Lee et al., 2003)

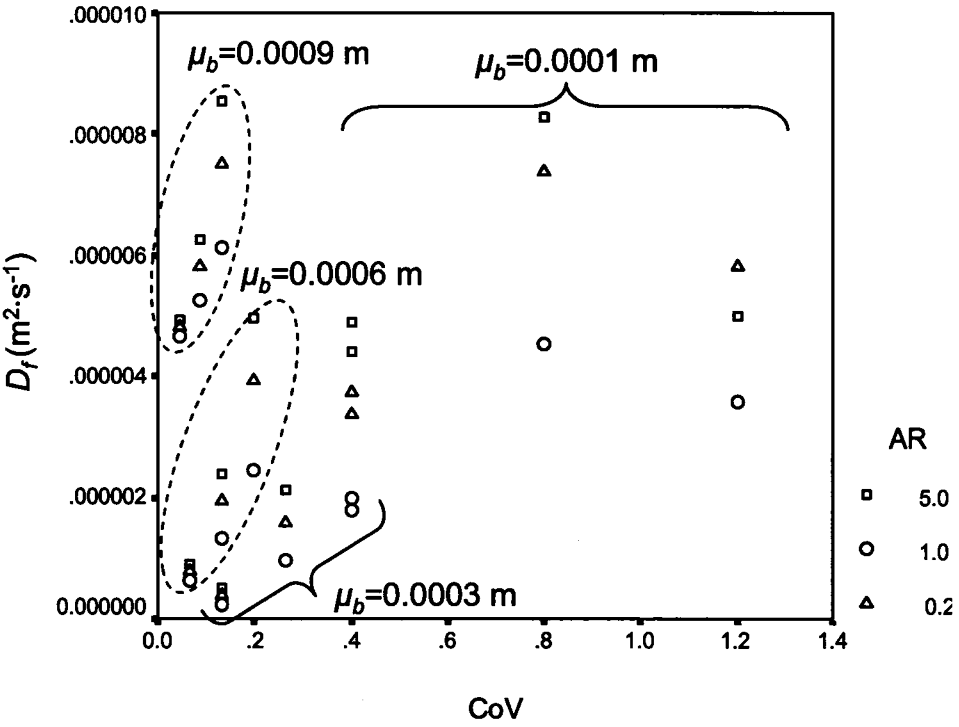

Figure 4.7. Dispersion coefficient vs. CoV for a range of ARs. Note that the hydraulic head loss across different fractures is 0.25m for μ_b = 100 μm, and 0.025m for μ_b = 300 μm, μ_b = 600 μm, and μ_b = 900 μm.

Chapter 5 Observation of a New Phenomenon for the Differential Transport of Colloids and Solutes in Single Fractures

Abstract

Investigations on differential transport between colloids and solutes in fractured media are generally based on the assumption (hereafter referred to as the Taylor-Aris assumption) that the velocity profile of colloids is statistically similar to that of solutes, except that colloids cannot enter the regions nearest the solid walls due to size and/or charge exclusion. This work demonstrated, through numerical simulations of both colloid and solute transport in single parallel-plate fractures using the random walk particle tracking (RWPT) method, that: 1) there exists a threshold value of aspect ratio δ ($\delta = 2r_c/b$, where r_c and b represent the colloid radius and fracture aperture respectively), δ_o, where the average velocities of colloids and solutes are similar. When $\delta > \delta_o$, the Taylor-Aris assumption is satisfied, and τ_p ($\tau_p = t_c/t_s$, where t_c and t_s represent colloid and solute retention times respectively) decreases as δ increases as is well documented in the hydrodynamic chromatography literatures. However, when $\delta < \delta_o$, the Taylor-Aris assumption is violated and τ_p increases as δ increases; and 2) the Taylor dispersion coefficient and its extension by James and Chrysikopoulos (2003) will overestimate the colloid dispersion coefficient significantly when the Taylor-Aris assumption is violated. Additionally, when the Taylor-Aris assumption is violated, numerical models simulating colloid and solute transport in variable-aperture fractures demonstrated that τ_p and $D_{L,coll}/D_{L,solute}$ ($D_{L,coll}$ and $D_{L,solute}$ represent the dispersion coefficients for colloids and solutes respectively) decrease with increasing CoV (CoV = σ_b/μ_b, where σ_b and μ_b represent the standard deviation and arithmetic mean of the aperture field). The anisotropy ratio (AR = λ_x/λ_y, where λ_x and λ_y are the correlation lengths of the aperture field along the x- and y- directions respectively) only plays a minor role compared to the

CoV. These observations have never been documented before to the knowledge of these authors, and have important implications towards the interpretation of colloid transport in both porous and fractured media.

5.1. Introduction

Experimental studies in both porous [1,2,3,4] and fractured [e.g., 5,6,7] media have demonstrated that the average transport velocity of colloid tracers may be larger than those of both water molecules and molecular-scale conservative tracers. This phenomenon is commonly referred to as differential transport. The pore-water velocity in an ideal pore throat or a parallel-plate fracture is generally parabolically distributed, with the maximum velocity occurring at the centerline and decreasing towards a zero velocity at the solid surface [8]. The Taylor-Aris transport theory assumes that conservative molecular-scale solutes, due to their relatively large diffusion coefficients, sample nearly the entire distribution of pore water velocities. Conversely, colloids are prevented from entering the regions nearest the walls due to their physical size (i.e., size exclusion) or repulsive interaction forces between the colloid and solid surface (i.e., charge exclusion). Therefore, colloids necessarily sample larger pore water velocities than the average water molecule or molecular-scale solute. Furthermore, when particulates are sized within the same range as the pore or aperture region in which they are present, they are excluded from these regions (i.e., pore exclusion) due to either size or charge, which enhances the relative velocity of these particulates even further [9].

The quantitative effect of size and charge exclusion on colloid transport in unconsolidated porous media has generally been evaluated through modifying the classical transport or attachment/detachment coefficients [10,1], reducing the kinematic porosity [9], employing a particle-based model [11] or an empirical model of travel time density function [12]. However, the effect of size or charge exclusion on colloid transport in fractured media has been studied by few researchers. Li and Jen (2001) [13] and Jen and Li (2001) [14] evaluated the effect of size and other external forces on colloid transport in single uniform fractures using a semi-analytical technique. James and Chrysikopoulos (2003) [15] derived expressions for the effective velocity and the effective dispersion coefficient for finite-sized spherical particles in a uniform-aperture fracture. Additionally, Chrysikopoulos and James (2003) [16] investigated the effect of aperture field anisotropy on the transport and dispersion of colloids.

Studies examining the effects of size and charge exclusion on colloid transport are typically based on the hypothesis, either explicitly or implicitly, that the velocity field sampled by colloids is statistically similar to that of the pore water velocity, except that colloids cannot enter the regions nearest to the walls where the velocity is lowest [e.g., 11]. This hypothesis will hereafter be referred to as the Taylor-Aris assumption. If the Taylor-Aris assumption is satisfied, differential advection is mainly due to size and/or charge exclusion, and the difference between the average transport velocities of colloids and solutes will increase with the ratio of colloid radius to fracture aperture, which is well documented in the hydrodynamic chromatography (HDC) literature [e.g., 17]. Due to the fact that colloids have very small diffusion coefficients, however, this assumption only holds true under certain conditions. For laminar flow in fractures, the driving force for lateral movement of colloids is Brownian diffusion. Colloid diffusion coefficients, D_c^* [$L^2 \cdot t^{-1}$], are typically evaluated using the Stokes-Einstein equation:

$$D_c^* = \frac{k_B T}{3\pi\eta d_c} \tag{5.1}$$

where k_B [$M \cdot L^2 \cdot t^{-2} \cdot T^{-1}$] is the Boltzmann constant, T [T] is the absolute temperature, η [$M \cdot L^{-1} \cdot t^{-1}$] is the dynamic viscosity, and d_c [L] is the colloid diameter. For a spherical colloid with a diameter of 1 μm in 20°C water, the diffusion coefficient is 4.3×10^{-13} $m^2 \cdot s^{-1}$, which is three orders of magnitude less than typical molecular solute diffusion coefficients (approximately 10^{-10} $m^2 \cdot s^{-1}$). If the colloid diffusion coefficient is sufficiently small, such that the colloid can only sample a small fraction of the entire velocity profile across the fracture aperture within the time scale of a transport experiment, the Taylor-Aris assumption will be violated. To the knowledge of these authors, there have been no studies reported in the literature investigating the consequences of violating the Taylor-Aris assumption in fractured systems.

This research employed a series of numerical simulation to investigate the differential transport (including both differential advection and differential dispersion) between colloids and solutes in parallel-plate fractures when the Taylor-Aris assumption is both satisfied and violated. In addition, this research evaluated the effect of aperture field heterogeneity and anisotropy ratio on differential transport in numerically generated variable-aperture fractures when the Taylor-Aris assumption is both satisfied and violated.

5.2. Methods

To achieve the goals of this research, both colloid and solute transport were simulated in a series of parallel-plate fractures with a range of apertures (Table 5.1), with the purpose of isolating the effect of fracture aperture on differential transport. Three additional numerical experiments (Table 5.2) were then designed to investigate the effects of the coefficient of variation (CoV = σ_b / μ_b, where σ_b is the standard deviation and μ_b is the arithmetic mean aperture), and anisotropy ratio (AR = λ_x/λ_y, where λ_x and λ_y are the correlation lengths of the aperture in the x- and y- directions respectively) of variable-aperture fields on differential transport. The following sections describe the generation of the aperture fields, flow field calculations, and the determination of colloid and solute transport parameters.

5.2.1 Fracture aperture field generation

It was assumed that aperture fields follow a log-normal distribution; the anisotropic covariance function of the log-aperture has the form [16]:

$$C_{\ln(b)}(\boldsymbol{r}) = \sigma_{\ln b}^2 \exp\left[-\left(\frac{r_x^2}{\lambda_x^2}+\frac{r_y^2}{\lambda_y^2}\right)^{\frac{1}{2}}\right] \tag{5.2}$$

where b [L] is the fracture aperture, $\sigma^2_{\ln b}$ is the variance of the ln-aperture, ln$b$, $\boldsymbol{r} = (r_x, r_y)^T$ is a two-dimensional vector whose magnitude is the separation distance between two aperture measurements, and λ_x [L] and λ_y [L] are the correlation length scales of ln$b$ in the x- and y- directions respectively. The arithmetic mean aperture and standard deviation are related to their log-transforms by:

$$\sigma_{\ln b} = \left[\ln\left(\frac{\sigma_b^2}{\mu_b^2} + 1\right)\right]^{\frac{1}{2}} \tag{5.3}$$

$$\mu_{\ln b} = \ln \mu_b - 0.5\sigma^2_{\ln b} \tag{5.4}$$

The quasi-three-dimensional fracture aperture fields employed in this research are 16.0 meters in the x-direction (parallel to the direction of flow) by 2.0 meters in the y-direction (perpendicular to the direction of flow) (Figure 5.1). Each aperture field was discretized into a grid of 400 elements (x-direction) by 50 elements (y-direction) such that each 4 cm by 4 cm element had a distinct aperture. The aperture fields were generated using SPRT2D [18], which is based on the Fast Fourier Transform technique. The parallel plate fracture aperture fields were generated by assuming a very small σ_b (1×10^{-10} m). For variable aperture fields, fifty aperture field realizations for each set of aperture field statistics were generated by changing the seed number supplied to the random field generator.

5.2.2 Flow Field Calculation

The steady state flow field in each fracture plane was obtained by solving the Reynolds equation using a fully implicit finite difference technique [16]:

$$\frac{\partial}{\partial x}\left[b^3(x,y)\frac{\partial h(x,y)}{\partial x}\right] + \frac{\partial}{\partial y}\left[b^3(x,y)\frac{\partial h(x,y)}{\partial y}\right] = 0 \tag{5.5a}$$

$$\left.\frac{\partial h(x,y)}{\partial y}\right|_{y=0.0} = 0 \tag{5.5b}$$

$$\frac{\partial h(x,y)}{\partial y}\bigg|_{y=2.0} = 0 \tag{5.5c}$$

$$h(x,y)\big|_{x=0.0} = h_0 \tag{5.5d}$$

$$h(x,y)\big|_{x=16.0} = 0 \tag{5.5e}$$

where x [L] is the coordinate along the fracture length in the direction of flow, y [L] is the coordinate along the fracture width perpendicular to the direction of flow, $h(x,y)$ [L] is the local hydraulic head, and $b(x,y)$ [L] is the local fracture aperture. The boundary conditions described in equation (5.5) represent no-flow boundaries on the sides of a horizontal fracture, and constant head upstream and downstream boundaries. The equivalent aperture between adjacent elements, in both the x- and y- directions, is approximated by the harmonic mean aperture of the two elements [5]. The average velocity components in both the x- and y- directions are calculated by [16]:

$$\bar{v}_x = -\frac{\gamma b^2(x,y)}{12\eta}\frac{\partial h(x,y)}{\partial x} \tag{5.6a}$$

$$\bar{v}_y = -\frac{\gamma b^2(x,y)}{12\eta}\frac{\partial h(x,y)}{\partial y} \tag{5.6b}$$

where γ [$M \cdot L^{-2} \cdot t^{-2}$] is the specific weight of the fluid, and η [$M \cdot L^{-1} \cdot t^{-1}$] is the dynamic viscosity of the fluid. Figure 5.1 gives a schematic illustration of the coordinate system and boundary conditions employed in this work, and Table 5.3 lists the parameters employed in the model.

5.2.3 Transport simulation

In this work, the random walk particle tracking (RWPT) technique was used to simulate colloid and molecular-scale solute transport in single fractures, based on the following assumptions: (1) both colloids and molecular-scale solutes were considered to be conservative, (2) the colloids are neutrally buoyant, and therefore sedimentation was neglected, and (3) the colloid-colloid and colloid-fracture wall interactions were not accounted for. The size exclusion process was implemented into the RWPT technique by preventing colloid particles from entering the region near the wall where the velocity is very small. In vector form, the RWPT equation is given by [19]:

$$\boldsymbol{X}^{n} = \boldsymbol{X}^{n-1} + A(\boldsymbol{X}^{n-1})\Delta t + \boldsymbol{B}\left(\boldsymbol{X}^{n-1}\right)\cdot \boldsymbol{Z}\sqrt{\Delta t} \tag{5.7}$$

where n [-] refers to the time step, $\boldsymbol{X}^{n}$ [L] is the three-dimensional particle position vector at time $n\Delta t$, $\mathrm{A}(\boldsymbol{X}^{n-1})$ is the absolute forcing vector evaluated at $\boldsymbol{X}^{n-1}$, $\boldsymbol{B}(\boldsymbol{X}^{n-1})$ is a deterministic scaling second-order tensor evaluated at $\boldsymbol{X}^{n-1}$, and $\boldsymbol{Z}$ is a vector of three independent normally distributed random numbers with a mean of zero and a unit variance.

The same discretization scheme was employed for both the transport and flow simulations, and the aperture within each discretized element remained constant. It was assumed that the aperture field is symmetric about the centre plane of the fracture. Upon calculation of the two-dimensional flow field, and imposing a parabolic velocity distribution across the fracture, the quasi-three-dimensional RWPT equations were employed to simulate transport processes [20]:

$$x^{n} = x^{n-1} + \bar{v}_x\left(x^{n-1}, y^{n-1}, z^{n-1}\right)\frac{3}{2}\left\{1 - 4\left[\frac{z}{b(x,y)}\right]^2\right\}\Delta t + Z(0,1)\sqrt{2D^{*}\Delta t} \tag{5.8a}$$

$$y^{n} = y^{n-1} + \bar{v}_y\left(x^{n-1}, y^{n-1}, z^{n-1}\right)\frac{3}{2}\left\{1 - 4\left[\frac{z}{b(x,y)}\right]^2\right\}\Delta t + Z(0,1)\sqrt{2D^{*}\Delta t} \tag{5.8b}$$

$$z^{n} = z^{n-1} + Z(0,1)\sqrt{2D^{*}\Delta t} \tag{5.8c}$$

where D^* [$L^2 \cdot t^{-1}$] is the diffusion coefficient ($D^* = D_c^*$ for colloids and $D^* = D_m^*$ for molecular-scale solutes, where D_m^* is the molecular diffusion coefficient).

The initial condition involved the instantaneous release of 10,000 conservative particles across the inlet of the fracture. The particles were then distributed according to the local volumetric flow rate in both the y and z directions as detailed by James et al. (2005) [20]. A constant time step of $\Delta t = 0.1$ s was employed in these simulations to achieve a balance between solution accuracy and computational efficiency. The random noise present in the stochastic simulations was smoothed out by using ensemble averages of the breakthrough curves generated by each of the 50 aperture field realizations [20]. Table 5.3 lists the RWPT model parameters.

5.2.4 Determination of the average transport velocities and dispersion coefficients for solute and colloid particles

The effluent breakthrough curves from the RWPT simulations were fit to the one-dimensional advection-dispersion equation (ADE) in order to obtain the average transport velocity and effective dispersion coefficient. The ADE is given by:

$$\frac{\partial C}{\partial t} = D_L \frac{\partial^2 C}{\partial x^2} - v_L \frac{\partial C}{\partial x} \tag{5.9a}$$

$$C(0,t) = \frac{M}{Q}\delta(t) \tag{5.9b}$$

$$C(x,0) = 0 \qquad x > 0 \tag{5.9c}$$

$$\lim_{x \to \infty} C(x,t) = 0 \tag{5.9d}$$

where $C(x,t)$ [$M \cdot L^{-3}$] is the tracer concentration, v_L [$L \cdot t^{-1}$] is the mean tracer transport velocity ($v_L = v_{L,coll}$ for colloids and $v_L = v_{L,solute}$ for molecular-scale solute), D_L [$L^2 \cdot t^{-1}$] is the longitudinal dispersion coefficient ($D_L = D_{L,coll}$ for colloids and $D_L = D_{L,solute}$ for molecular-scale solutes), M [M] is the mass of tracer injected, Q [$L^3 \cdot t^{-1}$] is the volumetric flow rate, x [L] is the spatial coordinate in the direction of flow, t [t] is the time, and $\delta(t)$ is the Dirac delta function for the time variable.

The analytical solution for equations (5.9a-d) is given by [21]:

$$C(x,t) = \frac{M}{Q}\frac{x}{\sqrt{4\pi D_L t^3}}\exp\left(-\frac{(x - v_L t)^2}{4D_L t}\right) \tag{5.10}$$

Although both the conventional procedures of fitting the one-dimensional analytical solution to the numerically generated breakthrough curves and the ordinary moment method [e.g., 22] yielded satisfactory results for symmetrically distributed breakthrough curves, these techniques were not suitable for the colloid breakthrough curves, which were seriously skewed. The ordinary moment method put a large weight on the tail portion of these skewed breakthrough curves, particularly for higher moments, resulting in unreasonably large dispersion coefficients and low velocities. In order to circumvent these shortcomings, the weighted moment method was employed to calculate the average transport velocity and dispersion coefficients for all breakthrough curves (both colloid and solute).

The nth weighted moment method is defined as [23]:

$$m_n = \frac{\int_0^\infty C t^n \exp(-st)dt}{\int_0^\infty C dt} \tag{5.11}$$

where s [-] is a weighting factor. Equation (5.11) was applied to the one-dimensional analytical solution (equation 5.10) for transport in parallel plate fractures, and the 0th, 1st and 2nd weighted moments were obtained as:

$$m_0 = \exp\left(\frac{xv - x\sqrt{4D_L s + v_L^{\ 2}}}{2D_L} \right) \tag{5.12a}$$

$$m_1 = \frac{x}{\sqrt{4D_L s + v_L^{\ 2}}} \exp\left(\frac{xv_L - x\sqrt{4D_L s + v_L^{\ 2}}}{2D_L} \right) \tag{5.12b}$$

$$m_2 = \left[\frac{x^2}{4D_L s + v_L^{\ 2}} + \frac{2D_L x}{\left(4D_L s + v_L^{\ 2}\right)\sqrt{4D_L s + v_L^{\ 2}}} \right] \exp\left(\frac{xv_L - x\sqrt{4D_L s + v_L^{\ 2}}}{2D_L} \right) \tag{5.12c}$$

The optimal determination of the weighting factor s is essential to the success of the weighted moment method. Anderson and White (1971) [24] suggested an empirical approximation for optimal s values:

$$s = \frac{n_{highest}}{t_{\max.input} + t_{\max.output} - \Delta t_D} \tag{5.13a}$$

where n_{highest} is the highest order of moment used to estimate the parameter, $t_{\mathrm{max.input}}$ and $t_{\mathrm{max.output}}$ are the times when the input and output signals reach their maximum values respectively, and Δt_{D} is the difference in time delay between the input and output signals. For the delta pulse input employed in this work, however, $t_{\mathrm{max.input}}$ is zero. Additionally, some of the output signals have no rising limb, and therefore $t_{\mathrm{max.output}}$ for these output signals is equal to Δt_{D}. This particular circumstance results in the denominator in equation (5.13a) equaling zero. In order to avoid this issue, a modified form of equation (5.13a) was employed:

$$s = \frac{n_{highest}}{t_{\max.output}} \tag{5.13b}$$

The average transport velocity, v_L, and dispersion coefficient, D_L, can be calculated from the combination of any two of the three weighted moments in equation (5.12). When calculating v_L and D_L for solute transport in parallel plate fractures, however, it was found that the combination of m_0 and m_1 gave the best results (i.e., v_L agrees very well with the fluid velocity, and D_L agrees very well with the Taylor dispersion coefficient). This validated the use of equation (5.13b) in determining the weighting factor s. Therefore, m_0 and m_1 were employed as the exclusive weighted moments in this work for calculating v_L and D_L.

5.3. Results and Analysis

Differential advection between colloids and solutes in parallel-plate channels/fractures is well documented in the HDC literature [e.g., 25, 26], and is characterized by the calibration relationship between the relative retention time, τ_p [–], and the relative colloid size with respect to the channel aperture, δ [-] [25]:

$$\tau_p = \frac{t_{c,peak}}{t_{s,peak}} = \frac{1}{1 + F\delta - G\delta^2} \tag{5.14a}$$

$$\tau_p = \frac{t_{c,peak}}{t_{s,peak}} = \frac{L_x / \bar{v}_{c,peak}}{L_x / \bar{v}_{s,peak}} = \frac{\bar{v}_{s,peak}}{\bar{v}_{c,peak}} \tag{5.14b}$$

where L_x [L] is the fracture length in the x-direction, and $t_{c,peak}$ [t] and $t_{s,peak}$ [t] are the retention times of the colloids and molecular-scale solutes respectively. The retention time of a particle is referred to as the time elapsed between the injection and elution of the maximum peak of that particle. Equation (5.14b) relates the retention times, $t_{c,peak}$ and $t_{s,peak}$, to their respective mean transport velocities, $\bar{v}_{c,peak}$ and $\bar{v}_{s,peak}$. The constants F and G are dependent on the conduit symmetry and G also depends on a retention model. δ [–] is the ratio of the colloid radius to half of the height of the channel through which it is traveling. For parallel-plate fractures, δ is defined as:

$$\delta = \frac{r_c}{R} \tag{5.15}$$

where r_c [L] is the radius of the colloid particles, and R [L] refers to half of the actual aperture, b, for parallel-plate fractures. For variable-aperture fractures, R [L] represents the half of the arithmetic mean aperture, μ_b, in this work. For impermeable hard spheres transported through parallel-plate fractures, equation (5.14a) becomes [25]:

$$\tau_p = \frac{1}{1+\delta-\delta^2} \tag{5.16}$$

Additionally, τ_m, the ratio of colloid to molecular-scale solute mean residence time, can be also employed to characterize the differential transport of colloids and molecular-scale solutes, and is defined as:

$$\tau_m = \frac{t_{c,mean}}{t_{s,mean}} = \frac{L_x / \bar{v}_{c,mean}}{L_x / \bar{v}_{s,mean}} = \frac{\bar{v}_{s,mean}}{\bar{v}_{c,mean}} \tag{5.16b}$$

where $t_{c,mean}$ [t] and $t_{s,mean}$ [t] represent the mean residence times for colloids and solutes respectively, $\bar{v}_{c,mean}$ [L·t^{-1}] and $\bar{v}_{s,mean}$ [L·t^{-1}] are the mean transport velocities for colloids and solutes respectively, and are based on the mean residence times. Figure 5.2 shows that the molecular-scale solute breakthrough curves are nearly normally distributed; however, the colloid breakthrough curves are typically skewed to the right with sharp fronts and long tails, particularly when the Taylor-Aris assumption is not satisfied. As a result, τ_m is similar to τ_p for molecular-scale solutes, but is much larger than τ_p for colloids due to the long tail of breakthrough curves. Since the determination of $t_{c,mean}$ depends on the weighting factor s, there is a degree of uncertainty in its calculation. By contrast, the determination of $t_{c,peak}$ is straightforward. Therefore, τ_p, and not τ_m, is used in this work.

5.3.1 Method employed to determine the validity of the Taylor-Aris assumption

James and Chrysikopoulos (2001) [27] derived an empirical expression to calculate the time, Δt_c [t], necessary for a colloid to travel, by diffusivity alone, a specified distance, L_z [L], in the z direction within a fracture aperture:

$$\Delta t_c = \exp\left\{\ln\left[\frac{L_z^{\ 2}}{D_c}\right] - 0.978 + 0.787Z(0,1)\right\} \tag{5.17a}$$

Equation (5.17a) shows that, if Brownian motion is the only driving force, Δt_c depends on L_z and D_c. To determine if the Taylor-Aris assumption is satisfied when colloid particles are transported in single fractures, L_z is replaced by the aperture, b, for parallel-plate fractures, or the arithmetic mean apertures, μ_b, for variable-aperture fractures. 5000 realizations of $Z(0,1)$ were generated, resulting in 5000 realizations of Δt_c. $\Delta \bar{t}_c$, the arithmetic mean value of Δt_c, are then compared with the colloid retention time, $t_{c,peak}$, to determine the validity of the Taylor-Aris assumption:

$$\begin{cases} \Delta \bar{t}_c < t_{c,peak} & \text{Taylor – Aris assumption satisfied} \\ \Delta \bar{t}_c > t_{c,peak} & \text{Taylor – Aris assumption violated} \end{cases} \tag{5.17b}$$

A value of $\Delta \bar{t}_c$ greater than $t_{c,peak}$ indicates that the colloid cannot sample the entire velocity profile across the aperture during the time it is traveling in the fracture, and the Taylor-Aris assumption is violated. Conversely, if $\Delta \bar{t}_c$ is less than $t_{c,peak}$, the Taylor-Aris assumption is satisfied. A critical value of the fracture aperture, b_0, can be determined for the validity of the Taylor-Aris assumption by setting $\Delta \bar{t}_c = t_{c,peak}$.

5.3.2 Mechanisms causing differential transport in parallel-plate fractures

Equation (5.17a) shows that the variables R (= 1/2b for parallel-plate fractures), D_c^* (thus r_c) and $t_{c,peak}$ are all required to determine the validity of the Taylor-Aris assumption. To investigate the dependence of τ_p on r_c, R, and $t_{c,peak}$, two groups of simulations were conducted in parallel-plate fractures, as shown in Table 5.4. In the Group I simulations, r_c was kept constant, and four different average fluid velocities across the aperture, $\bar{v}_x$, were applied to a series of parallel-plate fractures ($\bar{v}_y$ = 0 for parallel-plate fracture). In the

Group II simulations, *R* and the average fluid velocity, $\bar{v}_x$, remained unchanged, and seven different values of r_c were employed.

5.3.2.1 Group I simulations

The results of the Group I simulations are shown in Figure 5.3 (a), together with a HDC calibration curve based on equation (5.16), which illustrates the dependence of τ_p on δ. Figure 5.3(a) clearly shows that, for each case with a specific average fluid velocity, there exists a threshold value of δ_0. When $\delta > \delta_0$, the simulation results follow the same trend as that of the HDC calibration curve, that is, τ_p increases with decreasing δ. However, when $\delta < \delta_0$, the simulation results display an opposite trend to that of the HDC curve, that is, τ_p increases with increasing δ, and reaches a constant value asymptotically. This phenomenon is not exhibited by the HDC calibration curve, and has never been reported before to the knowledge of these authors. Figure 5.3(a) also shows that the threshold value, δ_0, increases with increasing average fluid velocity in the fractures. This phenomenon can be explained by considering the Taylor-Aris assumption.

The average velocity, $\bar{v}_{UL}$ [L·t^{-1}], for a colloid transported in a parallel-plate fracture is given by:

$$\bar{v}_{UL} = \frac{1}{z_U - z_L}\int_{z_L}^{z_U} v(z)dz \qquad (5.18)$$

where $v(z)$ [L·t^{-1}] is the colloid transport velocity at *z*, and z_U [L] and z_L [L] are the *z* coordinates indicating the upper and lower limit of the colloid particle transport zone, as shown in Figure 5.4. When $\delta > \delta_0$ (correspondingly $b < b_0$ since the colloid size is constant in Group I), $\Delta\bar{t}_c < t_{c,peak}$, thereby satisfying the Taylor-Aris assumption, and the colloid is able to sample the entire velocity profile (except the region very near the wall due to charge and/or size exclusion) before it exits the fracture. Under such conditions, the average transport velocity of colloids will be larger than that of molecular-scale solutes due to size and/or charge exclusion according to equation (5.18). This phenomenon coincides with the main retention mechanism of HDC, and therefore follows the same trend as that of HDC. It should be pointed out here that the Taylor-Aris assumption is satisfied for all molecular-scale solutes employed in these simulations.

However, when $\delta < \delta_0$ (and correspondingly $b > b_0$), the Taylor-Aris assumption is violated, and colloids are only able to traverse a fraction of the aperture in the z direction before they exit the fracture due to their low diffusivities (as illustrated in Figure 5.4). This results in two consequences.

The first consequence of violating the Taylor-Aris assumption is that the dispersion coefficients of colloid particles within the fracture will be smaller than the Taylor dispersion coefficient, D_{Taylor}, calculated using the following equation:

$$D_{Taylor} = D_c^* + \frac{1}{210}\frac{\bar{v}^2 b^2}{D_c^*} \tag{5.19}$$

where $\bar{v}$ [L·t^{-1}] is the mean fluid velocity across the aperture. This will be further discussed in Section 3.3.

Another consequence is that the colloid breakthrough curves will have sharp fronts and long tails, and the peak arrival time of the colloids will be earlier than that of molecular-scale solutes. Furthermore, the difference between peak arrival times of colloids and molecular-scale solutes is larger than that which can be explained by size and/or charge exclusion. For example, for the case of d_c = 1 μm and $\bar{v}_x = 1.14 \times 10^{-3}$ m/s, the RWPT simulation (Figure 5.3(a)) shows that, when $\delta < \delta_0 = 9.0 \times 10^{-3}$ (i.e., the Taylor-Aris assumption is violated), τ_p decreases dramatically and is much different from 1. However, the HDC calibration curve (in which the difference between peak arrival times of colloids and molecular-scale solutes is primarily caused by size and/or charge exclusion) shows that τ_p approaches 1 when $\delta < \delta_0 = 9.0 \times 10^{-3}$. This is due to the facts that: (1) A colloid with an initial position at the centerline will travel in a zone near the centerline until it exits the fracture (i.e., the Taylor-Aris assumption is not satisfied) due to its small diffusion coefficient. Therefore, its average transport velocity will be much larger than that of a solute. Similarly, a colloid starting in a region near a wall will travel in the region near that wall. Therefore, its average transport velocity will be smaller than that of a molecular solute. (2) The particle concentration distribution across the aperture is somewhat similar to that of the fluid velocity, with the highest concentration at the centerline and the lowest concentration near the walls [5,25]. These two factors result in the fact that the faster moving colloids near the centerline lead to sharper breakthrough curve fronts and earlier peak arrival times than molecular-scale solutes, and the slower moving colloids near the wall result in a long tail in the breakthrough curves. Another consequence is that the colloid residence time distribution is wider, and its macro-dispersion coefficient larger than that of a solute.

Several explanations have been proposed for the long tail observed for colloid breakthrough curves in fractured media, such as matrix diffusion [e.g., 28, 29], and diffusive exchange of tracer with immobile water in fractures [e.g., 30,31]. Becker and Shapiro (2000) [32] attributed the long tails on their breakthrough curves to the differential advection of tracer in channels with very different hydraulic conductivities, and advective mass exchange between mobile and immobile fluid. Harter et al. (2000) [33] attributed the long tail in skewed colloid breakthrough curves to reversible attachment. This work, on the other hand, demonstrates that the long tail can also be caused by the very different average colloid velocities across the aperture (i.e., larger average velocities at the centerline and smaller average velocities near the wall), when the Tayor-Aris assumption is not satisfied. This effect is expected to be more obvious in less heterogeneous fractures.

Figure 5.3(a) and Table 5.4 also show the relationship between the threshold value δ_0 (or b_0 when r_c remains constant) and the average fluid velocity in the fracture, which is that δ_0 increases with increasing average fluid velocity. This is due to the fact that an increasing average fluid velocity will lead to a smaller $t_{c,peak}$. By letting $\Delta\bar{t}_c = t_{c,peak}$ in equation (5.17a), a smaller $t_{c,peak}$ will results in a decrease in b_0. According to equation (5.15), a decrease in b_0 will result in an increase in δ_0 since r_c remains constant (i.e., 1 μm) in the Group I simulations. The calculated values of δ_0 for the four different average fluid velocities employed in this work are shown in Table 5.4. It is noted, however, that the calculated threshold values of δ_0 using equation (5.17) are consistently smaller (by a factor of about 3) than those observed in Figure 5.3(a). One explanation for this discrepancy is that the method employed to determine the validity of the Taylor-Aris assumption, described in Section 3.1, is only qualitatively correct. It is also observed from Figure 5.3(a) that, for larger average velocities ($\bar{v}_x = 1.14\times10^{-3}$ and 1.03×10^{-2} m/s in this research), τ_p reaches an asymptotic value (approximately 0.67) as δ decreases. This is due to the fact that, when the colloid retention time in the fracture is relatively small, colloids near the centerline, where the colloid concentration is the highest, only traverse a small distance in the z direction. Therefore their average velocity is similar in fractures with apertures larger than a certain value, resulting in similar peak arrival times. Additionally, Figure 5.3(a) also shows that for a specific δ, and thus b, τ_p decreases with increasing average fluid velocity. This indicates that, when the average fluid velocity increases, the average transport velocity of colloids traveling near the centerline, which determines the peak arrival time, increases to a larger extent than the average transport velocity of solutes.

5.3.2.2 Group II simulation

These simulations involved situations in which the fracture aperture remained constant while the colloid diameter changed. The results are shown in Table 5.4 and Figure 5.3 (b). For the range of colloid diameters and fracture apertures used in these simulations, the

Taylor-Aris assumption is only satisfied for d_c = 0.1 μm. It is clearly shown, however, that the relationship between τ_p and δ follows a trend similar to the HDC calibration curve, which is that τ_p decreases with increasing δ. The simulated results, however, deviate from the theoretical HDC curve significantly. For the HDC calibration curve, the Taylor-Aris assumption is satisfied, and it is well known that size/charge exclusion results in the fact that the average velocity of larger colloids ($\bar{v}_{c,larger}$), smaller colloids ($\bar{v}_{c,smaller}$), and molecular-scale solutes ($\bar{v}_{solute}$) will follow the relationship: $\bar{v}_{c,larger} > \bar{v}_{c,smaller} > \bar{v}_{solute}$. Therefore their respective retention times will follow: $t_{c,larger} < t_{c,smaller} < t_{solute}$. The above relationships hold even when the Taylor-Aris assumption is violated. Because the distance the larger colloids will traverse in the z direction will be statistically smaller than that of smaller colloids before they exit the fracture, the average velocity of a larger colloid starting from the centerline of the aperture, where the colloid concentration is the highest, is larger than that of a smaller colloid starting from the same position (equation 5.18). The deviation between the simulations and the HDC calibration in Figure 5.3(b) is due to the fact that the Taylor-Aris assumption is satisfied for the HDC calibration curve, but not for the present simulations.

5.3.2.3 Implications of the simulation results

The findings of this work, combined with the HDC calibration curve, shows that when R in equation (5.15) remains constant, the relationship between τ_p and δ always follows the same trend as the theoretical HDC calibration curve, whether the Taylor-Aris assumption is satisfied or not. When r_c remains constant in equation (5.15), however, there exists a value of δ_0 (thus b_0), where the average transport velocity for a colloid is similar to that of a molecular-scale solute. When $\delta > \delta_0$, τ_p decreases as δ increases; when $\delta < \delta_0$, τ_p decreases as δ decreases.

This finding has significant implications on interpreting the results of colloid and solute tracer tests in single fractures as well as in unconsolidated porous media. For example, Small (1974) [17] employed HDC experiments to show that velocity enhancement increases as the mean grain size of the packing bed decreases. However, Harter et al. (2000) [33] conducted experimental work on colloid transport in sandy soils and found that velocity enhancement increased as the mean grain size of the soil column increased. This seeming inconsistency disappears upon further analysis.

Following earlier work in the field of HDC, we use a parallel array of capillaries of equal size to represent the interstitial channels in porous media, and take as the equivalent capillary radius the hydraulic radius R_0 [34]:

$$R_0 = \frac{d_p}{3}\frac{\theta}{1-\theta} \tag{5.20}$$

where d_p [L] is the diameter of the media grains, and θ [-] is the porosity. Replacing the L_z in equation (5.17) with R_0, we calculated $\Delta\bar{t}_c$. Comparing $\Delta\bar{t}_c$ with the retention time $t_{c,peak}$, we can determine whether or not the Taylor-Aris assumption is satisfied. Table 5.5 shows that the Taylor-Aris assumption was satisfied in Small's (1974) [17] experiments, and therefore velocity enhancement increased as the mean grain size (thus R_0) of the packing bed decreased in his work. However, the Taylor-Aris assumption was violated in Harter et al.'s (2000) experiments [33] (Table 5.6), and the grain size of the porous media varied while the colloid size remained constant, thus velocity enhancement increased as the mean grain size (thus R_0) of the soil column increased.

5.3.3 The validity of the Taylor-Aris dispersion coefficient

By implicitly assuming that the Taylor-Aris assumption is satisfied, James and Chrysikopoulos (2003) [15] derived expressions for the effective velocity, v_{eff} [L·t^{-1}], and the effective dispersion coefficient, D_{eff} [L^2·t^{-1}], for neutrally buoyant, finite-sized spherical particles traveling in a uniform-aperture fracture as follows:

$$v_{eff} = \bar{v}_x \left[1 + \frac{d_c}{b} - \frac{1}{2}\left(\frac{d_c}{b}\right)^2 \right] \tag{5.21}$$

$$D_{eff} = D_c + \frac{1}{210}\frac{\bar{v}^2 b^2}{D_c}\left(1 - \frac{d_c}{b}\right)^6 \tag{5.22}$$

where $\bar{v}_x$ [$L{\cdot}t^{-1}$] is the mean fluid velocity across the aperture. The correction term in equation (5.21) (shown in square brackets) is typically very small, and therefore the difference between v_{eff} and $\bar{v}_x$ is also very small (up to 3% in this research). By contrast, the ratio of D_{eff}/D_{Taylor} ranged from 6% to 18% when b decreased from 100 μm to 30 μm in this research. When b≥150 μm in this work, the difference between D_{eff} and D_{Taylor} was negligible (less than 4%).

Figure 5.5 compares dispersion coefficients and average transport velocities for solutes and colloids in parallel-plate fractures (Group I simulation, $\bar{v}_x$=1.14×10^{-3} m/s) obtained using various methods. As shown in Figures 5.5 (a) and (b), the dispersion coefficient and transport velocity for a solute, calculated by the weighted moment method based on the numerically generated breakthrough curves, agrees very well with the Taylor dispersion coefficient and average fluid velocity respectively. This is expected, and confirms the validity of using the weighted moment method to calculate the dispersion coefficient and average transport velocity in this work. However, the story is very different for colloids. Figure 5.5 (c) shows that, when the Taylor-Aris assumption is satisfied (for b=30 μm, 50 μm, 70 μm, 90 μm, 100 μm in these simulations), D_{eff} from equation (5.22) agrees very well with D_L calculated using the weighted moment method based on the numerically generated breakthrough curves, with a difference of less than 5%. However, D_L is significantly smaller than D_{eff}, by up to 8 times, when the Taylor-Aris assumption is violated (for b≥150 μm in these simulations). Therefore, equation (5.22) will significantly overestimate the colloid dispersion coefficient when the Taylor-Aris assumption is violated.

Additionally, the difference between v_L (the mean colloid transport velocity, which is calculated using the weighted moment method and is based on the mean residence time, t_m.) and v_{eff} (obtained from equation (5.21)) increases as b increases (correspondingly as δ decreases), but the largest difference is less than 3%. Therefore, v_{eff} provides a good estimation of v_L whether or not the Taylor-Aris assumption is satisfied. However, $\bar{v}_{c,peak}$ (the mean colloid transport velocity based on $t_{c,peak}$, the retention time) is larger than v_{eff} by up to 32% when the Taylor-Aris assumption is violated. This is due to the fact that the colloid breakthrough curve is typically skewed right with a sharp front and long tail when the Taylor-Aris assumption is not satisfied. Therefore, t_m is typically much larger than $t_{c,peak}$, and v_L is typically much smaller than $\bar{v}_{c,peak}$.

5.3.4 Differential advection and dispersion through variable-aperture fractures: the effects of CoV and AR

The effect of CoV and AR on τ_p when the Taylor-Aris assumption is violated was also investigated. The experiment design is shown in Table 5.2, and the results are illustrated in Figures 5.6 and 5.7. Several important findings were identified upon examination. It should be pointed out here that Pe>>1 in the present simulations, that is, the transport is within the advection-dominated regime.

Figure 5.6 shows that τ_p decreases with increasing mean fluid velocity in variable-aperture fractures with arithmetic mean apertures of μ_b = 300 μm, 600 μm, and 900 μm respectively, which is consistent with the results from the simulations conducted in parallel-plate fractures shown in Figure 5.3(a). Figure 5.6 also shows that for fractures with a specific arithmetic mean aperture, μ_b, τ_p increases with increasing σ_b. This indicates that the velocity enhancement of colloids relative to conservative molecular-scale solutes decreases with increasing CoV for fractures with a specific average aperture. For μ_b = 300 μm and σ_b = 120 μm (CoV=0.4, the largest employed in these simulations), τ_p is near unity, which is consistent with experimental observations. Harvey et al. (1995)

[35] found that flagellated protozoa and microspheres did not exhibit significant velocity enhancement traveling in a sandy aquifer with moderate heterogeneity over distances of 1-3.6m. Figure 5.6 also shows that AR also plays a role in colloid velocity enhancement relative to solute tracers, however, its effect is much smaller than that of σ_b. Additionally, the effect of AR is not consistently demonstrated for different combinations of μ_b and σ_b. Therefore, the effect of AR merits further investigation.

Figures 5.7(a), (b), and (c) show plots of $D_{L,coll}/D_{L,solute}$ versus CoV and AR for μ_b = 300 μm, 600 μm, and 900 μm respectively. All of these figures show the same trend that the ratio of $D_{L,coll}/D_{L,solute}$ decreases (from about 700 to about 1) with increasing CoV. For example, the ratio of $D_{L,coll}/D_{L,solute}$ for parallel-plate fractures with b = 300 μm and hydraulic gradient = 0.00156 is 551. The ratio of $D_{L,coll}/D_{L,solute}$ for variable-aperture fractures (with the same dimensions and hydraulic gradient, μ_b = 300 μm, σ_b = 40 μm, 80 μm, and 120 μm) decreases from approximately 40 to 2 with increasing CoV. The AR plays a minor role compared to the CoV, and the results show that

$$\left(D_{L,coll}/D_{L,solute}\right)_{AR=1.0} > \left(D_{L,coll}/D_{L,solute}\right)_{AR=0.2} > \left(D_{L,coll}/D_{L,solute}\right)_{AR=5.0} \qquad (5.23)$$

The above discussion demonstrates a transition of τ_p and $D_{L,coll}/D_{L,solute}$ from parallel-plate to increasingly variable aperture fields. In parallel-plate fractures, a comparison of Figures 5.5 (a) and (c) shows that the ratio of $D_{L,coll}/D_{L,solute}$ is much larger than 1, whether or not the Taylor-Aris assumption is satisfied. Faster breakthrough of colloids relative to conservative solutes in parallel-plate fractures has been demonstrated through numerical simulation in this work (Figure 5.3(a) and (b)), through experiments [e.g., 25], and theoretical analysis [e.g., 15]. This phenomenon has been ascribed to size and/or charge exclusion when the Taylor-Aris assumption is satisfied [25,15]. However, when the Taylor-Aris assumption is violated, this phenomenon is due to the combined effects of the large difference between the diffusivity of colloids and solutes, together with the parabollically distributed velocity across the aperture, with size and/or charge exclusion playing a minor role.

In variable-aperture fractures, however, aperture field heterogeneity and, to a lesser extent, anisotropy become more dominant in determining the average transport velocity and macro-dispersion coefficient as these parameters increase [36] (Zheng et al., 2008). Under these circumstances, the effect of size and/or charge exclusion (when the Taylor-Aris assumption is satisfied) and the combined effect of the large difference between the diffusivity of colloids and solutes together with the parabollically distributed velocity profile across the aperture (when the Taylor-Aris assumption is not satisfied) will become less important. Therefore, the difference between the breakthrough time and macro-dispersion coefficient of colloids and solutes becomes smaller with increasing aperture field heterogeneity and anisotropy. It is hypothesized that, when solutes and colloids migrate in relatively large-scale single fractures for relatively long time periods, solutes will be able to enter small aperture regions while colloids will not due to pore exclusion; and solute will be able to enter stagnant regions due to their high diffusion coefficient while colloids will not. Under such conditions, colloid dispersion coefficients could be less than those of solute, although colloids still have faster breakthrough than solutes. Under these conditions, the faster breakthrough and smaller dispersion coefficients of colloids relative to solutes will be similar to those observed in unconsolidated porous media [e.g., 1,37,2].

5.4. Summary

Differential transport between colloids and molecular-scale solutes in single fractures was investigated using numerical simulations. The Reynolds equation was solved using a fully implicit finite difference technique to obtain the flow field in saturated single fractures. A quasi-three-dimensional RWPT technique was employed to simulate colloid and molecular-scale solute transport in both parallel-plate and variable-aperture fractures.

The formula developed by James and Chrysikopoulos (2001) was employed to determine whether the Taylor-Aris assumption is satisfied or violated.

For colloid and solute transport in parallel-plate fractures, it was demonstrated that there exists a threshold value of δ_0, the ratio of the colloid radius to half the aperture of the fracture, where the retention time for solute and colloid particles are very similar. When $\delta > \delta_0$, the Taylor-Aris assumption is satisfied, and the relative retention time τ_p decreases as δ increases, as is well documented in the HDC literature. Conversely, when $\delta < \delta_0$, the Taylor-Aris assumption is violated, and the relative retention time τ_p increases as δ decreases. To the best knowledge of these authors, this is the first time that this trend has been demonstrated. When the Taylor-Aris assumption is satisfied, the Taylor dispersion coefficient (D_{Taylor}) and its extension by James and Chrysikopoulos (2003) [15] (D_{eff}) give a good estimation of the actual colloid dispersion coefficient, however, when the Taylor-Aris assumption is violated, both D_{Taylor} and D_{eff} significantly overestimate the colloid dispersion coefficient. These results have important implications regarding the interpretation of tracer tests in both porous and fractured media, and help to explain previous, seemingly conflicting, results presented in the literature as discussed in Section 3.2.3.

Transport simulations were also conducted in variable-aperture fractures to investigate the influence of CoV and AR on the relative retention time τ_p and the ratio of $D_{L,coll}/D_{L,solute}$ for cases where $\delta < \delta_0$ (i.e., the Taylor-Aris assumption is violated). These results show that τ_p increases with increasing CoV, which means that the velocity enhancement of colloids relative to solutes decreases with increasing heterogeneity. On the other hand, the ratio of $D_{L,coll}/D_{L,solute}$ decreases by several orders of magnitude to about 1 with increasing CoV, which means that the difference between dispersion coefficients of colloids and solutes becomes smaller with increasing aperture field heterogeneity. These results also show that the AR also has an impact on τ_p and $D_{L,coll}/D_{L,solute}$, however, its influence is much smaller than that of the CoV.

Acknowledgement

This research was funded by the NSERC Discovery Grant Program (S. Dickson and Y. Guo). The authors would like to thank Dr. S. C. James for generously providing the flow code employed in this research. This work was made possible by the facilities of the Shared Hierarchical Academic Research Computing Network (SHARCNET:www.sharcnet.ca).

References

[1] D.F. Shonnard, R.T. Taylor, M.L. Hanna, C.O. Boro, A.G. Duba, Water Resour. Res. 30(1) (1994) 25.

[2] L.P. Pang, M. Close, M. Noonan, Ground Water, 36(1) (1998) 112.

[3] D.C. DeBorde, W.W. Woessner, Q.T. Kiley, P. Ball, Water Res., 33(10) (1999) 2229.

[4] P. Zhang, W.P. Johnson, M.J. Piana, C.C. Fuller, D.L. Naftz, Ground Water, 39(6) (2001) 831.

[5] P.W. Reimus, The use of synthetic colloids in tracer transport experiments in saturated rock fractures, Report LA-13004-T, Los Alamos National Laboratory, Los Alamos, N. M., 1995.

[6] L.D. Mckay, J. Fredericia, M. Lenczewski, J. Morthorst, K. E. Klint, Nord. Hydrol. 30 (1999) 333.

[7] L.D. Mckay, W.E. Sanford, J.M. Strong, Ground Water 38 (2000)139.

[8] G. De Marsily, Quantitative Hydrogeology, Academic, San Diego, Calif., 1986.

[9] H. Gvirtzman, S. M. Gorelick, Nature 352 (1991) 793.

[10] C.G. Engfield, G. Bengtsson, Ground Water 26 (1988) 64.

[11] T.D. Scheibe, B.D. Wood, Water Resour. Res. 39(4) (2003)1080.

[12] T.R. Ginn, Water Resour. Res. 38(4) (2002) 1041.

[13] S. Li, C. Jen, Nucl. Technol. 133 (2000) 253.

[14] C. Jen, S. Li, Waste Manage 21 (2001) 499.

[15] S.C. James, C. V. Chrysikopoulos, J. Colloid Interf. Sci. 263 (2003) 288.

[16] C.V. Chrysikopoulos, S. James, Transport Porous Med. 51 (2003) 191.

[17] H. Small, J. Colloid Interf. Sci. 48(1) (1974) 147.

[18] A.L. Gutjahr, Fast Fourier transform for random field generation, Report 4-R58-2690R, New Mexico Institute of Mining and Technology, Socorro, NM., 1989,

[19] A.F.B. Tompson, L.W. Gelhar, Water Resour. Res. 26(10) (1990) 2541.

[20] S.C. James, T.K. Bilezikjian, C.V. Chrysikopoulos, Stoch. Env. Res. Risk A. 19(4) (2005) 266.

[21] A. Kreft, A. Zuber, Chem. Eng. Sci. 33 (1978) 1471.

[22] C. Yu, A.W. Warrick, M.H. Conklin, Water Resour. Res. 35(11) (1999) 3567.

[23] M.A. Fahim, N. Wakao, Chem. Eng. J. 25 (1982) 1.

[24] A.S. Anderson, E.T. White, Chem. Eng. Sci., 26 (1971) 1203.

[25] E. Chmela, R. Tijssen, M.T. Blom, H.J.G.E. Gardeniers, A. van den Berg, Anal. Chem. 74 (2002) 3470.

[26] M.T. Blom, E. Chmela, R.E. Oosterbroek, R. Tijssen, A. van den Berg, Anal. Chem. 75 (2003) 6761.

[27] S.C. James, C.V. Chrysikopoulos, Chem. Eng. Sci. 56(23) (2001) 6535.

[28] P. Maloszewski, A. Zuber, Water Resour. Res. 29(8) (1993) 2723.

[29] A.F. Moench, Water Resour. Res. 31(8) (1995) 1823.

[30] K.G. Raven, K.S. Novakowski, P.A. Lapcevic, Water Resour. Res. 24(12) (1988) 2019.

[31] R. Haggerty, S.M. Gorelick, Water Resour. Res. 31(10) (1995) 2383.

[32] M.W. Becker, A.M. Shapiro, Water Resour. Res. 36(7) (2000) 1677.

[33] T. Harter, S. Wagner, E. R. Atwill, Environ. Sci. Technol. 34 (2000) 62.

[34] G. Stegeman, J.C. Kraak, H. Poppe, R. Tijssen, J. Chromatogr. A 657 (1993) 283.

[35] R.W. Harvey, N.E. Kinner, A. Bunn, D. MacDonald, D.W. Metge, Appl. Environ. Microb. 61(1) (1995) 209.

[36] Q. Zheng, S. E. Dickson, Y. Guo, submitted to J. Geophys. Res. (2008).

[37] P. Grindrod, M.S. Edwads, J.J.W. Higgo, G.M. Williams, J. Contam. Hydrol. 21 (1996) 243.

Tables

Table 5.1. Aperture field characteristics for the parallel-plate fractures.

Experiment number	Mean μ_b (m)	Standard deviation σ_b (m)	Coefficient of Variation (CoV[−]= σ_b / μ_b)	Longitudinal correlation length λ^b_x (m)	Transverse correlation length λ^b_y (m)	Anisotropic ratio (AR[−]= $\lambda^b_x / \lambda^b_y$)
1	0.00003	1.0E-10	3.33E-06	0.08	0.08	1.0
2	0.00005	1.0E-10	2.00E-06	0.08	0.08	1.0
3	0.00007	1.0E-10	1.43E-06	0.08	0.08	1.0
4	0.00009	1.0E-10	1.11E-06	0.08	0.08	1.0
5	0.0001	1.0E-10	1.00E-06	0.08	0.08	1.0
6	0.00015	1.0E-10	6.67E-07	0.08	0.08	1.0
7	0.0002	1.0E-10	5.0E-07	0.08	0.08	1.0
8	0.0003	1.0E-10	3.33E-07	0.08	0.08	1.0
9	0.0004	1.0E-10	2.50E-07	0.08	0.08	1.0
10	0.0005	1.0E-10	2.00E-07	0.08	0.08	1.0
11	0.0006	1.0E-10	1.67E-07	0.08	0.08	1.0
12	0.0007	1.0E-10	1.43E-07	0.08	0.08	1.0
13	0.0008	1.0E-10	1.25E-07	0.08	0.08	1.0
14	0.0009	1.0E-10	1.11E-07	0.08	0.08	1.0

Table 5.2. Aperture field characteristics for the variable-aperture fractures.

Experiment number	Mean μ_b (m)	Standard deviation σ_b (m)	coefficient of variation (CoV= σ_b / μ_b)	Longitudinal correlation length λ_x (m)	Transverse correlation length λ_y (m)	Anisotropic ratio (AR= λ_x/ λ_y)
1	0.0003	0.00004	0.13	0.40	0.08	5.0
2	0.0003	0.00008	0.27	0.40	0.08	5.0
3	0.0003	0.00012	0.40	0.40	0.08	5.0
4	0.0003	0.00004	0.13	0.08	0.08	1.0
5	0.0003	0.00008	0.27	0.08	0.08	1.0
6	0.0003	0.00012	0.40	0.08	0.08	1.0
7	0.0003	0.00004	0.13	0.08	0.40	0.2
8	0.0003	0.00008	0.27	0.08	0.40	0.2
9	0.0003	0.00012	0.40	0.08	0.40	0.2
10	0.0006	0.00004	0.07	0.40	0.08	5.0
11	0.0006	0.00008	0.13	0.40	0.08	5.0
12	0.0006	0.00012	0.20	0.40	0.08	5.0
13	0.0006	0.00004	0.07	0.08	0.08	1.0
14	0.0006	0.00008	0.13	0.08	0.08	1.0
15	0.0006	0.00012	0.20	0.08	0.08	1.0
16	0.0006	0.00004	0.07	0.08	0.40	0.2
17	0.0006	0.00008	0.13	0.08	0.40	0.2
18	0.0006	0.00012	0.20	0.08	0.40	0.2
19	0.0009	0.00004	0.04	0.40	0.08	5.0
20	0.0009	0.00008	0.09	0.40	0.08	5.0
21	0.0009	0.00012	0.13	0.40	0.08	5.0
22	0.0009	0.00004	0.04	0.08	0.08	1.0
23	0.0009	0.00008	0.09	0.08	0.08	1.0
24	0.0009	0.00012	0.13	0.08	0.08	1.0
25	0.0009	0.00004	0.04	0.08	0.40	0.2
26	0.0009	0.00008	0.09	0.08	0.40	0.2
27	0.0009	0.00012	0.13	0.08	0.40	0.2

Table 5.3. Parameters employed in the flow and transport simulations.

	Parameter	Value
Flow simulation	Fracture dimensions (length×width)	16.0 m×2.0 m
	Fracture discretization (elements×elements)	400×50
	Element size (*dx*×*dy*)	0.04 m×0.04 m
	Temperature	20 °C
	Dynamic viscosity	1.002×10^{-3} N·m·s^{-2}
	Specific weight	9789 N·m^{-3}
	Hydraulic gradient	0.25/16 for parallel-plate fractures, and 0.025/16 for variable-aperture fractures
Transport simulation	Molecular diffusion coefficient D_m^*	9.0×10^{-10} m^2·s
	Time step Δt	0.1 s for parallel-plate fractures, and 1.0 s for variable-aperture fractures

Table 5.4. Transport simulations in parallel-plate fractures: Group I and Group II simulations.

Group I				Group II			
b (μm)	d_c (μm)	$\bar{v}_x$ (m/s)	δ_0 and b_0	b (μm)	d_c (μm)	$\bar{v}_x$ (m/s)	δ_0 and r_0
30 50 70 90 100 150 200 300 400 500 600 700 800 900	1	1.14×10^{-5}	$\delta_0 = 1.0\times10^{-3}$ $b_0 = 1000$ μm	300	0.1 0.5 1.0 1.5 2.0 2.5 3.0	1.14×10^{-3}	$\delta_0=3.9\times10^{-4}$ $d_0=0.12$ μm
		3.18×10^{-5}	$\delta_0 = 1.6\times10^{-3}$ $b_0 = 600$ μm				
		1.14×10^{-3}	$\delta_0 = 9.0\times10^{-3}$ $b_0 = 110$ μm				
		1.03×10^{-2}	$\delta_0 = 2.6\times10^{-2}$ $b_0 = 40$ μm				

Table 5.5. Interpretation of the experimental results by Small (1974).

Particle diameter (μm)	R_0 (μm)	$\Delta\bar{t}$ (s)	Actual Retention time (s)	Taylor-Aris assumption satisfied?
0.088	3.3	1.2	Approximately 6000	Yes
0.091		1.2		Yes
0.109		1.4		Yes
0.176		2.3		Yes
0.234		3.1		Yes
0.357		4.7		Yes
0.500		6.6		Yes
0.721		9.5		Yes
0.810		10.7		Yes
1.099		14.5		Yes

Note:

1. This table is based on the data from Small (1974).

Table 5.6. Interpretation of the experimental results by Harter et al. (2000).

Porous media characteristics	CS fast	MS fast	FS fast	CS slow	MS slow
Velocity enhancement	19%	9%	0%	37%	11%
R_0 (μm)	467	135	62	467	135
$\Delta\bar{t}$ (s)	13206	110356	23276	13206	110356
Actual Retention time (s)	1217			12169	
Taylor-Aris assumption satisfied?	No	No	No	No	No

Note:

1. This table is based on the data from Harter et al. (2000).
2. CS: coarse sand, MS: medium sand, FS: fine sand, fast: high flow rate, slow: low flow rate.

Figures

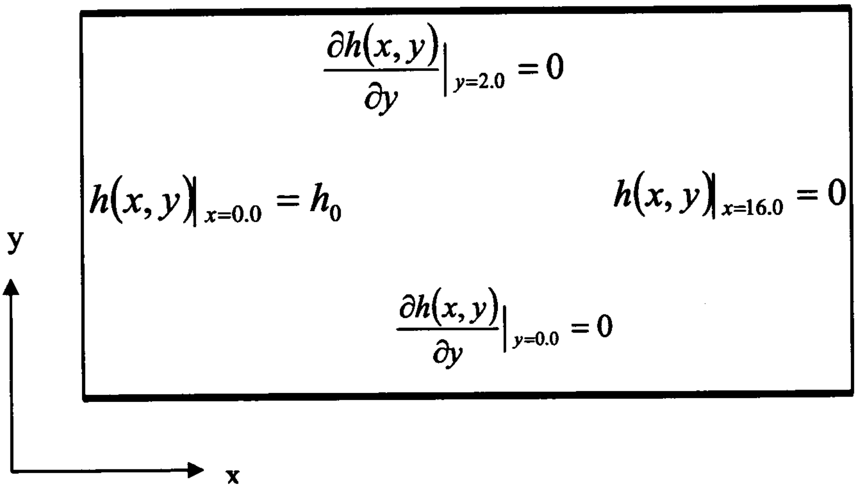

Figure 5.1. Schematic illustration of the coordinate system and boundary conditions for the flow and transport simulations.

(a)

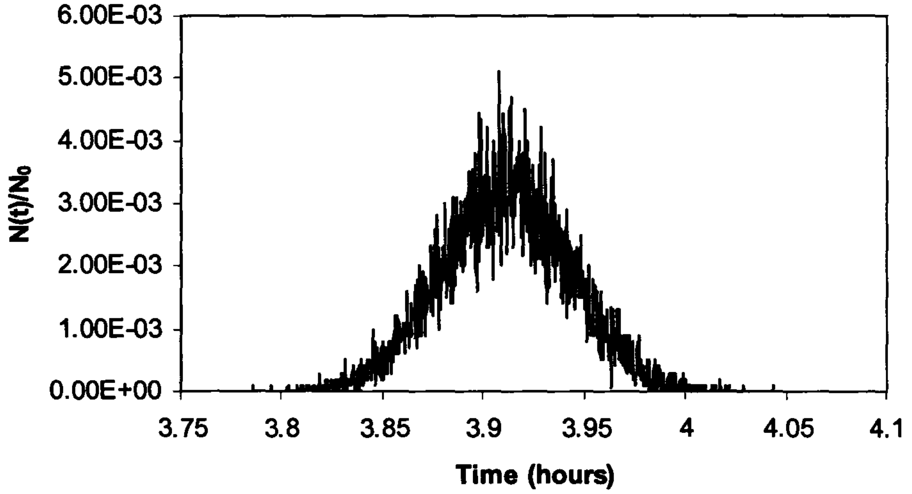

(b)

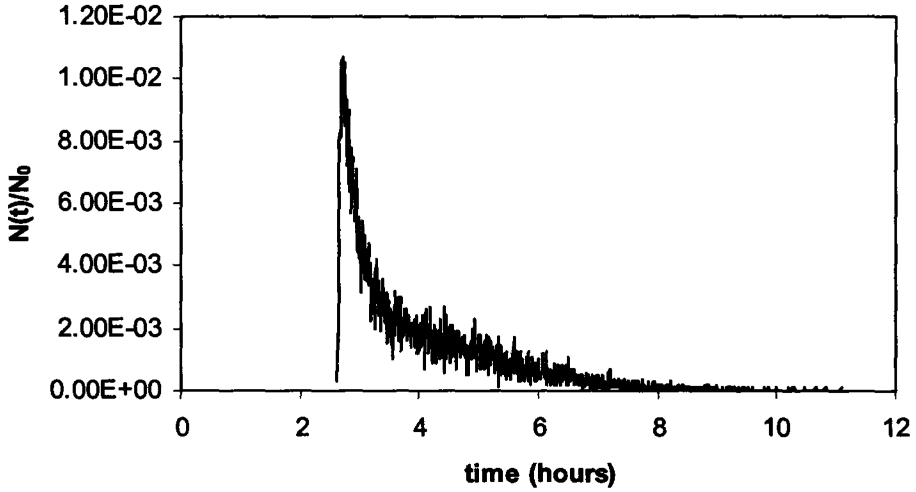

Figure 5.2. Typical Breakthrough curves for transport in parallel-plate fractures ($b = 300$ μm) for (a) a molecular-scale solute and (b) colloids. N(t) is the mass recovered at time t, and N_0 is the total mass injected at the inlet.

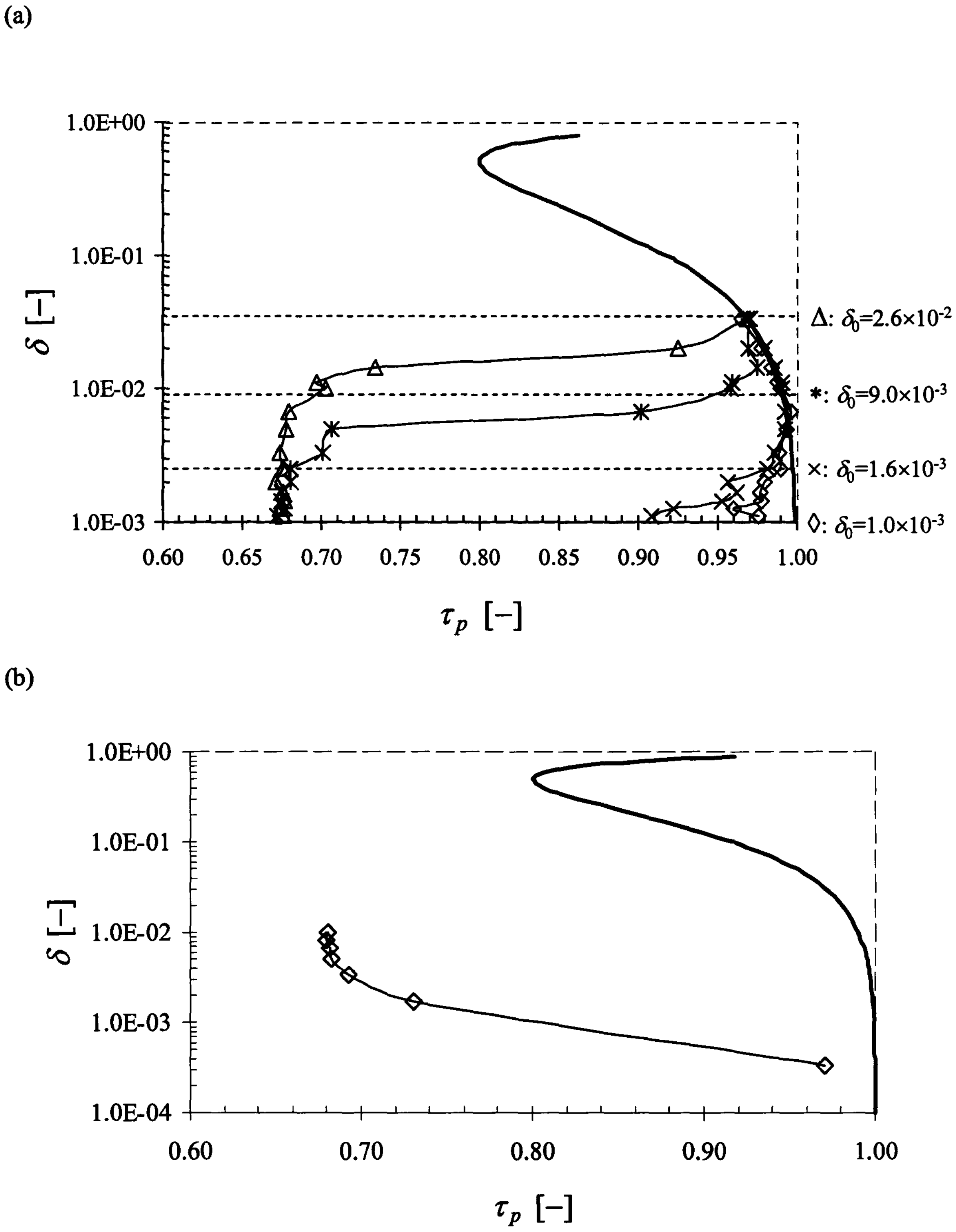
(a)
1.0E+00
1.0E-01
1.0E-02
1.0E-03
δ [–]
0.60
0.65
0.70
0.75
0.80
0.85
0.90
0.95
1.00
τ_p [–]
Δ: δ_0=2.6×10^-2
*: δ_0=9.0×10^-3
×: δ_0=1.6×10^-3
◊: δ_0=1.0×10^-3
(b)
1.0E+00
1.0E-01
1.0E-02
1.0E-03
1.0E-04
δ [–]
0.60
0.70
0.80
0.90
1.00
τ_p [–]

Figure 5.3. Dependence of δ on τ_p based on (a) Group I simulation results with constant r_c, —— : HDC calibration curve based on equation (5.16), ◊: simulation results with $\bar{v}_x = 1.14\times10^{-5}$ m/s, × simulation results with $\bar{v}_x = 3.18\times10^{-5}$ m/s, *: simulation results with $\bar{v}_x = 1.14\times10^{-3}$ m/s, Δ: simulation results with $\bar{v}_x = 1.03\times10^{-2}$ m/s; and (b) Group II simulation results with a constant b and $\bar{v}_x = 1.14\times10^{-3}$ m/s, —— : HDC calibration curve based on equation (5.16), ◊ simulation results.

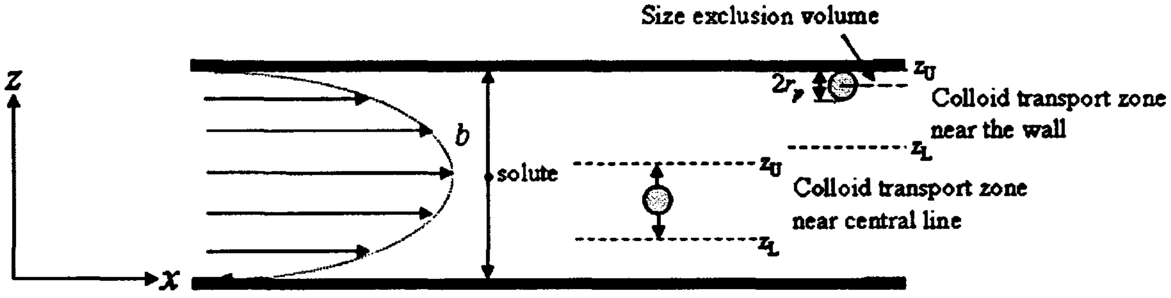

Figure 5.4. Schematic illustration of the velocity profile and the distance colloids and molecular-scale solutes traverse in the z direction before they exit a parallel-plate fracture.

(a)

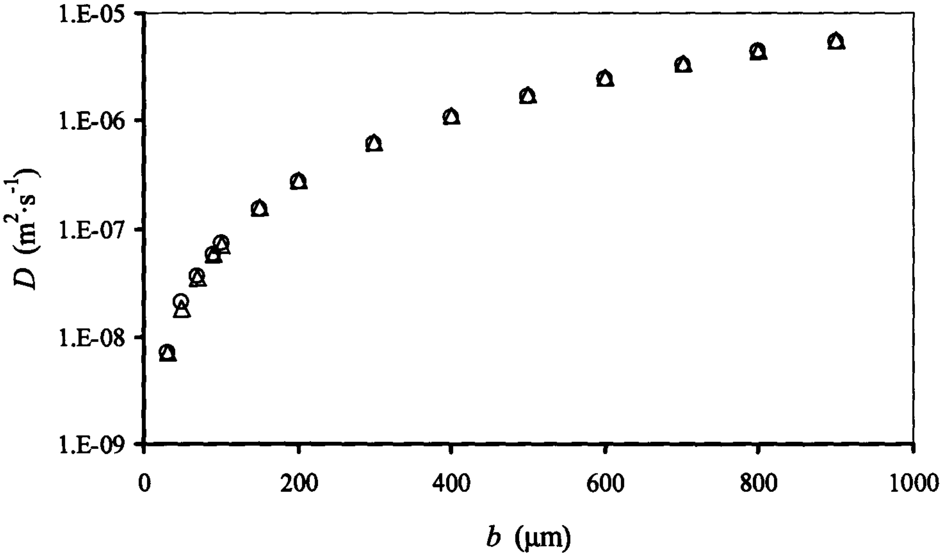

○: $D_{L,solute}$ based on the weighted moment method
Δ: D_{Taylor} from equation (5.19)

(b)

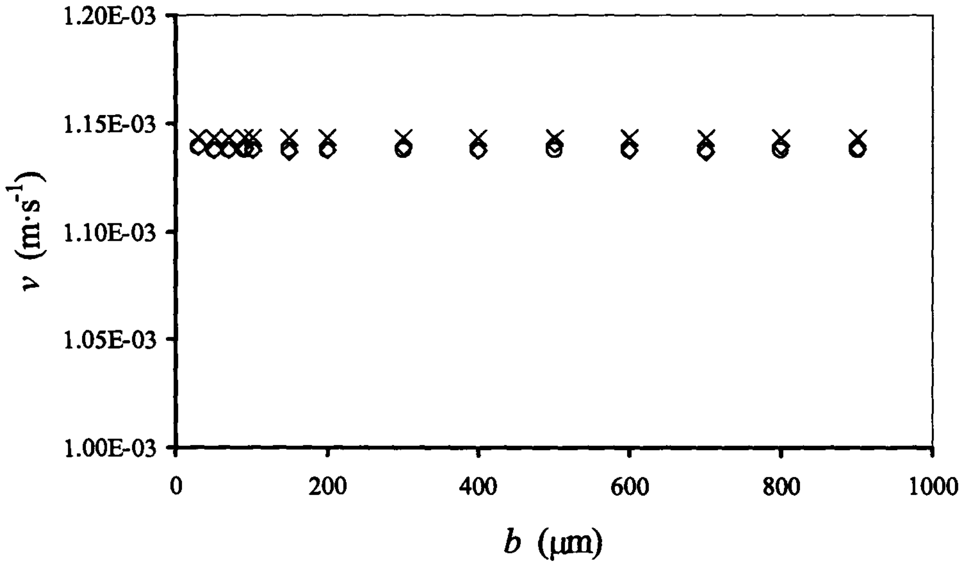

○: $v_{L,coll}$ based on the weighted moment method
◊: $\bar{v}_{s,peak}$ from equation (5.14b)
×: $\bar{v}_x$ the average fluid velocity

(c)

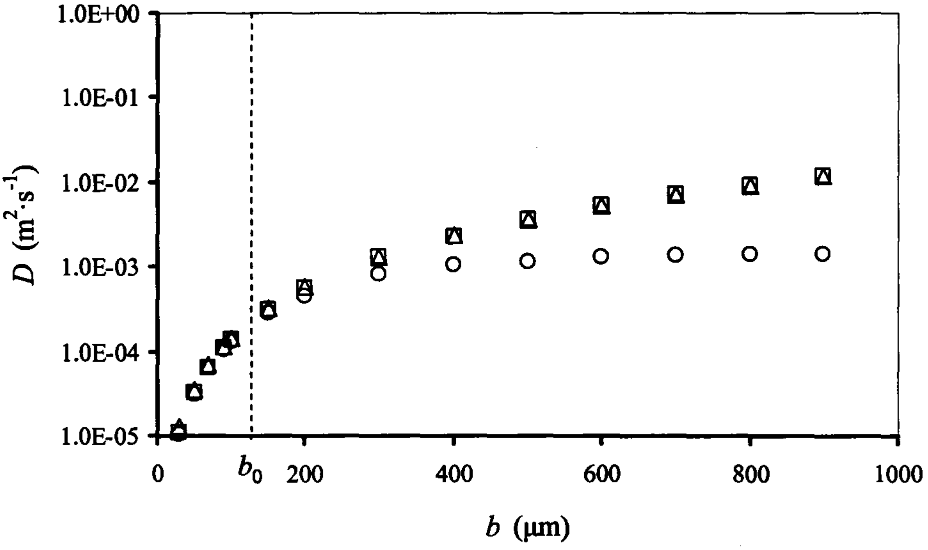

□: D_{eff} from equation (5.22)

○: $D_{L,coll}$ based on the weighted moment method

Δ: D_{Taylor} from equation (5.19)

(d)

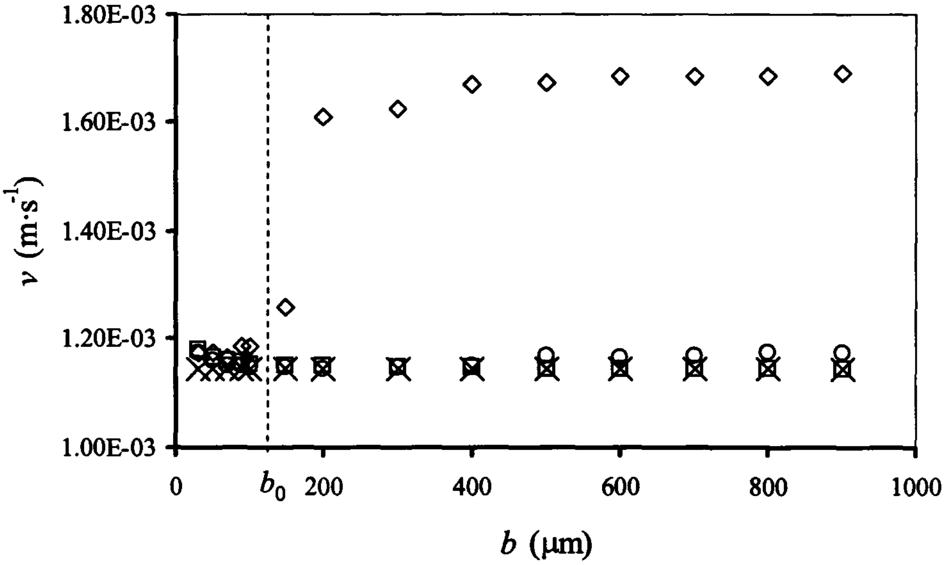

□: v_{eff} from equation (5.21)

○: v_L based on the weighted moment method

◊: $\overline{v}_{c,peak}$ from equation (5.14b)

×: $\overline{v}_x$ the average fluid velocity

Figure 5.5. A comparison of (a) the molecular-scale solute dispersion coefficients (*D*), (b) the molecular-scale solute transport velocities (*v*), (c) the colloid dispersion coefficients (D), and (d) the colloid transport velocities (*v*) in parallel-plate fractures for the Group I simulations with $\bar{v}_x = 1.14\times10^{-3}$ m·s^{-1}.

a)

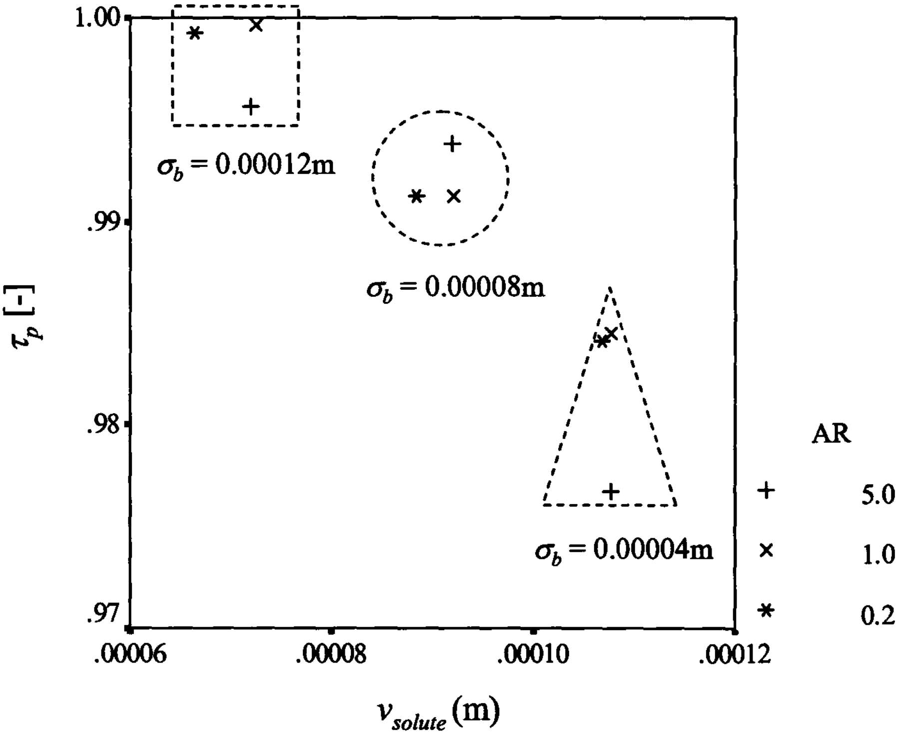
1.00
.99
.98
.97
τ_p [-]
.00006
.00008
.00010
.00012
v_{solute} (m)
σ_b = 0.00012m
σ_b = 0.00008m
σ_b = 0.00004m
AR
+ 5.0
× 1.0
* 0.2

b)

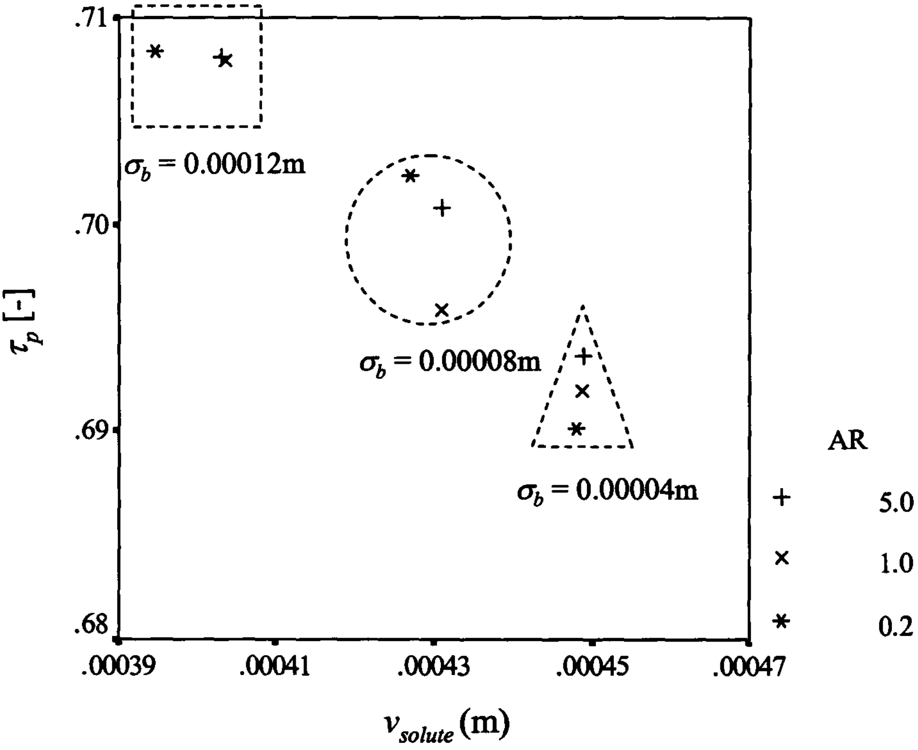
.71
.70
.69
.68
τ_p [-]
.00039
.00041
.00043
.00045
.00047
v_{solute} (m)
σ_b = 0.00012m
σ_b = 0.00008m
σ_b = 0.00004m
AR
+ 5.0
× 1.0
* 0.2

c)

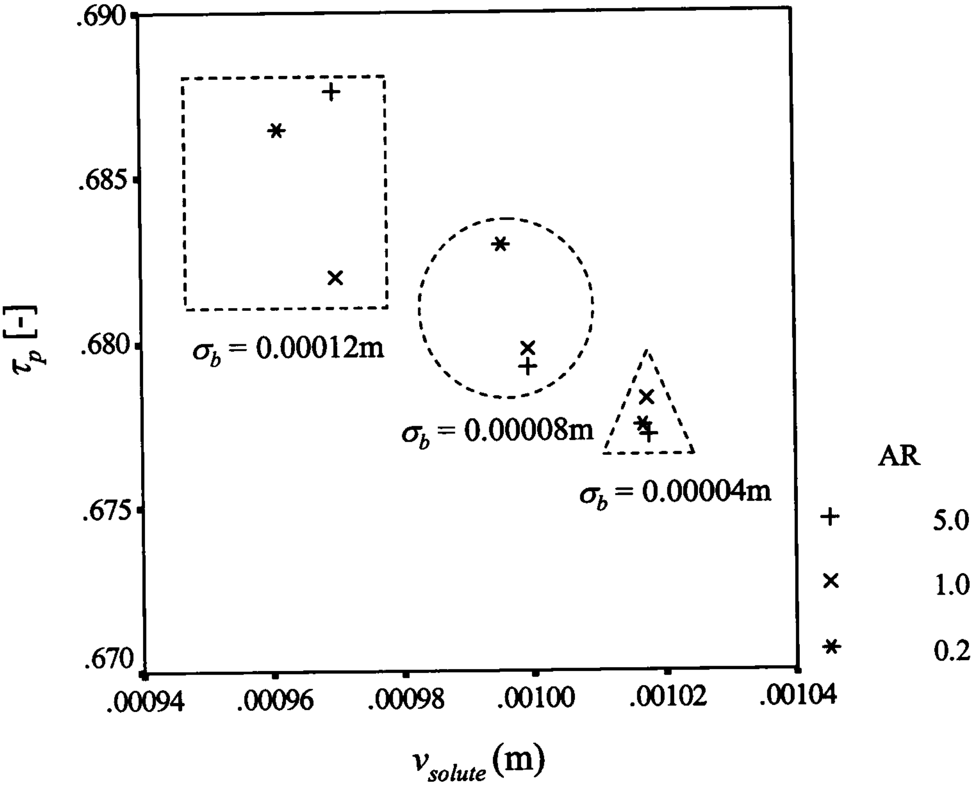

Figure 5.6. The effect of CoV and AR on τ_p, where (a) μ_b = 300μm, (b) μ_b = 600 μm, and (c) μ_b = 900 μm.

(a)

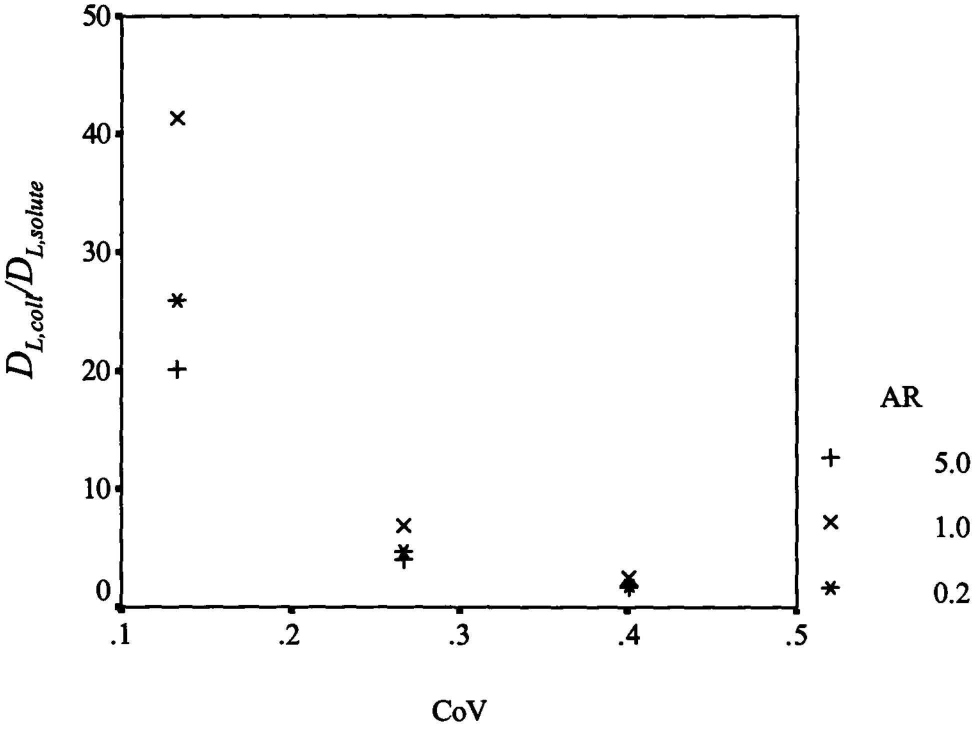
50
40
30
20
10
0
.1
.2
.3
.4
.5
CoV
$D_{L,coll}/D_{L,solute}$
AR
+ 5.0
× 1.0
* 0.2

(b)

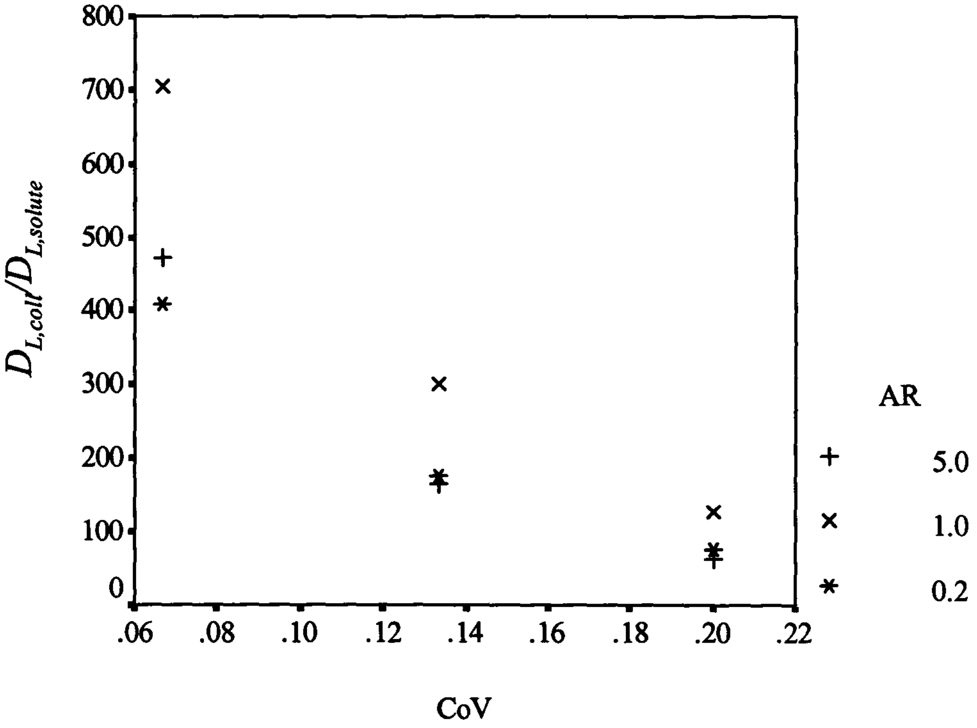
800
700
600
500
400
300
200
100
0
.06
.08
.10
.12
.14
.16
.18
.20
.22
CoV
$D_{L,coll}/D_{L,solute}$
AR
+ 5.0
× 1.0
* 0.2

(c)

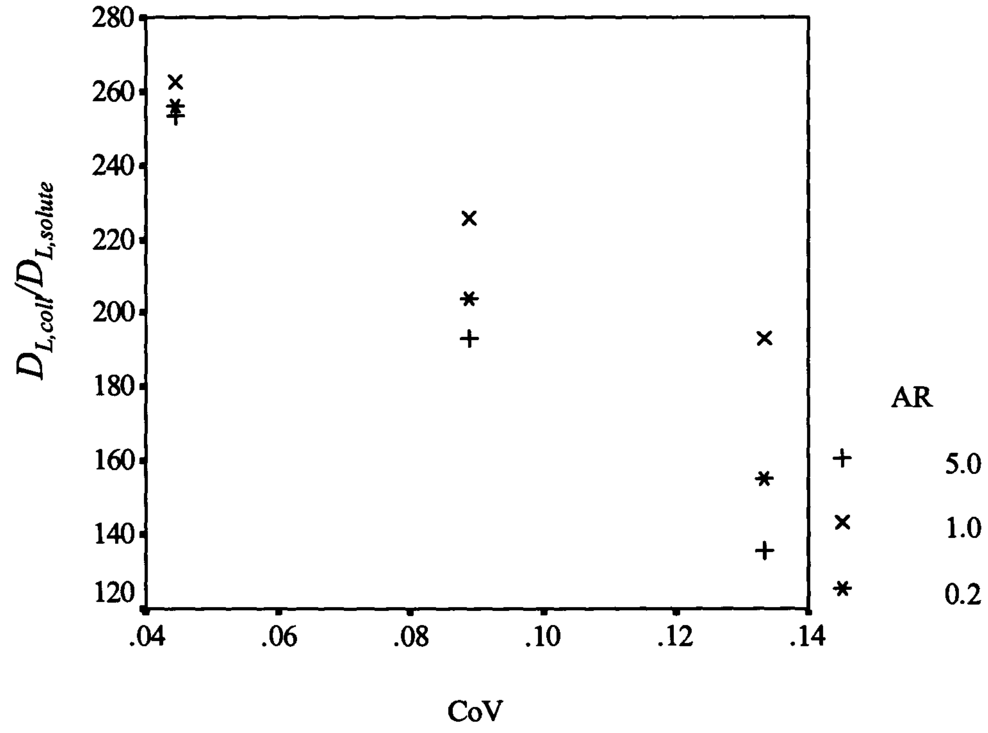

Figure 5.7. A comparison of colloid and solute dispersion coefficients in variable-aperture fractures, where (a) μ_b = 300μm, (b) μ_b = 600 μm, and (c) μ_b = 900 μm.

Chapter 6 Colloid transport in laboratory-scale variable-aperture fractures: Visualization experiments and modeling results

Abstract

A combination of physical experiments, numerical simulations and visualization techniques was employed to investigate colloid transport processes and the impact of aperture field variability, specific discharge, and ionic strength on these processes. The mean colloid transport velocity and dispersion coefficient were obtained by fitting the analytical solution of the one-dimensional advection-dispersion equation to the measured breakthrough curves. Two significant features were observed from the visual images of the colloid transport experiments: (1) colloids are transported along preferential pathways; and bypass some aperture regions, and (2) the colloid plume is irregular in shape, and becomes more irregular with increasing specific discharge, indicating non-Fickian transport. It is therefore postulated that the dispersivity cannot be completely determined by the aperture field statistics alone; it is also a function of specific discharge. The colloid recovery in each fracture was found to increase with increasing specific discharge. For all specific discharges, the colloid recovery was found to be larger in F2 and F3 than that in F1. This pattern is consistent with the relative magnitude of the arithmetic mean apertures of these three fractures, that is, $\mu_{b,F2}$ and $\mu_{b,F3}$ are similar, and both significantly larger than $\mu_{b,F1}$. The effect of ionic strength on colloid recovery did not follow the theoretical premise that colloid recovery increases with decreasing ionic strength. These observations indicate that the transport step (the step in which the colloids are transported from the bulk fluid to the vicinity of the fracture wall), and not the attachment step, plays the dominant role in the colloid sorption process. It was also found that the mean transport velocities and dispersion coefficients of the colloids are larger than those of the solutes in F3 (CoV=0.29), but similar to those of the solutes in F1 (CoV=0.78) and F2 (CoV=0.71). This supports the results of the numerical simulations, which indicated that

$v_{f,coll}/v_{f,solute}$ and $D_{f,coll}/D_{f,solute}$ decrease with increasing CoV. These findings have significant implications for the interpretation of field data gathered from fractured site investigations, and the prediction of colloid transport in fractured systems.

6.1. Introduction

An increasing interest in the transport of colloids and nano-particles (abiotic and biotic) in fractured media is motivated by several factors. Fractured geological formations are common sources of drinking water throughout the world. These same fractures also provide significant pathways for both chemical and particulate constituents to contaminate groundwater systems (Allen and Morrison, 1973). Colloids can be appropriate tracers to study the complex flow fields that develop in fractures (e.g., flow channeling) (Harvey, 1997). In their safety assessment of nuclear waste repositories, researchers have found that the sorption of radionuclides on colloids present in groundwater may significantly influence their transport through fractured media (van der Lee et al., 1992; Smith and Degueldre, 1993; Grindrod, 1993). Finally, field- and lab-scale bioremediation and bioaugmentation experiments have been conducted in fractured media to study the use of microbes to remediate contaminated fracture aquifers (e.g., Yager et al., 1997; McLinn and Rehm, 1997; Ross et al., 2001; Ross and Bickerton, 2002; Hill and Sleep, 2002). All of these challenges require a good understanding of the processes governing the transport of colloids under the specific physical, chemical, and biological conditions present in fracture systems. Relatively few theoretical and experimental efforts have been conducted to investigate colloid transport in fractures to date, however, and certain mechanisms remain unclear.

The scale of a single variable-aperture fracture, which is the basic constructive unit of fractured media, is an appropriate starting point for studies of the more complex mechanisms governing colloid transport in fracture networks. A host of complex and interacting processes, including advection, dispersion, attachment/detachment, straining, size/anion exclusion, sedimentation, etc., control colloid transport in fractures. The factors controlling these processes include, among others, fracture wall roughness, fracture wall surface chemistry, chemistry of the water matrix, colloid characteristics, and hydrodynamics. These factors are both complex and coupled (Ryan and Elimelech, 1996). When considering the effect of fracture wall roughness on colloid transport, it is necessary to distinguish between macroscopic- and microscopic- scale roughness. The macroscopic roughness determines the macrosopic aperture field variability (heterogeneity, anisotropic nature of the aperture field), and thus determines the hydrodynamics of the aperture field, including the occurrence of preferential flow paths (Rasmuson and Neretnieks, 1986), mobile and immobile regions within the aperture field (Dijk et al., 1999), and the velocity distribution across the aperture (Dijk et al., 1999; Brush and Thomson, 2003). These hydrodynamic properties, in turn, contribute to colloid transport. Additionally, the hydrodynamic shear (e.g., Hubbe, 1985; Hubbe, 1987; Degueldre et al., 1989; Sharma et al., 1992) and the occurrence of eddies and turbulent flow in the vicinity of the fracture walls (Dijk et al., 1999; Brush and Thomson, 2003) may influence the colloid attachment. Micro-scale roughness, on the other hand, plays its role mainly through influencing colloid attachment/detachment (Ryan and Elimelech, 1996). However, no complete theories exist for the prediction of colloid attachment onto real, rough surfaces.

Straining and sorption are among the primary mechanisms of colloid removal from groundwater in fractured media. Straining refers to the trapping of particles in down-gradient pore throats that are too small to allow particle passage (McDowell-Boyer et al., 1986). In principle, colloid straining in fractures primarily depends on the size of colloids relative to the aperture, however dead-end fractures also play a role in this process. Kosakowski (2004) conducted field experiments in a shear fractured zone, and found that the recoveries for different colloid sizes (from 50 nm to 500nm) decreased systematically with increasing size. They proposed that straining (referred as mechanical filtration) and/or gravitational settling are possible mechanisms for this phenomenon. Research on the effect of straining in fractured media is still in its infancy, and has not been addressed quantitatively to the knowledge of these authors.

The sorption process is typically divided into two sequential steps: transport and attachment (Elimelech and O'Melia, 1990). The rate at which each of these two steps occurs determines the overall kinetics of particle sorption. In the first step, a colloid is transported from the bulk fluid to the vicinity of a stationary surface. Transport of Brownian (submicron) particles is dominated by convection and diffusion, while that of larger (non-Brownian) particles is controlled by physical forces arising from gravity and fluid drag, and by interception due to the finite size of the particles (Yao et al., 1971; Tien, 1989). For colloids with a density different from the suspending fluid, gravitational sedimentation can also cause colloids to deviate from fluid streamlines and collide with the media surface. However, the role of sedimentation is not well defined for colloid transport in fractures.

Attachment, on the other hand, is dominated by the various chemical-colloidal interactions that act between particles and fracture wall surfaces at short distances, including Lifshitz-van der Waals forces, electrostatic forces, and acid-base interactions (Bos et al., 1999). These, in turn, are controlled by the surface chemistry of the colloids and geological media, and the chemistry of the water matrix. Previous research has demonstrated that attachment and detachment are influenced by solution ionic strength through the effect of electrostatic interactions, and colloid attachment to grain surfaces increased with increasing ionic strength (e.g., Fontes et al., 1991; McDowell-Boyer, 1992; Shonnard et al., 1994; Tan et al., 1994). However, Elimelech et al. (2000) observed that colloid attachment decreased with increasing ionic strength, and argued that the ionic strength plays an insignificant role in the attachment/detachment process. In addition, experimental observations of colloid transport are not always in agreement with colloid attachment theory (e.g., Elimelech and O'Melia, 1990). Therefore, the critical role of solution chemistry in the attachment step is poorly understood. Hydrodynamics also play an important role in the process of attachment/detachment. An increase in flow velocity increases hydrodynamic shear, which mobilize colloids. Degueldre et al. (1989) showed that groundwater flow in fractured media may produce velocities capable of causing colloid mobilization.

Early breakthrough of colloids relative to conservative solute tracers in fractures has been demonstrated by several investigations; however, different theories have been proposed to interpret these observations. For example, in a series solute and colloid field tracer experiments performed in fractured, fine-grained glacial tills (McKay et al., 1993; McKay et al., 1999), and in a highly weathered shale saprolite (McKay et al., 2000), it was found that the colloidal tracers arrived much earlier than the nonreactive solute tracers (bromide, chloride, or fluorescent dye), typically by factors of 10 to 100. The authors largely ascribed this to diffusion of the solutes, but not the colloids, into the fine pore structure. Reimus et al. (1995) found that synthetic colloids always arrived earlier than a non-sorbing solute (iodide) in their transport experiments conducted in a fracture system. They hypothesized that this effect was due to the larger size of colloids relative to solutes, which results in the colloids diffusing too slowly to enter the slowest velocity regions along the rough fracture walls. Analytical analyses (James and Chrysikopoulos, 2003) and numerical simulations (e.g., Zheng et al., 2008c) have demonstrated that size and/or charge exclusion can lead to faster colloid breakthrough relative to solute. In reality, some combination of these factors, depending on the site-specific conditions, likely causes the differential transport of solutes and colloids. These seeming discrepancies highlight the need for laboratory experiments with isolated factors to provide insights to the roles of different mechanisms on the differential transport of colloids and solutes.

The objective of this research was to investigate the role of selected factors (i.e., aperture field variability, specific discharge, and ionic strength) on colloid transport in laboratory-scale single variable-aperture fractures under controlled chemical and physical conditions.

Colloid transport experiments were conducted in three variable-aperture fractures with different aperture fields, using water matricies of varying ionic strengths, under a range of specific discharges. Colloid transport and retention was assessed by measuring the effluent colloid concentration over time. The data were interpreted with the aid of conservative tracer (bromide) studies, and one-dimensional analytical advection-dispersion analysis. Three dimensional numerical simulations were conducted to aid with the interpretation of the experiments and differentiate between, the roles of sedimentation, straining, and attachment/detachment in colloid transport through fractures.

6.2. Materials and Methods

6.2.1 Experimental Investigations

A 3^3 factorial experiment was designed to investigate the effect of aperture field, specific discharge, and ionic strength on colloid transport in single fractures (Table 6.1). Three synthetic fracture replicas were fabricated based on the method presented by Dickson (2001), and an impervious epoxy (STYCAST 1264 A/B, Emerson & Cuming) was employed thus negating any matrix effects on flow and transport in the synthetic fractures. The aperture fields were characterized through a series of hydraulic and solute transport tests in combination with the light transmission technique. The hydraulic and tracer experiments are described in Zheng et al. (2008a).

6.2.1.1 Aperture Field Characterization

Each of the three fracture replicas, hereafter referred to as F1, F2 and F3, were measured directly using the light transmission technique described by Renshaw et al. (2000). The technique is based on measuring the intensity of light transmitted through the transparent fracture cast, filled first with Milli-Q water and subsequently dyed Milli-Q water, at each pixel on a digital image. A light-absorbing dye (Acid Red 052, Spectra Colors Corp.) was used to dye the Milli-Q water. A scientific grade charge-coupled device (CCD) camera ($\mathrm{CoolSNAP_{ES}}$, Photometrics) was employed to shoot 100 images, 50 Milli-Q-filled and 50 dye-filled, which were then averaged. The light intensity at each pixel was then related to the aperture at that pixel through the Beer-Lambert Law. The pixel size of each measured aperture field is dependent on the dimensions of the fracture, and is listed in Table 6.2. The reader is referred to Renshaw et al. (2000) for a discussion of the light transmission technique and Detwiler et al. (1999) for a discussion of the associated error.

The Beer-Lambert law describes the absorbance of monochromatic light by a dyed solution as a function of the distance through the solution (b) and the dye concentration (C_{dye}), and is given as:

$$A_{ij} = ln\left(I_{cl_{ij}} / I_{dye_{ij}}\right) = \varepsilon C_{dye,ij} b_{ij} \tag{6.1}$$

where A_{ij} [-] is the absorbance, I_{clij} [$M \cdot L^2 \cdot t^{-3} \cdot sr^{-1}$] and I_{dyeij} [$M \cdot L^2 \cdot t^{-3} \cdot sr^{-1}$] are the light intensities transmitted through the clear and dyed solutions respectively, ε [$L^2.mol^{-1}$] is the absorptivity of the light-absorbing solute, and i and j refer to the row and column index of each pixel in the images. If the light source is polychromatic, the linear relationship between absorbance and concentration (equation 6.1) is only approximate. Despite efforts to remove the influence of polychromatic light sources by reducing the measured wavelength with a band-pass filter (585nm ± 20 nm, HQ585/40, Chroma Technology Corp.) on the camera lens, some nonlinearity remained. Slight nonlinearity in dye absorbance results in aperture measurement errors that increase with dye concentration. However, reducing dye concentration results in an increase in random errors due to signal noise (Detwiler et al., 1999). Therefore, a solution concentration of 0.0126 g/L was chosen to minimize nonlinearity in dye absorbance, and the random errors were reduced through averaging 50 images of each field. The root mean square error (RMSE) of the aperture field measurement ranges from 0.3% to 0.9% under these conditions, and are listed in Table 6.2. Figure 6.1 illustrates the measured aperture fields for F1, F2 and F3 respectively, and Table 6.2 gives the aperture field statistics for each of these fractures. A comparison of these measured aperture field statistics with those obtained through hydraulic and solute tracer tests provide further experimental support to the conclusion presented by Zheng et al. (2008a) (Chapter 3 of this thesis), that the mass balance aperture represents the arithmetic mean of the aperture field.

6.2.1.2 Colloid Transport Experiments

Carboxylate-modified (CM) nile red fluorescent microspheres with excitation/emission maxima of 535/575 nm (Fluospheres, Molecular Probes Inc.) were employed as the colloid tracers. These microspheres are spherical and monodisperse with a diameter of 1 μm, and have a specific density of 1.05. The surface of these microspheres is highly charged, and relatively hydrophilic. The CM microspheres are coated with a hydrophilic polymer containing multiple carboxylic acids, which gives them a negative charge at pHs greater than 5. The surface charges range from 0.1 to 2.0 milliequivalents/gram, and therefore, these colloids are stable when present in relatively high concentrations of electrolytes (up to 1 M univalent salt). Univalent salt (NaBr) solutions, with ionic strengths of 0.01, 0.001 and 0.0001 respectively, were selected to prepare the solution in order to maintain stability of the microspheres throughout the experiments. The pH of the NaBr solutions was approximately 7.7. Prior to each experiment, the microsphere vial was sonicated for two minutes to maintain the micospheres in a monodisperse state. The bright fluorescent dye contained inside each microsphere enables their detection by Fluorescence Spectrophotometer with a detection limit on the order of 10^5 particles/mL. The samples collected from the tracer tests were analyzed using a Fluorescence Spectrophotometer (Cary Eclipse, Varian).

The experimental setup, illustrated in Figure 6.2, involved sealing the two opposite long edges of each fracture replica to serve as no-flow boundaries and operating the remaining two edges as constant-pressure boundaries (refer to Zheng et al., 2008a for details). The fractures were oriented horizontally for all characterization and colloid experiments. The recirculation systems for the upstream and downstream flow manifolds are illustrated in Figure 6.2 (a), and consist of Teflon tubing strung through two bolt holes; one located at each the highest and lowest points of the manifold. The solution in the upstream and downstream flow manifolds was re-circulated using a peristaltic pump (MasterFlex, L/S 7543-20) throughout the duration of each experiment.

The procedure for conducting the colloid tracer experiments involved first saturating the fracture plane with degassed deionized water equilibrated to room temperature. A carbon dioxide flush was conducted prior to fracture saturation to remove any air present in the system. Next, in order to investigate the effect of ionic strength on colloid attachment/detachment, the NaBr solution was pumped through the fracture at a specific discharge of 1.09 mm/s for approximately 5 hours (at least 20 pore volumes) to replace the distilled water with the NaBr solution throughout the entire aperture field. The colloid tracer tests then began through establishing an exponentially decreasing input function in the upstream flow manifold (Zheng et al., 2008a). Samples were collected at E2 (Figure 6.2(a)) every one minute until the effluent colloid concentration was below the detection limit of the Fluorescence Spectrophotometer. Each time a colloid tracer test was finished, the fracture replica was separated, and each fracture wall was put in the ultrasonic sonicator for at least half an hour to remove any attached colloids. The fracture walls were then re-assembled for the next colloid tracer test. Each time a fracture plane was re-saturated, hydraulic tests were performed to ensure that the equivalent hydraulic aperture remained unchanged.

A visualization system was designed to visualize the colloid transport process in the fracture replicas (Figure 6.3). This system employed an excitation light source and a camera (CoolSNAP$_{ES}$, Photometrics) with a band-pass emission filter (HQ585/40m, Chroma Technology Corp.) attached to the lens. The excitation source consists of a grid of 3 × 6 Light-emitting Diode (LED, Luxeon V Star, Future Electronics Inc.). The LED has a bandwidth from 520 nm to 580 nm with maximum light intensity at 550 nm. Each LED is covered by a cleanup excitation filter (510nm ± 10nm, D510/20x, Chroma Technology Corp.) to narrow down the bandwidth of the excitation light source. A light diffuser is located above the excitation light source to make the excitation light as uniform as possible. In order to reduce the errors caused by the photoleaching effect of the fluorescent colloid as much as possible, the excitation light source was turned on just before each picture was taken, and turned off immediately afterwards.

6.2.1.3 Colloid Transport: One Dimensional Simulations

Assuming that the experimental fractures can be represented by parallel plates with an 'equivalent aperture', the advection-dispersion equation (ADE) governing tracer transport in a one-dimensional parallel-plate fracture was used to model colloid transport in single fractures:

$$\frac{\partial C(x,t)}{\partial t} = D_{f,coll}\frac{\partial^2 C(x,t)}{\partial x^2} - v_{f,coll}\frac{\partial C(x,t)}{\partial x} - \frac{2}{\mu_b}\frac{\partial S(x,t)}{\partial t} \tag{6.2a}$$

$$C(x,0) = 0,\ x > 0 \tag{6.2b}$$

$$\left.\frac{\partial C(x,t)}{\partial x}\right|_{(\infty,t)} = \text{(finite)},\ t \geq 0 \tag{6.2c}$$

$$C(0,t) = C_0 \exp(-\lambda t) \tag{6.2d}$$

where equation (6.2d) is the exponentially decreasing input function at the fracture inlet, x [L] is the distance along the x-axis in the direction of flow, μ_b [L] is the arithmetic mean aperture, t [T] is the time from the beginning of the tracer test, $C(x,t)$ [particles·L^{-3}] is the colloid concentration at distance x and time t, S [particles·L^{-2}] is the concentration of colloids sorbed on the fracture wall, $v_{f,coll}$ [L·T^{-1}] is the mean transport velocity of colloids, $D_{f,coll}$ [L^2·T^{-1}] is the hydrodynamic dispersion coefficient, C_0 [particles·L^{-3}] is the concentration at x = 0 and t = 0 and λ [T^{-1}] is the decay constant in the exponential function.

The last term on the right hand of equation (6.2a) represents the mass transfer of colloids between the aqueous phase and fracture walls. At the microsacle, the interaction of colloids with fracture walls is influenced by various physico-chemical mechanisms, such as van der Waals forces, electric double layer forces, and Brownian motion. At the macroscale, however, the mass transfer is modeled with a lumped coefficient. For linear equilibrium and irreversible kinetic sorption models, the colloid concentration in the aqueous phase and on the fracture walls is related respectively by:

$$S = k_e C \tag{6.3a}$$

$$\frac{\partial S}{\partial t} = k_{ir} C \tag{6.3b}$$

where k_e [L] is the distribution coefficient, and k_{ir} [$L \cdot t^{-1}$] is the first-order decay rate constant. It is assumed that equilibrium sorption, kinetic irreversible sorption or both occurs in colloid transport process in fractures. Upon substitution of equations (6.3a) and (6.3b) into equation (6.2a), the governing differential equation becomes

$$R\frac{\partial C(x,t)}{\partial t} = D_{f,coll}\frac{\partial^2 C(x,t)}{\partial x^2} - v_{f,coll}\frac{\partial C(x,t)}{\partial x} - \frac{2k_{ir}}{b}C \tag{6.4a}$$

with

$$R = 1 + \frac{2k_e}{\mu_b} \tag{6.4b}$$

where R [-] is the retardation factor.

The solution to (4a) with the boundary and initial conditions (2b), (2c), and (2d) is (van Genuchten, 1981):

$$\begin{aligned} C(x,t) = C_0\, exp(-\lambda t)\Bigg\{ & \frac{1}{2} exp\left[\frac{(v_{f,coll} - \xi)x}{2D_{f,coll}}\right] erfc\left[\frac{Rx - \xi t}{\sqrt{4D_{f,coll}Rt}}\right] \\ & + \frac{1}{2} exp\left[\frac{(v_{f,coll} + \xi)x}{2D_{f,coll}}\right] erfc\left[\frac{Rx + \xi t}{\sqrt{4D_{f,coll}Rt}}\right]\Bigg\} \end{aligned} \tag{6.5a}$$

with

$$\xi = v_{f,coll}\left[1 + 4D_{f,coll}(2k_{ir}/b - \lambda R)/v_{f,coll}^{\;2}\right]^{1/2} \tag{6.5b}$$

and (Tang et al., 1981):

$$D_{f,coll} = \alpha_L v_{f,coll} + D^{*}_{coll} \tag{6.5c}$$

$$D^{*}_{coll} = \frac{kT}{3\pi\mu d_c} \tag{6.5d}$$

where α_L [L] is the longitudinal dispersivity, $D_{coll}{}^{*}$ [$L^2 \cdot t^{-1}$] is the colloid diffusivity in water, k [$M \cdot L^2 \cdot t^{-2} \cdot T^{-1}$] is the Boltzman constant, T [K] is the absolute temperature, η [$M \cdot L^{-1} \cdot t^{-1}$] is the fluid dynamic viscosity, and d_c [L] is the colloid diameter.

Due to the significant volume of the flow manifolds at the upstream and downstream ends of each experimental fracture, the measured concentration was adjusted to represent the actual concentration of the solute entering and exiting the fracture. The upstream manifold was modeled using a mass balance on a completely mixed continuous flow reactor:

$$QC_{in}(t) - QC_{out}(t) = V_{ol,up}\frac{dC_{out}(t)}{dt} \tag{6.6a}$$

$$C_{out}(t)\big|_{t=0} = \frac{M}{V_{ol,up}} \tag{6.6b}$$

where Q ($L^3 \cdot T^{-1}$) represents the flow rate through the system, $C_{in}(t)$ (particles$\cdot L^{-3}$) represents the concentration of the colloids entering the manifold at time t, $C_{out}(t)$ (particles$\cdot L^{-3}$) represents the concentration of the colloids exiting the flow manifold at time t (i.e., entering the fracture), $V_{ol,up,}$(L^3) represents the combined volume of the upstream manifold and re-circulation system, and M (particles) is the number of colloids injected. Equation (6.6b) assumes that the colloid concentration at t=0 is uniform in the upstream manifold. The solution to equations (6.6a) and (6.6b) is:

$$C_{out}(t) = \frac{M}{V_{ol,up}} exp\left(-\frac{Q}{V_{ol,up}}t\right) \tag{6.7}$$

Equation (6.7) indicates that the colloid concentration in the upstream manifold decreased exponentially over the course of each tracer experiment. Therefore, the constants C_0 and λ in equations (6.2) and (6.5) are given by:

$$\lambda = \frac{Q}{V_{ol,up}} \tag{6.8a}$$

$$C_0 = \frac{M}{V_{ol,up}} \tag{6.8b}$$

The authors have shown before that the exponentially decreasing input function (7) is a good approximation of the actual input function (Zheng et al., 2008a).

Similarly, the measured concentration of each sample taken from the downstream manifold was adjusted using equation (6.9) to reflect the concentration exiting the fracture.

$$C_{eff-frac}(t) = \frac{V_{ol,down}}{Q}\left(\frac{C_{eff}^{t+\Delta t} - C_{eff}^{t-\Delta t}}{2\Delta t}\right) + C_{eff}^{t} \tag{6.9}$$

where $C_{eff\text{-}frac}$ (particles·L^{-3}) represents the solute concentration exiting the fracture at time t, C_{eff} (particles·L^{-3}) represents the concentration measured in the effluent manifold at time t, and Δt (T) is the time between sampling events, $V_{ol,down}$ (L^3) represents the combined volume of the upstream manifold and re-circulation system.

Additionally, all effluent samples were corrected for time due to the tubing volume, V_{E1-E2}, (see Figure 6.2a) between the downstream flow manifold and the sampling point as follows:

$$t_{corr} = t_{mea} - \frac{V_{E1-E2}}{Q} \tag{6.10}$$

where t_{corr} (T) represents the corrected time of each sampling event and t_{mea} (T) represents the time from the start of the experiment at which the sample was actually taken.

The adjusted experimental breakthrough curves were fit to equation (6.5a) using PEST (Watermark Numerical Computing, Version 9.0). Both the dispersivity (α_L) and the specific discharge (v) were employed as the fitting parameters.

It is noteworthy that an "effective volume", rather than the actual volume, of the downstream re-circulation system was employed in equation (6.9) as there was likely a dead volume present in the downstream flow manifolds of F2 and F3. When the effluent concentration profiles from F1 were adjusted using the actual manifold volume of 17 mL in equation (6.9), the analytical and experimental breakthrough curves matched well. However, for F2 and F3, the simulated breakthrough curves fit the experimental observations best when the values of $V_{ol,down}$ in equation (6.9) were reduced to 17 mL. Since the pump capacity and tubing lengths of the downstream recirculation systems are identical for F1, F2, and F3, it is reasonable that the "effective volume" of the downstream manifolds, which represent the volumes completely mixed by the recirculation system, are also identical.

6.2.2 Numerical Investigation

Numerical simulations were conducted with the intent to provide insight into the conceptual modeling of colloid transport through variable-aperture fractures, and aid in the interpretation of the physical model experiments.

6.2.2.1 Flow Field Calculation

The steady state flow field in each fracture plane was obtained by solving the Reynolds equation using a fully implicit finite difference technique (Chrysikopoulos and James, 2003):

$$\frac{\partial}{\partial x}\left[b^3(x,y)\frac{\partial h(x,y)}{\partial x}\right]+\frac{\partial}{\partial y}\left[b^3(x,y)\frac{\partial h(x,y)}{\partial y}\right]=0 \qquad (6.11a)$$

$$\left.\frac{\partial h(x,y)}{\partial y}\right|_{y=0.0}=0 \qquad (6.11b)$$

$$\left.\frac{\partial h(x,y)}{\partial y}\right|_{y=y_w}=0 \qquad (6.11c)$$

$$h(x,y)\big|_{x=0.0}=h_0 \qquad (6.11d)$$

$$h(x,y)\big|_{x=x_L}=0 \qquad (6.11e)$$

where x [L] is the coordinate along the fracture length in the flow direction, x_L [L] is the fracture length, y [L] is the coordinate along the fracture width perpendicular to the direction of flow, y_w [L] is the fracture width, $h(x,y)$ [L] is the local hydraulic head, and $b(x,y)$ [L] is the local fracture aperture. The boundary conditions described in equation (6.11) represent no-flow boundaries on the sides of a horizontal fracture, and constant head boundaries at the upstream and downstream ends. The equivalent aperture between adjacent elements, in both the x- and y- directions, is approximated by the harmonic mean aperture of the two elements (Reimus, 1995). The average velocity component in both x- and y- directions are calculated by (Chrysikopoulos and James, 2003):

$$\bar{v}_x = -\frac{\gamma b^2(x,y)}{12\eta}\frac{\partial h(x,y)}{\partial x} \tag{6.12a}$$

$$\bar{v}_y = -\frac{\gamma b^2(x,y)}{12\eta}\frac{\partial h(x,y)}{\partial y} \tag{6.12b}$$

where γ [M·L^{-2}·t^{-2}] is the specific weight of the fluid, and η [M·L^{-1}·t^{-1}] is the dynamic viscosity of the fluid. Figure 6.4 gives a schematic illustration of the coordinate system and boundary conditions employed in this work, and Table 6.3 lists the parameters employed in the model.

6.2.2.2 Transport simulation

In this work, the random walk particle tracking (RWPT) technique was used to simulate the colloid and molecular-scale solute transport in single fractures, based on the assumption that the colloid-colloid interactions were negligible. The same discretization scheme was employed for both the transport and flow simulations, and the aperture within each discretized element remained constant. It was assumed that the aperture field is symmetric about the centre plane of the fracture. Upon calculation of the two-dimensional flow field, and imposing a parabolic velocity profile across the fracture, the quasi-three-dimensional RWPT equations were employed to simulate the transport process (James et al., 2005):

$$x^n = x^{n-1} + \bar{v}_x\left(x^{n-1}, y^{n-1}, z^{n-1}\right)\frac{3}{2}\left\{1 - 4\left[\frac{z}{b(x,y)}\right]^2\right\}\Delta t + Z(0,1)\sqrt{2D^*_{coll}\Delta t} \tag{6.13a}$$

$$y^n = y^{n-1} + \bar{v}_y\left(x^{n-1}, y^{n-1}, z^{n-1}\right)\frac{3}{2}\left\{1 - 4\left[\frac{z}{b(x,y)}\right]^2\right\}\Delta t + Z(0,1)\sqrt{2D^*_{coll}\Delta t} \tag{6.13b}$$

$$z^n = z^{n-1} + Z(0,1)\sqrt{2D^*_{coll}\Delta t} \tag{6.13c}$$

where D_{coll}^{*} [$L^2 \cdot t^{-1}$] is the diffusion coefficient of the colloids, and $Z(0,1)$ is a normally distributed random number with a mean of zero and a unit variance.

The initial condition involved the instantaneous release of 10,000 particles across the inlet of the fracture. The particles were then distributed according to the local volumetric flow rate in both the y and z directions as detailed by James et al. (2005). A constant time step of Δt =0.1 s was employed in these simulation to achieve a balance between solution accuracy and computational efficiency. Table 6.3 lists the RWPT model parameters.

6.2.2.3 Colloid Attachment

When a colloid encounters a fracture wall, it either reflects back into the fracture or attaches onto the fracture wall. In this work, the probability of colloid attachment onto a fracture wall, p_a, following a collision is represented by an equation derived from the Boltzmann law (Adamczyk et al., 1991):

$$p_a = exp\left(-\frac{\Phi_n}{k_B T}\right) \tag{6.14}$$

where Φ_n [$M \cdot L^2 \cdot t^{-2}$] is the repulsive interaction energy between the particle and the fracture surface, k_B [$M \cdot L^2 \cdot t^{-2} \cdot T^{-1}$] is the Boltzmann's constant, and T [T] is the absolute temperature of the solvent. A value of Φ_n = 10 kT is suggested by Adamczyk et al. (1992a,b) as a general approximation assuming low sodium and calcium concentrations (Missana et al., 2003). In this research, however, a value of Φ_n = 4 kT was employed in order to match the experimental colloid recovery. A value of $\Phi_n \rightarrow \infty$ implies infinite repulsion and no wall deposition.

To ultimately determine whether a particle will attach onto the wall, a uniformly distributed random number between zero and one, $U(0,1)$, is generated each time a wall collision is recorded, and the occurrence of attachment is determined as follows:

$$\begin{cases} U(0,1) < p_a & \text{colloid attached} \\ U(0,1) > p_a & \text{colloid reflected back into the fracture} \end{cases} \tag{6.15}$$

If the particle is reflected back into the fracture, its *x*- and *y*- coordinates remain unchanged, whereas the *z*-coordinate is set a distance away from the wall equal to the distance that the particle would have obtained had it penetrated the rock matrix plus the particle diameter.

6.2.2.4 Colloid Sedimentation

For a particle with a density different than the suspending fluid, gravitational sedimentation can cause the particle to deviate from fluid streamlines and collide with the media surface, thus enhancing the probability of attachment onto the media surface. The Stokes settling velocity of spherical particles, derived from the balance between gravitational, buoyant, and viscous forces is (McDowell-Boyer et al., 1986):

$$v_{Stokes} = \frac{g}{18\mu}(\rho_p - \rho_f)d_p^2 \tag{6.16}$$

where g [L·t^{-2}] is the gravitational acceleration, and ρ_p [M·L^{-3}] and ρ_f [M·L^{-3}] are the particle and fluid densities, respectively.

The effect of gravitational settling on each colloid is incorporated into the particle tracking equations in the *z*- direction as follows:

$$z^n = z^{n-1} + Z(0,1)\sqrt{2D^*_{coll}\Delta t} + v_{Stokes}\Delta t \tag{6.17}$$

The transport of colloids in the *x*- and *y*- directions is not affected by gravitational settling.

6.2.2.5 Size Exclusion and Straining

A mechanistic model was adopted to represent the processes of straining and size exclusion in these simulations. Straining was incorporated through comparing the colloid diameter with the local fracture aperture each time a colloid moves to a new position. If the colloid diameter is equal to or larger than the local aperture, it is strained. Size exclusion was implemented in the RWPT technique by assuming that there is a layer of fluid along the fracture walls from which colloids are excluded. The thickness of this layer of fluid is assumed to be equal to the radius of the colloids (0.5 μm). Since the center of a colloid represents its actual position, and the velocity of the center of the colloid represents its actual velocity, the result of this assumption is that colloids cannot sample the lowest velocity near the fracture wall. Pore exclusion was not incorporated into the current RWPT method, as it is beyond the scope of this work.

6.3. Results and Discussion

6.3.1 Experimental Observations

Figure 6.5 shows the experimental breakthrough curve for the colloid tracer test through F1 with v_c = 1.67 mm/s, together with the analytical breakthrough curve fit. All other breakthrough curves together with the ADE fitting curves are presented as supplemental materials, and are typical of that shown in Figure 6.5. It should be reiterated here that these experiments were conducted under flow conditions in which inertial forces were negligible, and therefore the cubic law has been demonstrated to be a reasonable measure of the flow rate (e.g., Brush and Thomson, 2003).

The measured breakthrough curves demonstrate non-Fickian transport behavior, i.e., early breakthrough times and long tails. An interesting phenomenon is that, at the lowest flow rates, the ADE curves fit the measured data well. However, the difference between the ADE solution and the measured breakthrough curves, especially at the early and late breakthrough times, become more substantial as the specific discharge increases. One potential explanation for this is the interaction that occurs between slower and faster flow pathways at the slower flow rates, which essentially "evens out" the tracer breakthrough concentrations. As a result, the overall transport appears more Fickian-like. At higher flow rates, however, there is increasing deviation from Fickian behavior, as the effects of tracer retarded in slower flow pathways become more important. Levy and Berkowitz

(2003) and Berkowitz and Scher (2008) observed similar phenomena for solute transport through mid-scale porous media.

6.3.1.1 Effect of Specific Discharge on Dispersivity

The fitted values for α_L, v and k_{ir} are reported in Table 6.1 for all 27 experiments. The 95% confidence intervals of the fitted value of k_e show that in most experiments k_e is not significantly different from 0, which indicates that reversible sorption does not have a significant influence on colloid transport and thus k_e is not reported in Table 6.1. After each experiment, the fracture was flushed using deionized water for at least 6 hours, and colloids were observed to be retained within the fracture. These observations confirm that irreversible sorption is the dominant sorption process.

The magnitude of the fit dispersivities relative to that of the fracture length is within the range of those reported by others (e.g., Thompson and Brown, 1991; Keller et al., 1995). Upon close examination of Table 6.1, it was found that dispersivity increases with increasing specific discharge for all three fractures. The dispersivities obtained through solute transport in the same three fractures also increases with increasing specific discharge, although at different rates (as discussed in section 2.6). If a linear relationship between the hydrodynamic dispersion coefficient and the specific discharge within fractures is assumed, the experimental data presented by Dronfield and Silliman [1993] and Detwiler et al. [2000] also demonstrate an increase in dispersivity with the specific discharge. Dronfield and Silliman [1993] derived a unique dispersivity for each aperture field in their research by assuming that the hydrodynamic dispersion coefficient is a function of the velocity raised to a power n ($D = \alpha v^n$), and demonstrated that n took on values ranging from 1.3 to 2.0 depending on the fracture roughness. Detwiler et al. [2000] expressed the hydrodynamic dispersion coefficient as a sum of molecular diffusion, geometric dispersion, and Taylor dispersion, and obtained coefficients representing the contributions of the different components.

Figure 6.6 (a) and (b) displays a set of images taken at various times/travel distance during the colloid tracer experiment in F1, with I_c = 0.1 mM, under different specific discharges. These images provide a qualitative picture of the colloid transport patterns in variable-aperture fractures, and reveal several features upon examination. First, colloids are transported along preferential pathways, bypassing some aperture regions. A comparison of these preferential paths with the aperture field data presented in Figure 6.1(a) reveals that the preferential pathways develop along the larger inter-connected aperture regions connecting the upstream and downstream ends of the fracture. This channeling phenomenon has been well documented for solute transport in single fractures (e.g., Moreno et al., 1990; Keller et al., 1999), however, this is the first time it has been visually demonstrated for colloid transport in laboratory-scale single fractures to the knowledge of these authors.

A second interesting phenomenon emerges upon the examination of Figure 6.6 (a) and (b), which is that the plume is irregular in shape, and becomes more irregular with increasing specific discharge. This is particularly noticeable at early times. It is obvious that the colloid development deviates from the Fickian process, particularly when the specific discharge is larger. This phenomenon explains why the ADE does not adequately describe the colloid breakthrough curves, particularly when the specific discharge is large. In addition, the specific discharge also influences the aperture regions bypassed by the plume. As a result, the colloids are exposed to a different degree of heterogeneity in the fracture with different specific discharge. The conventional theory asserts that dispersivity is an intrinsic function of the media property and consequently a constant value for a given medium (Fried and Combarnous, 1971; Bouwer, 1978). Our observations, however, indicate that the dispersivity is a function of specific discharge, and thus the residence time. This is consistent with the conclusions by Gelhar et al. (1992), Neuman (1990), and Dagan (1988) that dispersivity is a function of problem scale and/or time before the Fickian transport regime is reached at which an asymptotic value of dispersivity is obtained.

The above observations that (1) colloids are transported along preferential pathways and bypass some aperture regions, and (2) the colloid plume becomes more irregular in shape with increasing specific discharge lead to one important corollary: one cannot obtain a complete functional form of dispersivity based solely on an analysis of the aperture field for non-Fickian transport. Berkowitz and Scher (2008) arrived at similar conclusions through analyzing solute transport in laboratory-scale porous media. Gelhar (1993) developed an expression for macrodispersivity in variable-aperture fractures through a stochastic analysis of flow and solute transport. However, researchers have demonstrated that the dispersivities calculated using Gelhar's expression are different from those obtained through the moment method or fitting the one-dimensional ADE to the measured and simulated breakthrough curves by a factor of up to 2 (e.g., Keller et al., 1995; Keller et al., 1999; Lee et al., 2003; Zheng et al., 2008b). The above corollary can explain these differences (at least partially). In addition, the stochastic analysis by Gelhar (1993) assumes a statistically stationary random field. However, small scale fractures, like the three fractures employed in this work, do not usually satisfy this assumption. This also contributes the difference between the theoretically and experimentally determined dispersivities.

6.3.1.2 Effect of Aperture Field, Specific Discharge and Ionic Strength on Colloid Recovery in Single Fractures

Colloid recovery is defined as the ratio of the number of colloids recovered at the outlet to the total number released at the inlet. Figure 6.7 shows the interacting influence of aperture field variability, specific discharge and ionic strength on colloid recovery. Close examination of this figure reveals several trends, although not all data points follow the trends strictly. Figures 6.7(a), (b), and (c) illustrate a general trend that the colloid recovery increases with increasing specific discharge in each fracture. Figure 6.7(d) shows that for each specific discharge, the colloid recovery in F2 and F3 are usually larger than that in F1. Considering that the aperture field statistics for the three fracture replicas follows the following relationship:

$$CoV_{F1} > CoV_{F2} > CoV_{F3} \tag{6.18a}$$

$$\mu_{b,F3} > \mu_{b,F2} > \mu_{b,F1} \tag{6.18b}$$

it is concluded that the arithmetic mean aperture, and not the CoV, plays the more important role in the attachment process. One possible reason for this phenomenon is that, for a given specific discharge, colloids transported in fractures with smaller mean apertures will collide with the fracture walls more frequently, resulting in larger probability for attachment onto the fracture walls. Similarly, for a specific fracture, a larger specific discharge results in a smaller residence time, and decreases the probability of collision with, and therefore attachment to, the fracture walls. Another possible reason for increased colloid recovery with increasing specific discharge is that an increase in specific discharge leads to a larger hydrodynamic shear force, and therefore increases the possibility of colloid detachment from the fracture walls (Ryan and Elimelech, 1996). This analysis indicates that of the two steps that determine the overall kinetics of sorption (i.e., transport and attachment), the transport step is the controlling factor for colloid sorption under the conditions present in this research.

The conclusion that the kinetics of the sorption process is primarily controlled by the transport step is further supported by the fact that, as the ionic strength is increased by two orders of magnitude (from 10^{-4} M to 10^{-2} M), the colloid recovery does not show a consistent trend in any of the three experimental fractures (Figures 6.7 (a), (b) and (c)). Theoretically, an increase in ionic strength will cause "thinning" of the diffusion layers between the colloids and the grains (or fracture walls), decrease the repulsive interactions, and promote colloid attachment. Therefore, if the attachment step is the rate-limiting step, the colloid recovery should be dependent on the ionic strength. Since no obvious trend was observed about this dependence, it is most likely that the probability that a colloid be transported near to a fracture wall, such that the electrical double layer forces are important, is low due to the relative large specific discharges and mean apertures. It could also be due to the fact, however, that the fracture walls are chemically heterogeneous. Elimelech et al. (2000) demonstrated through a series of laboratory experiments that colloid deposition kinetics is controlled by the degree of patchwise chemical heterogeneity on the sand surface in the porous media; the ionic strength, which ranged from 10^{-4} to 10^{-2}, played an insignificant role in these experiments. This is less likely to be the reason for the low degree of correlation between colloid recovery and ionic strength, however, as the matrix material employed in these experiments was consistent (epoxy, STYCAST 1264 A/B), and was not chemically altered in any way. Characterization of the physicochemical properties of the fracture walls will help clarify this question.

Straining played a minor role in terms of colloid retention mechanisms, as the aperture regions measuring less than 1 μm account for only 3.0% of the measured points in F1, 6.0% in F2, and 0.02% in F3. Although the regions with a measured aperture of less than 1 μm in F2 account for a larger percentage of the total measured points, those points are mainly located along the two edges of the fracture, and thus contributed little to colloid straining, as the colloid plume migrated primarily along the interconnected larger aperture regions toward the center of F2. This conclusion is further supported by the results of the numerical simulation as described in Section 3.2.2.

6.3.1.3 Comparison of solute and colloid transport in variable-aperture fractures

Size and charge exclusion refers to the phenomenon that colloids are prevented from entering the regions nearest to the fracture walls due to their physical size (size exclusion) or the repulsive interaction forces between the colloids and walls (charge exclusion). The phenomenon in which colloids are directed through only the larger aperture regions, and are excluded from regions with smaller apertures due to either size or charge is referred to as pore exclusion in this research. The separation of particle sizes due to differential advection in both uniform porous media (e.g., Small, 1974) and parallel-plate fractures (e.g., Chmela et al., 2002) is well established in the hydrodynamic chromatography literature, and has been contributed to size and/or charge exclusion. Differential advection between colloids and solute tracers has also been observed in variable-aperture fractured media (e.g., Reimus et al., 1995; McKay et al., 1999; McKay et al., 2000). Differential dispersion has also been observed in variable-aperture fractures. For example, Grindrod et al. (1996) argued that dispersion coefficients of colloidal particles can be 20% less than those for solutes.

However, inconsistencies also exist in terms of the methods employed to determine the occurrence of differential transport. Zhang et al. (2001) analyzed the different methods employed in the literature to identify differential advection, and argued that the velocity obtained through fitting effluent breakthrough curves to the ADE is a reliable indicator of differential advection even if tracer sorption exists. In this research, the mean transport velocities ($v_{f,coll}$ and $v_{f,solute}$ for colloids and solutes respectively) and dispersion coefficients ($D_{f,coll}$ and $D_{f,solute}$ for colloids and solutes respectively) obtained from the fitting procedure as described in Section 2.3 were used to identify differential transport behaviour between the colloid and the solute tracers. Figure 6.8(a) compares typical normalized breakthrough curves for the colloid and solute tracers in F1 with v_c = 1.67 mm/s and I_c = 0.01 M. Figures 6.8(b) and (c) compare the mean transport velocities and macro-dispersion coefficients for all three fractures, and show that $v_{f,coll}$ and $D_{f,coll}$ are similar to $v_{f,solute}$ and $D_{f,solute}$ in F1 and F2. In F3, however, $v_{f,coll}$ and $D_{f,coll}$ are much larger than $v_{f,solute}$ and $D_{f,solute}$ respectively; and these differences increase with increasing specific discharge.

This phenomenon can be explained through examining the change in transport velocity and macro-dispersion coefficient as a fracture transitions from parallel-plate to variable-aperture. Faster breakthrough of colloids relative to conservative solutes in parallel-plate fractures has been demonstrated through experiments (e.g., Chmela et al., 2002), numerical simulation (e.g., Zheng et al., 2008c), and theoretical analysis (e.g., James and

Chrysikopoulos, 2003). These phenomena were ascribed to size and/or charge exclusion when the Taylor-Aris assumption is satisfied (Chmela et al., 2002). In contrast, however, when the Taylor-Aris assumption is not satisfied, differential transport is due to the combined effects of the large difference in diffusivity of colloids and solutes, and the parabollically distributed velocity profile across the aperture; size and/or charge exclusion plays a minor role in this circumstance (Zheng et al., 2008c). Whether the Taylor-Aris assumption is satisfied or not, macro-dispersion coefficients of colloids are much larger than those of solutes in parallel-plate fractures (by up to three orders of magnitude for colloids with a diameter of 1 μm).

In variable-aperture fractures, however, the heterogeneity of the aperture field, and to a lesser extent, the anisotropy of the aperture field, will become more dominant in determining the average colloid transport velocity and macro-dispersion coefficient. As Zheng et al. (2008b) demonstrated, this effect increases with increasing heterogeneity (i.e., CoV), and the difference between the breakthrough times and macro-dispersion coefficients of colloids and solutes becomes smaller with increasing aperture field heterogeneity. It is hypothesized that, when solutes and colloids advect in relatively large-scale single fractures and for extended periods of time, solutes are able to enter smaller aperture regions while colloids cannot due to pore exclusion. Solutes are also able to enter stagnant regions due to their high diffusion coefficients relative to colloids. Under these conditions, the colloids will have faster breakthroughs and smaller dispersion coefficients than solutes, which is similar to those observed in porous media (e.g., Shonnard et al., 1994; Grindrod et al., 1996; Pang et al. 1998).

The CoVs of F1 and F2 are 0.78 and 0.71 respectively, while the CoV of F3 is only 0.29. Based on the above discussion, it is reasonable to deduce that, in F1 and F2, the heterogeneity plays the dominant role in determining the average transport velocity and macro-dispersion coefficient. Therefore the difference between the average transport velocity and macro-dispersion coefficient of colloids and solutes is not obvious. However, in F3, due to the low CoV, the parabolic Poiseulle velocity profile still plays a relatively significant role in determining the colloid breakthrough velocity, and thus the ratios of $v_{f,coll}/v_{f,solute}$ and $D_{f,coll}/D_{f,solute}$ are larger than those in F1 and F2. This can be explained by the fact that, in F3, the solute is able to sample the entire velocity profile before exiting the fracture due to its large diffusivity; colloids, however, are only able to sample a small range of streamlines before exiting the fracture due to their relatively small diffusivity. Therefore, colloids starting on the center streamline will travel along the center streamline, resulting in faster breakthrough than the solute. On the other hand, colloids starting from streamlines closest to the walls will tend to remain in the regions nearest the walls, resulting in smaller average velocities than the solute. Therefore, the colloid residence time distribution will be wider than that of a solute, and its macro-dispersion coefficient will be larger than that of the solute.

When the specific discharge increases, the difference between the fluid velocities of the centre streamlines and those nearest the fracture walls also becomes larger. Due to their small diffusivity, colloids sample a narrower range of streamlines before exiting the fracture at higher specific discharges. This leads to two important results with respect to colloid transport: (1) a wider residence time distribution, and thus a larger dispersion coefficient; and (2) faster breakthroughs occur at higher specific discharges. Although $v_{f,solute}$ and $D_{f,solute}$ also become larger when the specific discharge increases, $v_{f,coll}$ and $D_{f,coll}$ increase to a larger extent. Therefore, the ratios of $v_{f,coll}$ to $v_{f,solute}$ and $D_{f,coll}$ to $D_{f,solute}$ become larger when the specific discharge increases (Figure 6.8). This observation is supported by the pore-scale experiments conducted by Sirivithayapakorn and Keller (2003), who observed that increasing the pore water velocity will increase the colloid to pore water velocity ratio.

The early arrival of colloids relative to solute tracers has been demonstrated in a series of field experiments in fractured media, and was attributed to the diffusion of solutes, but not colloids, into the porous matrix (e.g., McKay et al., 1993; McKay et al., 1999;

McKay et al., 2000). It should be pointed out here that the epoxy used to cast the fracture replicas is non-porous, and thus the effect of matrix diffusion is excluded in this research. It was observed in the pore-scale experiments by Sirivithayapakorn and Keller (2003) that, if the size of the pore throat is smaller than 1.5 times (1.5 μm for this research) the diameter of the colloids, the colloids cannot enter this pore throat due to pore exclusion. The aperture regions measuring less than 1.5 μm in F1, F2, and F3 only account for approximately 3.0%, 6.0%, and 0.02% of the total aperture field respectively. Although in F2, the aperture regions with apertures less than 1.5 μm account for a relative larger percentage, they are mainly located outside the main plume pathways. Therefore, pore exclusion also plays a relative insignificant role in F2. It is possible, however, that immobile fluid regions account for a more significant portion of the fracture volume (Dijk et al., 1999). Because the diffusivity of NaBr is three orders of magnitude larger than that of colloids, NaBr could move into and out of immobile fluid region in a relatively short period of time compared to the colloids. However, in theses experiments, with mean residence time ranging from 5 minutes to 20 minutes, the NaBr molecule can only travel about 1 mm under the driving force of diffusion alone according to the formulation by Reimus and James (2002). Therefore, the effect of immobile fluid regions is likely also negligible in these experiments.

Detwiler et al. (2000) calculated an "effective" Taylor dispersion coefficient for solute transported in a variable-aperture fracture using the following equation:

$$D_{Taylor} = \frac{v_{f,coll}^{2} \langle b_a \rangle^{2}}{210 D_{coll}^{*}} + D_{coll}^{*} \tag{6.19}$$

where $<b_a>$ [L] is the arithmetic mean aperture of the measured aperture field, $v_{f,coll}$ [$L \cdot t^{-1}$] is the mean transport velocity of colloids obtained through the fitting procedure, and D_{coll}^{*} is the colloid diffusivity as given by equation (6.5d). Equation (6.19) was used in this research to calculate the Taylor dispersion coefficients for colloids in the experimental fractures. Figure 6.9 shows the ratio of D_{Taylor} to $D_{f,coll}$ for all three fractures. It is obvious that D_{Taylor} is larger than $D_{f,coll}$ by more than one order of magnitude. This can be attributed to the fact that the Taylor-Aris assumption is not satisfied under the conditions in these experiments (Table 6.4), and therefore the Taylor dispersion coefficient equation is not valid (Zheng et al., 2008c).

6.3.2 Numerical Simulation Results

The RWPT technique has been used by others to model colloid transport in fractures (e.g., Reimus, 1995; James and Chrysikopoulos, 1999; James et al., 2005). Although the colloid tracer laboratory experiments provide an overall colloid recovery, it is very difficult to identify the contribution from each of the different mechanisms (i.e., straining, attachment, sedimentation) from the data they produced. Numerical simulations, on the other hand, provide insights on the effect of these different mechanisms. A comparison of the results of the physical experiments and numerical simulations also provides insight towards the effectiveness of the RWPT technique for simulating colloid transport in fractures.

6.3.2.1 Replication of the interim concentration field in variable-aperture fracture

Figure 6.10 illustrates the simulated colloid plumes in the measured aperture field of F1 under a series of specified hydraulic gradients (the measured hydraulic gradients in F1 corresponding to the different specific discharges) at different time steps. Comparing the simulation results with the experimental images, several similarities are identified. First, the RWPT simulation clearly shows the channeling effect of colloid transport. Second, at early times the colloids mainly enter the fracture in the middle section of the inlet. Midway across the fracture (in the x-direction), the plume becomes wider along the y-direction. Near the outlet, the plume narrows down again and exits the fracture near the mid-section of the outlet. A comparison of the colloid plume with the measured aperture field of F1 shows that the colloids are mainly transported through the larger aperture regions. The simulation reproduces these features well qualitatively.

In spite of the similarities between the experimental and simulated results mentioned above, the differences are even more obvious. The largest difference is that the simulated colloid plume advances faster than that in the experimental images. In addition, the shape of the simulated plume is different from that in the experimental images. This discrepancy is likely due to the fact that the Reynolds equation overestimates flow through variable-aperture fractures. This has been demonstrated by Nicholl et al. (1999) and Brush and Thomson (2003), and is further demonstrated in this work. For example, the specific discharges employed in the physical experiments through F1 are 0.55 mm/s, 1.09 mm/s, and 1.67 mm/s. The simulated specific discharges, obtained by solving the Reynolds Equation, based on the measured aperture field of F1 and the corresponding hydraulic head loss across F1 measured in the physical experiments, are 0.95 mm/s, 1.95 mm/s, and 2.83 mm/s respectively; obviously larger than the specific discharges calculated during the physical experiments. Therefore, it may be necessary to solve the three dimensional Stokes equations in situations where improved accuracy is required (Nicholl et al., 1999).

6.3.2.2 Effect of straining, attachment and sedimentation on the colloid recovery

The relative importance of straining, attachment, and sedimentation on colloid recovery in F1 were investigated, and are presented in Table 6.5. The results show that the colloid retention due to straining does not play an important role among the various mechanisms in F1, accounting for only about 1% (as a percent of the total number of colloids injected in the inlet). This is consistent with the aperture field of F1 employed in the simulations, which indicated that only 0.8% of the aperture field has an aperture less than 1 μm. It should be pointed out here that, due to the limitations of computation resource, the aperture field of F1 in the simulations was obtained by converting each immediately adjacent 6 by 6 pixels of the directly measured aperture field into one element with an aperture equal to the arithmetic average of these 6 by 6 pixels.

Table 6.5 shows that sedimentation has a significant impact on colloid retention, although the density difference between water and the colloids is only about 5.3%. For example, under a specific discharge of 0.55 mm/s, colloid retention due to attachment when ρ_p = 997 kg/m^3 and ρ_f = 997 kg/m^3 is only about 0.9%; however, colloid retention due to sedimentation and subsequent attachment increases to 13.2% when ρ_p = 1050 kg/m^3 and ρ_f = 997 kg/m^3. The kinetics of sorption is determined by two sequential steps: transport and attachment. Since Φ_n, the repulsive energy of interaction between the particle and the fracture surface, is kept constant in the simulation, the controlling step is that in which the colloids are transported from the bulk fluid to the vicinity of a stationary surface. The effect of sedimentation on colloid retention demonstrates that sedimentation plays a dominant role in transporting colloids from the bulk fluid to the fracture wall, which significantly increases the probability of colloids colliding with, and attaching onto, the fracture wall.

Table 6.5 also shows that the effect of sedimentation on colloid retention becomes more important with decreasing specific discharge. In these simulations, the colloid retention increased from 3.9% to 11.3% when the specific discharge (v_c) decreased from v_c = 1.67 to v_c =0.55 mm/s. This is consistent with the experimental trend (Figure 6.11). However, the simulated colloid loss is consistently smaller than those in experiments, due to the fact that the simulated specific discharges based on the Reynolds equation are overestimated. The overestimated specific discharges lead to a decreased colloid residence time in the fracture, and thus a decrease in the frequency with which the colloids collide with, and subsequently attach to, the fracture wall. Therefore, the colloid retention decreases with increasing specific discharges. This phenomenon further supports the hypothesis that the transport process (the process in which the colloids are transported from the bulk of the fluid to the vicinity of a stationary surface) is the controlling factor in the kinetics of colloid sorption under the conditions existing in this research.

6.4. Summary

A 3^3 factorial laboratory-scale physical model experiment was conducted together with a series of numerical simulations to investigate colloid transport processes and the impact of aperture field variability, specific discharge, and ionic strength on these processes. Aperture fields of three fracture replicas were measured using a light transmission technique. A visualization system was designed to observe colloid transport through one of the experimental fractures. The mean transport velocity and dispersivity of the colloids were obtained by fitting the analytical solution of the one-dimensional ADE to the measured breakthrough curves. The flow fields for the colloid transport simulation through the measured aperture field were obtained by solving the Reynolds equation, and the quasi-three-dimensional velocity profiles were generated by imposing a parabolic velocity distribution across the aperture. A three-dimensional RWPT technique was employed to simulate colloid transport.

Two significant features were observed from the laboratory experiments: (1) colloids are transported along preferential pathways, typically the interconnected larger aperture regions, and bypass some aperture regions; and (2) the colloid plume is irregular in shape, and becomes more irregular with increasing specific discharge, indicating non-Fickian transport. These observations lead to one important corollary, which is that the dispersivity cannot be completely determined by the aperture field statistics alone; it is also a function of specific discharge. This is believed to explain (at least partially) the difference between the dispersivities obtained from the physical experiments and those from the expression by Gelhar (1993), and provides a basis for more realistic conceptual model development.

The colloid recovery in each fracture was found to increase with increasing specific discharge. For each specific discharge, it was found that the colloid recoveries in F2 and F3 were similar, and were generally larger than the recovery in F1. This is consistent with the fact that the arithmetic mean apertures of F2 and F3 were similar ($\mu_{b,F2}$ = 1.57 mm,

$\mu_{b,F3}$ = 1.75 mm), and larger than that of F1 ($\mu_{b,F1}$ = 0.88 mm). The effect of ionic strength on colloid transport did not follow the theoretical analysis that colloid recovery increases with decreasing ionic strength. These observations lead to the conclusion that the transport step (the step in which the colloids are transported from the bulk fluid to the vicinity of the fracture wall), and not the attachment step, plays the dominant role in the colloid sorption process. The numerical simulations provided insight towards the contributions of different mechanisms on colloid retention, and supported the conclusion that the transport step plays the dominant role in the sorption process. They also showed that sedimentation plays an important role in colloid transport from the bulk fluid to the fracture wall. However, the simulations showed that colloid retention due to straining only accounted for about 1% of the colloid released.

The effect of aperture field variability on differential transport between colloids and solutes was also investigated based on the mean transport velocities and dispersion coefficients obtained through the fitting procedures. In F3 (CoV=0.29), colloids have larger mean transport velocities and dispersion coefficients than solute. However, in F1 (CoV=0.78) and F2 (CoV=0.71), the difference between the mean transport velocities and dispersion coefficients of colloids and solutes is not significant. This phenomenon was explained through the transition of the dominant factors in differential transport from parallel-plate to variable-aperture fractures. Size and/or charge exclusion (for cases where the Taylor-Aris assumption is satisfied) and the combined effect of the very small diffusivity of colloids relative to solutes (for cases Taylor-Aris assumption is not satisfied) and the parabollically distributed velocity profile across the aperture results in the faster transport and larger dispersion coefficients of colloids relative to solutes in parallel-plate fractures. It is hypothesized, however, that with increasing CoVs, the above two mechanisms will become less important, and pore exclusion and preferential pathways induced by aperture field variability (heterogeneity) will play a more important role in determining the colloid and solute transport processes. This hypothesis is consistent with results from the previous physical experiments and numerical simulations.

Acknowledgement

Funding for this work was provided by the NSERC Discovery Grant Program. The authors would like to thank Dr. S. C. James for generously providing the codes employed in this research. This work was made possible by the facilities of the Shared Hierarchical Academic Research Computing Network (SHARCNET:www.sharcnet.ca).

References

Adamczyk, Z., Siwek, B., Zembala, M., 1991. Kinetics of localized adsorption of particles on homogeneous surfaces. J. Colloid Interf. Sci. 151(2), 351-367.

Adamczyk, Z., Siwek, B., Zembala, M., 1992a. Reversible and irreversible adsorption of particles on homogeneous surfaces. Colloids Surf. A Physicochem. Eng. Aspects. 62, 119-130.

Adamczyk, Z., Siwek, B., Zembala, M., 1992b. Kinetics of localized adsorption of colloid particles. Langmuir. 8, 2605-2610.

Allen, M.J., Morrison, S.M., 1973. Bacterial movement through fractured bedrock. Ground Water 11(2), 6-10.

Berkowitz, B., Scher, H., 2008. Exploring the nature of non-Fickian transport in laboratory Experiments. Adv. Water Resour. in press.

Bos, R., van der Mei, H.C., Busscher, H.J., 1999. Physico-chemistry of initial microbial adhesive interactions-its mechanisms and methods for study. FEMS Microbiol. Rev. 23, 179-230.

Bouwer, H., 1978. Groundwater Hydrology, McGraw-Hill, New York.

Brush, D.J., Thomson, N.R., 2003. Fluid flow in synthetic rough-walled fractures: Navier-Stokes, Stokes, and local cubic law simulations. Water Resour. Res. 39(4), 1085, doi:10.1029/2002WR001346.

Cohen, B., 1922. Disinfection studies: the effects of temperature and hydrogen ion concentration upon the viability of Bact. coli and Bact. typhosum in water. J. Bacteriol. 7(2):183-230.

Chmela, E., Tijssen, R., Blom, M.T., Gardeniers, H.J.G.E., van den Berg, A., 2002. A chip system for size separation of macromolecules and particles by hydrodynamic chromatography. Anal. Chem. 74, 3470-3475.

Chrysikopoulos, C.V., James, S.C., 2003. Transport of neutrally buoyant and dense variably sized colloids in a two-dimensional fracture with anisotropic aperture. Transport Porous Med. 51, 191-210.

Dagan, G., 1988. Time-dependent macrodispersion for solute transport in anisotropic heterogeneous aquifers. Water Resour. Res. 24(9), 1491-1500.

Detwiler, R.L., Pringle, S.E., Glass, R.J., 1999. Measurement of fracture aperture fields using transmitted light: An evaluation of measurement errors and their influence on simulations of flow and transport through a single fractures. Water Resour. Res. 35(9), 2605-2617.

Detwiler, R.L., Rajaram, H., Glass, R.J., 2000. Solute transport in variable-aperture fractures: an investigation of the relative importance of Taylor dispersion and macrodispersion. Water Resour. Res. 36(7), 1611-1625.

Degueldre, C., Baeyens, B., Goerlich, W., Riga, J., Verbist, J., Stadelmann, P., 1989. Colloids in water from a subsurface fracture in granitic rock, Grimsel Test Site, Switzerland. Geochim. Cosmochim. Acta 53, 603-610.

Dijk, P., Berkowitz, B., Bendel, P., 1999. Investigation of flow in water saturated rock fractures using nuclear magnetic resonance imaging (NMRI). Water Resour. Res. 35(2), 347-360.

Dickson, S.E., 2001. Dissolution of entrapped DVAPLS in variable aperture fractures. Ph.D. thesis, University of Waterloo, Waterloo, Ontario, Canada.

Dronfield, D.G., Silliman, S. E., 1993. Velocity dependence of dispersion for transport through a single fracture of variable roughness. Water Resour. Res. 29(10), 3477-3483.

Elimelech, M., Nagai, M., Ko, C., Ryan, J.N., 2000. Relative insignificance of mineral grain zeta potential to colloid transport in geochemically heterogeneous porous media. Environ. Sci. Technol. 34, 2143-2148.

Elimelech, M., O'Melia, C. R., 1990. Effect of particle size on collision efficiency in the deposition of Brownian particles with electrostatic energy barriers. Langmuir 6(6), 1153-1163.

Fahim, M.A., Wakao, N., 1982. Parameter estimation from tracer response measurements. Chem. Eng. J. 25, 1-8.

Fontes, D.E., Mills, A.L., Hornberger, G.M., Herman, J.S., 1991. Physical and chemical factors influencing transport of microorganisms through porous media. Appl. Environ. Microbiol. 57, 2473-2481.

Fried, J.J., Combarnous, M.A., 1971. Dispersion in porous media. Adv. Hydrosci. 7, 169-282.

Gelhar, L.W., Welty, C., Rehfeldt, K.R., 1992. A critical review of data on field-scale dispersion in aquifers. Water Resour. Res. 28(7), 1955-1974.

Gelhar, L.W., 1993. Stochastic Subsurface Hydrology, Prentice-Hall, Old Tappan, N. J.

Grindrod, P., 1993. The impact of colloids on the migration and dispersal of radionuclides within fractured rock. J. Contam. Hydrol. 13: 167-181.

Grindrod, P., Edwads, M.S., Higgo, J. J.W., Williams, G.M., 1996. Analysis of colloid and tracer breakthrough curves. J. Contam. Hydrol. 21, 243-253.

Harvey, R.W., 1997. Microorganisms as tracers in groundwater injection and recovery experiments: a review. FEMS Microbiol. Rev. 20:461-472.

Hill, D.D., Sleep, B.E., 2002. Effects of biofilm growth on flow and transport through a glass parallel plate fracture. J. Contam. Hydrol. 56:227-246.

Hubbe, M.A., 1985. Detachment of colloidal hydrous oxide spheres from flat solids exposed to flow, 2 mechanism of release. Colloid Surface 16, 249-270.

Hubbe, M.A., 1987. Detachment of colloidal hydrous oxide spheres from flat solids exposed to flow, 4 Effect of polyeletrolytes. Colloid Surface 25, 325-339.

James, S.C., Chrysikopoulos, C.V., 1999. Transport of polydisperse colloid suspensions in a single fracture. Water Resour. Res. 35 (3), 707-718.

James, S.C., Chrysikopoulos, C.V., 2003. Effective velocity and effective dispersion coefficient for finite-sized particles flowing in a uniform fracture. J. Colloid Interf. Sci. 263, 288-295.

James, S.C., Bilezikjian, T.K., Chrysikopoulos, C.V., 2005. Contaminant transport in a fracture with spatially variable aperture in the presence of monodisperse and polydisperse colloids. Stoch. Env. Res. Risk A. 19(4), 266-279.

Keller, A.A., Roberts, P.V., Kitanidis, P.K., 1995. Prediction of single phase transport parameters in a variable aperture fracture. Geophys. Res. Lett. 22(11), 1425-1428.

Keller, A.A., Roberts, P.V., Blunt, M.J., 1999. Effect of fracture aperture variations on the dispersion of contaminants. Water Resour. Res. 35(1), 55-63.

Kosakowski, G., 2004. Anomalous transport of colloids and solutes in a shear zone. J. Contam. Hydrol. 72, 23-46.

Lee, J., Kang, J. M., Choe, J., 2003. Experimental analysis on the effects of variable apertures on tracer transport. Water Resour. Res. 39(1), 1015, doi: 10.1029/2001WR001246.

Levy, M., Berkowitz, B., 2003. Measurement and analysis of non-Fikian dispersion in heterogeneous porous media. J. Contam. Hydrol. 64, 203-226.

McDowell-Boyer, L.M., Hunt, J.R., Sitar N., 1986. Particle transport through porous media. Water Resour. Res. 22:1901-1921.

McDowell-Boyer, L.M., 1992. Chemical mobilization of micro-sized particles in saturated porous media under steady flow conditions. Environ. Sci. Technol. 26, 586-593.

Mckay, L.D., Cherry, J.A., Bales, R.C., Yahya, M.T., Gerba, C.P., 1993. A field example of bacteriophage as tracers of fracture flow. Environ. Sci. Technol. 27, 1075-1079.

Mckay, L.D., Fredericia, J., Lenczewski, M., Morthorst, J., Klint, K.E., 1999. Spatial variability on contaminant transport in a fractured till, Avedore Denmark. Nord. Hydrol. 30, 333-360.

Mckay, L.D., Sanford, W.E., Strong, J.M., 2000. Field scale migration of colloidal tracers in a fractured shale saprolite. Ground Water, 38, 139-147.

McLinn, E.L., Rehm, B.W., 1997. Biodegradation of petroleum hydrocarbons in fractured, unsaturated dolomite at a field site. Ground Water Monit. Rem. 17(4):73–80.

Missana T., Mingarro, M., Gutierrez, M.G., Alonso, U., Geckeis, H., Schaefer, T., Rabung, T., Vejmelka, P., Marquardt, C., Ota, K., 2003. Gts phase V CRR experiment, Technical Report, Rep. NTB 03-02, NAGRA, Baden, p100.

Moreno, L., Tsang, C.F., Tsang, Y.W., Neretnieks, I., 1990. Some anomalous features of flow and solute transport arising from fracture aperture variability. Water Resour. Res. 26(10), 2377-2391.

Neuman, S. P., 1990. Universal scaling of hydraulic conductivities and dispersivities in geological media. Water Resour. Res. 26(8), 1749-1758.

Nicholl, M.J., Rajaram, H., Glass, R. J., Detwiler, R. L., 1999. Saturated flow in a single fracture: Evaluation of the Reynolds equation in measured aperture fields. Water Resour. Res. 35(11), 3361-3373.

Pang, L.P., Close, M., Noonan, M., 1998. *Rhodamine WT* and *Bacillus subtilis* transport through an alluvial gravel aquifer. Ground Water 36, 112-122.

Rasmuson, A., Neretnieks, I., 1986. Radionuclide transport in fast channels in crystalline rock. Water Resour. Res. 22, 1247-1256.

Reimus, P.W., Robinson, B.A., Nuttall, H.E., Kale, R., 1995. Simultaneous transport of synthetic colloids and a nonsorbing solute through single saturated natural fractures. Mater. Res. Soc. Symp. Proc. 353, 363-370.

Reimus, P.W., 1995. The use of synthetic colloids in tracer transport experiments in saturated rock fractures. Ph.D. thesis, Los Alamos National Laboratory, LA-13004-T.

Reimus, P.W., James, S.C., 2002. Determining the random time step in a constant spatial step particle tracking algorithm. Chem. Eng. Sci. 57, 4429-4434.

Renshaw, C.E., Dadakis, J.S., Brown, S.R., 2000. Measuring fracture apertures: a comparison of methods. Geophys. Res. Lett. 27(2), 289-292.

Ross, N., Villemur, R., Deschenes, L., Samson, R., 2001. Clogging of a limestone fracture by stimulating groundwater microbes. Wat. Res. 35(8):2029-2037.

Ross, N., Bickerton, G., 2002. Application of biobarriers for groundwater containment at fractured bedrock sites. Remediation Journal 3(3), 5-21.

Ryan, J.N., Elimelech, M., 1996. Colloid mobilization and transport in groundwater. Colloid Surfaces A 107, 1-56.

Sharma, M.M., Chamoun, H., Sita Rama Sarma, D.S.H., Schechter, R.S., 1992, Factors controlling the hydrodynamic detachment of particles from surfaces. J. Colloid Interf. Sci. 149, 121-134.

Shonnard, D.R., Taylor, R.T., Hanna, M.L., Boro, C.O., Duba, A.G., 1994. Injection-attachment of methylosinus-trichosporium OB3b in a two-dimensional miniature sand-filled aquifer simulator. Water Resour. Res. 30, 25-35.

Sirivithayapakorn, S., Keller, A., 2003. Transport of colloids in saturated porous media: A pore-scale observation of the size exclusion effect and colloid acceleration. Water Resour. Res. 39(4), 1109, doi: 10.1029/2002WR001583.

Small, H., 1974. Hydrodynamic chromatography: A techniques for size analysis of colloidal particles. J. Colloid Interf. Sci. 48, 147-161.

Smith, P.A., Degueldre, C., 1993. Colloid-facilitated transport of radionuclides through fractured media. J. Contam. Hydrol. 13: 143-166.

Tan, Y., Gannon, J.T., Baveye, P., Alexander M., 1994. Transport of bacteria in an aquifer sand: experiments and model simulations. Water Resour. Res. 30 (12), 3243-3252.

Tang, D.H., Frind, E.O., Sudicky, E.A., 1981. Contaminant transport in fractured porous media: analytical solution for a single fracture. Water Resour. Res. 17(3), 555-564.

Thompson, M.E., Brown, S.R., 1991. The effect of anisotropic surface roughness on flow and transport in fractures. J. Geophys. Res. 96(B13), 21923-21932.

Tien, C., 1989. Granular Filtration of Aerosols and Hydrosols, Butterworths Publishers, Stoneham, MA.

Tsang, Y.W., 1992. Usage of 'equivalent apertures' for rock fractures as derived from hydraulic and tracer tests. Water Resour. Res. 28(5), 1451-1455.

Van der Lee, J., Ledoux, E., de Marsily, G., 1992. Modeling of colloidal uranium transport in a fractured medium. J. Hydrol. 139(1-4):135-158.

Van Genuchten, M.Th., 1981. Analytical solutions for chemical transport with simultaneous adsorption, zero-order production, first-order decay. J. Hydrol. 49, 213-233.

Yager, R.M., Bilotta, S.E., Mann, C.L., Madsen, E.L., 1997. Metabolic adaptation and in situ attenuation of chlorinated ethenes by naturally occurring microorganisms in a fractured dolomite aquifer near Niagara Falls, New York. Environ. Sci. Technol. 31(11):3138–3147.

Yao, K.M., Habibian, M.T., O'Melia, C.R., 1971. Water and waste water filtration: concepts and applications. Environ. Sci. Technol. 5 (11), 1105-1112.

Yates, M.V., Yates, S.R., 1988. Modeling microbial fate in the subsurface environment. Crit. Rev. Environ. Control, 17, 307-344.

Zhang, P., Johnson, W.P., Piana, M.J., Fuller, C.C., Naftz, D.L., 2001. Potential artifacts in interpretation of differential breakthrough of colloids and dissolved tracers in the context of transport in a zero-valent iron permeable reactive barrier. Ground Water, 39(6), 831-840.

Zheng, Q., Dickson, S.E., Guo, Y., 2008a. On the appropriate "equivalent aperture" for the description of solute transport in single fractures: Laboratory-scale experiments, Water Resour. Res. 44, W04502, doi:10.1029/2007WR005970.

Zheng, Q., Dickson, S.E., Guo, Y., 2008b. The influence of aperture field heterogeneity and anisotropy on dispersion regimes and dispersivity in single fractures, submitted to J. Geophys. Res.

Zheng, Q., Dickson, S.E., Guo, Y., 2008c. Observation of a new phenomenon for the differential transport of colloids and solutes in single, variable-aperture fractures. submitted to J. Colloid Interf. Sci.

Tables

Table 6.1. Colloid transport experiments and results.

Fracture	v_c (mm/s)	Ionic Strength	α_L (mm) 95% confidence limit	$v_{f,coll}$ (mm/s) 95% confidence limit	k_{ir}	Correlation Coefficient	Colloid Recovery
F1 Length: 241.5mm Width: 149.0mm	0.55	0.0001	120 (68, 172)	0.30 (0.24, 0.36)	1.00E-07 (4.31E-08, 1.57E-07)	0.9178	0.675
	0.55	0.001	120 (87, 154)	0.40 (0.35, 0.45)	8.00E-08 (3.87E-08, 1.21E-07)	0.9638	0.726
	0.55	0.01	120 (71, 169)	0.30 (0.25, 0.36)	1.00E-07 (4.56E-08, 1.54E-07)	0.9229	0.599
	1.09	0.0001	150 (110, 190)	0.65 (0.57, 0.73)	8.01E-08 (1.46E-09, 1.59E-07)	0.9741	0.789
	1.09	0.001	150 (106, 194)	0.60 (0.52, 0.68)	1.00E-07 (1.45E-08, 1.86E-07)	0.9681	0.796
	1.09	0.01	150 (107, 193)	0.58 (0.50, 0.66)	8.04E-08 (1.87E-09, 1.59E-07)	0.969	0.763
	1.67	0.0001	170 (96, 244)	0.75 (0.58, 0.92)	2.51E-07 (5.43E-08, 4.47E-07)	0.9647	0.735
	1.67	0.001	150 (122, 178)	0.80 (0.73, 0.87)	1.00E-07 (1.84E-08, 1.82E-07)	0.9883	0.857
	1.67	0.01	150 (130, 170)	0.82 (0.77, 0.87)	8.00E-08 (1.89E-08, 1.41E-07)	0.9923	0.890
F2 Length: 350.0mm Width: 214.5mm	0.55	0.0001	150 (135, 165)	0.21 (0.20, 0.21)	1.00E-07 (8.57E-08, 1.15E-07)	0.9925	0.765
	0.55	0.001	150 (133, 167)	0.19 (0.18, 0.20)	1.00E-07 (8.41E-08, 1.16E-07)	0.9875	0.806
	0.55	0.01	150 (131, 169)	0.19 (0.18, 0.20)	1.00E-07 (8.17E-08, 1.18E-07)	0.9848	0.767
	1.09	0.0001	160 (144, 176)	0.38 (0.36, 0.40)	1.00E-07 (7.31E-08, 1.27E-07)	0.9933	0.895
	1.09	0.001	160 (144, 176)	0.40 (0.38, 0.42)	2.00E-07 (1.70E-07, 2.30E-07)	0.9939	0.798

	1.09	0.01	160 (141, 179)	0.37 (0.35, 0.39)	2.00E-07 (1.65E-07, 2.35E-07)	0.9923	0.784
	1.67	0.0001	200 (182, 218)	0.58 (0.56, 0.61)	5.00E-08 (1.11E-08, 8.90E-08)	0.9905	0.934
	1.67	0.001	180 (159, 201)	0.52 (0.49, 0.55)	5.01E-08 (9.14E-10, 9.92E-08)	0.9941	0.860
	1.67	0.01	200 (180, 220)	0.52 (0.49, 0.55)	5.17E-08 (1.24E-09, 1.02E-07)	0.995	0.872
F3 Length: 349.0mm Width: 230.0mm	0.55	0.0001	141 (121, 160)	0.29 (0.27, 0.31)	1.96E-07 (1.69E-07, 2.23E-07)	0.9882	0.797
	0.55	0.001	150 (126, 174)	0.27 (0.25, 0.29)	1.00E-07 (7.18E-08, 1.28E-07)	0.9843	0.809
	0.55	0.01	150 (119, 181)	0.28 (0.26, 0.31)	1.00E-07 (6.32E-08, 1.37E-07)	0.9739	0.744
	1.09	0.0001	270 (203, 337)	0.45 (0.39, 0.51)	1.00E-07 (2.50E-08, 1.75E-07)	0.9755	0.901
	1.09	0.001	250 (199, 301)	0.45 (0.34, 0.56)	1.00E-07 (2.12E-07, 4.12E-07)	0.9809	0.846
	1.09	0.01	250 (195, 305)	0.45 (0.40, 0.50)	1.00E-07 (3.11E-08, 1.69E-07)	0.9769	0.808
	1.67	0.0001	280 (223, 337)	0.66 (0.58, 0.74)	2.00E-07 (8.15E-08, 3.19E-07)	0.9871	0.824
	1.67	0.001	270 (230, 311)	0.66 (0.61, 0.72)	2.15E-07 (1.31E-07, 3.00E-07)	0.991	0.925
	1.67	0.01	280 (210, 349)	0.61 (0.53, 0.70)	2.00E-07 (6.43E-08, 3.36E-07)	0.9816	0.817

Table 6.2. Aperture field characteristics derived from the direct aperture field measurement, solute tracer and hydraulic tests.

Fracture ID		F1	F2	F3
Dimensions (mm × mm)		241.5 × 149.0	350.0 × 214.5	349.0 × 230.0
Resolution (mm× mm)		0.17 × 0.17	0.26 × 0.26	0.25 × 0.25
Arithmetic mean aperture ($<b_a>$, mm)		0.88 (RMSE= 0.9%)	1.57 (RMSE = 0.3%)[1]	1.75 (RMSE=0.7%)
Standard deviation (σ, mm)		0.69	1.12	0.51
Coefficient of variation ($=\sigma/<b_a>$)		0.78	0.71	0.29
Geometric mean aperture ($<b_g>$, mm)		0.61	0.90	1.64
Harmonic mean aperture ($<b_h>$, mm)		0.19	0.13	1.41
Fracture volume (mL)		33 (RMSE=0.9%)	102 (RMSE = 0.3%)[1]	124 (RMSE= 0.7%)
[2]μ_m (mm)	v_c = 0.55 mm/s	0.79	1.53	1.49
	v_c = 1.09 mm/s	0.93	1.58	1.54
	v_c = 1.67 mm/s	1.08	1.71	1.93
[2]μ_c (mm)		0.40	0.54	0.60

[1] $\text{RMSE} = \frac{\sigma(x)}{x}$, where x represents $<b_a>$ or fracture volume.

[2] μ_m and μ_c refers to the mass balance aperture and cubic law aperture derived from the solute tracer and hydraulic tests (Zheng et al., 2008a)

Table 6.3. Flow and transport parameters employed for the RWPT simulation in F1.

	Parameter	Value
Flow simulation	Fracture dimensions (length×width)	225.8 mm×138.9 mm
	Fracture discretization (elements×elements)	169×104
	Element size (dx×dy)	1.3 mm×1.3 mm
	Temperature	20 °C
	Dynamic viscosity η	1.002×10^{-3} N·m·s^{-2}
	Specific weight γ	9789 N·m^{-3}
Transport simulation	Time step Δt	0.1 s

Table 6.4. Determination of meeting the requirements for the Taylor-Aris assumption in F1.

Specific discharge	v_c = 1.67 mm/s	v_c = 1.09 mm/s	v_c = 0.55 mm./s
R_0 (mm)	0.88		
$\Delta\bar{t}_{coll}$ (s)	9.37×10^5		
Mean residence time of colloids, $t_{m,coll}$ (s)	286	371	690
Taylor-Aris assumption satisfied for colloids?	No	No	No
$\Delta\bar{t}_{solute}$ (s)	201		
Mean residence time of solute, $t_{m,solute}$ (s)	385	500	856
Taylor-Aris assumption satisfied for solute?	Yes	Yes	Yes

Notes: (1) R_0 represents the measured arithmetic mean aperture of F1. (2) $\Delta\bar{t}_{coll}$ and $\Delta\bar{t}_{solute}$ represents respectively the average time needed for colloid of 1 μm in diameter and solute tracer (Br$^-$) to transverse across the average aperture with diffusion being the only driving force (Zheng et al., submitted, 2008c). (3) The mean residence time is calculated using the following equation (Fahim and Wakao, 1982):

$$t_m = \frac{\int_0^\infty C_{outlet}(t)t\,dt}{\int_0^\infty C_{outlet}(t)dt} - \frac{\int_0^\infty C_{inlet}(t)t\,dt}{\int_0^\infty C_{inlet}(t)dt}$$

where t_m [T] is the mean residence time of colloid transport, and $C_{inlet}(t)$ and $C_{outlet}(t)$ represent the tracer concentration at time t in the upstream and downstream manifolds respectively. (4) If $t_m < \Delta\bar{t}$, then Taylor-Aris assumption is not satisfied; otherwise, Taylor-Aris assumption is satisfied (Zheng et al., submitted, 2008c).

Table 6.5. Effects of straining, sedimentation and attachment on colloid retention in F1.

Factors		Colloid loss caused as percent of the total colloid number released at the inlet under different specific discharges		
		$v_c = 0.55$ mm·s^{-1}	$v_c = 1.09$ mm·s^{-1}	$v_c = 1.67$ mm·s^{-1}
Straining	Straining = false Sedimentation = true Attachment = false	0.0%	0.0%	0.0%
	Straining = true Sedimentation = true Attachment = false	1.0%	0.6%	0.7%
	colloid loss caused by straining	1.0%	0.6%	0.7%
Sedimentation	Straining = true Sedimentation = false Attachment = true	1.9%	1.2%	1.1%
	Straining = true Sedimentation = true Attachment = true	13.2%	6.9%	5.0%
	colloid loss caused by sedimentation	11.3%	5.7%	3.9%
Attachment	Straining = true Sedimentation = true Attachment = false	1.0%	0.6%	0.7%
	Straining = true Sedimentation = true Attachment = true	13.2%	6.9%	5.0%
	colloid loss caused by attachment	12.2%	6.3%	4.3%

Note:

1. If straining = true, the straining mechanisms was considered in the RWPT modeling; otherwise, if straining = false, the straining mechanisms was not considered.

2. The colloid loss caused by a factor under a specific discharge is the difference between the colloid loss when this factor was considered and when it was not considered, while all other factors were kept the same. For example, the colloid loss caused by straining is the difference between the colloid loss when (Straining = false, Sedimentation = false, and Attachment = false) and when (Straining = true, Sedimentation = false, and Attachment = false).

3. When sedimentation = false, $\rho_p = 997$ kg·m^3, $\rho_f = 997$ kg·m^3; and when sedimentation = true, $\rho_p = 1050$ kg·m^3, $\rho_f = 997$ kg·m^3.

Figures

a)

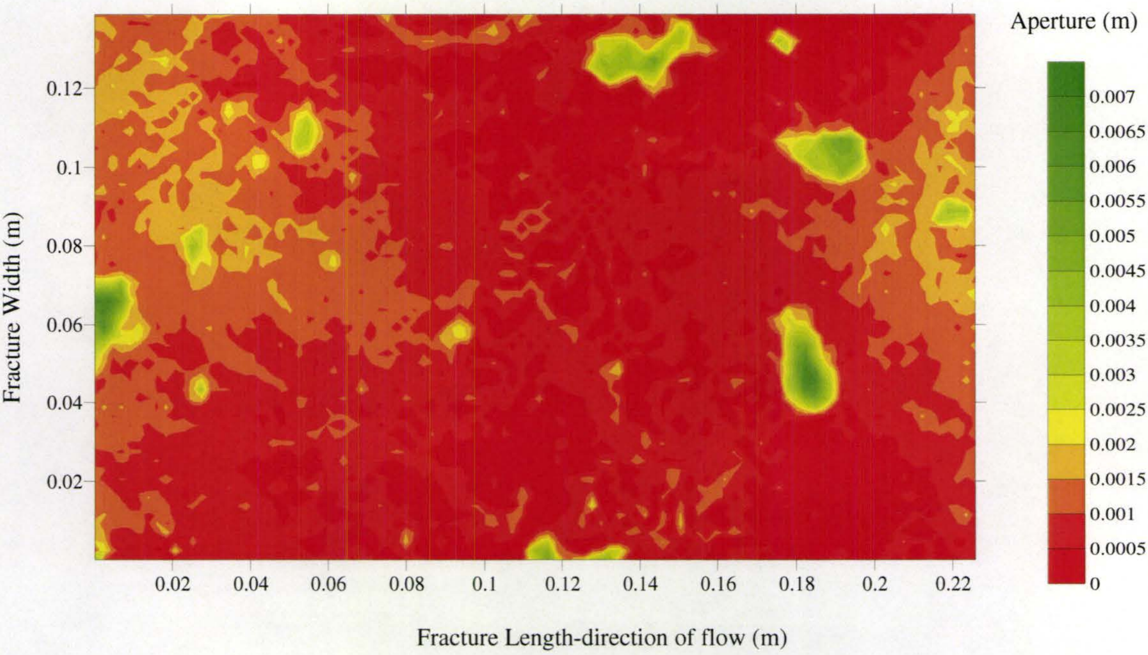
Aperture (m)
0.007
0.0065
0.006
0.0055
0.005
0.0045
0.004
0.0035
0.003
0.0025
0.002
0.0015
0.001
0.0005
0
Fracture Width (m)
0.12
0.1
0.08
0.06
0.04
0.02
0.02
0.04
0.06
0.08
0.1
0.12
0.14
0.16
0.18
0.2
0.22
Fracture Length-direction of flow (m)

b)

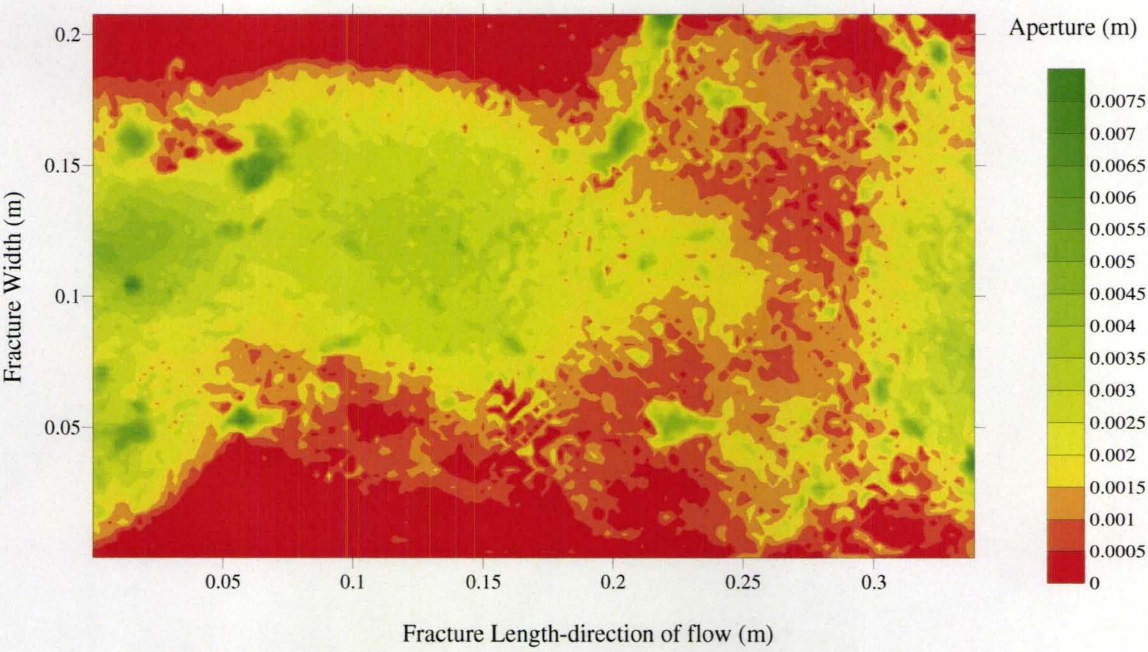
Aperture (m)
0.0075
0.007
0.0065
0.006
0.0055
0.005
0.0045
0.004
0.0035
0.003
0.0025
0.002
0.0015
0.001
0.0005
0
Fracture Width (m)
0.2
0.15
0.1
0.05
0.05
0.1
0.15
0.2
0.25
0.3
Fracture Length-direction of flow (m)

c)

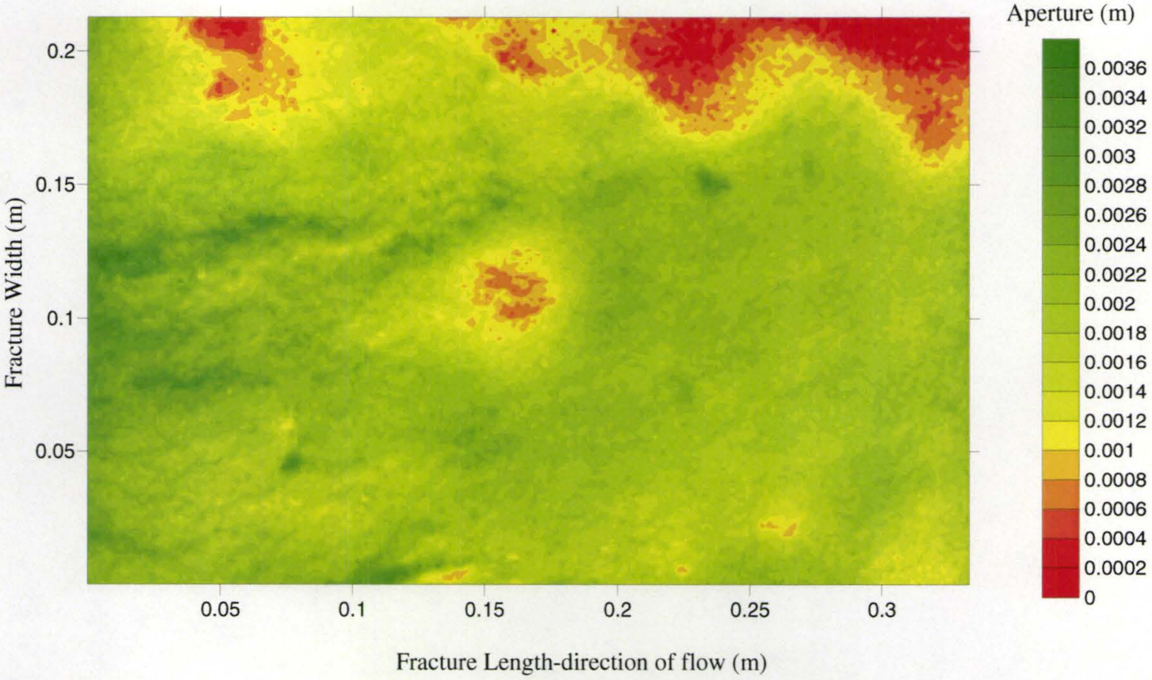

Figure 6.1. Plan view of the aperture fields for a) F1, b) F2, and c) F3 measured using the light transmission technique.

(a)

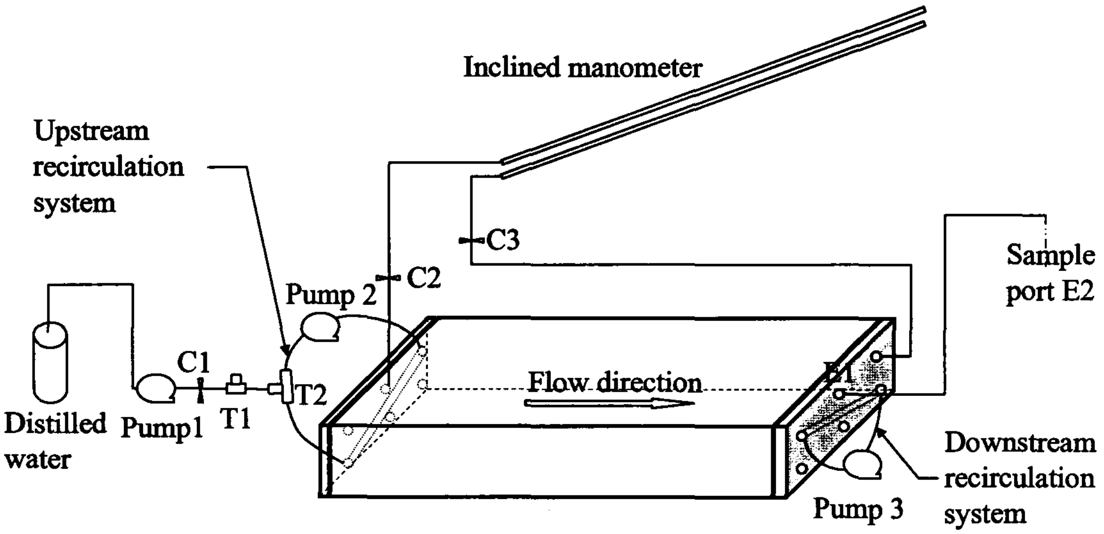
Inclined manometer
Upstream recirculation system
C3
C2
Pump 2
Sample port E2
C1
Flow direction
E1
T2
Distilled water
Pump1
T1
Downstream recirculation system
Pump 3

(b)

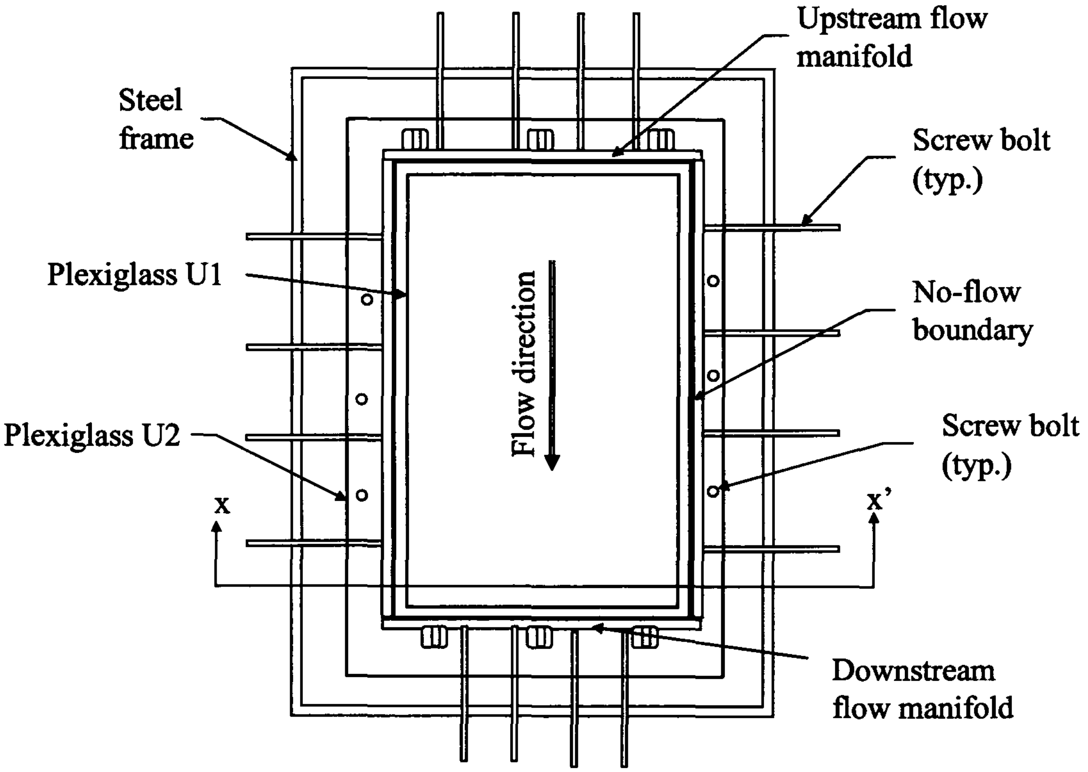
Upstream flow manifold
Steel frame
Screw bolt (typ.)
Plexiglass U1
Flow direction
No-flow boundary
Plexiglass U2
Screw bolt (typ.)
x
x'
Downstream flow manifold

(c)

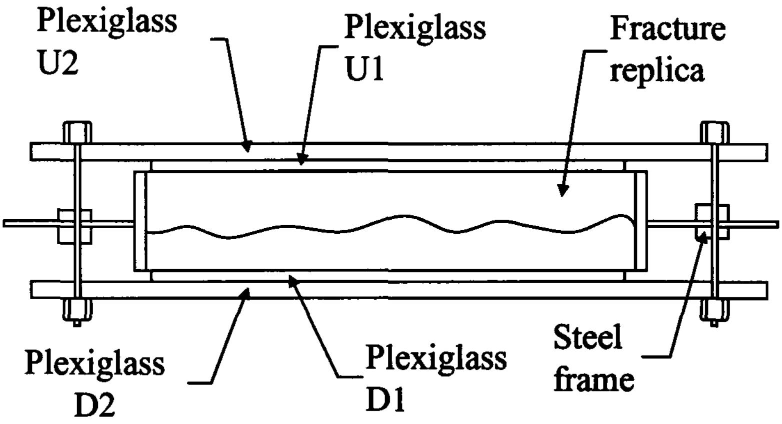

Figure 6.2. Schematic diagram of the experimental apparatus for the hydraulic and tracer tests showing a) the experimental setup, b) a plan view of the fracture mounted in the steel frame, and c) a cross-section *x*-*x*′ of the experimental fracture mounted in the steel frame.

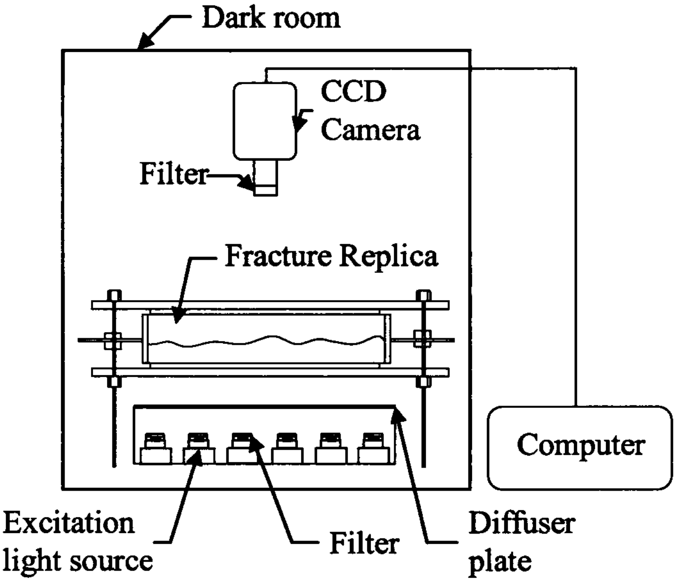

Figure 6.3. Schematic diagram of the visualization system.

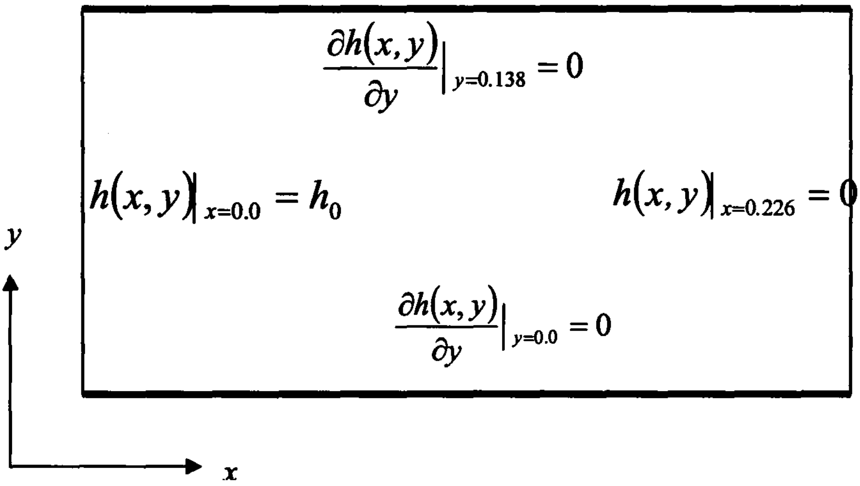

Figure 6.4. Schematic diagram of the coordinate system and boundary conditions for the flow and colloid transport simulations.

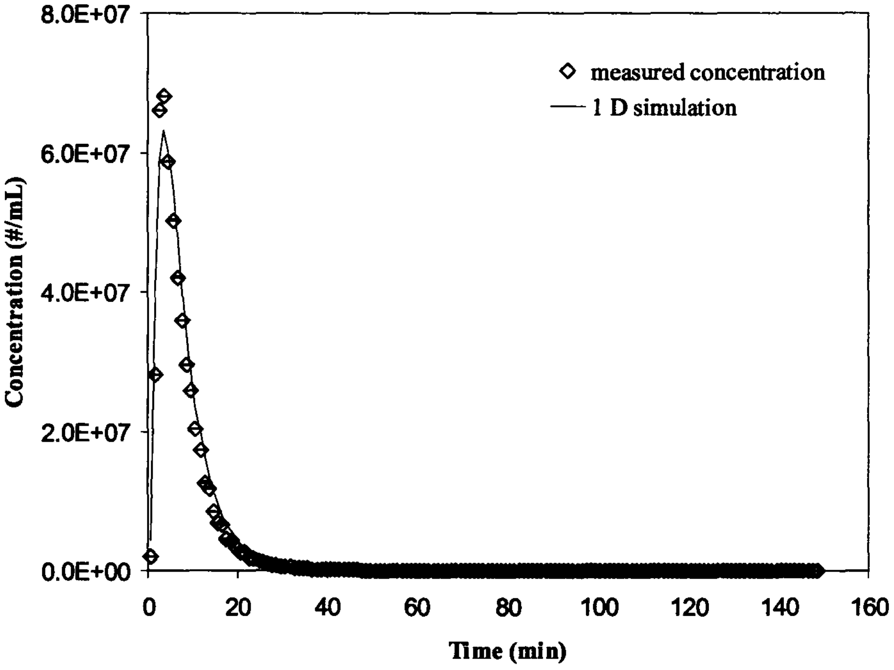

Figure 6.5. Breakthrough curves for the colloid tracer test in F1 with v_c = 1.67 mm/s, and I_c = 0.01. ◇: experimental measurement (error bars represent one standard deviation, on the order of magnitude 10^3 to 10^4); and —— : one dimensional simulation employing both $v_{f,coll}$ and α_L as fitting parameters.

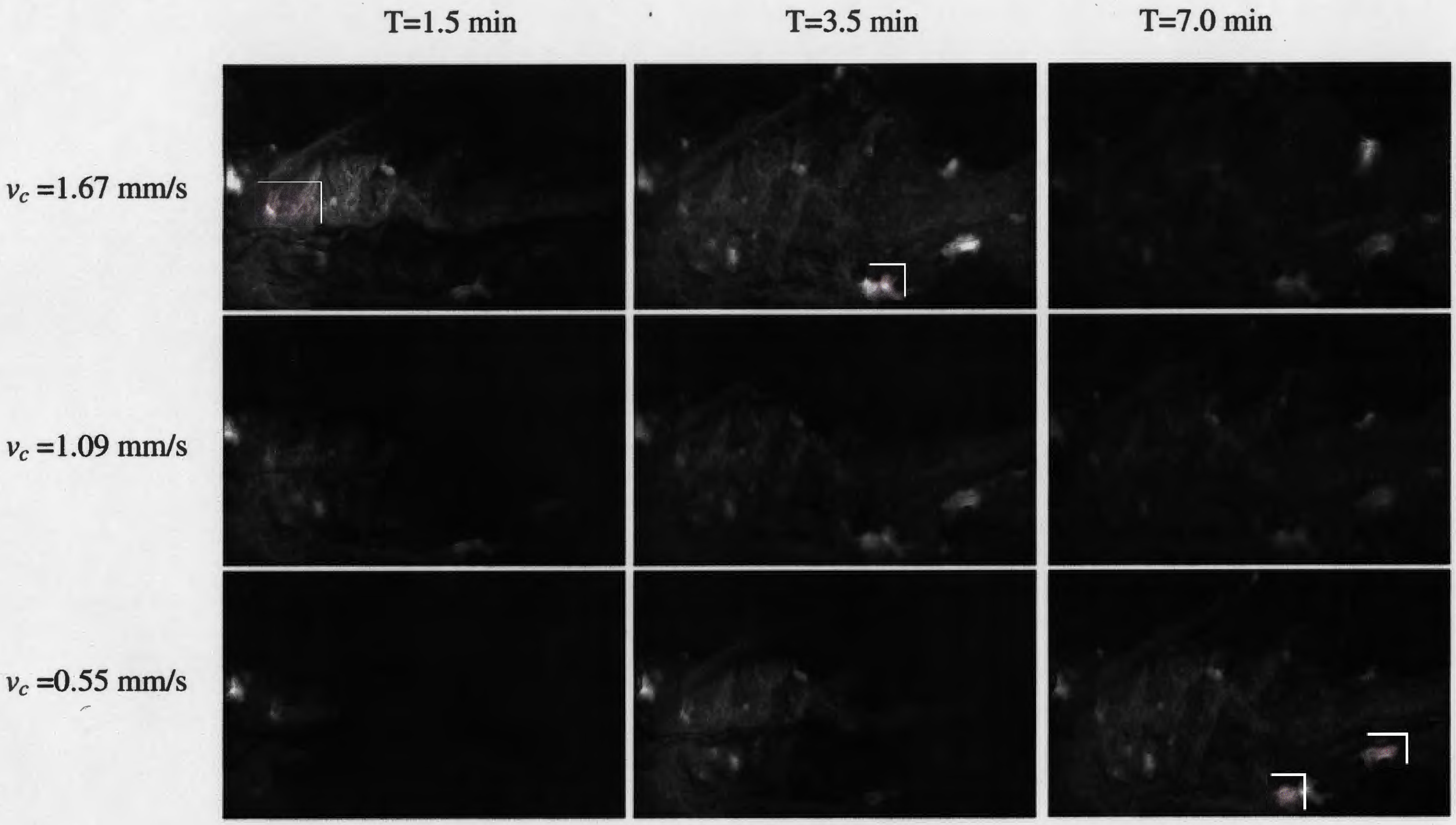

Figure 6.6(a). Visualization of the colloid transport plume development in F1 under a range of specific discharges at various time steps (I_c = 0.1 mM).

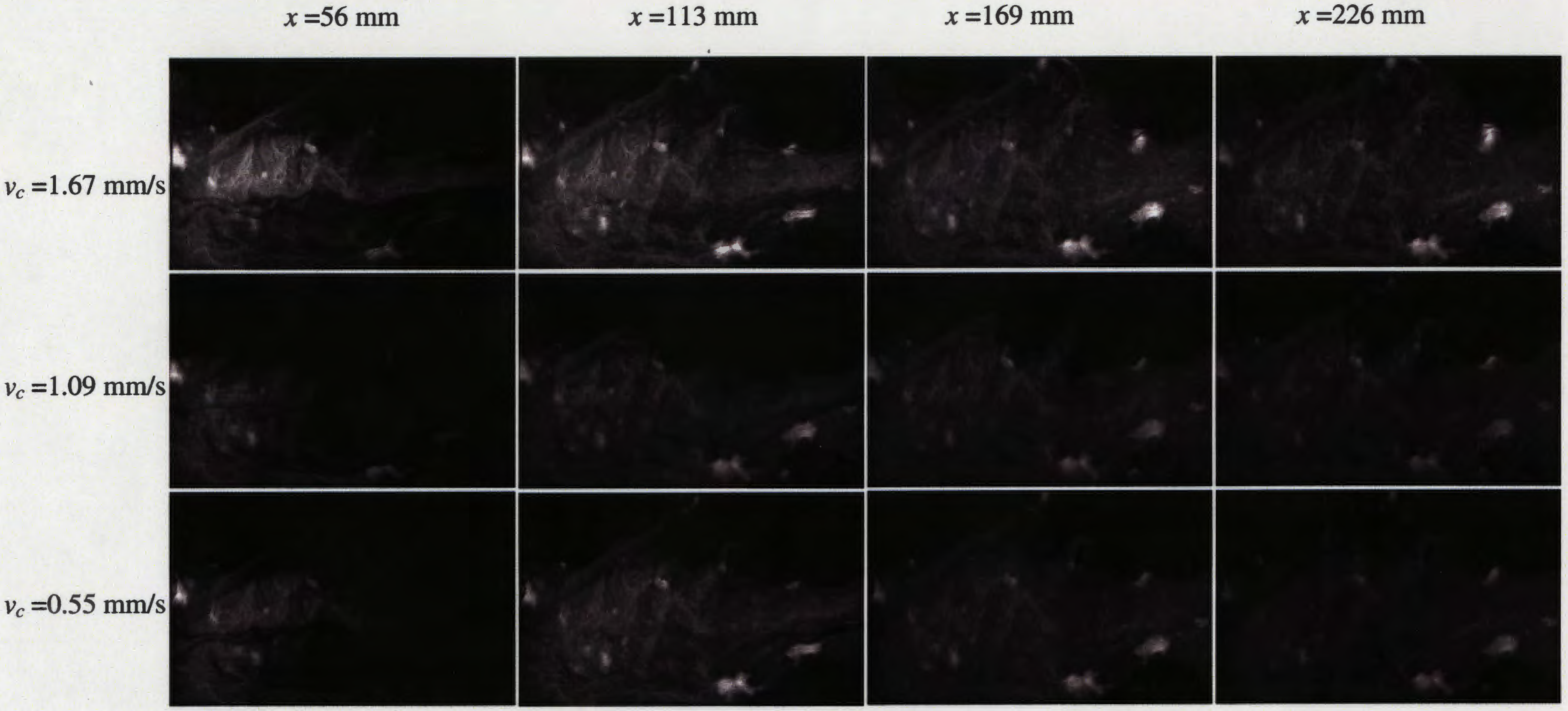

Figure 6.6(b). Visualization of the colloid transport plume development in F1 under a range of specific discharges at various travel distance of the center of mass (I_c = 0.1 mM). The travel distance of the center of mass is calculated based on the colloid mean transport velocity $v_{f,coll}$ in Table 6.1.

(a)

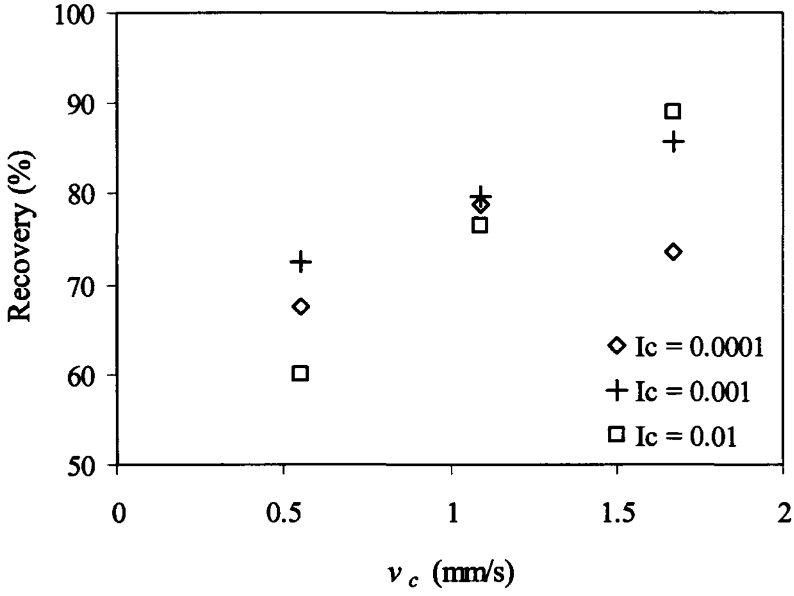
Recovery (%)
100
90
80
70
60
50
0
0.5
1
1.5
2
v_c (mm/s)
◇ Ic = 0.0001
+ Ic = 0.001
□ Ic = 0.01

(b)

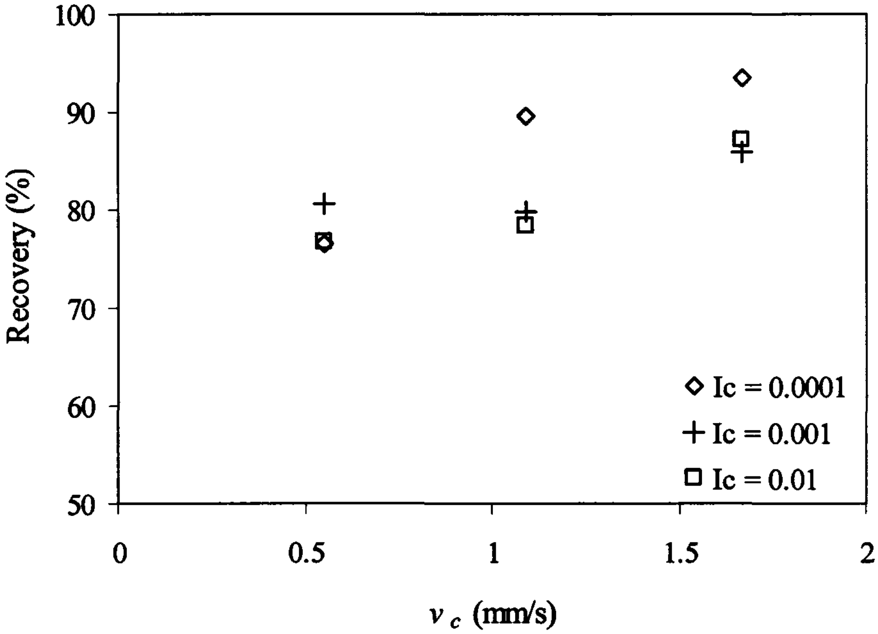
Recovery (%)
100
90
80
70
60
50
0
0.5
1
1.5
2
v_c (mm/s)
◇ Ic = 0.0001
+ Ic = 0.001
□ Ic = 0.01

(c)

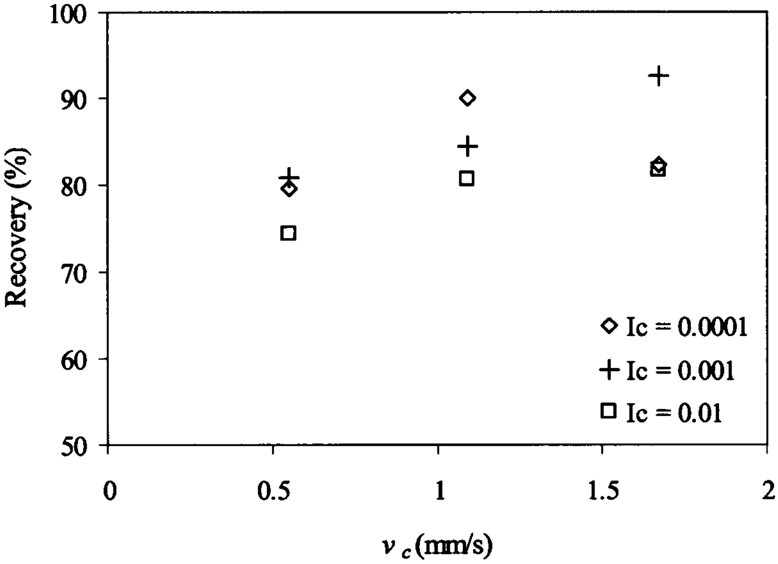
Recovery (%)
100
90
80
70
60
50
0
0.5
1
1.5
2
v_c (mm/s)
◇ Ic = 0.0001
+ Ic = 0.001
□ Ic = 0.01

(d)

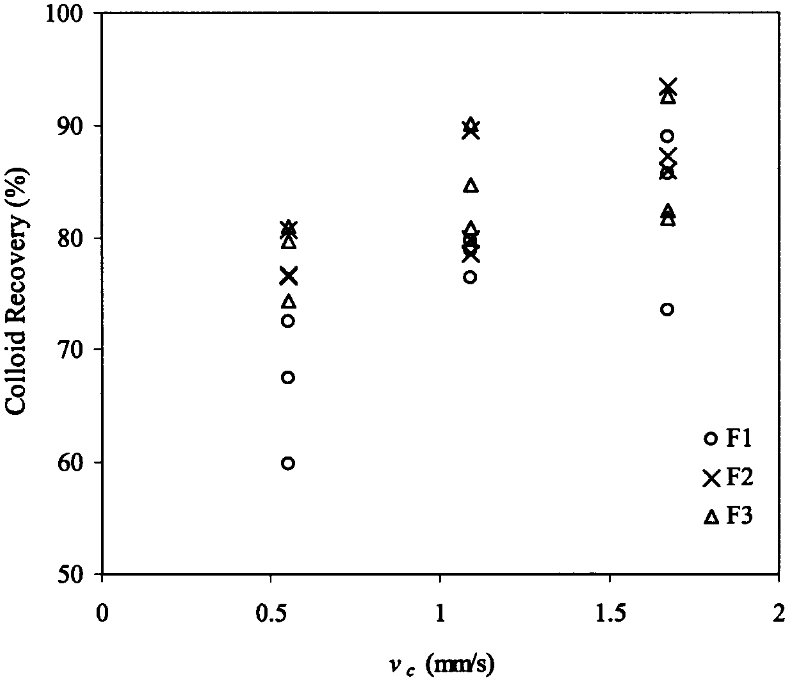
Colloid Recovery (%)
100
90
80
70
60
50
0
0.5
1
1.5
2
v_c (mm/s)
○ F1
× F2
△ F3

Figure 6.7. Effect of specific discharge (v_c) and ionic strength (I_c) on colloid recovery in (a) F1, (b) F2, and (c) F3. (d) shows the effect of specific discharge (v_c), ionic strength (I_c) and aperture field variability on colloid recovery in F1, F2, and F3.

(a)

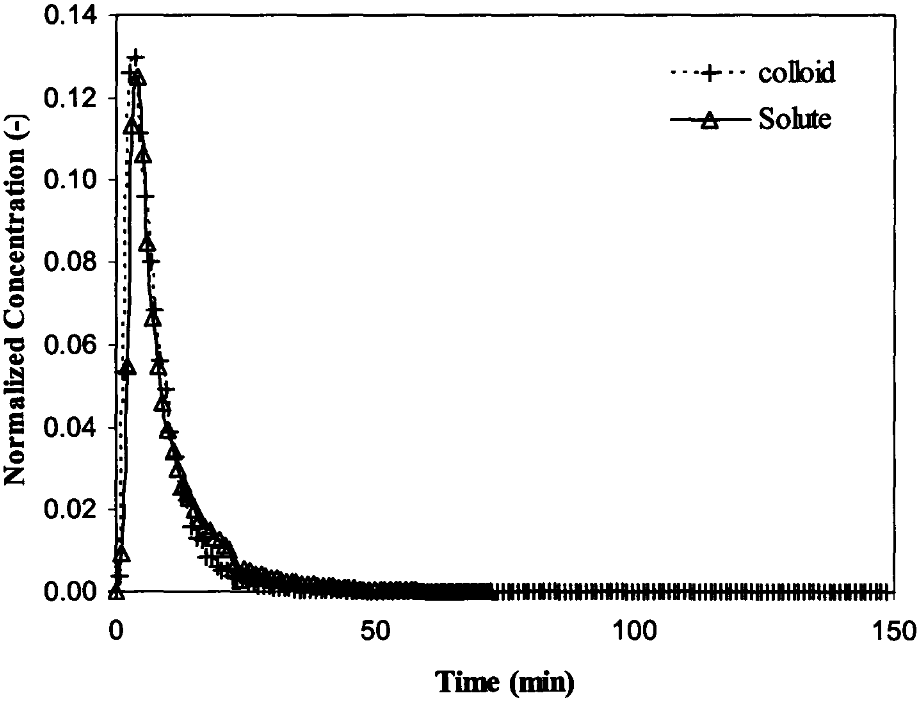
0.14
0.12
0.10
0.08
0.06
0.04
0.02
0.00
Normalized Concentration (-)
0
50
100
150
Time (min)
colloid
Solute

(b)

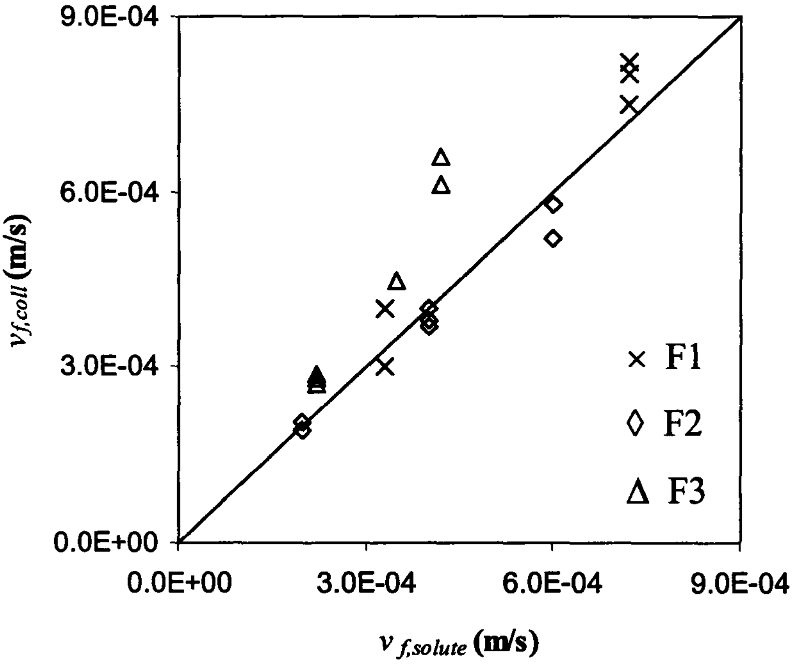
9.0E-04
6.0E-04
3.0E-04
0.0E+00
$v_{f,coll}$ (m/s)
0.0E+00
3.0E-04
6.0E-04
9.0E-04
$v_{f,solute}$ (m/s)
× F1
◊ F2
Δ F3

(c)

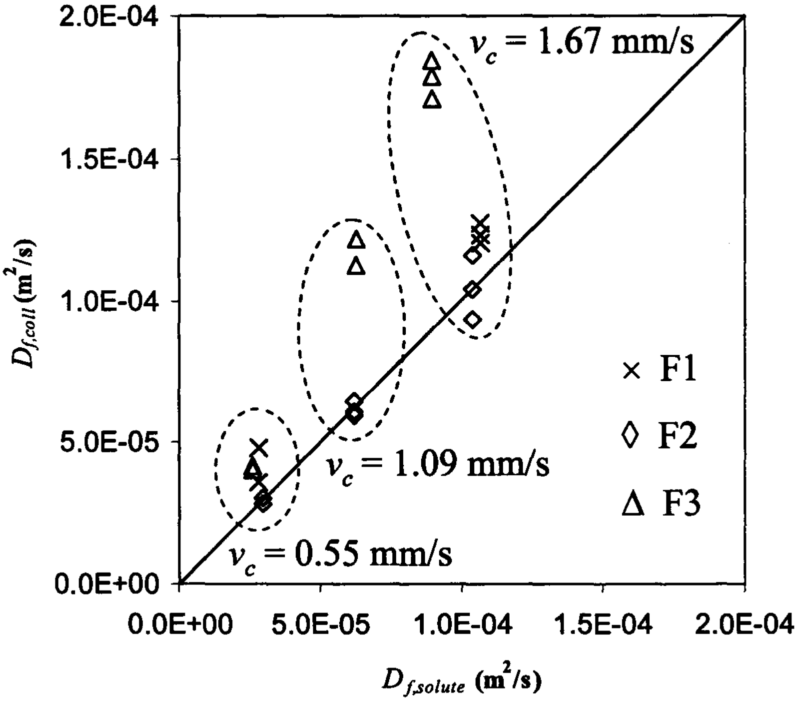

Figure 6.8. Comparison of colloid and solute transport in terms of (a) the typical normalized breakthrough curves for F1 (v_c = 1.67 mm/s, I_c = 0.01), where the normalized concentration $= \frac{C(t)}{\int_0^\infty C(t)dt}$, and $C(t)$ is the effluent concentration, (b) the mean transport velocity, and (c) the longitudinal dispersion coefficient for solutes and colloids.

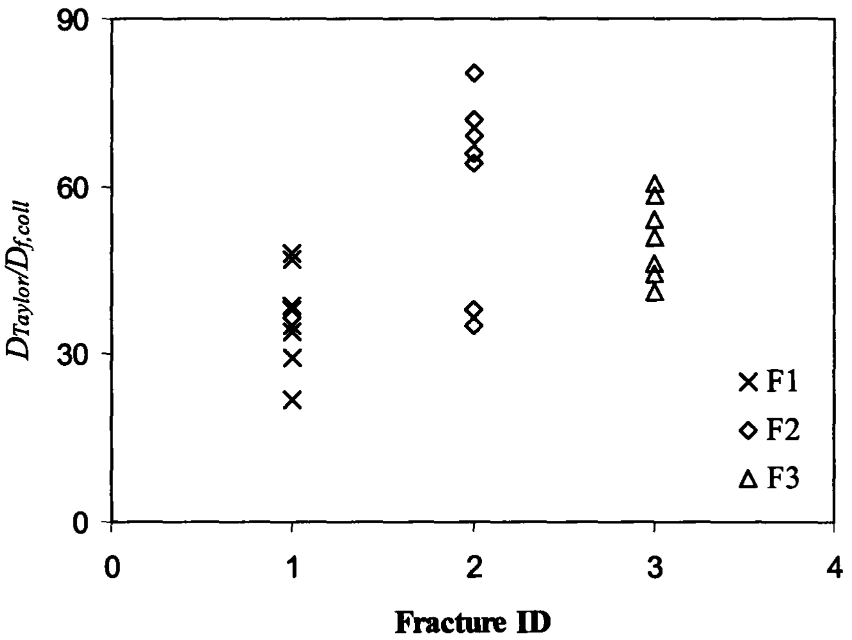

Figure 6.9. Comparison of the Taylor and longitudinal dispersion coefficients obtained through fitting the ADE to the experimental colloid breakthrough curves.

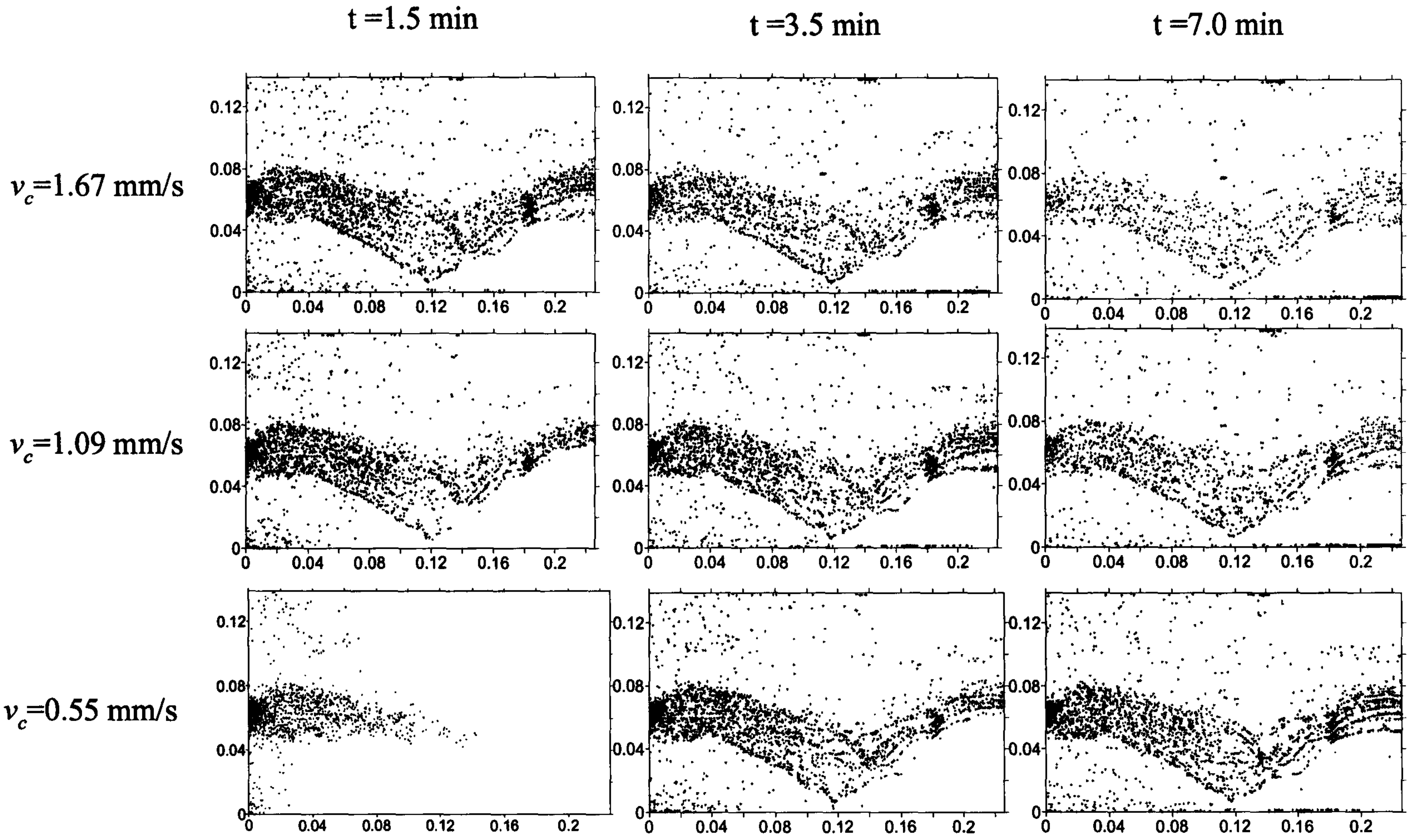

Figure 6.10. Colloid plume development simulated using the Reynolds equation in combination with RWPT in F1, at various times, under a range of specific discharges.

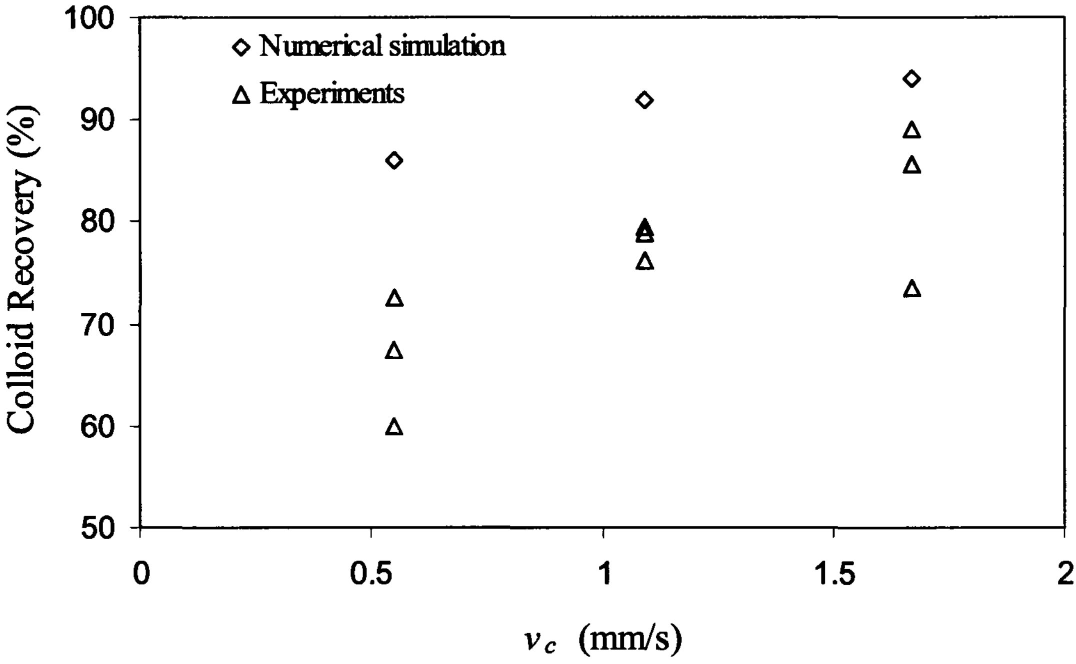

Figure 6.11. Effects of specific discharge on colloid recovery in F1 based on numerical simulation and laboratory experiments.

Chapter 7 Conclusions and Research Recommendations

Contributions made in this thesis take the form of technical journal papers. This chapter summarizes the key conclusions from each paper, and recommends future research.

7.1 Conclusions

A series laboratory-scale conservative solute tracer experiments through three distinct fracture replicas presented in Chapter 3 demonstrated that:

1. Among the three equivalent apertures defined by Tsang (1992), the mass balance aperture is the only equivalent aperture appropriate for describing solute transport in single variable-aperture fractures.
2. The close agreement between the experimental mass balance aperture and the arithmetic mean aperture from the direct aperture measurement in F2 (and direct measurement data for F1 and F3 presented in Chapter 6) supports Tsang's (1992) argument that the mass balance aperture represents the true arithmetic mean aperture.

Chapter 4 presents a full factorial design of numerical simulations investigating the effect of aperture field statistics (i.e., μ_b, σ_b, and AR) on dispersivity and dispersion regimes. The primary conclusions are:

3. The arithmetic mean aperture μ_b and, to a lesser degree, the standard deviation σ_b, influence the value of D_{Taylor}/D_G, and hence the dominant dispersion regime. When the hydraulic gradient is fixed, D_{Taylor} accounts for a larger fraction of D_{TL} for aperture fields with a larger CoV. The influence of AR on dispersion regimes, however, seems insignificant for the correlation structure of the aperture fields employed in this research.

4. The simulation results also revealed the interactive effects of the CoV and AR on dispersivity in fractures. It was found that the dispersivity, as well as the spread of dispersivity, increases as the CoV increases. The effect of the AR is significant only when the CoV is large. Therefore, if the CoV is not large (<0.2), the isotropic dispersivity tensor can be used to replace the anisotropic dispersivity tensor in numerical models simulating solute transport in variable-aperture fractures without introducing unacceptable errors.

Numerical simulations conducted to investigate differential transport between colloids and molecular-scale solutes in single fractures are presented in Chapter 5, and yielded the following conclusions:

5. A concept, the Taylor-Aris assumption, was proposed, and the formula developed by James and Chrysikopoulos (2001) can be employed to determine whether the Taylor-Aris assumption is satisfied or violated.
6. For colloid and solute transport in parallel-plate fractures, it was demonstrated that there exists a threshold value of δ_0, the ratio of the colloid radius to half the fracture aperture, where the retention time for solutes and colloids are very similar. When $\delta > \delta_0$, the Taylor-Aris assumption is satisfied, and the relative retention time τ_p decreases as δ increases, as is well documented in the HDC literature. Conversely, when $\delta < \delta_0$, the Taylor-Aris assumption is violated, and the relative retention time, τ_p, increases as δ decreases. This phenomenon for differential transport has not been reported before. Additionally, when the Taylor-Aris assumption is violated, the retention time for colloids is much smaller than that for molecular-scale solutes. This large difference cannot be explained by size and/or charge exclusion alone; it is primarily due to the combined effects of the small diffusion coefficients of colloids relative to solutes, together with the parabolic velocity profile across the aperture.

7. When the Taylor-Aris assumption is violated, the Taylor dispersion coefficient and its extension by James and Chrysikopoulos (2003) will significantly overestimate the colloid dispersion coefficient in single fractures.
8. The results of simulations conducted in variable-aperture fractures show that τ_p increases with increasing CoV, which means that the velocity enhancement of colloids relative to solutes decreases with increasing heterogeneity. Additionally, the ratio of $D_{L,coll}/D_{L,solute}$ decreases by several orders of magnitude to approximately one with increasing CoV, which means that the difference between the dispersion coefficients of colloids and solutes will become smaller with increasing heterogeneity. The results also show that the AR does have an impact on τ_p and $D_{L,coll}/D_{L,solute}$, however, its influence is much smaller than that of the CoV.

Chapter 6 presented a 3^3 factorial series of laboratory-scale colloid tracer tests conducted to investigate the impact of aperture field variability, specific discharge, and ionic strength on colloid transport processes. Numerical simulations and visualization techniques provided further insights on several transport processes (i.e., dispersivity, straining, size exclusion, and gravitational settling). The findings from this work include:

9. In the physical experiments, (1) colloids migrated along preferential pathways, which were composed of larger aperture regions interconnected from the inlet to outlet sides of the fracture, and bypass some aperture regions; (2) the colloid plume is irregular in shape, and becomes more irregular with increasing specific discharge, indicating non-Fickian transport. These two phenomena lead to one important corollary: the dispersivity cannot be determined by the aperture field statistics alone; it is also a function of specific discharge. This is believed to explain (at least partially) the difference between the dispersivities obtained from physical experiments and those from the expression developed by Gelhar (1993).
10. The colloid recovery in each fracture was found to increase with increasing specific discharge. For each specific discharge, the colloid recoveries in F2 and

F3 were similar, and larger than that in F1. This pattern is consistent with the relative magnitude of the arithmetic mean apertures of these three fractures, that is, $\mu_{b,F2}$ and $\mu_{b,F3}$ are similar, and both significantly larger than $\mu_{b,F1}$. The effect of ionic strength on colloid recovery did not follow the theoretical premise that colloid recovery increases with decreasing ionic strength. These observations lead to the conclusion that the transport step (the step in which the colloids are transported from the bulk fluid to the vicinity of the fracture wall), and not the attachment step, plays the dominant role in the colloid sorption process. The numerical simulations support this conclusion.

11. The numerical simulations demonstrated that gravitational settling plays an important role in colloid transport from the bulk fluid to the fracture wall, resulting in significant colloid retention due to this mechanism. In contrast, the colloid retention caused by straining only accounted for an insignificant fraction (approximately 1% in F1) of the colloids released.
12. The difference between the transport velocities and dispersion coefficients (obtained through fitting procedures) of colloids and solutes decreased with increasing CoV. Specifically, it was observed that in F3 (CoV=0.29), colloids had significantly larger mean transport velocities and dispersion coefficients than solutes. However, in F1 (CoV=0.78) and F2 (CoV=0.71), the difference between the colloid and solute transport velocities and dispersion coefficients was not significant. This is consistent with the simulation results from Chapter 5.

7.2 Future research recommendations

- Numerical simulations using aperture fields with a larger range of correlation lengths and ARs would help to clarify the effect of anisotropy on dispersion regime and differential transport.
- Inclusion of the pore exclusion mechanism in the RWPT model would improve the prediction of colloid transport in single variable-aperture fractures.

- Characterization of the fracture and colloid surface properties would enhance our understanding of the effect of ionic strength on colloid recovery.
- Laboratory experiments through parallel-plate fractures under controlled conditions by keeping colloid diameter constant while changing the fracture aperture, and by keeping the fracture aperture unchanged while varying the colloid diameter would complement the differential transport findings from Chapter 5.
- Larger scale experiments on colloid transport in variable-aperture fractures would enhance our understanding of the different transport mechanisms.

Appendix A Supplemental Information for Chapter 3

This appendix contains plots of the experimental breakthrough curves associated with each of the nine solute trace tests except the one already presented in Chapter 3 (Figure 3.4). Each figure shows the solute breakthrough curve, three one-free-parameter fitting curves based on the cubic law aperture, frictional loss aperture, and the mass balance aperture respectively, and one two-free-parameter fitting curve, which employed the solute transport velocity and dispersion coefficient as the free parameters. The experimental breakthrough curves for the solute tracer test in F1, with v_c = 1.09 mm/s, was not included here due to the fact that, the upstream recirculation pump was not turned on during this tracer test, and therefore the concentration profile in the upstream manifold was not exponentially decreasing.

(a)

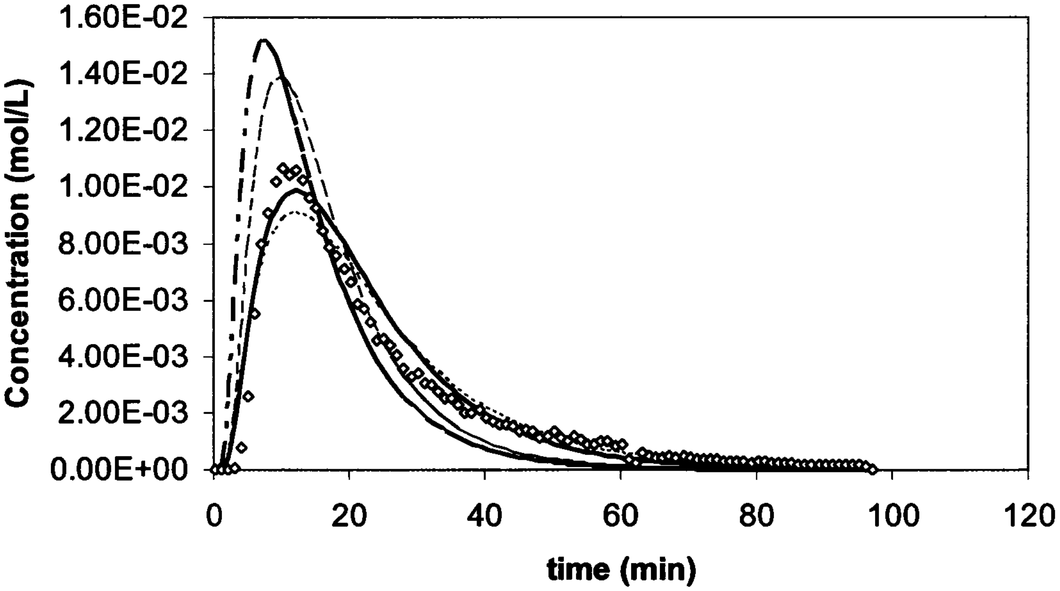
Concentration (mol/L)
1.60E-02
1.40E-02
1.20E-02
1.00E-02
8.00E-03
6.00E-03
4.00E-03
2.00E-03
0.00E+00
0
20
40
60
80
100
120
time (min)

(b)

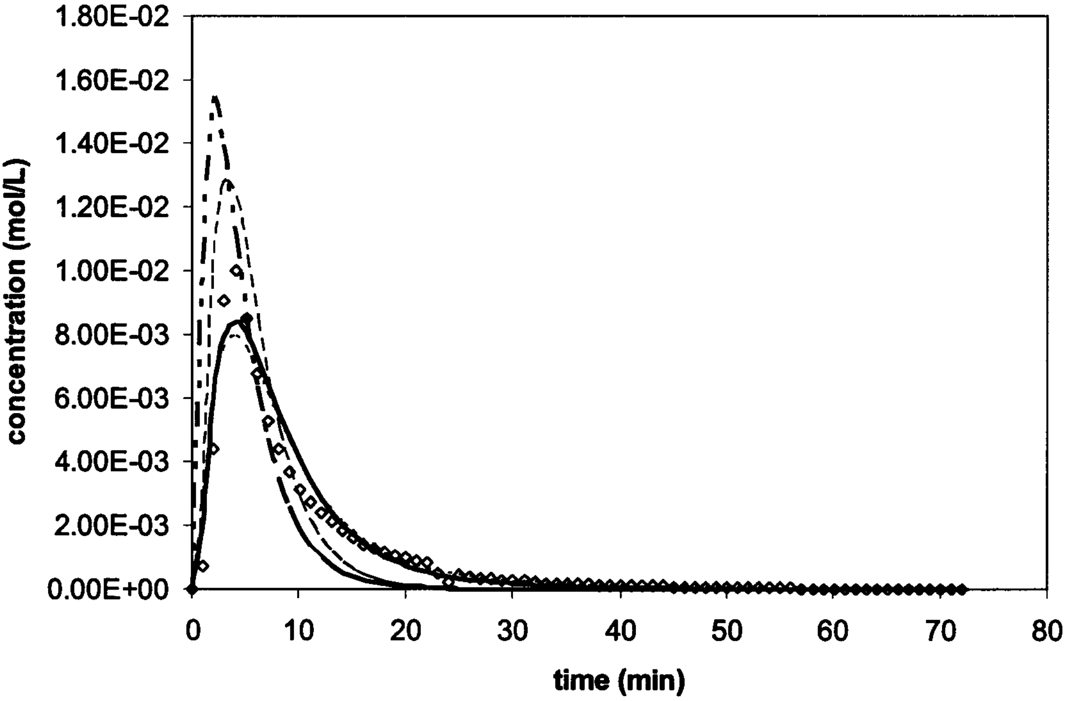
concentration (mol/L)
1.80E-02
1.60E-02
1.40E-02
1.20E-02
1.00E-02
8.00E-03
6.00E-03
4.00E-03
2.00E-03
0.00E+00
0
10
20
30
40
50
60
70
80
time (min)

(c)

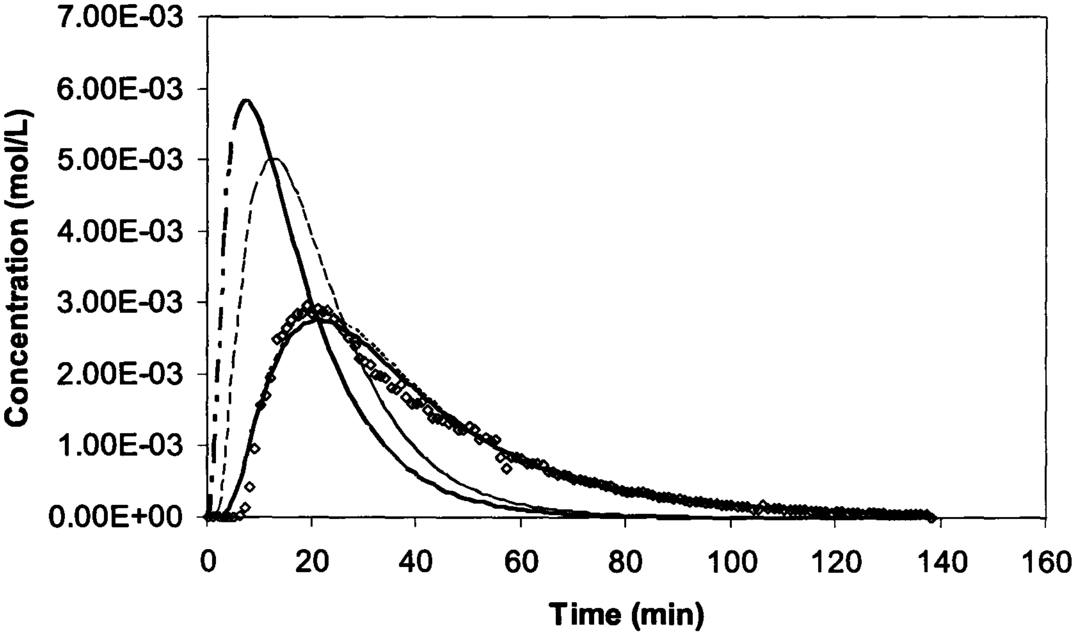
7.00E-03
6.00E-03
5.00E-03
4.00E-03
3.00E-03
2.00E-03
1.00E-03
0.00E+00
Concentration (mol/L)
0
20
40
60
80
100
120
140
160
Time (min)

(d)

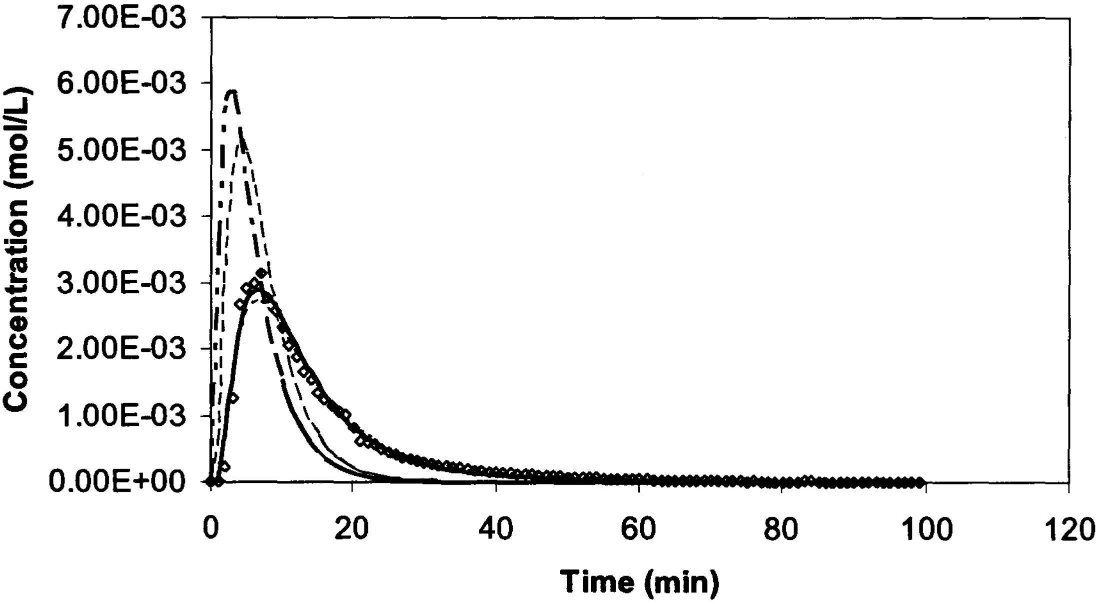
7.00E-03
6.00E-03
5.00E-03
4.00E-03
3.00E-03
2.00E-03
1.00E-03
0.00E+00
Concentration (mol/L)
0
20
40
60
80
100
120
Time (min)

(e)

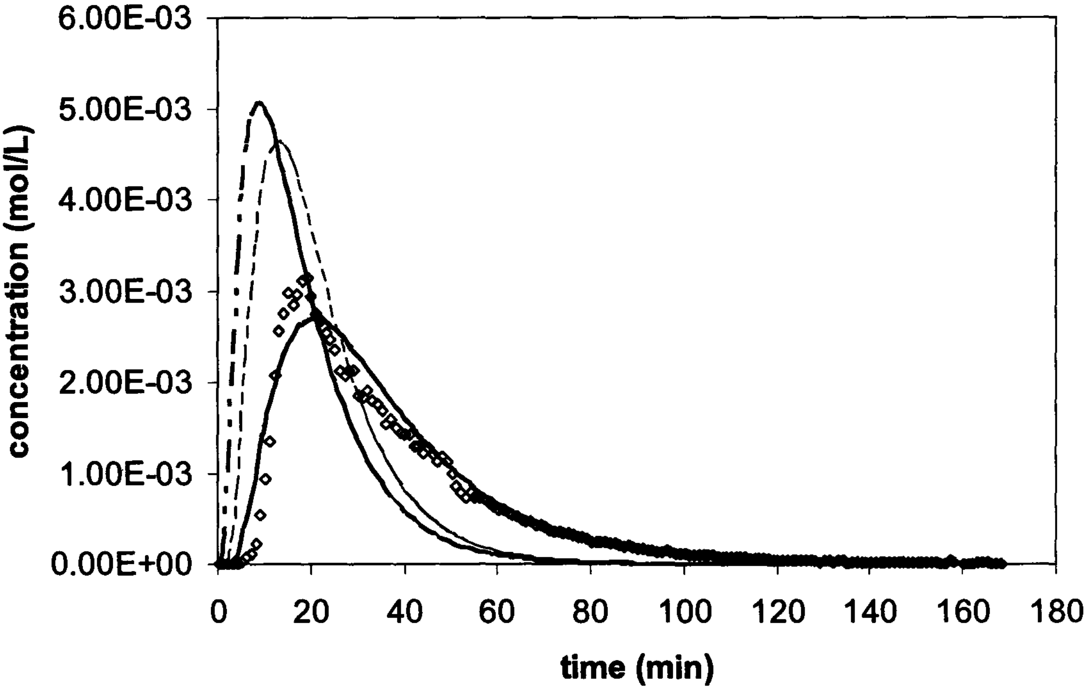
6.00E-03
5.00E-03
4.00E-03
3.00E-03
2.00E-03
1.00E-03
0.00E+00
concentration (mol/L)
0
20
40
60
80
100
120
140
160
180
time (min)

(f)

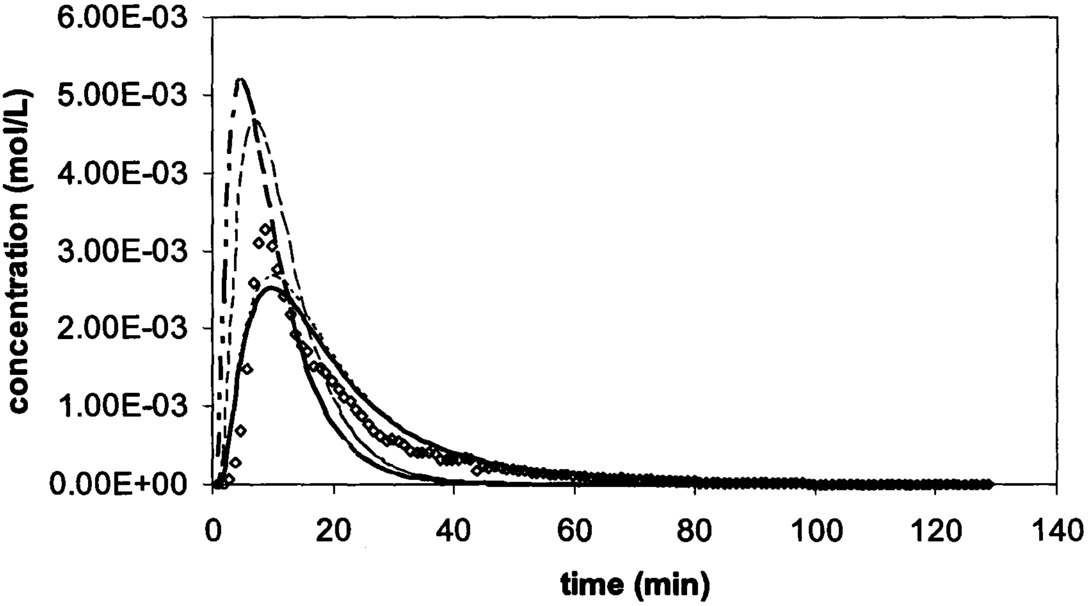
6.00E-03
5.00E-03
4.00E-03
3.00E-03
2.00E-03
1.00E-03
0.00E+00
concentration (mol/L)
0
20
40
60
80
100
120
140
time (min)

(g)

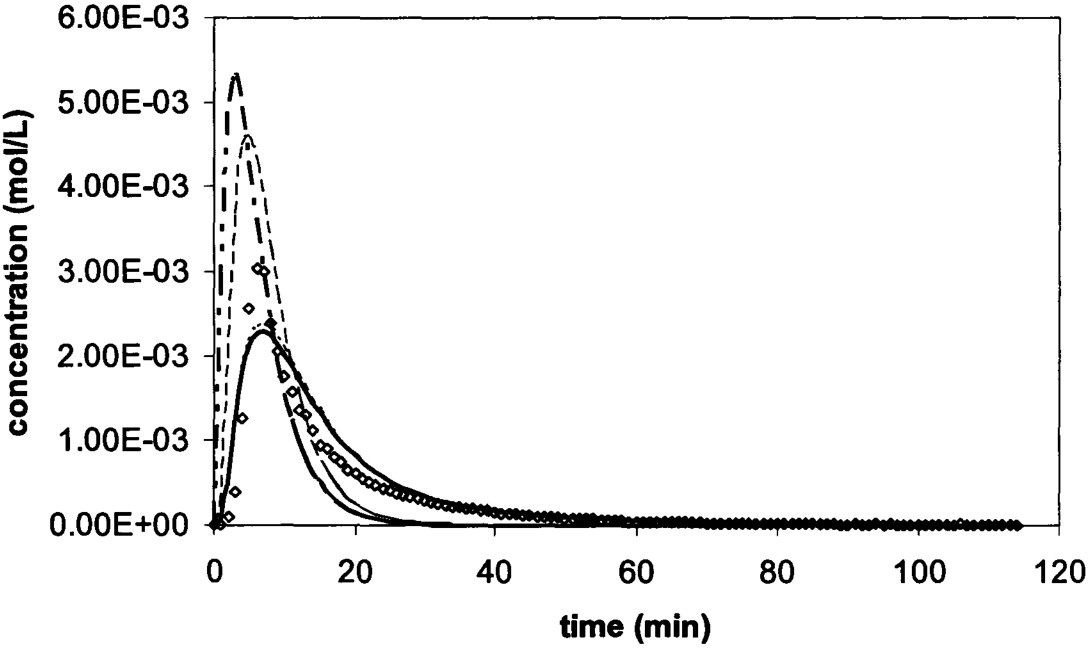

Figure A1. Breakthrough curves for the solute tracer test in a) F1 with $v_c = 0.56$ mm/s, b) F1 with $v_c = 1.67$ mm/s, c) F2 with $v_c = 0.56$ mm/s, d) F2 with $v_c = 1.67$ mm/s, e) F3 with $v_c = 0.56$ mm/s, f) F3 with $v_c = 1.09$ mm/s and g) F3 with $v_c = 1.67$ mm/s, where v_c is the specific discharge based on the cubic law aperture. ◊: experimental measurement; - - - - : simulation based on μ_c from physical experiment breakthrough curves and α_c as the fitting parameter; ··········· : simulation based on μ_m from physical experiment breakthrough curves and α_m as the fitting parameter; — · · : simulation based on μ_l from the physical experiment breakthrough curves and α_l as the fitting parameter, and ——— : simulation employing both v_f and α_f as fitting parameters.

Appendix B Supplemental Information for Chapter 6

This appendix contains plots of the experimental breakthrough curves and the corresponding one-dimensional fitting curves associated with each of the 27 colloid transport experiments, except the one presented in Chapter 6 (Figure 6.5 and 6.8(a)). In addition, plots showing the comparison of the normalized colloid and solute breakthrough curves for each specific discharge were also included, with the intention of demonstrating the differential transport between the colloid and solute. The normalized concentration is equal to $\frac{C(t)}{\int_0^\infty C(t)dt}$, where $C(t)$ is the effluent concentration. These figures show that differential transport is most obvious in F3, and not very obvious in F1 and F2.

(a)

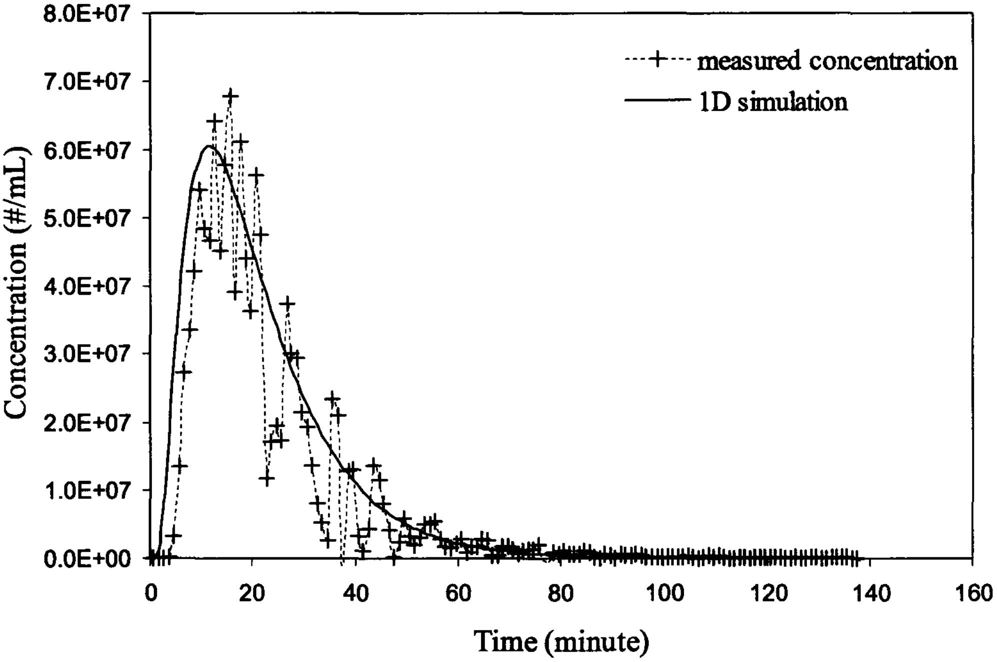

(b)

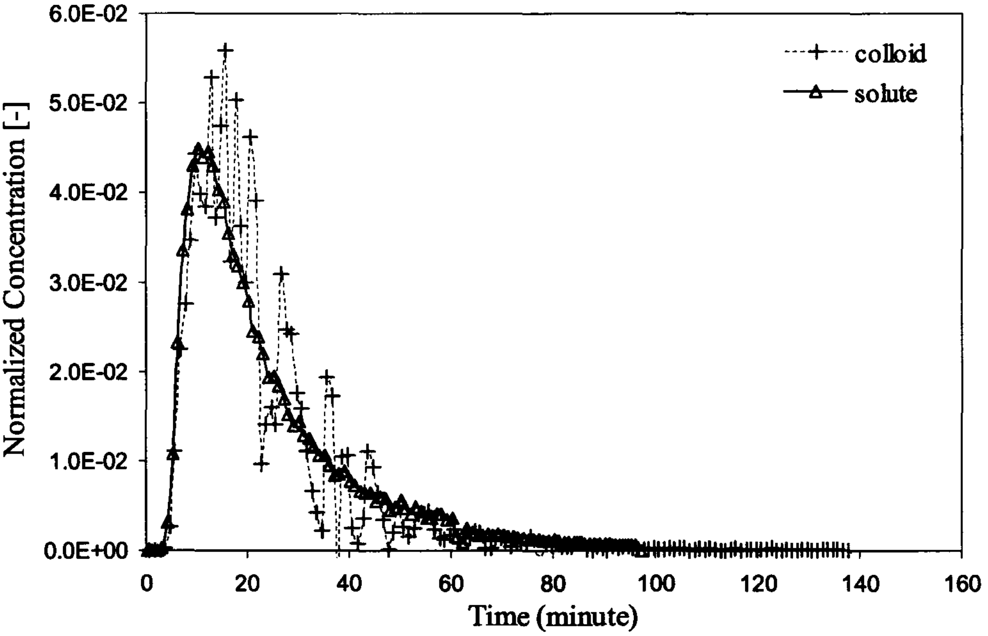

Figure B1.1 (a) Breakthrough curves for the colloid tracer tests in F1 with v_c = 0.55 mm/s, and Ic = 0.0001 and the one dimensional fitting results, and (b) comparison of the normalized colloid and solute breakthrough curves.

(a)

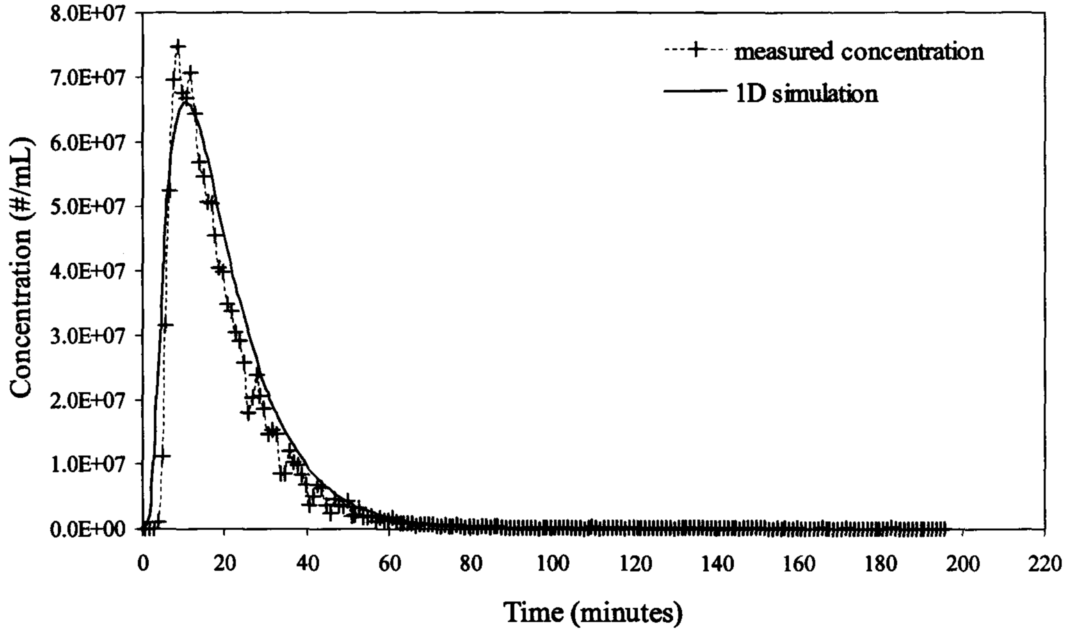

(b)

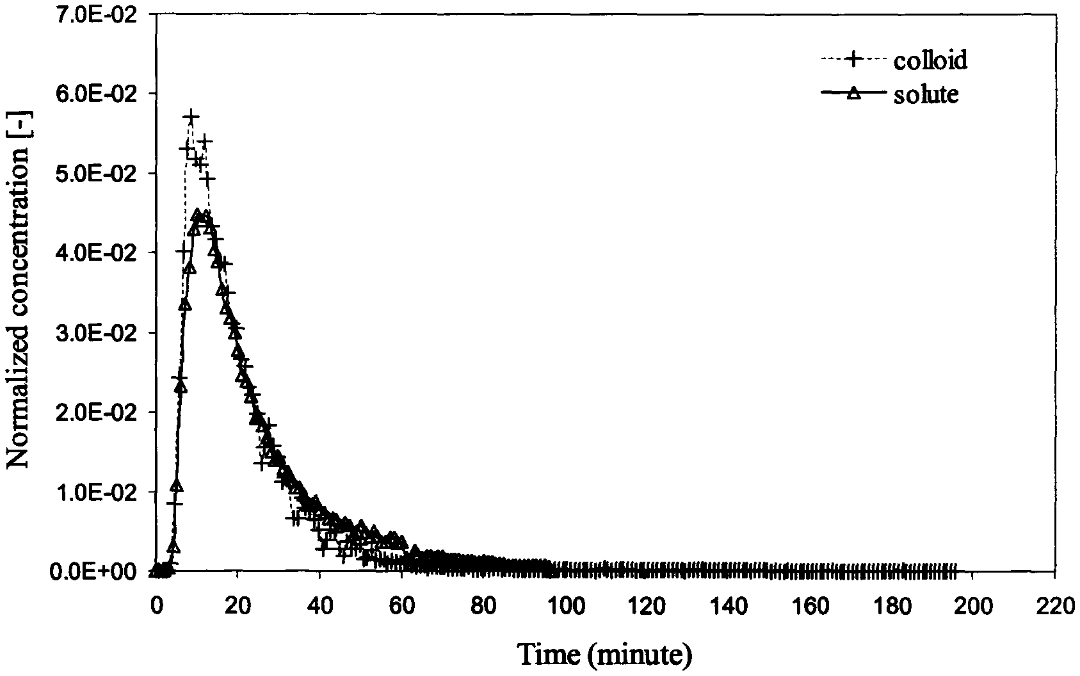

Figure B1.2 (a) Breakthrough curves for the colloid tracer tests in F1 with v_c = 0.55 mm/s, and Ic = 0.001 and the one dimensional fitting results, and (b) comparison of the normalized colloid and solute breakthrough curves.

(a)

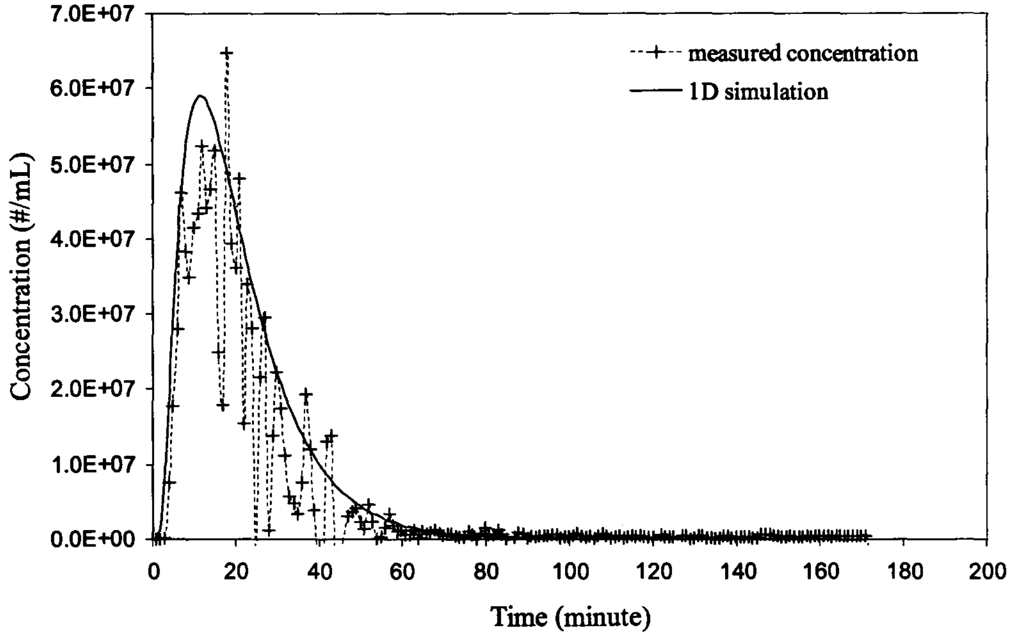

(b)

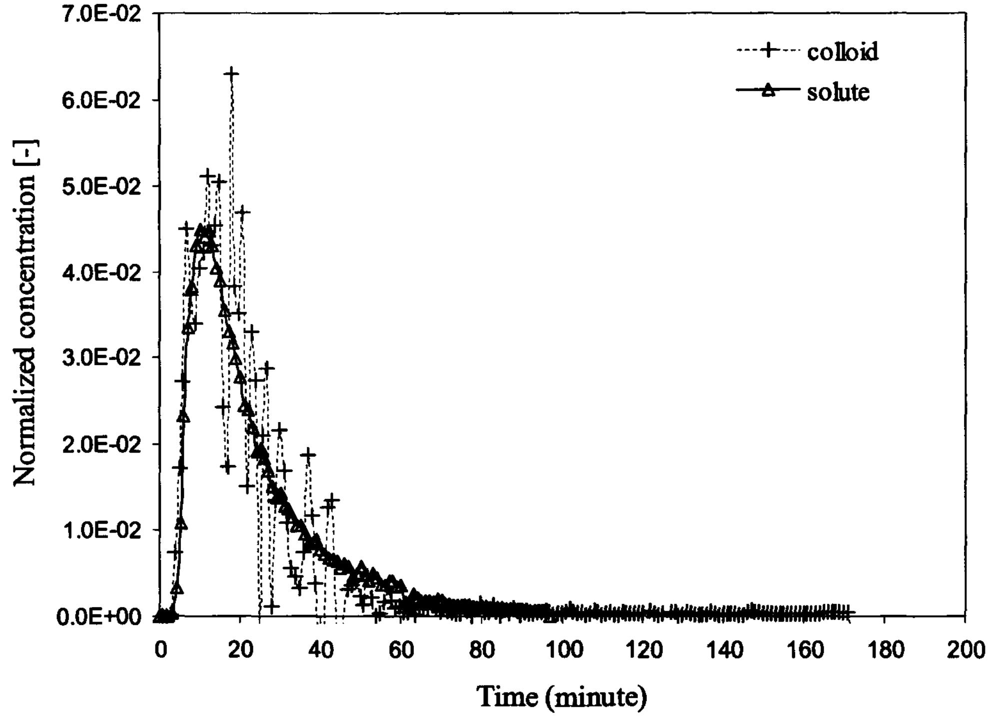

Figure B1.3 (a) Breakthrough curves for the colloid tracer tests in F1 with v_c = 0.55 mm/s, and Ic = 0.01 and the one dimensional fitting results, and (b) comparison of the normalized colloid and solute breakthrough curves.

(a)

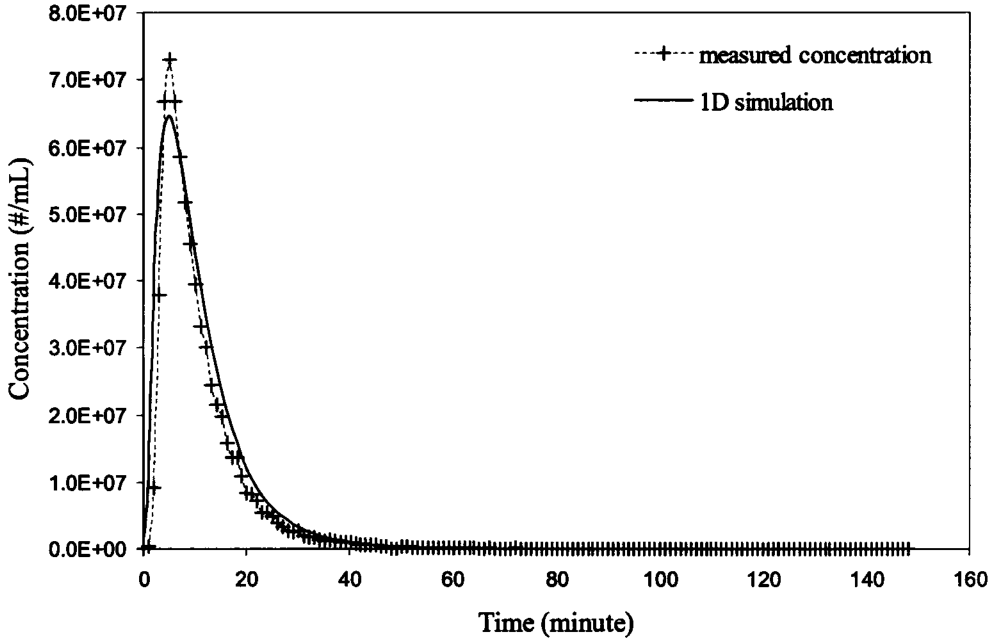

(b)

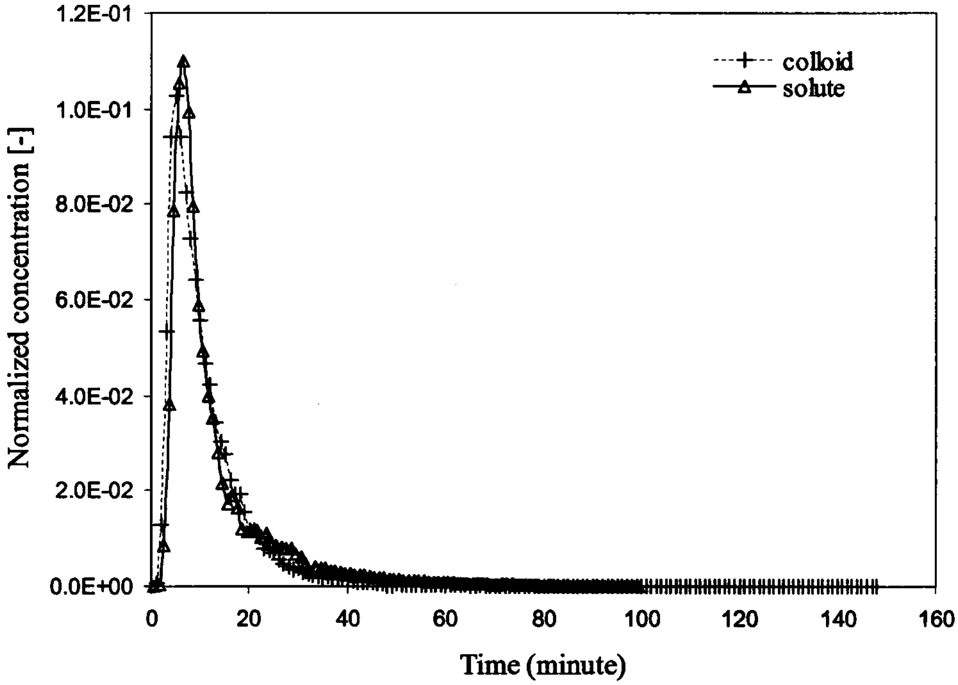

Figure B1.4 (a) Breakthrough curves for the colloid tracer tests in F1 with v_c = 1.09 mm/s, and Ic = 0.0001 and the one dimensional fitting results, and (b) comparison of the normalized colloid and solute breakthrough curves.

(a)

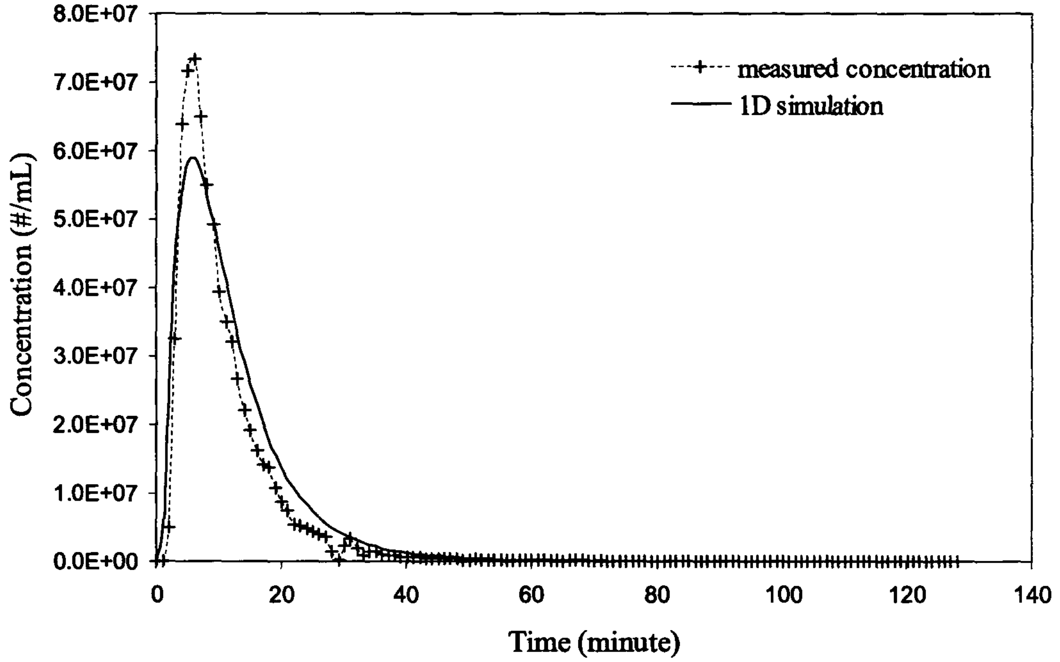

(b)

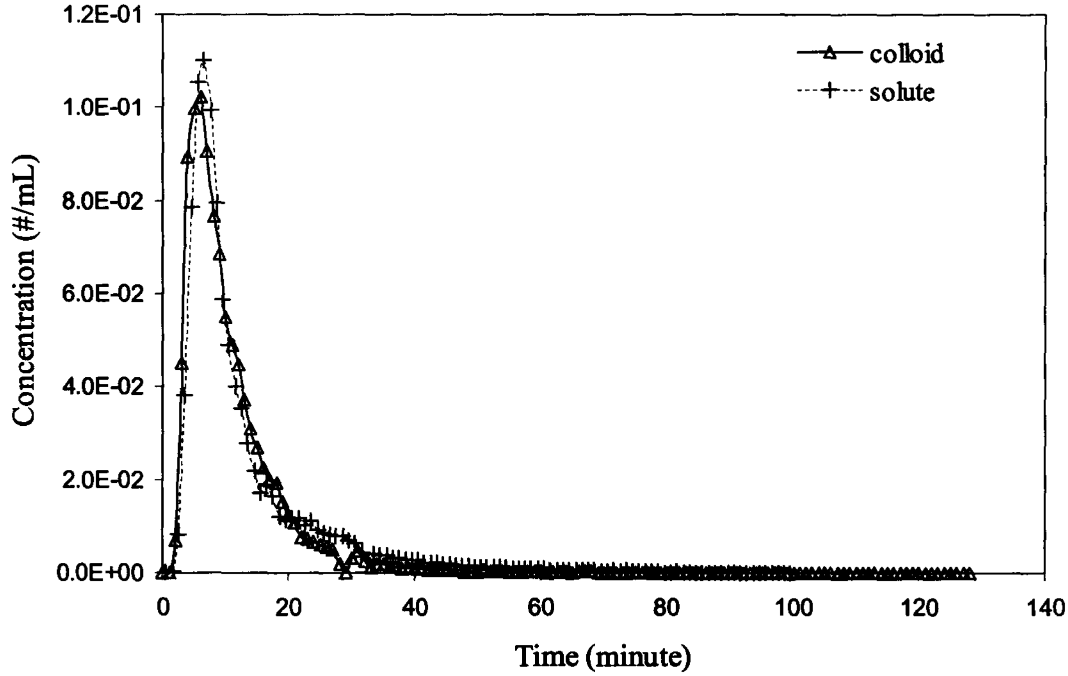

Figure B1.5 (a) Breakthrough curves for the colloid tracer tests in F1 with $v_c = 1.09$ mm/s, and Ic = 0.001 and the one dimensional fitting results, and (b) comparison of the normalized colloid and solute breakthrough curves.

(a)

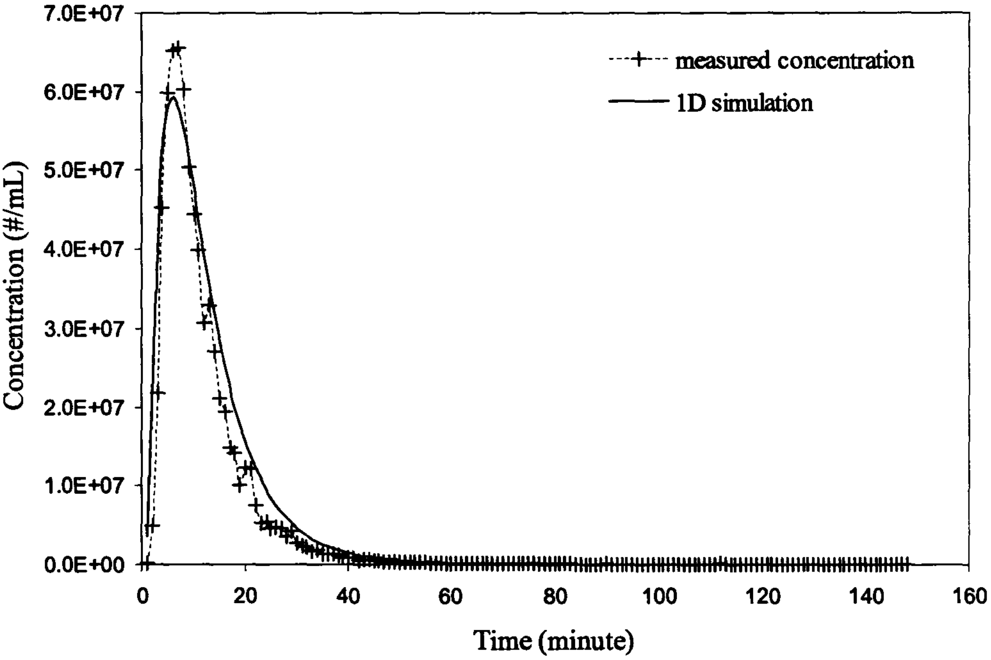

(b)

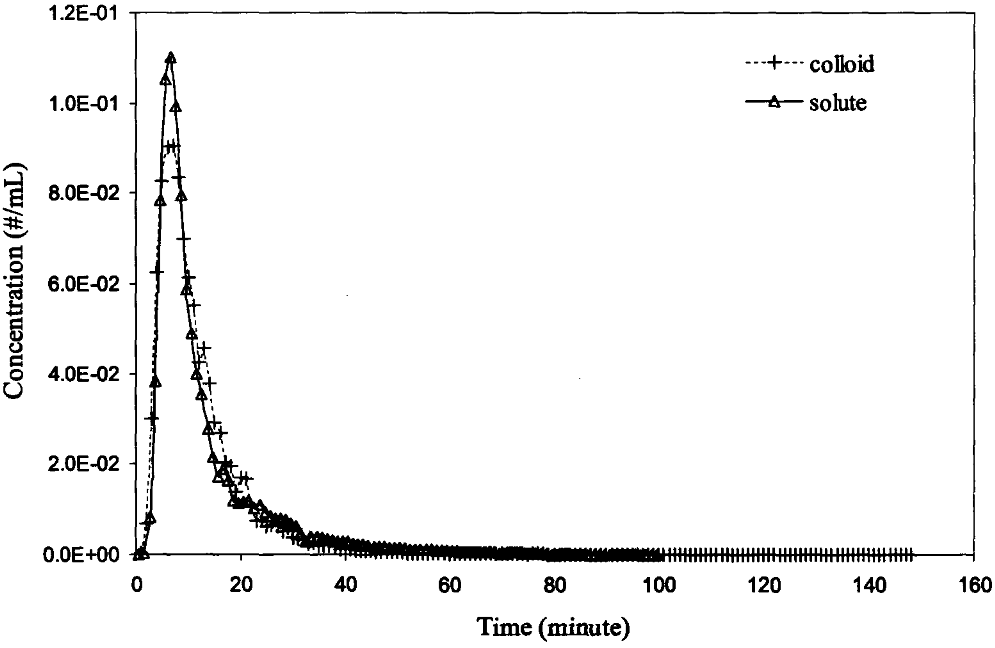

Figure B1.6 (a) Breakthrough curves for the colloid tracer tests in F1 with v_c = 1.09 mm/s, and Ic = 0.01 and the one dimensional fitting results, and (b) comparison of the normalized colloid and solute breakthrough curves.

(a)

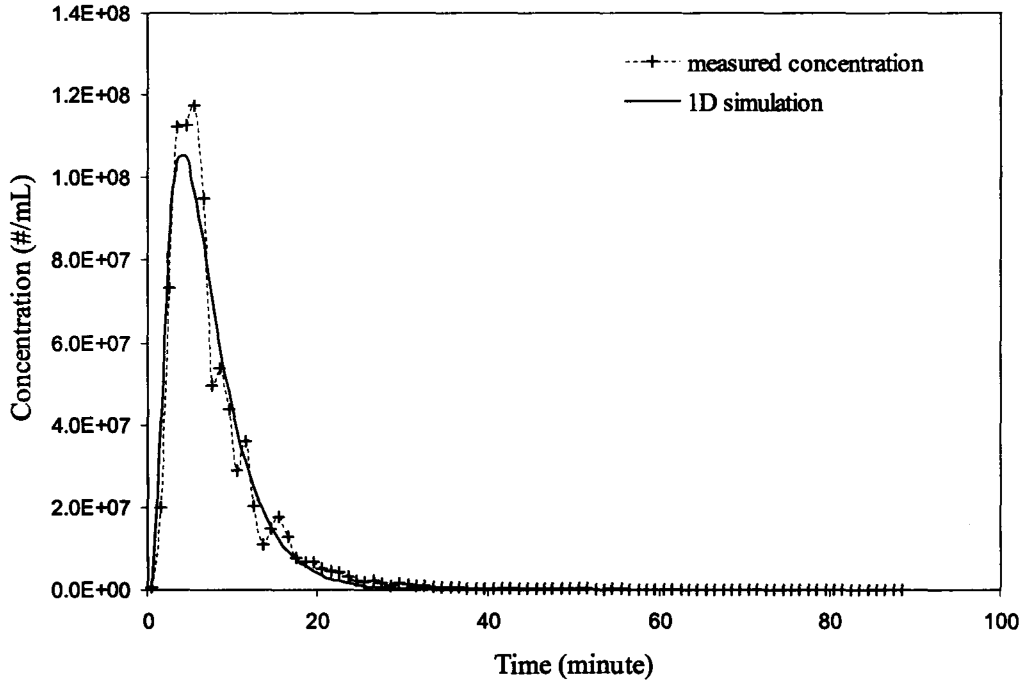

(b)

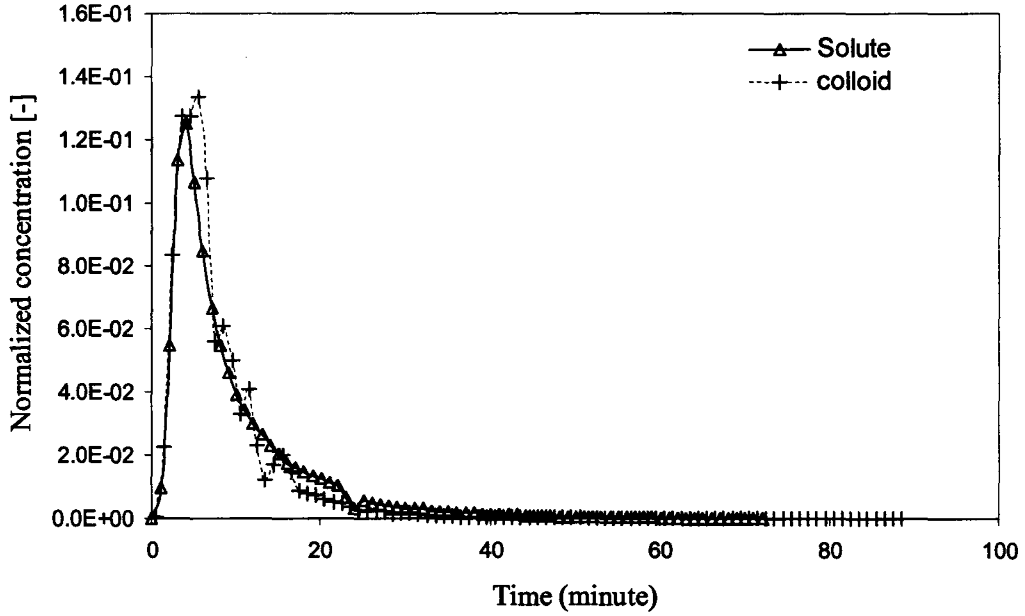

Figure B1.7 (a) Breakthrough curves for the colloid tracer tests in F1 with v_c =1.67 mm/s, and Ic = 0.0001 and the one dimensional fitting results, and (b) comparison of the normalized colloid and solute breakthrough curves.

(a)

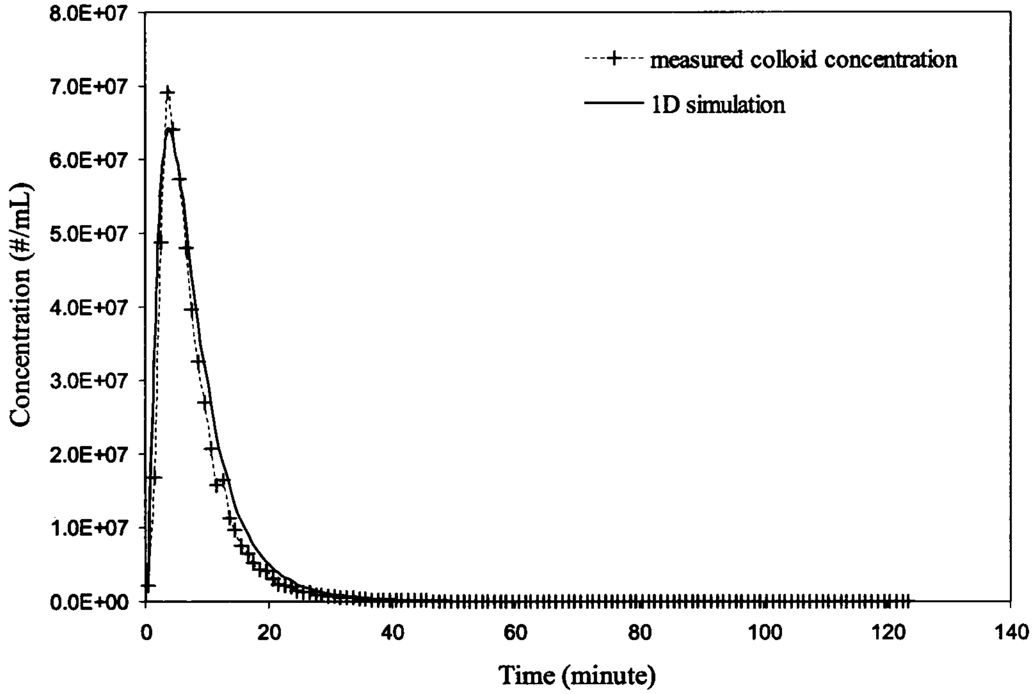

(b)

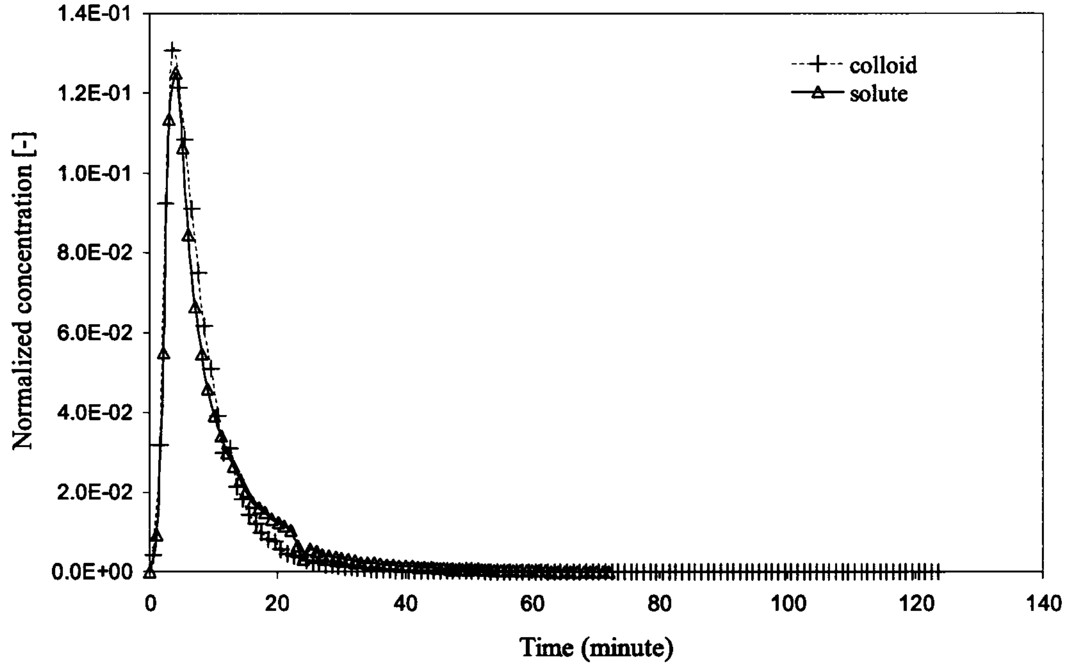

Figure B1.8 (a) Breakthrough curves for the colloid tracer tests in F1 with $v_c = 1.67$ mm/s, and Ic = 0.001 and the one dimensional fitting results, and (b) comparison of the normalized colloid and solute breakthrough curves.

(a)

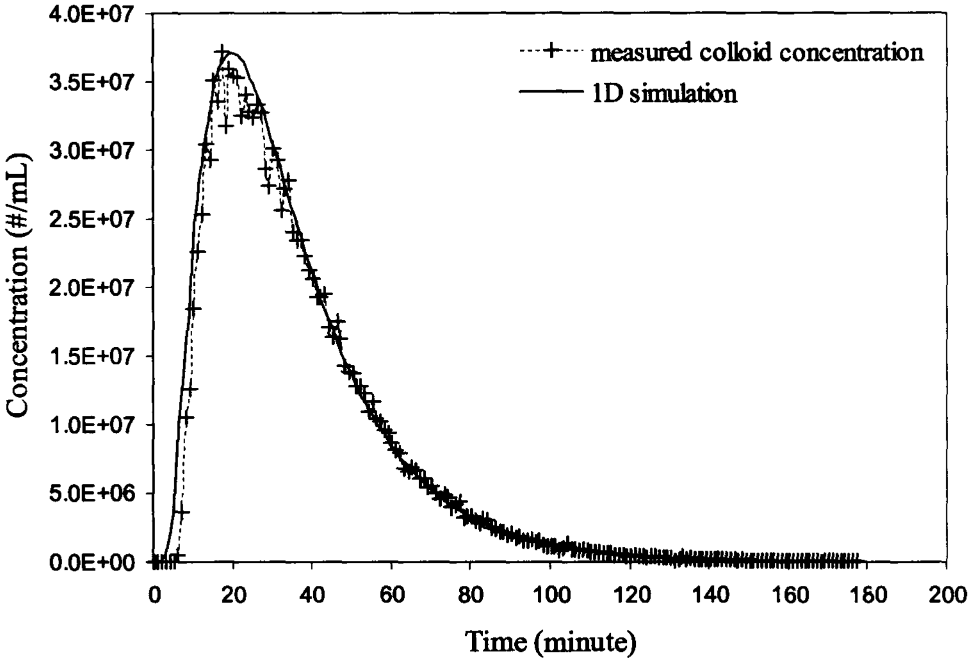

(b)

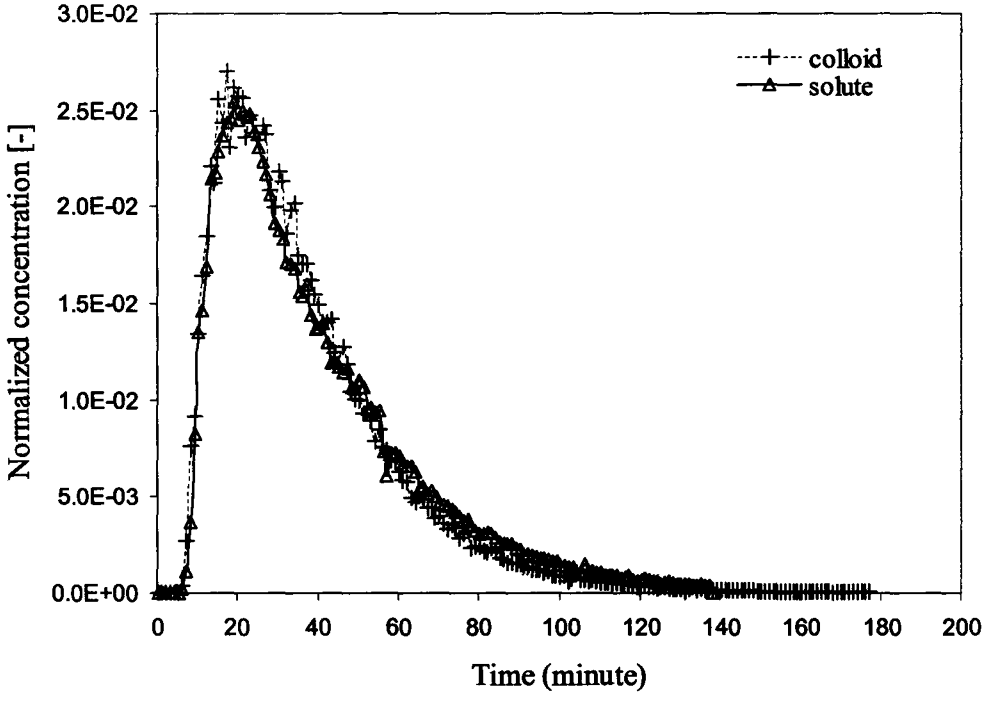

Figure B2.1 (a) Breakthrough curves for the colloid tracer tests in F2 with $v_c = 0.55$ mm/s, and Ic = 0.0001 and the one dimensional fitting results, and (b) comparison of the normalized colloid and solute breakthrough curves.

(a)

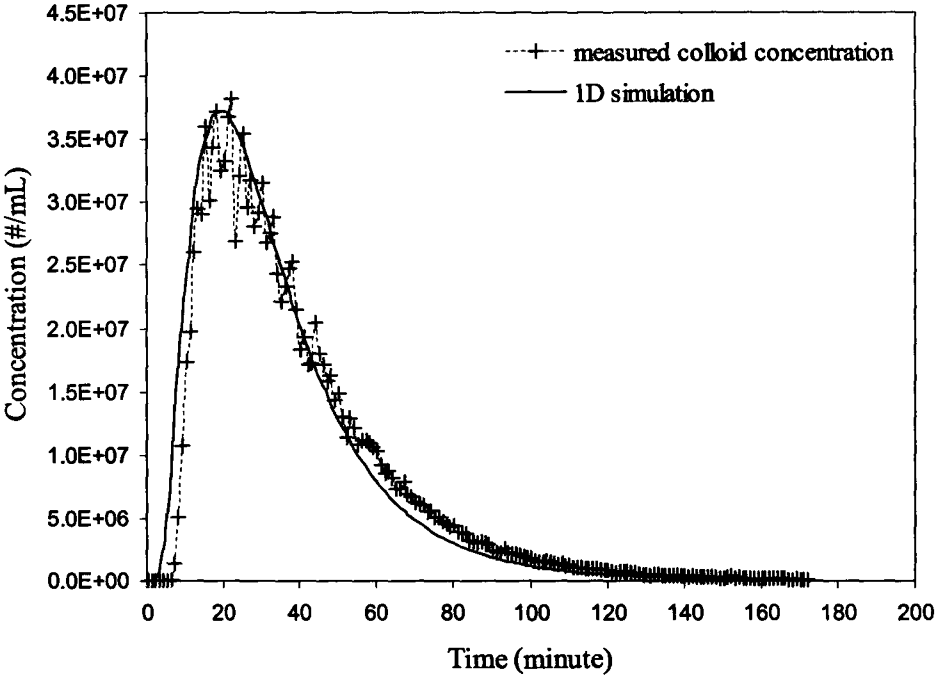

(b)

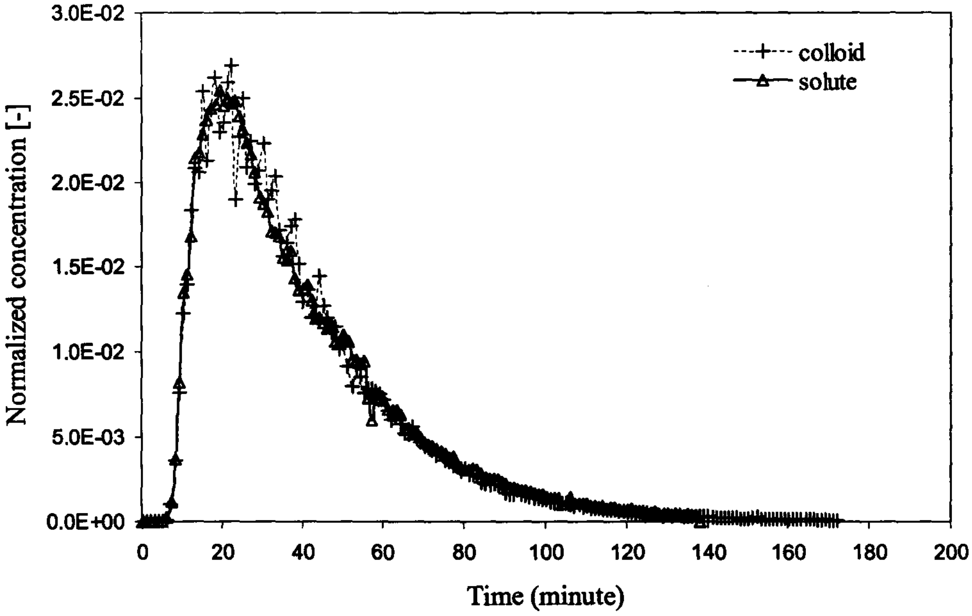

Figure B2.2 (a) Breakthrough curves for the colloid tracer tests in F2 with v_c = 0.55 mm/s, and Ic = 0.001 and the one dimensional fitting results, and (b) comparison of the normalized colloid and solute breakthrough curves.

(a)

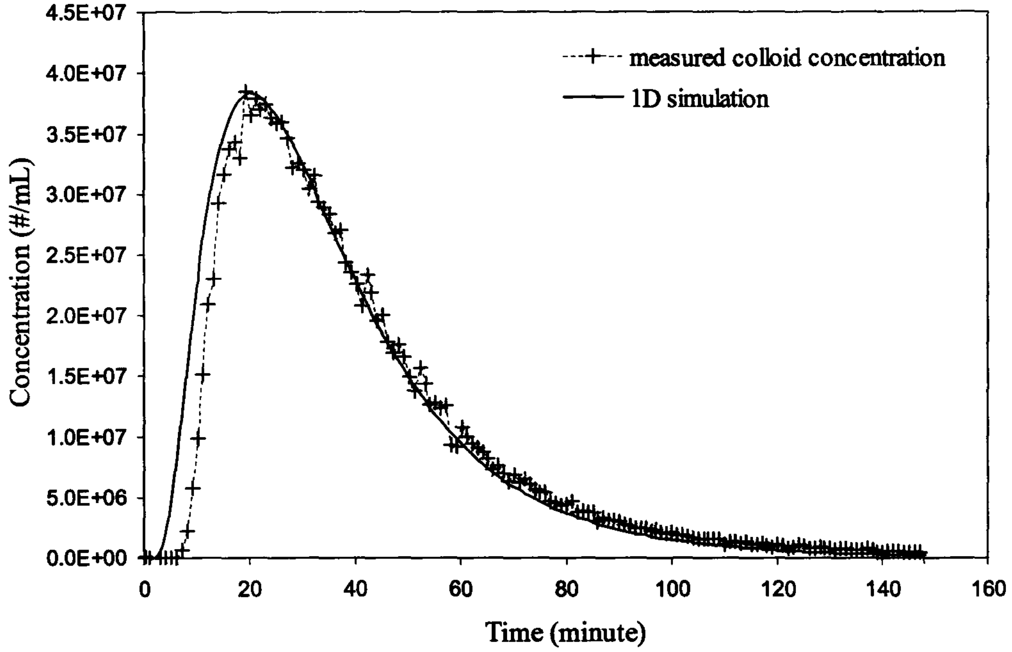

(b)

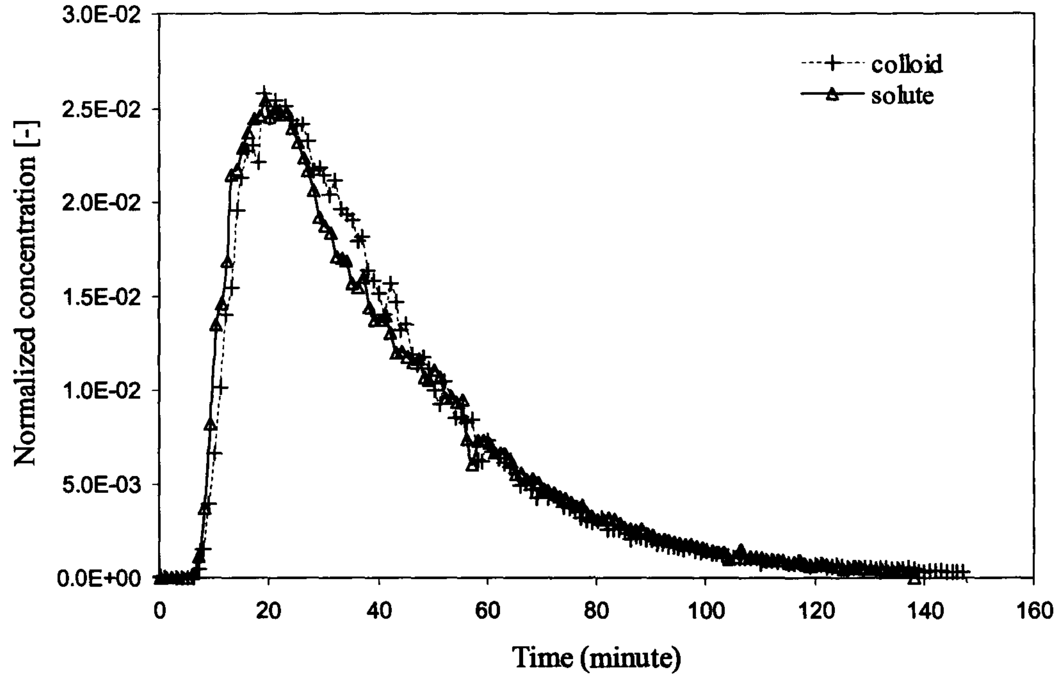

Figure B2.3 (a) Breakthrough curves for the colloid tracer tests in F2 with v_c = 0.55 mm/s, and Ic = 0.01 and the one dimensional fitting results, and (b) comparison of the normalized colloid and solute breakthrough curves.

(a)

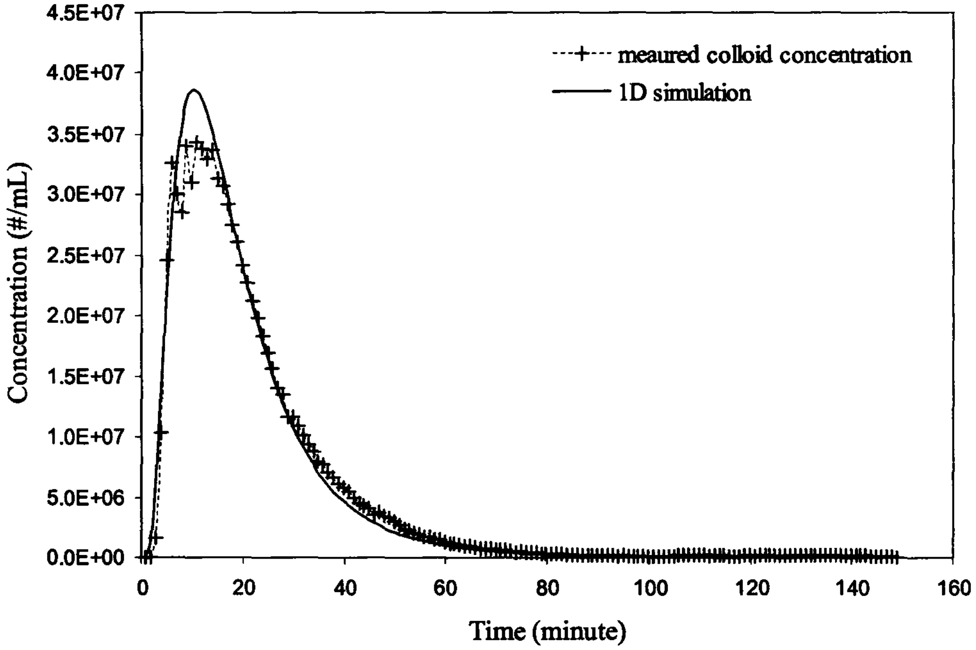

(b)

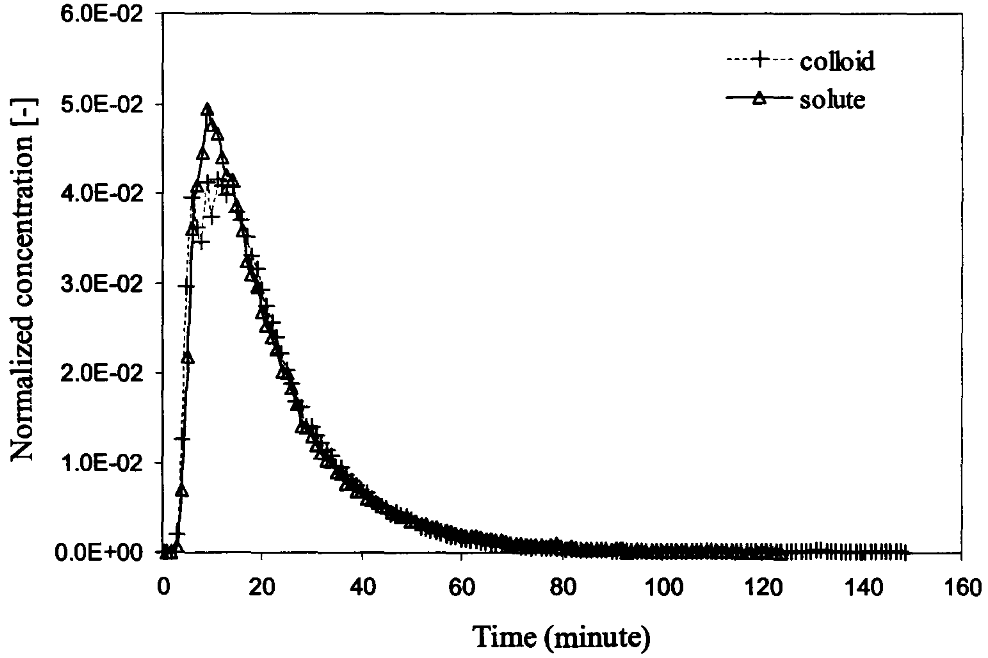

Figure B2.4 (a) Breakthrough curves for the colloid tracer tests in F2 with v_c = 1.09 mm/s, and Ic = 0.0001 and the one dimensional fitting results, and (b) comparison of the normalized colloid and solute breakthrough curves.

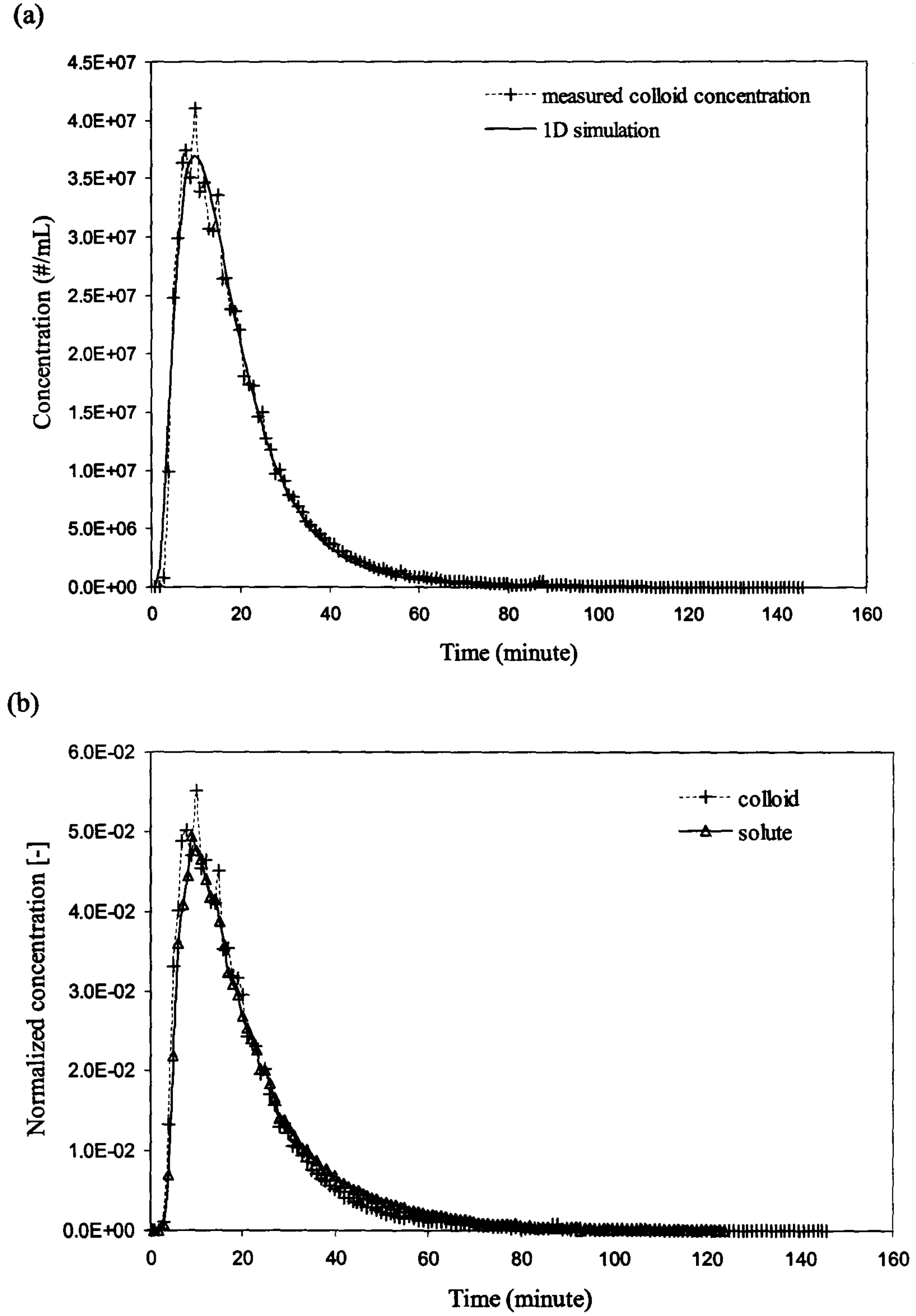

Figure B2.5 (a) Breakthrough curves for the colloid tracer tests in F2 with v_c = 1.09 mm/s, and Ic = 0.001 and the one dimensional fitting results, and (b) comparison of the normalized colloid and solute breakthrough curves.

(a)

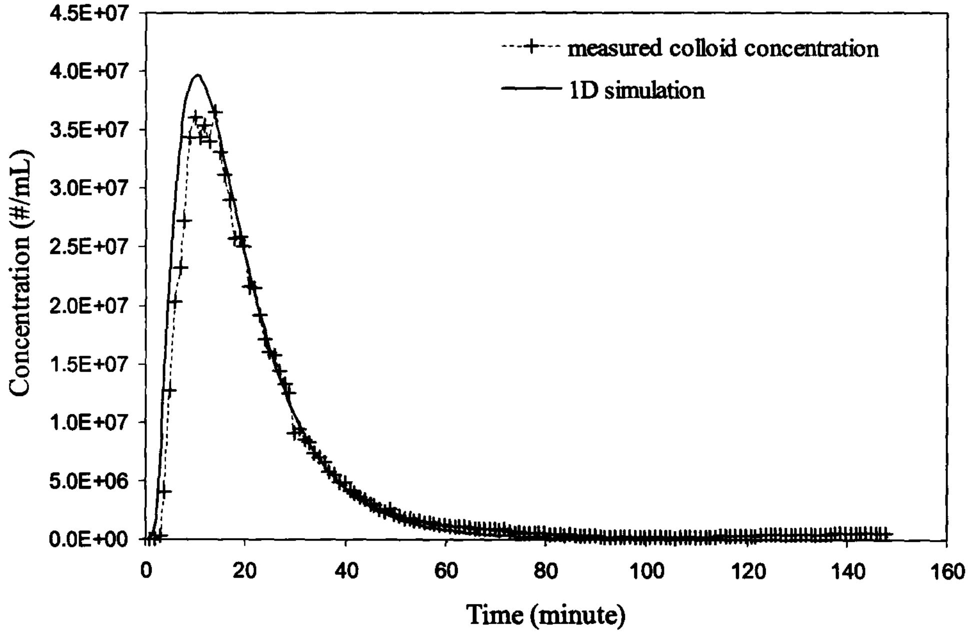

(b)

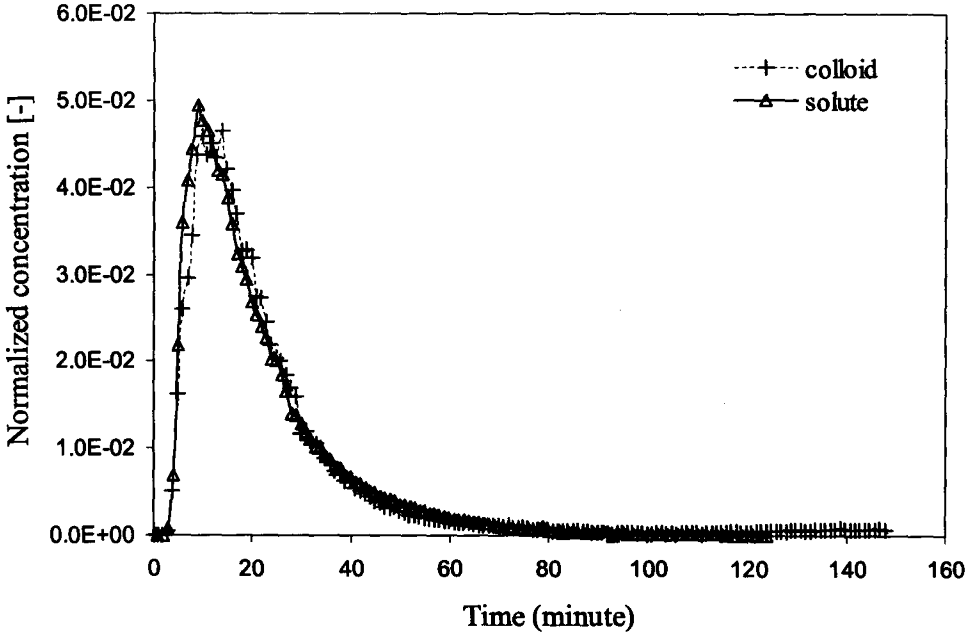

Figure B2.6 (a) Breakthrough curves for the colloid tracer tests in F2 with $v_c = 1.09$ mm/s, and Ic = 0.01 and the one dimensional fitting results, and (b) comparison of the normalized colloid and solute breakthrough curves.

(a)

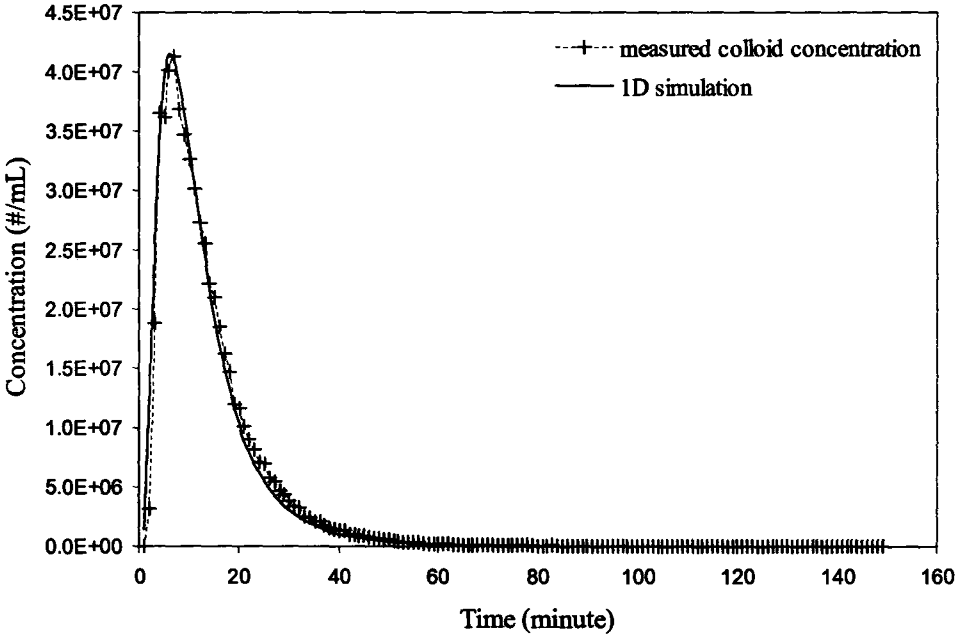

(b)

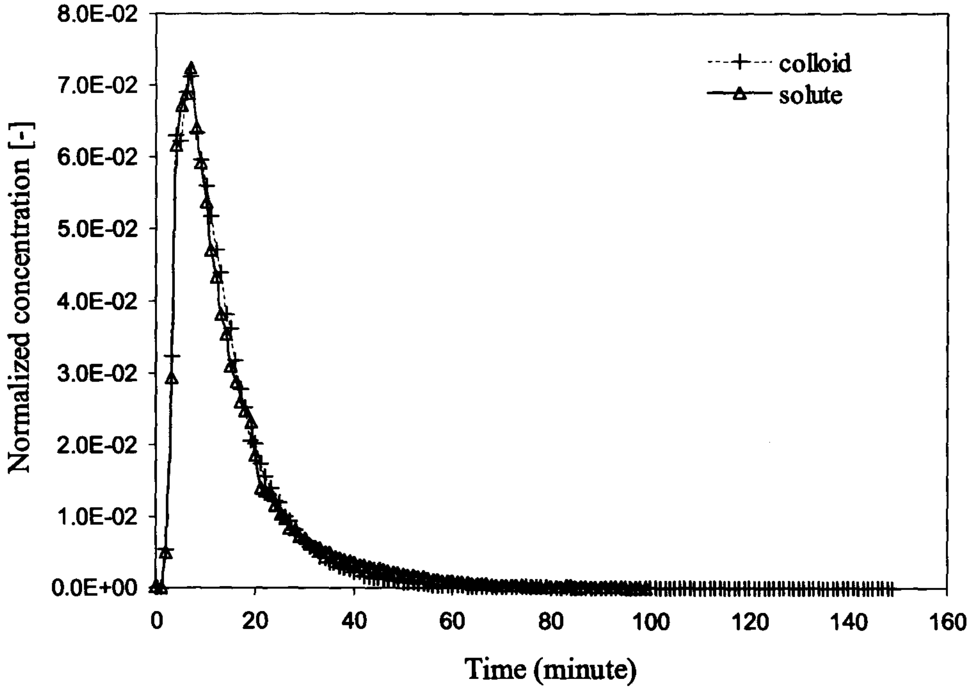

Figure B2.7 (a) Breakthrough curves for the colloid tracer tests in F2 with v_c = 1.67 mm/s, and Ic = 0.0001 and the one dimensional fitting results, and (b) comparison of the normalized colloid and solute breakthrough curves.

(a)

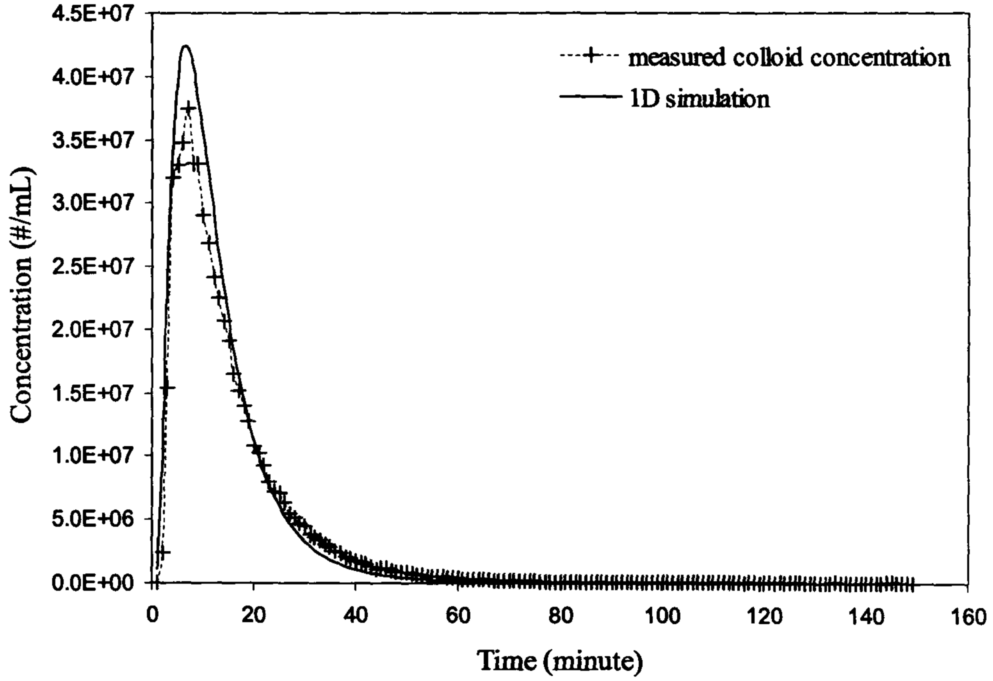

(b)

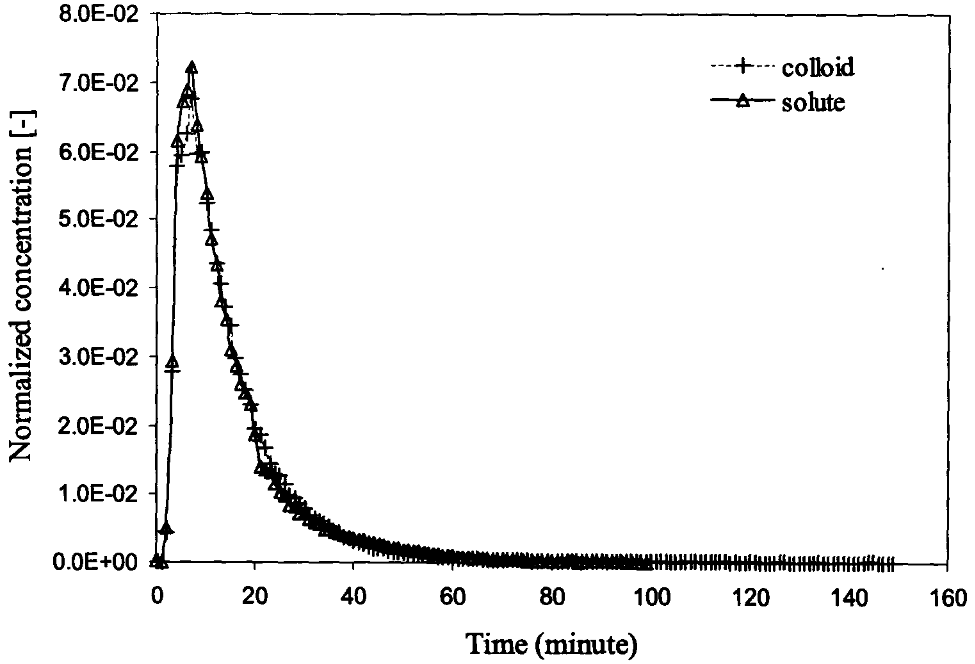

Figure B2.8 (a) Breakthrough curves for the colloid tracer tests in F2 with v_c = 1.67 mm/s, and Ic = 0.001 and the one dimensional fitting results, and (b) comparison of the normalized colloid and solute breakthrough curves.

(a)

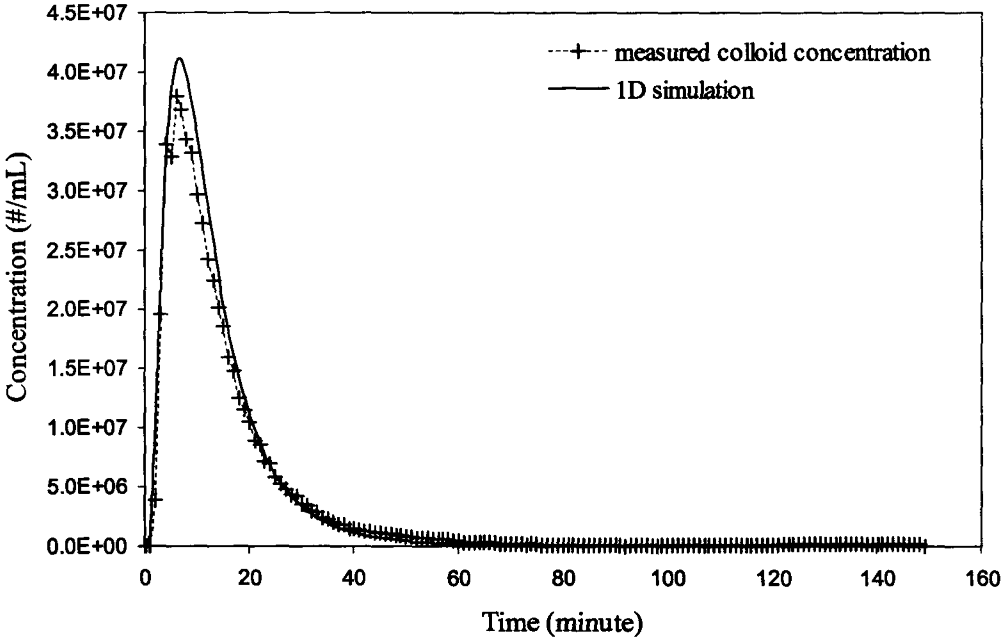

(b)

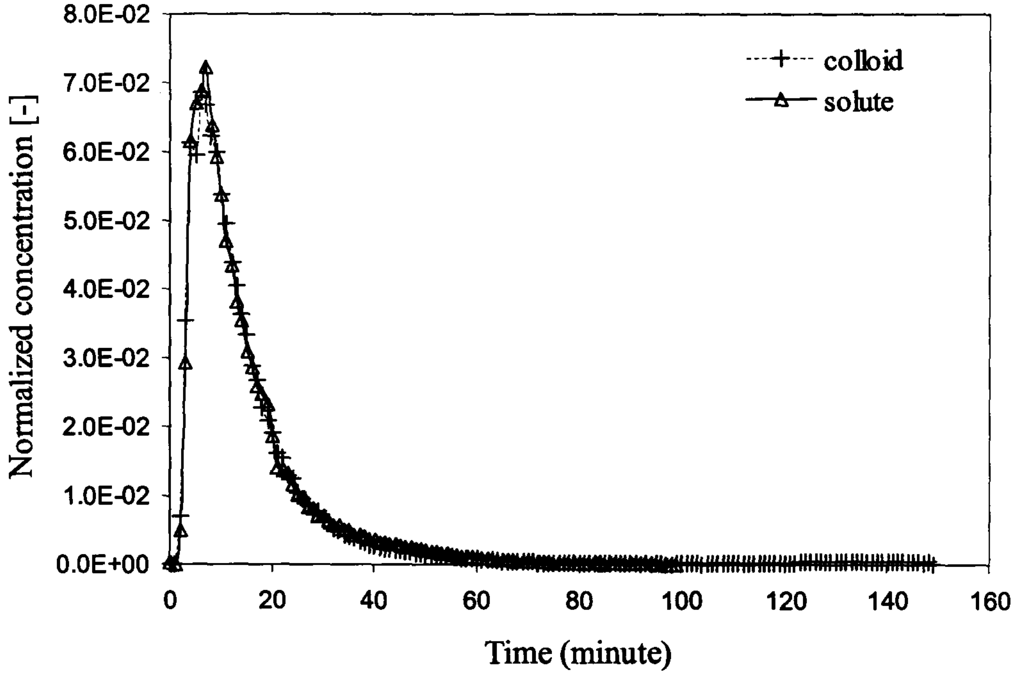

Figure B2.9 (a) Breakthrough curves for the colloid tracer tests in F2 with $v_c = 1.67$ mm/s, and Ic = 0.01 and the one dimensional fitting results, and (b) comparison of the normalized colloid and solute breakthrough curves.

(a)

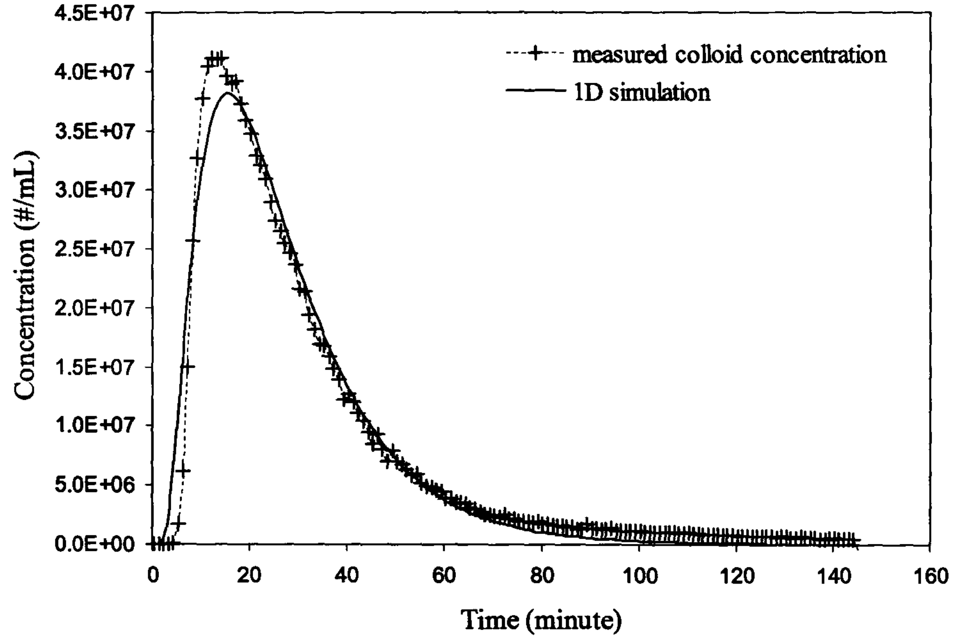

(b)

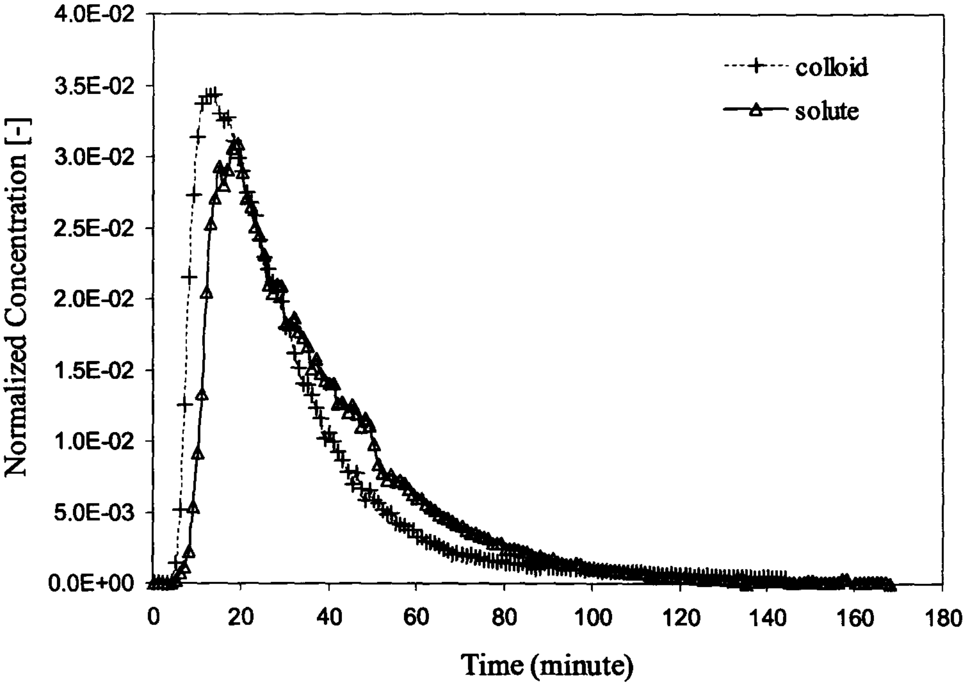

Figure B3.1 (a) Breakthrough curves for the colloid tracer tests in F3 with $v_c = 0.55$ mm/s, and Ic = 0.0001 and the one dimensional fitting results, and (b) comparison of the normalized colloid and solute breakthrough curves.

(a)

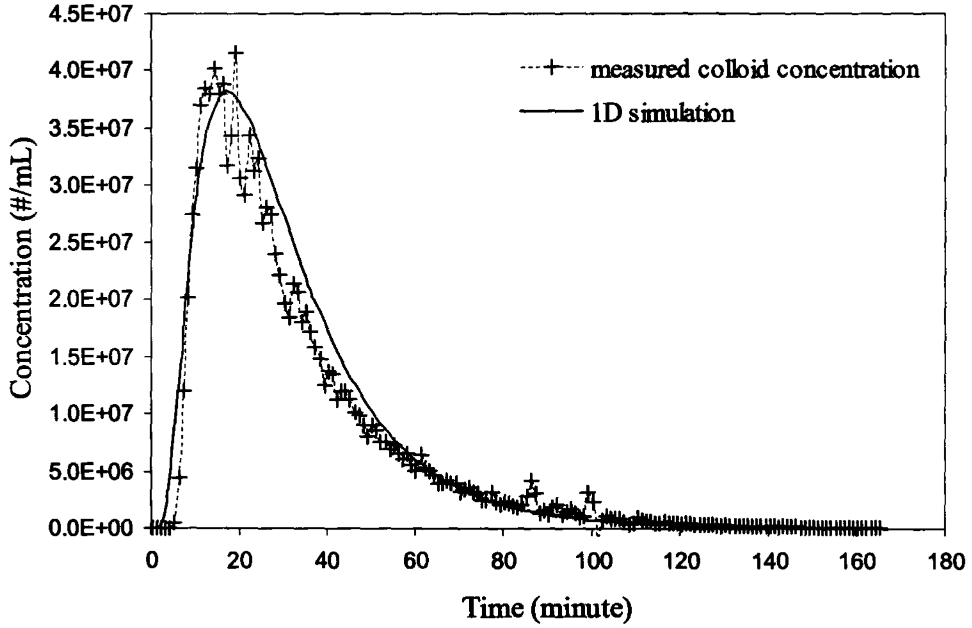

(b)

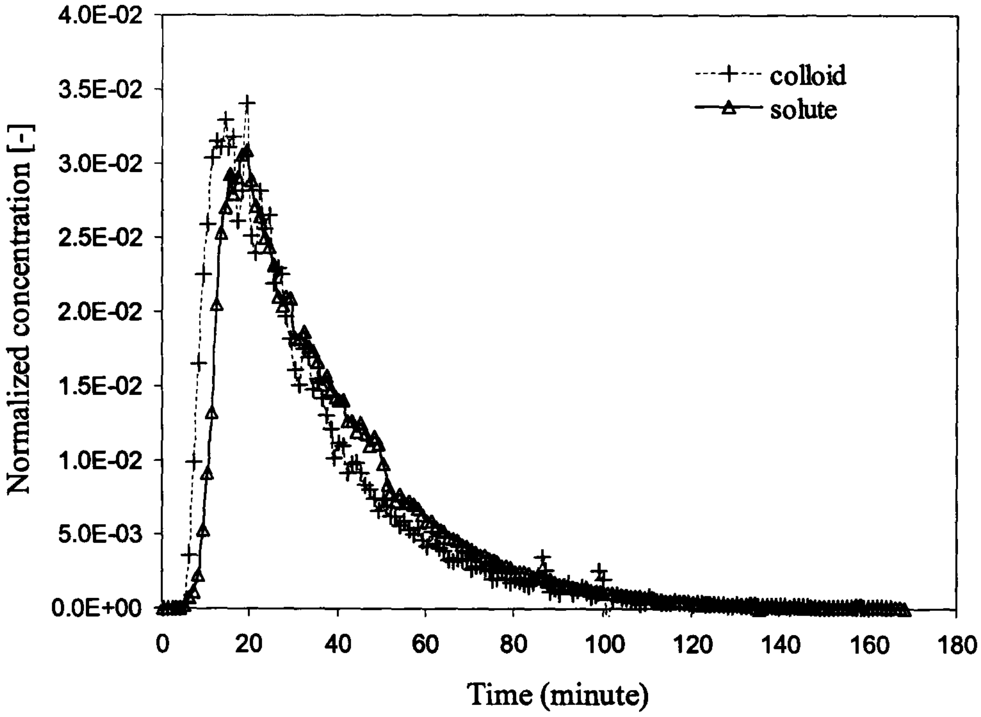

Figure B3.2 (a) Breakthrough curves for the colloid tracer tests in F3 with $v_c = 0.55$ mm/s, and Ic = 0.001 and the one dimensional fitting results, and (b) comparison of the normalized colloid and solute breakthrough curves.

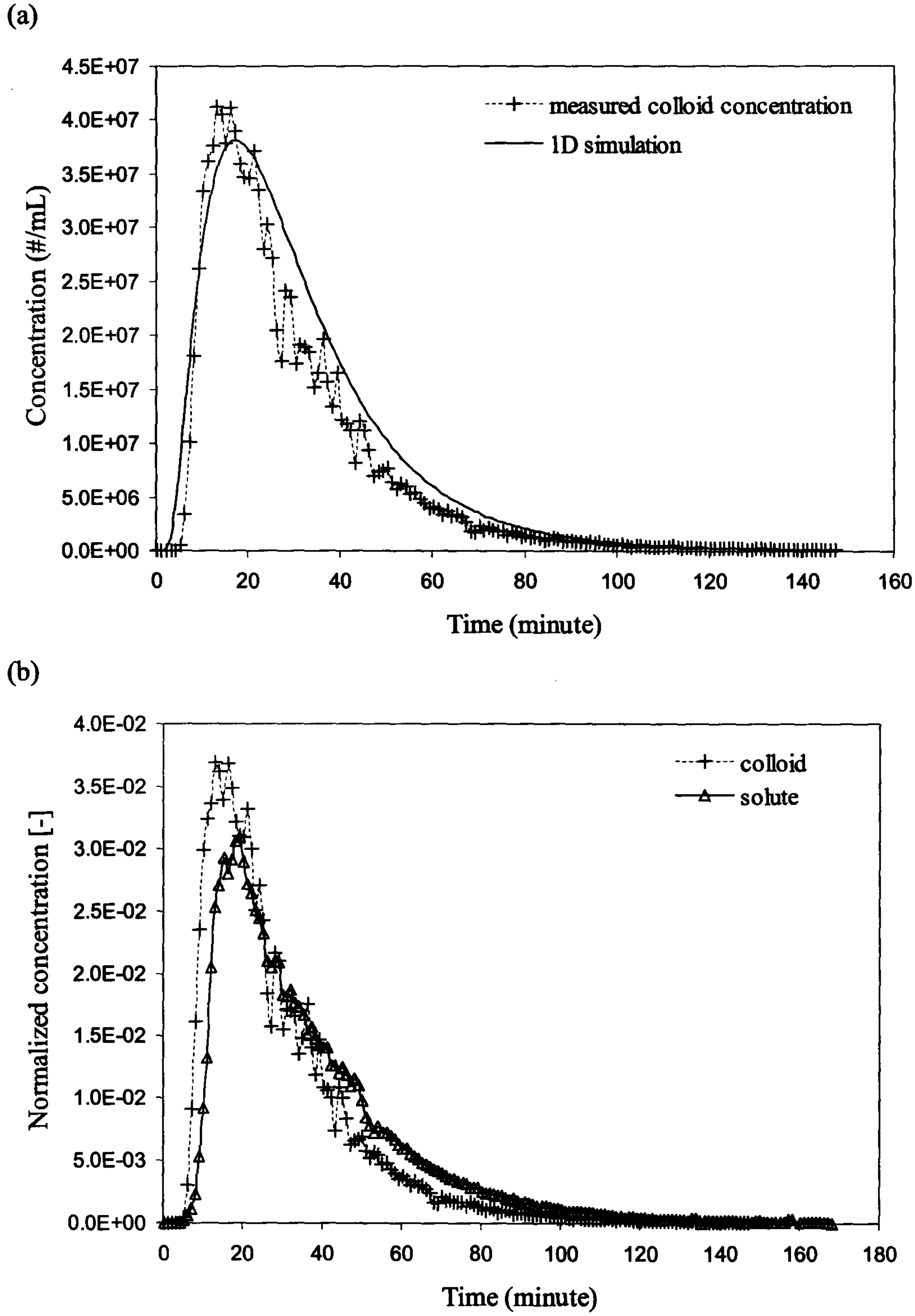

Figure B3.3 (a) Breakthrough curves for the colloid tracer tests in F3 with $v_c = 0.55$ mm/s, and Ic = 0.01 and the one dimensional fitting results, and (b) comparison of the normalized colloid and solute breakthrough curves.

(a)

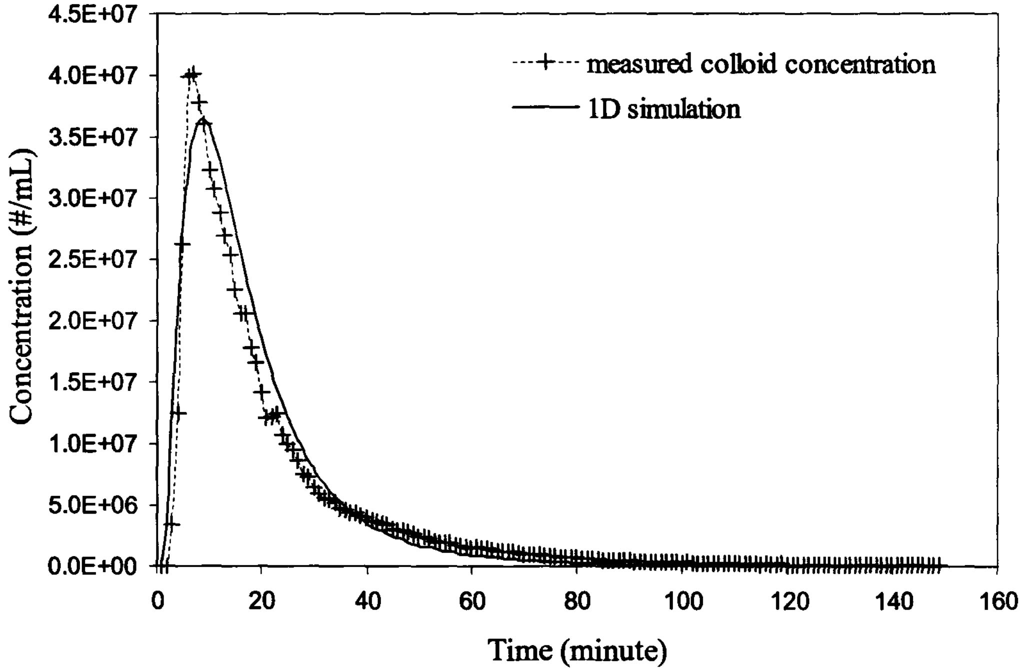

(b)

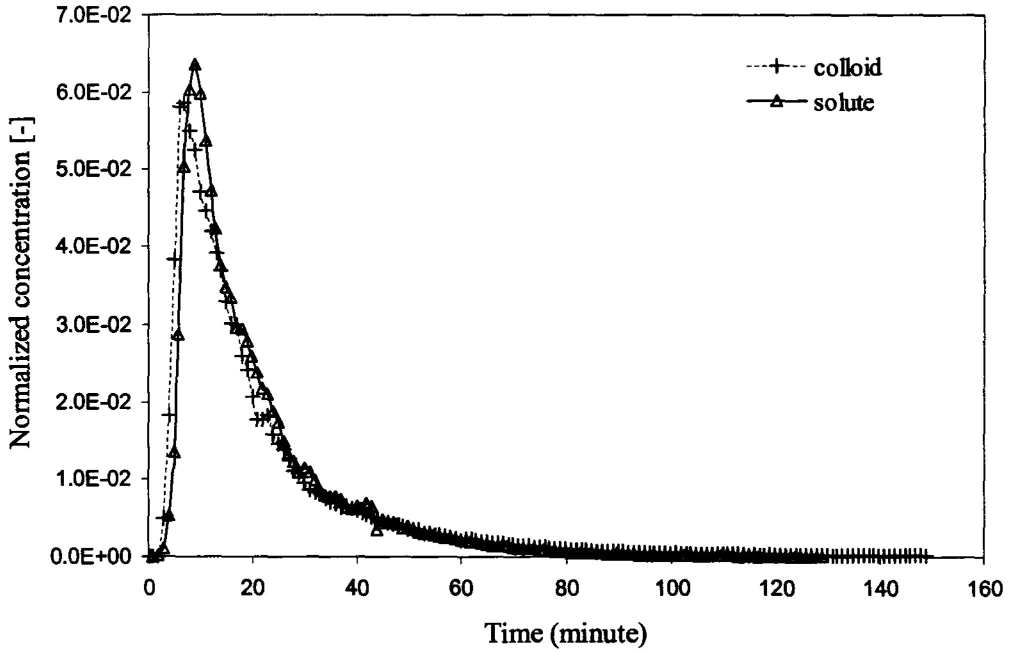

Figure B3.4 (a) Breakthrough curves for the colloid tracer tests in F3 with $v_c = 1.09$ mm/s, and Ic = 0.0001 and the one dimensional fitting results, and (b) comparison of the normalized colloid and solute breakthrough curves.

(a)

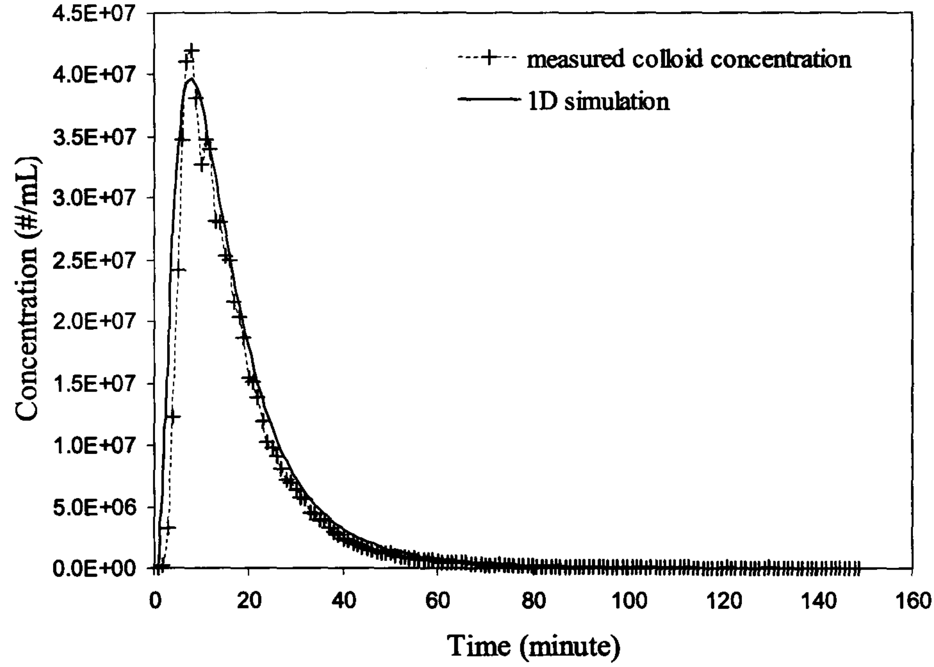

(b)

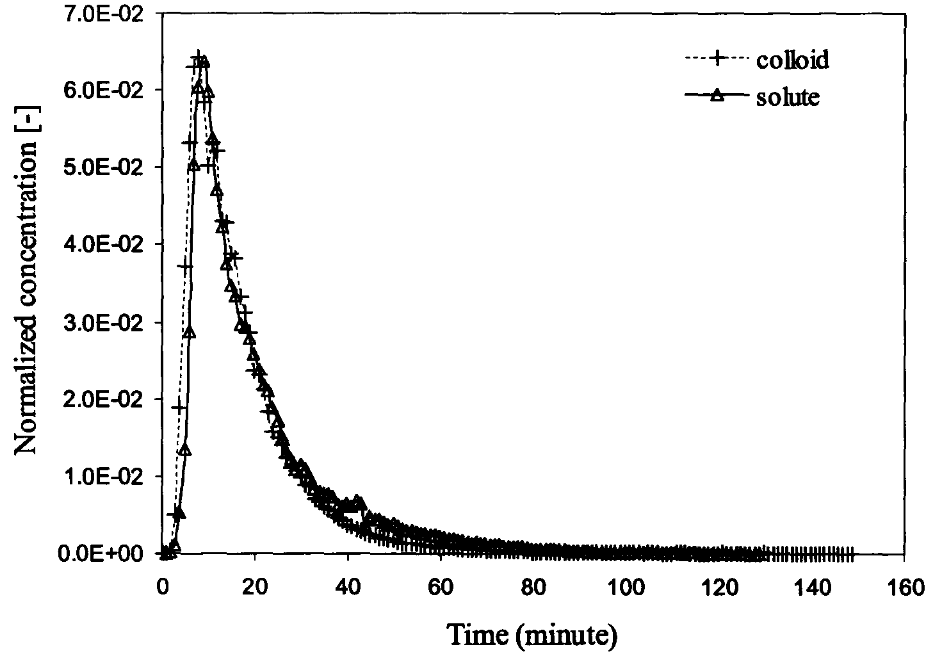

Figure B3.5 (a) Breakthrough curves for the colloid tracer tests in F3 with v_c =1.09 mm/s, and Ic = 0.001 and the one dimensional fitting results, and (b) comparison of the normalized colloid and solute breakthrough curves.

(a)

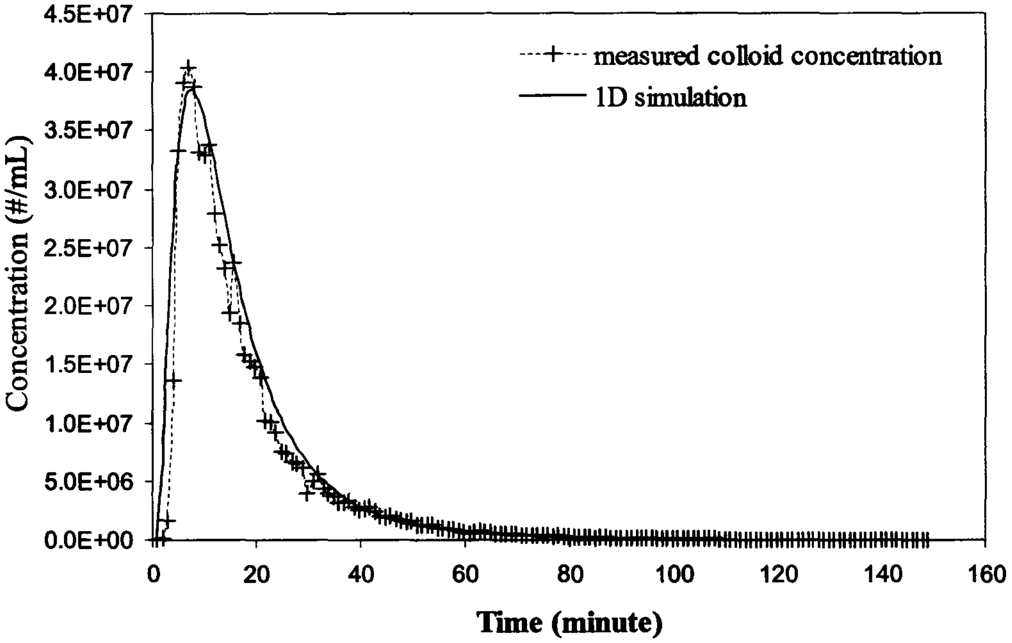

(b)

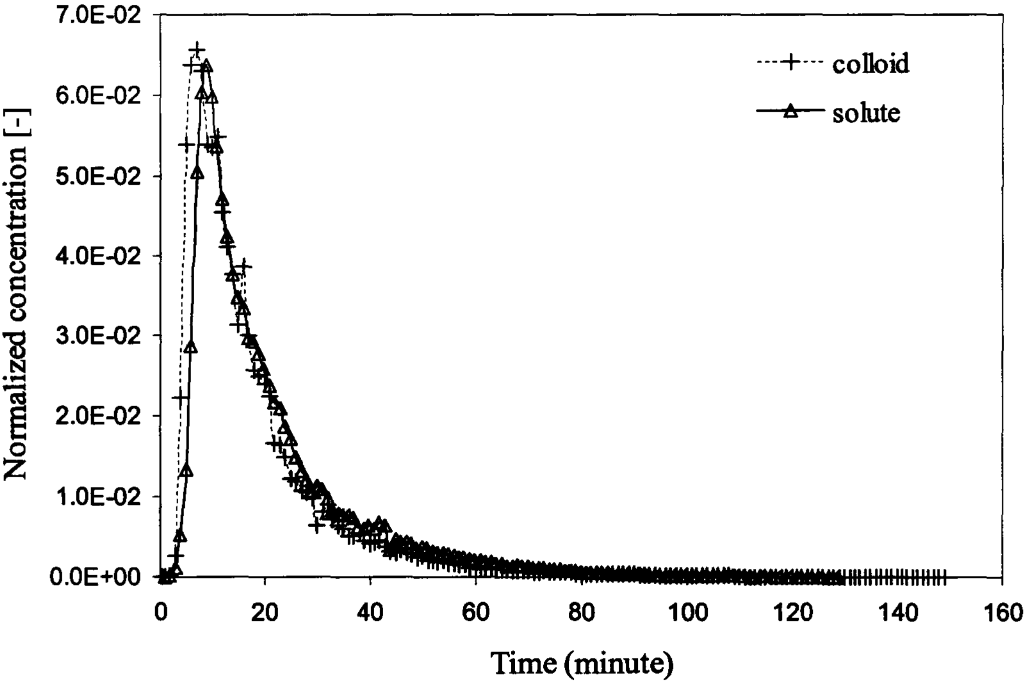

Figure B3.6 (a) Breakthrough curves for the colloid tracer tests in F3 with $v_c = 1.09$ mm/s, and Ic = 0.01 and the one dimensional fitting results, and (b) comparison of the normalized colloid and solute breakthrough curves.

(a)

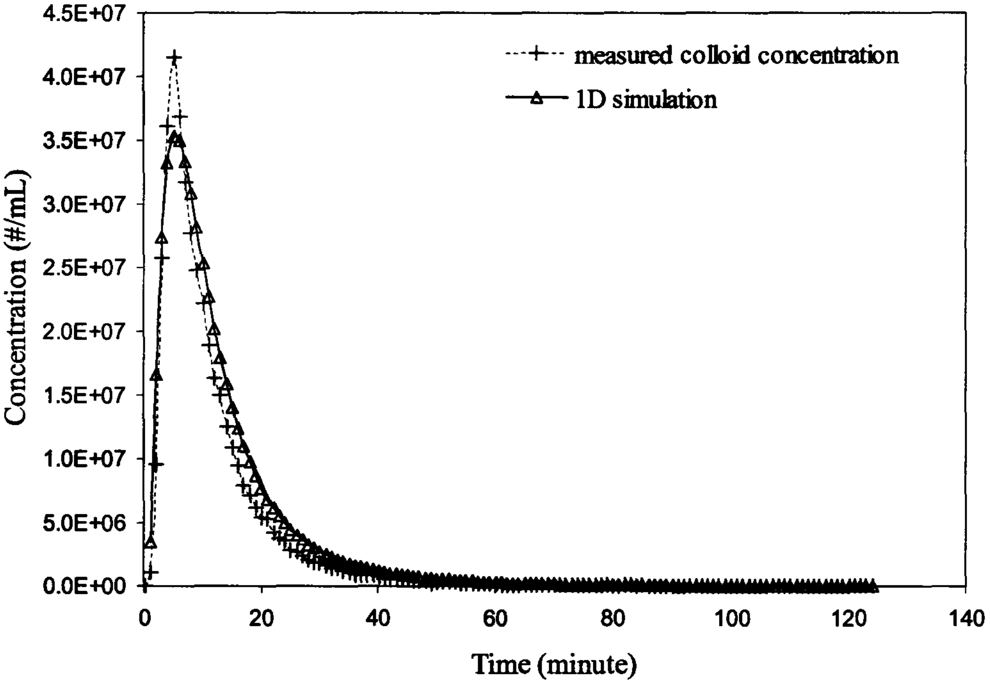

(b)

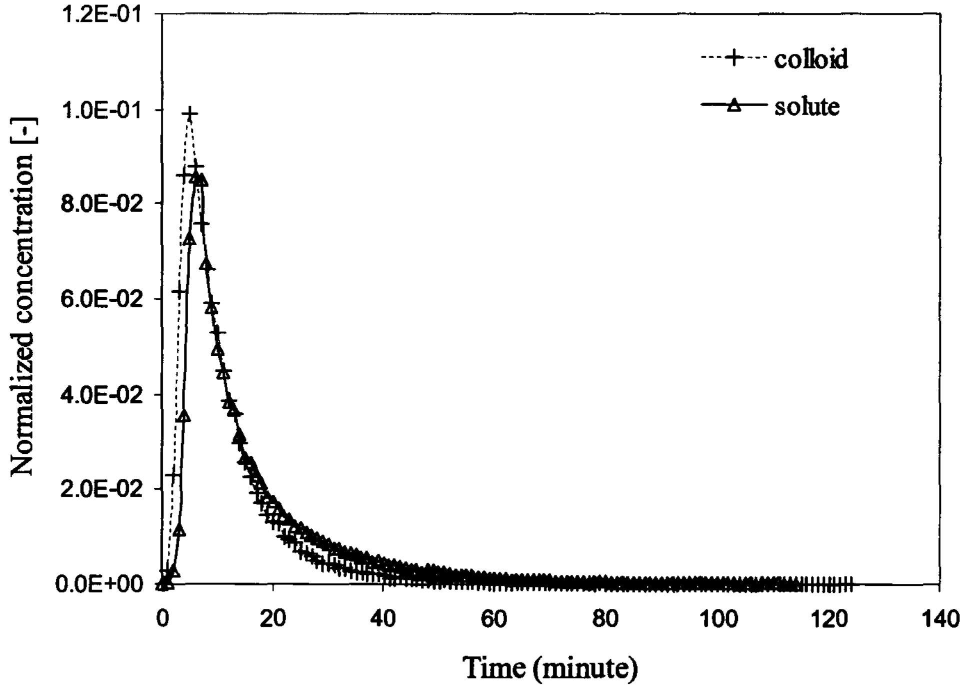

Figure B3.7 (a) Breakthrough curves for the colloid tracer tests in F3 with v_c = 1.67 mm/s, and Ic = 0.0001 and the one dimensional fitting results, and (b) comparison of the normalized colloid and solute breakthrough curves.

(a)

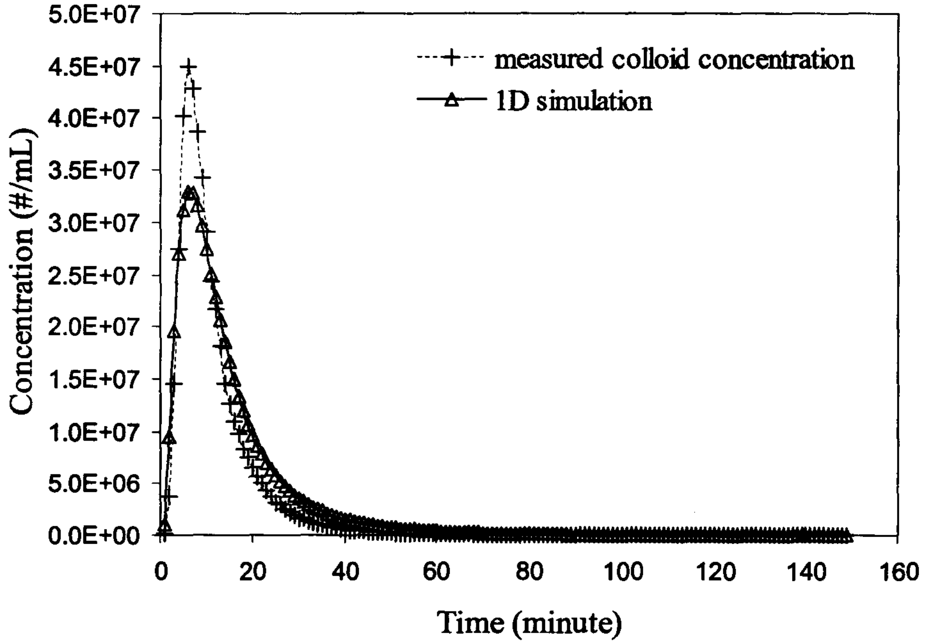

(b)

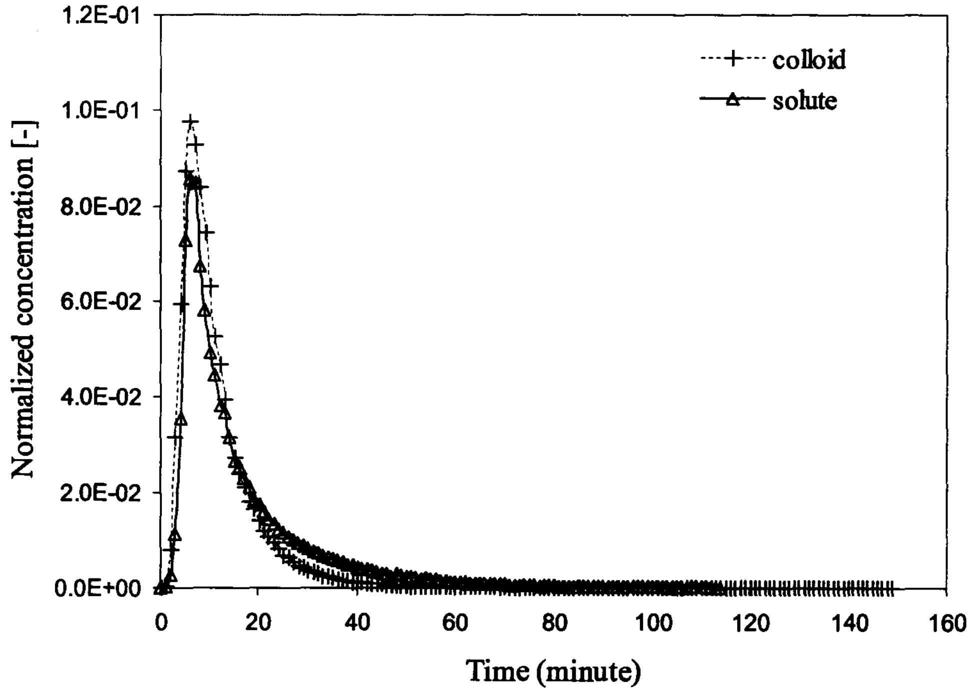

Figure B3.8 (a) Breakthrough curves for the colloid tracer tests in F3 with $v_c = 1.67$ mm/s, and Ic = 0.001 and the one dimensional fitting results, and (b) comparison of the normalized colloid and solute breakthrough curves.

(a)

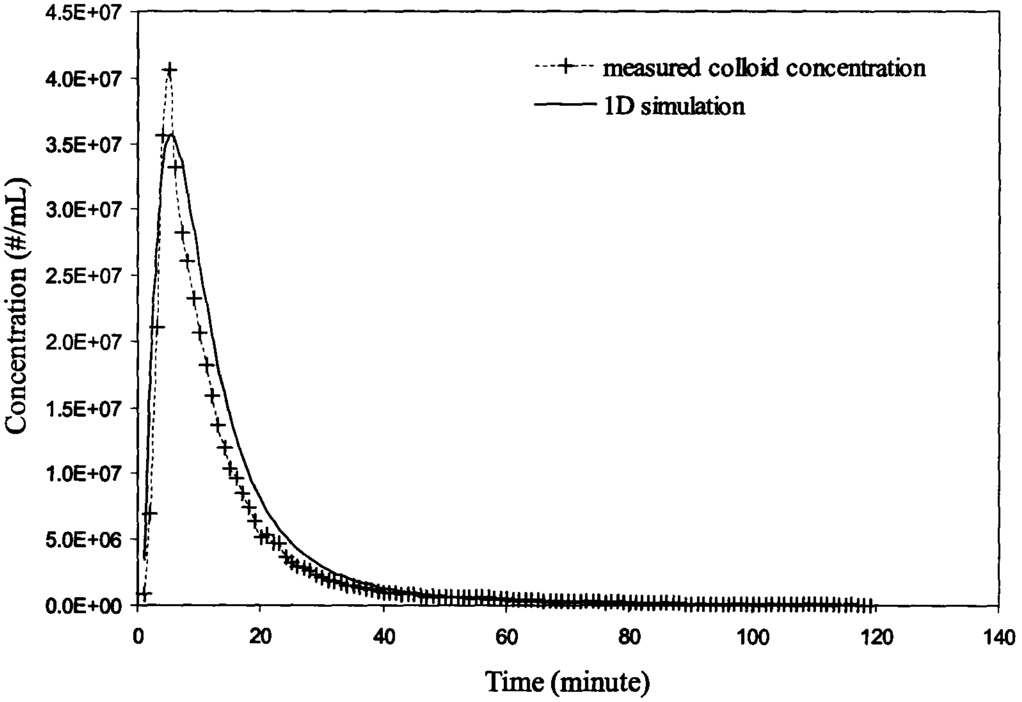

(b)

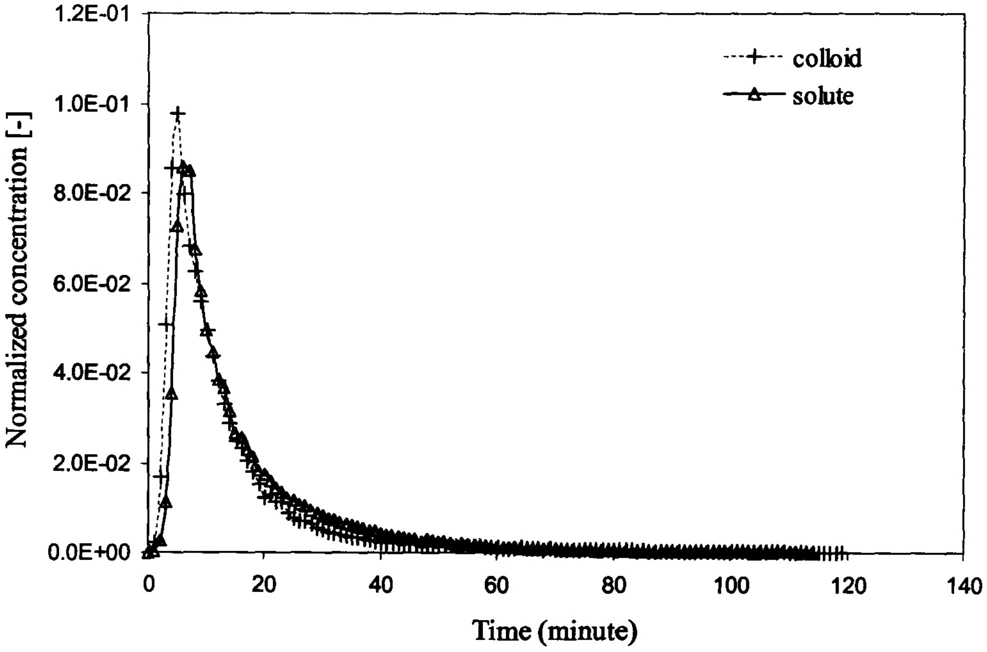

Figure B3.9 (a) Breakthrough curves for the colloid tracer tests in F3 with v_c = 1.67 mm/s, and Ic = 0.01 and the one dimensional fitting results, and (b) comparison of the normalized colloid and solute breakthrough curves.